Design and development of detector modules for a highly compact and portable preclinical PET system

by

Fazal ur-Rehman

A Thesis submitted to the Faculty of Graduate Studies of

The University of Manitoba

in partial fulfilment of the requirements of the degree of

DOCTOR OF PHILOSOPHY

Department of Physics & Astronomy

University of Manitoba

Winnipeg

Abstract of the dissertation

Preclinical PET systems image animal models of chronic human disease that are used to evaluate new therapeutic strategies for the treatment of cancer and other diseases. Once these animals are out of a controlled environment for PET imaging, they typically can not be taken back as they may have been exposed to outside disease. A highly compact PET system is thus required to be developed that can operate within a bio-safety cabinet inside a barrier facility.

We investigated using 100-mm-long LYSO scintillator crystals oriented in the axial direction and read out at both ends by position sensitive photomultiplier tubes (PSPMTs) to construct a compact PET. The optimization of light collection for axial encoding of events was carried out using different reflector materials and surface treatments of $3 \times 2 \times 100$ mm^3 and $2 \times 2 \times 100$ mm^3 polished crystals. The detector response was examined by irradiating the crystals at discrete positions using an electronically collimated 511 keV photon beam. The ratio of two PSPMT signals was used to find the axial-resolution while their sum was used to determine the energy resolution. We then explored the effects of creating systematic band patterns of surface roughing on 1 to 4 long surfaces of the crystals to modulate light-transport with the goal of further improving axial-resolution. These experimental results were used to benchmark DETECT2000 Monte Carlo simulations for our detector geometry. The axial-positioning calibration was carried out by evaluating a uniform flood-irradiation method and comparing with the collimated-irradiation method using $2 \times 2 \times 100$ mm^3 crystal detectors.

The best axial-positioning resolution of 3.4 mm was achieved in this study for 2 × 2 × 100 mm^3 Teflon-wrapped crystals with banding-patterns on only two opposite surfaces, fulfilling the design criteria of our proposed PET. The benchmarked DETECT2000 models can now be used to predict the performance of a complete detector module design. The calibration methods agreed if the trigger threshold energies were adjusted to give similar single event rates in both PSPMTs for uniform flood-irradiation. The implementation of flood-irradiation method in our complete PET scanner will provide a simple axial-positioning calibration.

Acknowledgements

The research project was funded by the Natural Sciences and Engineering Research Council, Manitoba Health Research Council and Health Sciences Center Foundation. Medical Devices at the CancerCare, Manitoba is thankfully acknowledged for the construction of the experimental setup used in this project.

I would like to extend my sincere gratitude to my supervisor, Dr. Andrew L. Goertzen, for his guidance, support and leadership throughout my PhD studies. I feel honoured to work under the supervision of an intellectual Professor and Scientist who not only mentor me but also put me on the road of my professional career ahead. I would like to thank my advisory committee, Dr. Kumar Sharma, Dr. Idris Elbakri and Dr. Jitendra Paliwal, for their questions, comments, feedback and guidance that kept me on the right track during the execution of the project. I thankfully acknowledge the thoughtful questions and feedback of my external examiner, Dr. Todd Peterson, Institute of Imaging Science, Vanderbilt University, USA.

I am grateful to all graduate students in Medical Physics, Bryan McIntosh, Ganiyu Asuni, Chen-Yi Liu, Leonid Lamwertz, Eric Berg for their company and fruitful discussion over the years. I also thank Dr. Geoff Dean, Dr. Esmat Elhami, and Dr. Xuezhu Zhang for their friendship and technical discussion.

I thank my parents, Qalandar Jan and Abdul Rahim (Rahimahullau), for their continuous support and encouragement over the years. Without them it could not have been possible for me to climb the stairs of success.

Finally, I must thank my wife, Fahmeeda, for her exciting company on the bumpy road to PhD. Fahmeeda I admire your continuous support and encouragement to reach at this

point. Your patience during the prolonged sickness of our daughter, Hafsa, since 2008, is unforgettable while going back and forth to children hospital and doing my PhD courses' assignments sitting in the hospital. The company of my sons, Osama and Abdul-Rafey, in this journey is memorable. I have a couple of chapters in mind to write on this topic along with my PhD Thesis.

Table of contents

List of tables

List of figures

List of copyrighted material

Chapter 1 Global Scope and Objective

1.1 Motivation for work

Preclinical PET systems can image animal models of chronic human disease that are used to evaluate new therapeutic strategies for the treatment of cancer and other diseases. In many cases, these animals have to be kept under controlled environmental conditions, such as bio-safety cabinets, when being handled. Once the animals are out of a controlled environment for PET imaging, they typically can not be taken back as they may have been exposed to outside disease that could be transferred to other animals in the facility. This is problematic for long-term repeat imaging of a single animal. For these reasons, a highly compact and portable PET system is required to be designed and developed that can operate within a bio-safety cabinet inside a barrier facility or alternatively on a laboratory bench top without the need for a dedicated PET imaging suite that requires a substantial financial investment. The design criteria for this system are low cost, low complexity, high sensitivity and should image the entire mouse in 1 bed position with an isotropic spatial resolution of better than 3 mm. A mock-up of our proposed design concept for a highly compact geometry, portable PET imaging system that will allow operation in a laboratory setting or in a biosafety cabinet is shown in figure 1.1. In this global context, the objective of my research project is to design and develop a high sensitivity dual-ended readout detector module to be used in a highly compact and portable geometry positron emission tomography (PET) scanner. We propose to make use of arrays of long thin scintillator crystals oriented in the axial direction and read out at both ends by low cost position sensitive photomultiplier tubes (PSPMTs) to construct a compact animal PET system.

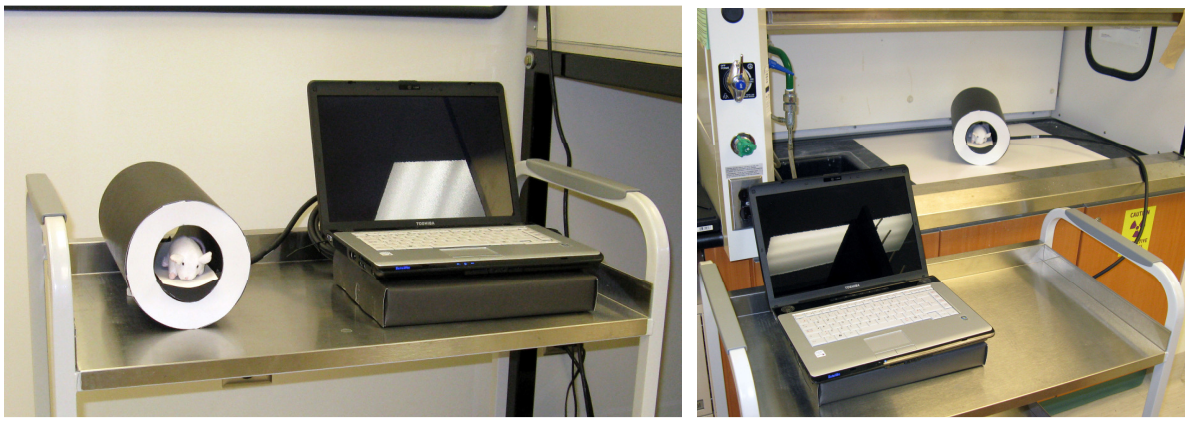

Figure 1.1 Photographs of a mock-up of our design concept for a highly compact geometry, portable PET imaging system. On the left, the system is shown on a laboratory cart. The cylindrical detector gantry has a rat sized stuffed animal in it for scale. The laptop computer for data acquisition sits on top of a compact electronics cabinet. On the right, the system is shown within a laboratory fume hood with comparable dimensions to a biosafety cabinet.

1.2 Specific Objectives

To achieve the above mentioned goals, the research work for my Ph.D. consists of the following projects related to the development of compact detectors:

a) Optimize the light output of long, thin LYSO crystals readout at either end by photodetectors for spatial and energy resolution using:

   (i) Different reflector materials and (ii) surface treatment of the crystals

b) Calibrate the dual-ended readout of axially oriented LYSO crystals for use in a compact PET system

c) Determine the DETECT2000 simulation parameters required to give good agreement with our measured data, on the surface treatment/reflectors for improving spatial resolution, in order to benchmark the simulation for this detector geometry and allow the future use of Monte Carlo simulation in refining our detector designs.

1.3 Overview of Thesis

Chapter 2 gives the introduction and background of positron emission tomography. Chapter 3 illustrates the details of the experimental setup and data acquisition for the project. Observations on our dual-ended readout of 100 mm LYSO crystal such as light output, energy resolution, spatial resolution and the effect of reflectors on these parameters are given in Chapter 4. Chapter 5 discusses the calibration of dual-ended readout of axially oriented 100 mm long crystals for use in a compact PET system. Use of systematic surface roughing to enhance the spatial resolution in the light sharing direction of dual-ended readout of axially-oriented 100 mm long LYSO crystals for use in a compact PET imaging system are described in Chapter 6. The benchmarking of DETECT2000 Monte Carlo simulation for optical photon tracking in scintillation crystals using our measured results for our unique geometry are also described in Chapter 6. Chapter 7 gives the discussion and conclusion of the project. Future directions of the project based on the work done in this project are also proposed in this chapter.

Chapter 2 Introduction and Background

2.1 PET Imaging

2.1.1 Principles of PET

Positron emission tomography (PET) is a powerful and sensitive Nuclear Medicine technique for biological functional imaging, allowing quantitative imaging of the bio-distribution of tracers chemically labeled with positron emitting radioisotopes that are called radiotracers (1). The emission of a positron from a radiotracer and the subsequent detection process in PET imaging is described in sections 2.1.1.1 and 2.1.1.2. The injected radiotracer compound into the body of the patient is not meant to have a pharmacological effect; rather it images the molecular interactions of biological processes. Commonly used radioisotopes in PET imaging are given in Table 2.1. Among these, ^{18}F has the longest half life and is used to make ^{18}F-fluorodeoxeglocose (FDG) (2) (3), an analogue of glucose, which is the most common radiotracer used in PET imaging in oncology, providing information on tumor size and activity. This radiotracer serves as a marker of glucose metabolism (4) after it is injected into the patient and is taken up preferentially by cells that are actively using glucose, such as cancerous cells, at a significantly higher rate than the normal cells. As a result, tumors appear in the image as a "hot-spot" of uptake. Because of this ability to find metastatic disease, FDG PET is considered the standard of care for staging many types of cancer and for evaluating response to treatment, in particular for lung tumors and lymphomas (5). ^{18}F-fluorothymidine (FLT) is another promising radiotracer for clinical use (6) and is an analog of thymidine, a marker of DNA synthesis that makes it useful to differentiate

tumor from inflammation (7). In contrast, both conditions appear similar when imaged with FDG as both the tumor and inflammation actively use glucose. Comparative studies of brain function with and without degenerative disease (e.g. Alzheimer's disease) and evaluation of the viability of cardiac tissue and hence to detect the signs of coronary artery disease is another use of FDG (1).

Table 2.1 Commonly used positron-emitting radioisotopes in PET. Data taken from (12) and (13)

Radioisotope	^{15}O	^{13}N	^{11}C	^{18}F	^{68}Ga	^{82}Rb
Half-life (min)	2	10	20.4	110	68	1.3
Maximum Kinetic energy (MeV)	1.732	1.198	0.960	0.633	1.880	4.39
Average kinetic energy (MeV)	0.735	0.491	0.385	0.242	0.783	1.32
Average range in water (mm)	2.7	2.0	1.7	1.4	1.7	4.24[a]
FWHM[*] (mm)	0.501[b]	0.282[b]	0.28	0.22	1.35	2.60

[*]Full width at half maximum
[a]Taken from (8)
[b]Taken from (10)

2.1.1.1 Positron Decay

In decay by positron emission, a positron is emitted when a proton from an unstable proton-rich nucleus of an atom is converted to a neutron with the emission of a neutrino as shown below:

$$p \rightarrow n + \beta^{+} + \nu \tag{2.1}$$

The nuclear reaction itself is governed by the following equation:

$${}^{A}_{z}X \rightarrow {}^{A}_{z-1}Y + \beta^{+} + \nu \tag{2.2}$$

Here Z is atomic number and A is mass number of the radioisotope. Each positron (β^+) emitted has a variable energy from more than zero to a maximum energy E_{max} due to sharing its energy with the neutrino, resulting in a continuous spectrum of positron energy (8). Two anti-parallel 511 keV photons are created when the emitted positron from the radiotracer injected either annihilates with an electron directly or combines with it for a short period of time to form a positronium (9) in tissue after losing its energy in multiple Coulomb interactions with other electrons in the surrounding tissue as shown in figure 2.1. A positronium is a hydrogen–like atom in which an electron is orbiting a positron. The rest mass energy of an electron and a positron, 511 keV each, is converted to two annihilation photons emitted in nearly 180^o co-linearity to conserve the momentum. A PET image is created by detecting these two anti-parallel 511 keV photons as described in the following section.

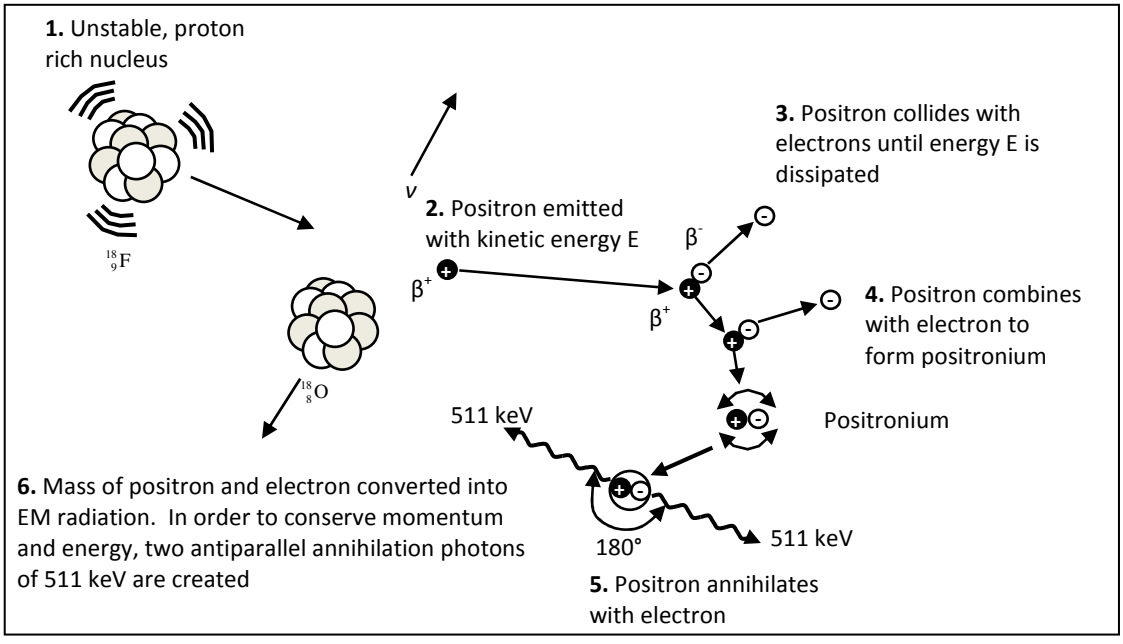

Figure 2.1Creation of two anti-parallel 511 keV photons in an annihilation process (Courtesy of Dr. Andrew L. Goertzen, Department of Radiology, University of Manitoba)

2.1.1.2 Signal Detection in PET

The two anti-parallel 511 keV annihilation photons are detected in electronic coincidence in an opposing pair of γ-ray detectors in a ring of detectors placed around patient body or scanning object as shown in figure 2.2.

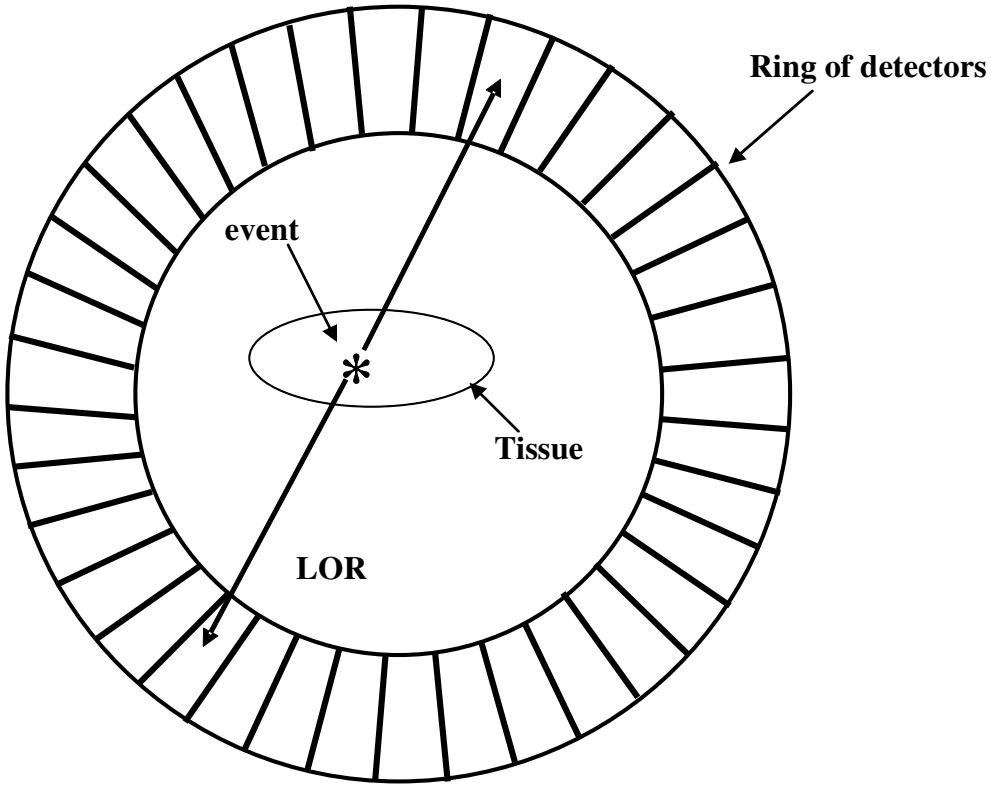

Figure 2.2 Signal detection in PET: Two 511 keV annihilation photons are detected in coincidence by drawing a line-of-response (LOR) between two opposing detectors in a PET ring.

During this detection process, a line of response (LOR) is drawn between the two detectors and the angle and the displacement of the LOR from the central axis of the ring is determined. The detected pair of 511 keV photons in coincidence is referred to as a true coincidence event in PET imaging. The distribution of the tracer injected is imaged by acquiring a large number of coincidence events. The resulting image shows higher activity in those parts of the tissue where higher uptake of the tracer took place. The role of PET detectors in a PET imaging system is to efficiently detect the pairs of 511 keV

photons emitted in the positron annihilation process. Coincidence events could also be detected and misplaced in an incorrect LOR as illustrated in the following section.

2.1.1.3 Types of Events in PET

There are three types of coincidence events in PET imaging; namely true, scattered and random as shown in Fig. 2.3. When two annihilation photons are detected in coincidence, within a coincidence timing window, from the same positron annihilation without either of them being scattered in the patient body or camera gantry then this event is a true coincidence event (Figure 2.3 (a)). The scattered event occurs when one or both annihilation photons from the same positron annihilation are detected in coincidence after being scattered in the body or camera gantry resulting in an inaccurate LOR detection (Figure 2.3 (b)). Although the scattered event is a real coincidence as both the photons belong to the same positron annihilation, the resulting LOR is misplaced from the true one due to the deflection of one or both of the photons.

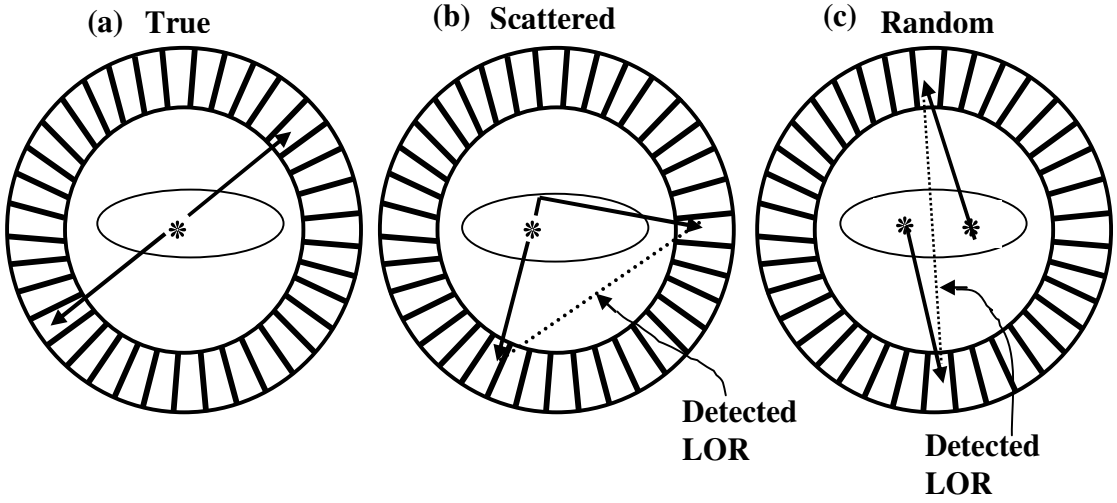

Figure 2.3 Types of events in PET

These scattered events generate structured background pattern in the image that degrades its contrast. Finally, if two photons from two different positron annihilations are detected in coincidence then such an event is known as a random coincidence (Figure 2.3 (c)). This event is also called an accidental coincidence and is a source of unwanted background counts. The random count rate 'R' in an opposing pair of detectors is given by the following equation:

$$R = 2\tau S_1 S_2 \tag{2.3}$$

Where 2τ is the coincidence timing window and S_1 and S_2 are the single count rates in the two detectors. The 2τ in equation (2.3) comes from the fact that if the detector 1 registers a signal at time *t* then any signal registered between $t- \tau$ and $t + \tau$ in detector 2 will be a coincidence event.

The random count rate is proportional to the square of the activity present in the scanning object due to the product of single count rates in equation (2.3). It means that the greater the total activity present in an object under study, the higher will be the random count rate. Again, these random events cause degradation of image contrast and produce an inaccuracy in quantification of activity in the scanning object, especially, in high count rate applications, if not corrected for by subtracting from the measured data.

2.1.1.4 Two fundamental physical resolution limits in PET: Positron Physics

The positron range and annihilation photons non-co-linearity are the two fundamental (inherent) physical limits of spatial resolution in PET due to positron physics explained in the next two sub-sections. Both of these result in a blurring in the image that can not be reduced by improving the performance of a PET system. The effect of physical limits of spatial resolution namely; positron range, annihilation photon non-

co-linearity in PET have been studied for the most commonly used PET radioisotopes in water using Monte Carlo simulation and experiments (8) (10) (12) (13), as given in Table 1.

2.1.1.4.1 Positron Range Effect

As described before in section 2.1.1.1, the positron emitted from the radiotracer injected in the body slows down after multiple Coulomb interactions with the electrons in the surrounding tissues before it annihilates with an electron (11) resulting in two anti-parallel 511 keV photons. The range of the positron, the mean distance travelled by the positron in the tissue until it annihilates with the electron, is the linear distance or separation between the point of positron emission and its annihilation point as shown in the figure 2.4.

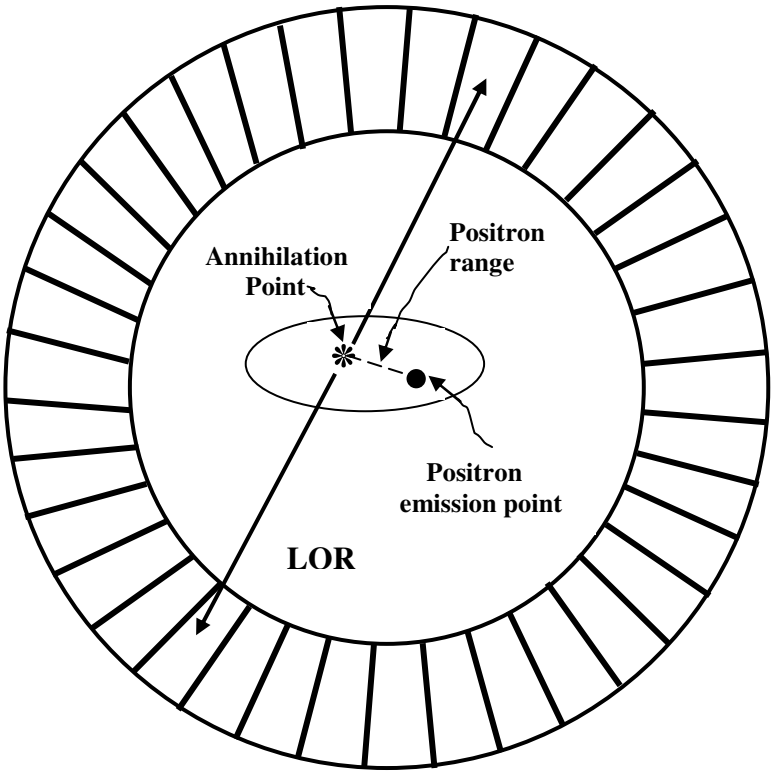

Figure 2.4 Positron range effect: The positron range separates the annihilation point (the detection point) and the emission point in a PET scanner

This range of positron emitted depends upon the positron energy and the density of the surrounding material. Higher energy positrons will have larger range in a low-density material and a higher density material will shorten the range of a particular energy positron. This range of positron emitted from different PET radioisotopes, given in Table 2.1, is about 1-2 mm in water (12)(13) except ^{82}Rb which has a range of 4.24 mm in water, a major constituent of body tissue. An ideal PET scanner should image the positron emission point and accurately measure the actual activity distribution based on positron emission points in the scanning object but the positron range, given in Table 2.1 for PET radioisotopes, separates the emission point and annihilation point and PET scanners can only image the annihilation point instead based on the two annihilation photons detection in coincidence. This positron range effect degrades the image spatial resolution resulting in a blurring in the image that can not be reduced by improving the performance of a scanner. The influence of positron range on spatial resolution for the commonly used positron-emitting PET radioisotopes has been studied theoretically and experimentally by several groups (13)(14) (15)(16)(17). ^{82}Rb has the largest positron range effect amongst the commonly used PET radioisotopes listed in Table 2.1 on the PET spatial resolution due to the relatively highest kinetic energy of its positron. Fortunately, ^{18}F on the other hand has the shortest positron range resulting in relatively the least effect on spatial resolution.

2.1.1.4.2 Annihilation photons non-co-linearity

Generally, when an emitted positron slows down and reaches thermal equilibrium with an electron (not at rest) then the annihilation takes place. Due to residual momenta of positron and electron, the two annihilation photons are no longer co-linear. As a result

the detected line-of-response (LOR) does not pass through the point of annihilation as shown in figure 2.5. This angular deviation from 180^o co-linearity in biological tissue, mostly water, is estimated as 0.5^o FWHM of the Gaussian distribution (18)(19).

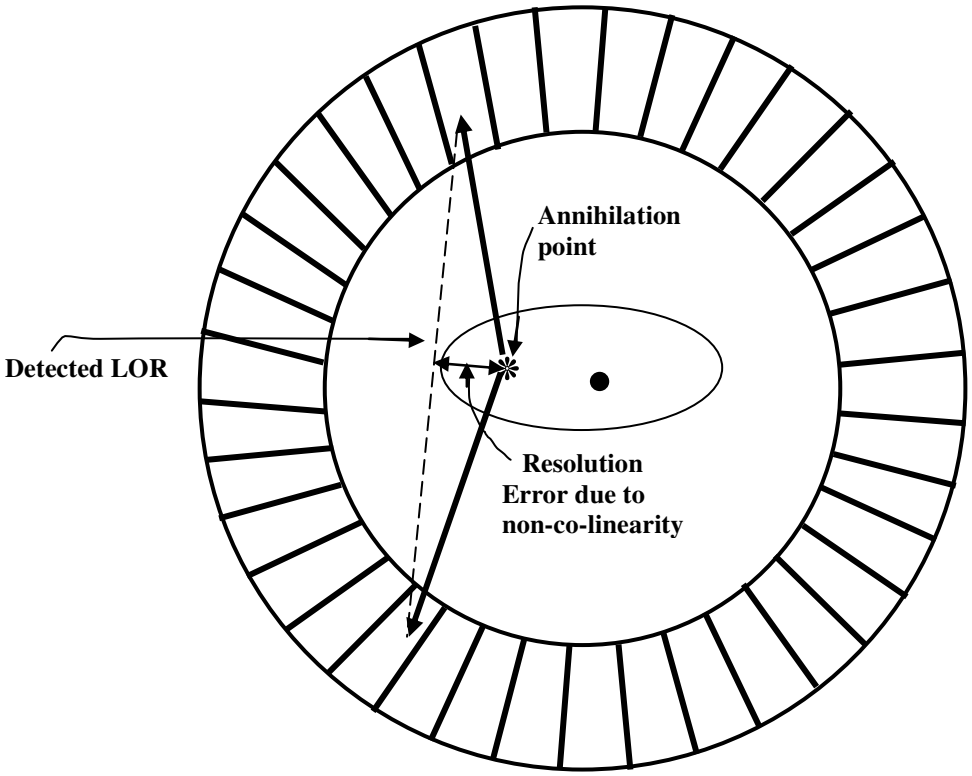

Figure 2.5 Non-co-linearity of 511 keV annihilation photons in a PET scanner

For a detector ring of diameter D, this contribution to the spatial resolution at the centre would be (20):

$$FWHM \approx \Delta\theta \times D/4 \tag{2.4}$$

Both FWHM and D are measured in meters in equation (2.4). With $\Delta\theta = 0.5^o = 8.7$ milli-radian, this contribution to the spatial resolution would be 2.2 mm for a 1 m ring diameter. Therefore the non-co-linearity of two annihilation photons will degrade the

spatial resolution and result in a blurring in the image as is the case with positron range and, hence, both are the built-in fundamental resolution limits of a PET imaging system.

2.1.2 Image Formation Process

If two photons are detected within a very small timing window, normally < 10 ns, then this is a prompt coincidence event. As described earlier in section 2.1.1.2, an LOR is drawn between the two detectors where the photons were detected in coincidence. The recorded LOR is stored in a 2D data structure array called a sinogram. The sinogram represents tomographic data in 2–dimensions where the azimuthal angle of the LOR is on the vertical axis while the displacement of the LOR from the scanner central axis is on the horizontal axis. During the image scanning period, typically millions of events are collected and the number of events at each azimuthal angle and LOR displacement is recorded in the data map creating a sinogram image as shown in figure 2.6.

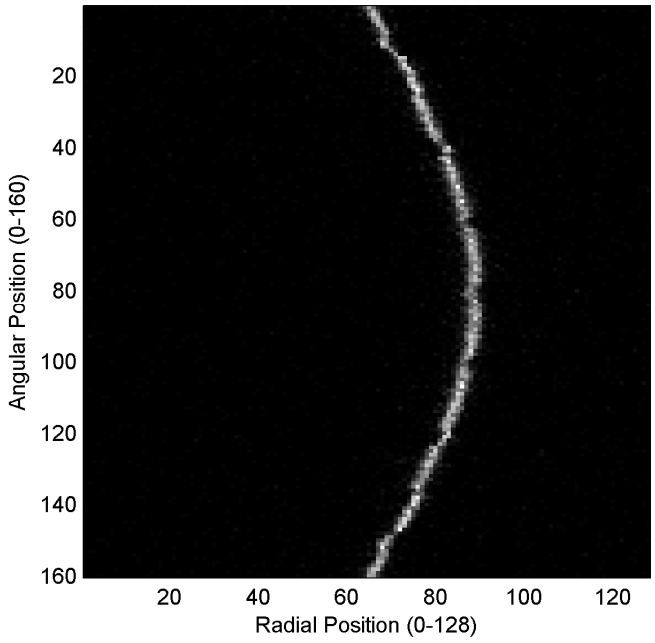

Figure 2.6 An example sinogram image of a line source in a PET scanner (Courtesy of Bryan McIntosh, Department of Physics & Astronomy, University of Manitoba)

A point or a line source will result in a sine wave pattern in the image, lending to the name “sinogram”. In the case of more complex objects, the resulting sinogram image will be the overlapping projection of many sine waves. During scanning, the object is divided into a large number of slices corresponding to the positions along the scanner central axis. The slice position is considered the 3rd dimension of the PET acquisition data that is why the word ‘tomography’ (tomo means slice) is used in positron emission tomography. Generally most PET scanners consist of multiple rings along their z-axis; each slice corresponds to a ring that detects 511 keV annihilation events in coincidence with itself or any other possible ring in the scanner. These slices are organized with ring difference which is the difference between the ring numbers detecting the annihilation photons in coincidence. Maximum ring difference during the PET image processing defines how oblique a line of response is before it is rejected. If a ring difference of 0 is used then it means the coincidence events are recorded only in the same ring. If the events in a ring are recorded in coincidence with the adjacent rings on its left and right sides, the ring difference would be -1 and +1 respectively. Similarly, the events recorded in a ring in coincidence with the rings 2 apart on its left and right would correspond to ring differences of -2 and +2, respectively and so on. As an example, for a 90-ring PET scanner with a maximum possible ring difference of 89, there would be a total of 8100 sinograms that come from all 90 × 90 possible ring pairs where the events were recorded in coincidence. Compared to the reconstruction of images from the data obtained from the coincidences only within each individual crystal ring, reconstructing images from the coincidence data acquired with all allowed ring differences (3D mode) results in dramatic improvement in sensitivity but is more time consuming. Therefore the axial data from

multiple sinogram slices that correspond to a similar position along the scanner axis are often combined together to create a new sinogram with fewer axial slices but with a greater number of events in each slice using, for example, single slice rebinning (SSRB) (21). How many oblique lines of response will be binned in such a sinogram during the scanning process is defined by the span. The resulting sinogram can be reconstructed using the standard filtered back projection (FBP) algorithm (22). A limitation of the SSRB technique for rebinning the axial data is that it gives accurate results only for small axial FOV scanners or if the radiotracer activity is located close to the centre of the FOV. If the distribution of the radiotracer injected is farther from the central axis of the scanner the accuracy of the SSRB process is lost and hence more advanced rebinning algorithms such as multi-slice rebinning (MSRB) or Fourier rebinning (FORE), described in (23), are used. In addition to FBP, other algorithms used for PET image reconstruction are ordered-subsets expectation-maximization (OSEM) (24) and maximum-likelihood expectation-maximization (ML-EM) (25), that are based on iterative statistical methods. Compared to analytic image reconstruction techniques such as FBP (linear method), iterative statistical methods of reconstruction give improved signal-to-noise ratio and image quality and provide a better spatial resolution, however, spatial resolution of an image strongly depends on scanning object size due to their non-linear behavior (26).

2.1.2.1 Factors affecting PET image spatial resolution and image quality

2.1.2.1.1 Depth-of-interaction (DOI) resolution effect or parallax error

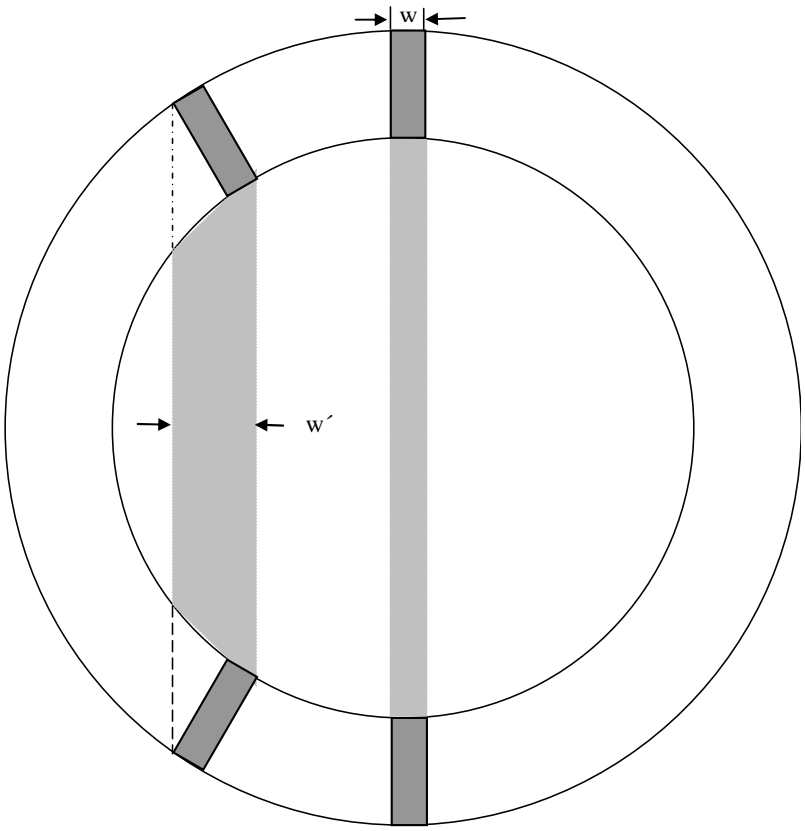

Figure 2.7 Depth of interaction or parallax error due to the radial off set from the centre of a scanner

The in-plane spatial resolution of a PET scanner with a circular ring of detectors depends on the width of the scintillation crystal used. If w is the width of the discrete crystal elements in detector modules of a PET scanner ring then the spatial resolution at the centre of the scanner would be w/2 (27). For an activity distribution with the object away from the center in the radial direction the apparent width of the crystal seen by the detected γ-events in the shaded region shown in figure 2.7 would be increased to w´ resulting in a degraded resolution of w´/2 at the mid point of the two opposing detectors in the ring (27). This is because the depth of interaction of γ-photons within the crystal is

not known. This is called the depth-of-interaction (DOI) effect or parallax error in spatial resolution. This effect increases with the distance from the centre of the scanner in the radial direction and will be further increased with an increase in the length of the crystal. The effect will be more pronounced for the scanner with a smaller ring diameter such as an animal PET scanner due to the small volume of the scanning object compared to a clinical PET system. To minimize the magnitude of the effect a shorter crystal could be used for the construction of PET detectors and/or the ring diameter could be increased. In both the cases the sensitivity of the system would be reduced because of reduced solid angle coverage. So there is always a compromise between the spatial resolution and the sensitivity of the system in a conventional PET design. The parallax error in a PET scanner could be minimized if the detectors can measure the depth-of-interaction of the annihilation photons in the interacting crystals and thereby improve the spatial resolution mainly along the radial direction at the off centre region without decreasing the crystal length and hence maintain high sensitivity. This will allow uniform spatial resolution in all directions (28). Therefore many DOI detector designs have been investigated to add DOI capability to PET scanners as will be discussed in section 2.3.5.

2.1.2.1.2 Photon attenuation within the scanning object and its correction.

The attenuation length of 511 keV annihilation photons in biological tissue (mostly water) is 10.4 cm corresponding to a linear attenuation coefficient of 0.096 cm^{-1}. The size of the chest and head of a human body is around 20 cm (20). The exponential attenuation law ($I = I_o e^{-\mu x}$, where I is transmitted intensity through a thickness x, I_o is original intensity and μ is attenuation coefficient) determines that around 85% of annihilation photons will be attenuated in the patient body and only 15% will have no interaction

within the biological tissue. Absorption of these photons will reduce the number of detected photons resulting in reduced photon statistics in the image data that decreases the image quality. To obtain quantitative information, an accurate attenuation correction can be performed by measuring a transmission profile through the patient body or a scanning object such as a phantom generally with a coincidence source such as ^{68}Ge (transmission scan) as well as measuring the counts without the scanning object or a patient (blank scan). Consider a radiotracer source at depth 'd' of a scanning object having a thickness 'D' placed between two opposing pair of detectors in a PET ring as shown in figure 2.8.

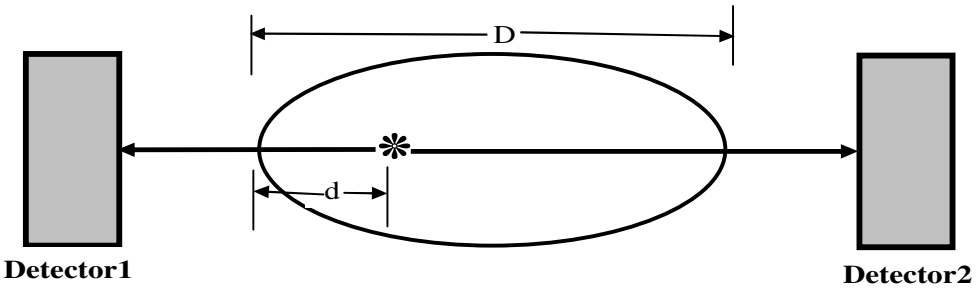

Figure 2.8 Photon attenuation within the scanning object: The transmitted photons are detected by two detectors Detector 1 and Detector 2 in coincidence.

The probability of an annihilation event detected by detector 1 is given by the following exponential equation

$$\frac{I_1}{I_o} = e^{-\mu d} \tag{2.5}$$

Where I_1 is the transmission intensity of all the annihilation photons detected by detector 1 after attenuation through thickness d, I_o is the original intensity before attenuation and μ is the linear attenuation coefficient of 511 keV γ-photons in biological tissue. Now the

probability of an annihilation event detected in coincidence by detector 2 is given by the equation

$$\frac{I_2}{I_o} = e^{-\mu(D-d)} \tag{2.6}$$

Here I_2 is the transmission intensity of all the annihilation photons detected by the detector 2 after the attenuation in thickness *D-d*. The probability of both the photons being detected in coincidence then would be

$$(\frac{I_1}{I_o})(\frac{I_2}{I_o}) = e^{-\mu d} \cdot e^{-\mu(D-d)} = e^{-\mu D} \tag{2.7}$$

The combined transmission intensity of coincident events is then given by

$$I = I_o\, e^{-\mu D} \tag{2.8}$$

and the original intensity without any attenuation is then written as

$$I_o = I \quad e^{\mu D} \tag{2.9}$$

Equation (2.9) implies that the original intensity can be recovered by multiplying the scan count with a factor $e^{\mu D}$ therefore this factor is called an attenuation correction factor. Equation (2.9) could be re-written as $\frac{I_o}{I} = e^{\mu D}$ which means,

$$\frac{Blank\ scan\ count}{Transmission\ scan\ count} = Correction\ \ factor \tag{2.10}$$

The correction factor so obtained is multiplied by the sinogram data for attenuation correction. A coincidence source with known activity, normally ^{68}Ge, or a single photon source, such as ^{137}Cs or an x-ray CT scanner can be used to generate the attenuation map by measuring the transmission profile through a patient. The attenuation correction is by

far the largest correction in clinical PET (29) due to the fact that the attenuation through the body could be about a factor of 10 while for a small animal PET this could be about a factor of 2 (30).

2.2 Animal PET

2.2.1 Motivation for animal PET imaging

Due to genetic homology between animals and humans, complex animal models of human disease are available that can be used to evaluate new therapeutic strategies for the treatment of cancer and other disease. There can be a large variability in the degree of severity, the time of onset and course of progress in an animal model of diseases such as neurodegenerative disorders, inflammatory and viral diseases, as is the case with humans. Due to this large variability, the ability of tracking a disease process longitudinally in the same animal over a time range of hours to years will be essential if the therapeutic strategy under investigation is to be translated to clinics for the treatment of patients. In recent years there has been extensive interest in using PET to examine animal models of human disease (1) (31). However, clinical PET scanners do not have satisfactory spatial resolution or sensitivity for studies of small animals such as rats and mice, therefore dedicated animal systems are required. Generally the size of the organs of these animals is around 10 times smaller than that of a human; therefore, higher spatial resolution and higher sensitivity are required (32). Detector ring diameter and scintillator crystal element size must be reduced to improve detection efficiency and spatial resolution.

Early small animal PET scanners were developed as research tools and prototypes (33)(34)(35)(36)(37)(38). The University of California at Los Angeles (UCLA) group developed a prototype dedicated animal PET system, microPET (39), with a spatial

resolution of 2 mm that attracted the attention of biologists to image mice and rats. The microPET P4 scanner from Concorde Microsystems (40) was an early commercialized small animal system, developed in the late 1990s, that evolved from the original UCLA prototype microPET design. This system uses LSO scintillators with high light output allowing high spatial resolution with small crystal size and high energy resolution. After the release of first commercial microPET P4 system, many commercial small animal PET scanners, including microPET R4 designed for rodents only (41), that uses the same detector technology as microPET P4, were developed and made available (40)(42)(43)(44)(41)(45). Each system aimed to enhance sensitivity and/or spatial resolution. Availability of these commercial animal PET systems has made it possible to use them extensively in evaluating animal models of human disease (46)(47). Monitoring the distribution of radio-labeled cells in vivo (48), monitoring the growth of tumor xenografts (49)(50), evaluating cardiac function (51), studying animal models in food sciences (52) and studying reporter gene expression (53) (54) (55) are a few examples among the many uses of small animal PET imaging. In these studies, imaging is carried out non-invasively, enabling the animal to serve as its own control which is a key feature of small animal PET imaging.

Animal PET scanners have been used for radiotracer development beyond FDG. In these studies, small animals such as mice, rats and rabbits have been used for preclinical trials of these drugs (56)(57)(58) before these drugs reach clinical trial. As a research tool in these studies, PET imaging enables the rapid, dynamic and whole body characterization of the bio-distribution of radio-labeled compounds.

2.2.2 Design of conventional animal PET systems

Most common current designs of preclinical PET systems use modular detectors in which 2D arrays of thin scintillation crystals having dimensions 1×1×10 mm^3 to 2×2×10 mm^3 are oriented radially in a ring (40) (41) (44) (59) (60). A schematic of this detector arrangement is shown in figure 2.9.

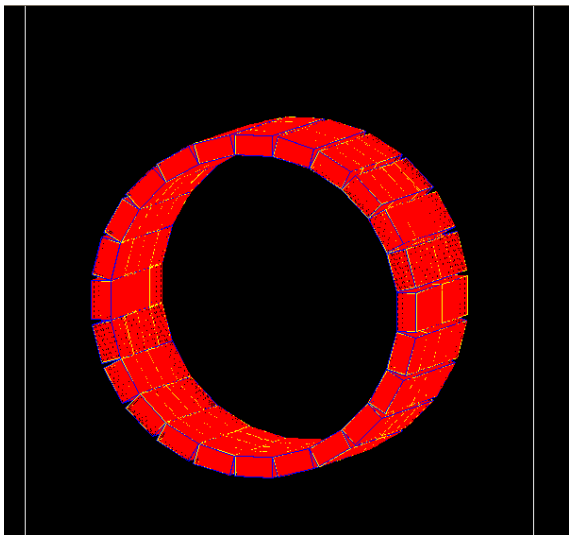

Figure 2.9 Schematic of detector arrangement in a cylindrical type PET camera. Note the 2D arrays of scintillation crystals oriented in the radial direction.

These arrays are commonly coupled through light-guides to photodetectors such as position sensitive photomultiplier tubes (PSPMTs). The location of interaction of a detected γ-ray event is determined by identifying the crystal in which the interaction occurred. As an example, the Siemens Inveon small animal PET system uses detectors with a 20×20 array of 1.51×1.51×10 mm^3 LSO crystals with a pitch of 1.59 mm coupled via a tapered light guide to a Hamamatsu R8900-C12 PSPMT (61)(62). A schematic of a complete PET detector ring system similar to those used in the Siemens Family of conventional animal PET systems is shown in figure 2.10.

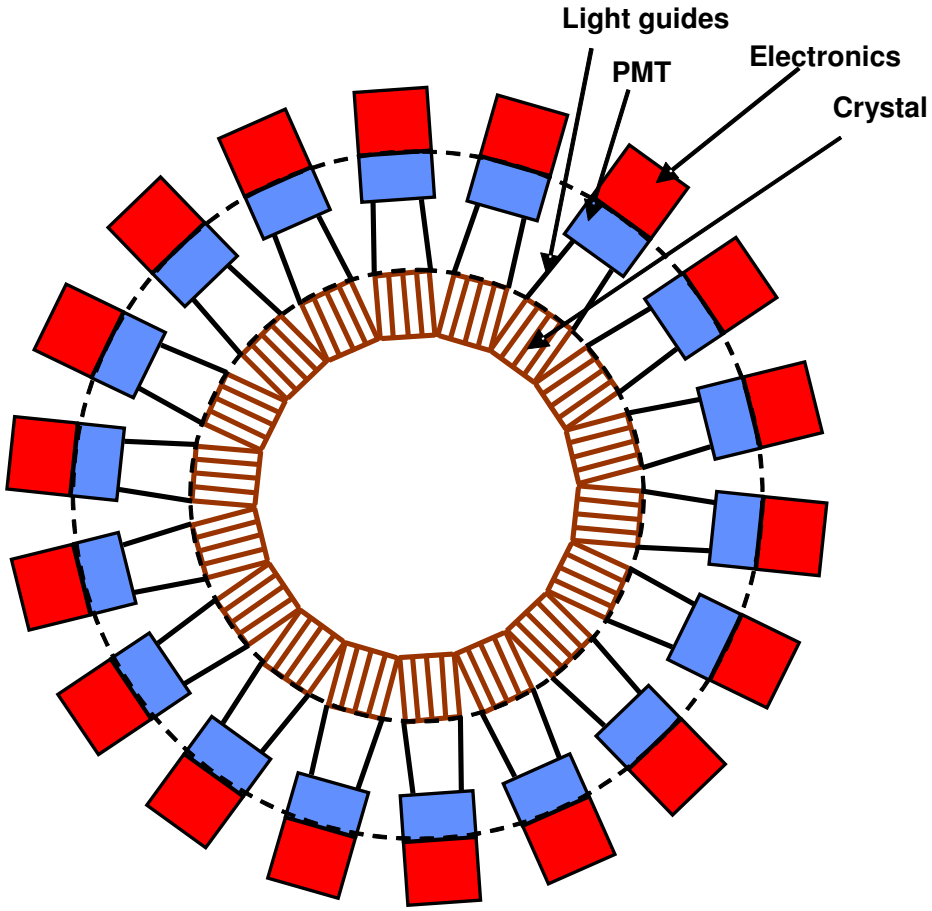

Figure 2.10 Schematic of a complete ring detector used in a conventional cylindrical type PET camera.

There are two limitations of this design for achieving a compact geometry: first, the overall diameter of the detector ring is large due to the combined lengths of the crystal, light guide, PSPMT and detector electronics as shown in figure 2.10 and hence can not fit in to a bio-safety cabinet. Secondly, a large number of electronics channels must be digitized. This large number of electronics channels results in the need to have a large electronics cabinet as a part of the system gantry. Due to these two limitations it is difficult to implement this design for a compact geometry.

2.2.3 Measuring performance of animal PET systems

Small animal PET scanners are extensively used for preclinical drug development, evaluation of therapeutic strategies using animal models of human disease and biological research. What type of scanner is most suitable for the intended study or application is based on the scanner performance. The parameters significantly influencing the data quality in a system are, at minimum, spatial resolution, sensitivity, scatter and count rate performance. Therefore assessing performance of small animal PET systems is an essential task and is carried out by measuring spatial resolution, sensitivity, scatter fraction and counting rate performance using the National Electrical Manufacturers Association (NEMA) standards.

2.2.3.1 NEMA NU 4-2008 standard for performance measurements of animal PET

Early performance measurements of small animal PET scanners were based on non-standardized phantoms and procedures due to the non-availability of an agreed-upon method. Substantial variation of phantoms and procedures was observed between different research groups (40)(41)(37)(63)(36)(34)(38)(64)(65)(33)(35)(66). As a result, a direct comparison of performance parameters of different scanners was not adequate. Keeping in view this difficulty, there was a strong need and demand for standardization of the assessment of performance of small animal PET systems. Therefore NEMA prepared standards/protocols for the performance measurements of small animal scanners given in its publication NU 4-2008 (67). The performance measurements of clinical PET scanners are carried out using NEMA standard NU 2-2001 (67) which was updated to NU 2-2007. The performance evaluation procedures outlined in NEMA standards are independent of system design and are applied to a wide range of scanner models and

geometries including multi-ring, continuous detector, time-of-flight PET and other imaging systems with coincidence capability. The spatial resolution measurement for small animal PET to be performed as per the NEMA standards is described in the following section.

2.2.3.1.1 Spatial Resolution

A ^{22}Na source is used to measure full width at half maximum (FWHM) and full width at tenth maximum (FWTM) spatial resolutions in image. The typical values of FWHM spatial resolution are about 2-3 mm and those of FWTM are about 3-5 mm. Goertzen et al. (68) carried out the spatial resolution measurement as a part of the performance evaluation of a collection of commercial preclinical PET imaging systems manufactured after 2000 using NEMA NU 4-2008 standard and demonstrated a NEMA comparison of eleven commercial preclinical imaging systems for the first time. As an example of spatial resolution measurement in this study, for axial center of FOV at 5 mm radial off-set, FWHM/FWTM spatial resolutions in the radial, tangential and axial direction were 2.29/4.03, 2.18/3.18 and 2.20/4.58 mm, respectively for microPET P4 system and 2.13/4.90, 2.21/4.22 and 2.72/5.59, respectively for microPET R4 system. For ¼ axial FOV at 5 mm radial off-set, FWHM/FWTM spatial resolutions in the radial, tangential and axial direction were 2.34/4.22, 2.14/3.77 and 1.75/4.22 mm, respectively for microPET P4 system and 2.06/5.24, 2.18/4.14 and 2.37/4.88, respectively for microPET R4 system. An energy window of 350-650 keV was used in these studies.

2.3 Scintillation Detectors for PET imaging

The function of a scintillation detector is to stop an incident γ-ray and convert its energy into scintillation light. This scintillation light is subsequently detected by a

photodetector that converts the emitted light into an electrical charge. Detectors for PET imaging must have a high stopping power, that is a high probability of totally absorbing the incident 511 keV annihilation photons. These detectors should have fast decay times, allowing the detection of two annihilation photons in coincidence with a narrow time window (i.e. good timing resolution), thereby reducing the random events and improving the count rate performance. At the same time they should provide high light yield to achieve good energy resolution for Compton scatter elimination from the PET data and provide accurate and high spatial resolution to localize the interaction position to a small spatial volume. Scintillation detectors must provide an output signal that is proportional to the γ-ray energy deposited for measuring the incident energy. In addition, these detectors must be inexpensive to be manufactured.

2.3.1 Interaction of 511 keV photons with matter

A 511 keV annihilation photon will interact with the PET detector crystal with three possible interaction processes: 1) photoelectric absorption; 2) Compton scattering; and 3) Rayleigh scattering, also called coherent scattering. Coherent scattering is an interaction of a photon with an atom as a whole. Due to the larger mass of the atom very little recoil energy is absorbed by the atom in this process. As a result a minimal deflection of the photon occurs with essentially no loss of energy and hence coherent scattering can be ignored in PET imaging. Therefore only two processes, photoelectric absorption and Compton scattering, are important in PET imaging and are described in sections 2.3.1.1 and 2.3.1.2 followed by section 2.3.2 which describes the Physics of Scintillation light in.

2.3.1.1 Photoelectric absorption

In the photoelectric interaction, when a γ-ray photon of energy $h\upsilon$ interacts with an atom of absorbing material it transfers all of its energy to a bound electron with a binding energy, also called the work function, φ, and completely disappears. As a result the electron is ejected with energy E_e, *given* by

$$E_e = h\nu - \varphi \tag{2.11}$$

The incident energy of the γ-ray must exceed the binding energy or work function of the electron in a bound shell for the photoelectric absorption process to occur as is obvious from equation (2.11). As a result of the ejection of the electron, known as a photoelectron, a vacancy is created in the bound shell that is filled by higher orbit electrons resulting in the emission of one or more X-rays that are mostly absorbed locally through photoelectric absorption. An Auger electron may also be emitted in place of an X-ray but the probability of emission is very small. The most probable ejection of an electron in the photoelectric absorption process is from the inner most K shell. The kinetic energy transferred to the photoelectron is deposited locally near the photoelectric interaction in the crystal material first through e^- collisions (excitation and ionization). In scintillation crystals the excitation of electrons results in a scintillation process whose physics is explained in section 2.3.2.

The photoelectric absorption cross-section τ varies with γ-ray energy E and atomic number Z of the absorbing material according to the following equation (8):

$$\tau \propto \rho \frac{Z^4}{E^3} \tag{2.12}$$

where ρ is the density of the absorbing material. While high density material increases the probability of interaction of a γ-ray photon, the absorption cross-section has a strong dependence on Z i.e. a higher Z value increases the number of photoelectric events in the material. As is obvious from equation (2.12), the photoelectric absorption process is dominant for low E and high z.

2.3.1.2 Compton scattering

When a high energy γ-ray photon, such as a 511 keV annihilation photon, interacts with an atom of absorbing material it can transfer a part of its energy to an electron initially at rest and scatter away with a lesser energy. This process is known as Compton scattering.

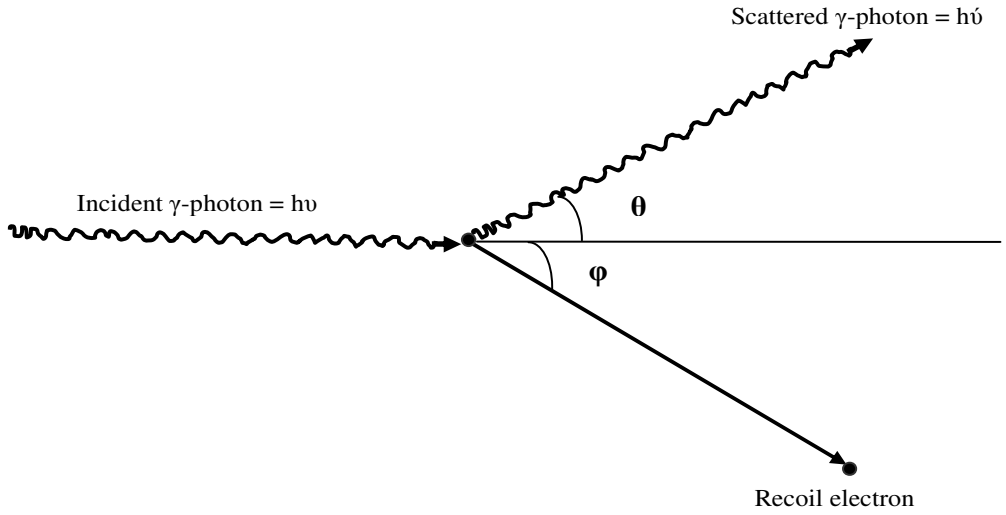

Figure 2.11 Schematic diagram showing a γ-photon interaction with matter via Compton scattering

Consider an incident γ-ray photon of energy $h\upsilon$ scattered with a lesser energy $h\nu'$ through an angle θ with its initial direction after transferring a part of its energy to an electron as shown in the figure 2.11. The electron recoils at an angle φ with respect to the original direction of the γ-ray photon.

The energy of the scattered photon as a function of scattering angle θ is given by the following relation after considering the conservation of energy and momentum before and after collision:

$$h\nu' = \frac{h\nu}{\left[1 + \frac{h\nu}{m_O c^2}(1 - \cos\theta)\right]} \tag{2.13}$$

Then the energy E_e transferred to the recoil electron would be given by

$$E_e = h\nu - h\nu' \tag{2.14}$$

where $m_o c^2$ is the rest mass energy of the electron. From the equation it is obvious that if the scattering angle θ is small then most of the energy will be retained by the scattered photon and subsequently the energy transferred to the electron will be very small. The energy of the γ-ray photon transferred to the recoil electron ranges from 0 to a maximum possible energy which occurs at $\theta = 180^o$ (see equations (2.13) and (2.14)). The angular distribution of scattered photons is given by the Klein-Nishina formula of scattering cross-section (68)(69). Small scattering angles in the forward direction are most favoured at 511 keV-photon energy (70). Subsequently the scattered photon can then interact with the crystal material via the photoelectric absorption process or further Compton scatter. In all cases of energetic ejected electrons, this energy is deposited locally in the crystal material, resulting in emission of scintillation light as described in section 2.3.2.

The Compton scattering cross-section σ is given by (8)

$$\sigma \propto \rho \frac{Z}{A} \tag{2.15}$$

Where ρ is the density, Z is the atomic number and A is the mass number of the interacting material such as a scintillation crystal. From equation (2.15) it is obvious that there is a high probability of interaction of photons in high density material and that the Compton scattering essentially goes with the electron density.

Comparing equation (2.15) with (2.12), Compton scattering has a relatively weak dependence on Z and therefore higher Z values will increase the number of photoelectric events in the material compared to Compton scattering. This strong dependence of photoelectric absorption cross-section on the atomic number of the absorbing material is a primary reason for selecting high-Z materials as scintillation crystals for PET imaging systems, in addition to other scintillation properties such as decay time and light yield. Photoelectric absorption is preferable in almost all nuclear medicine imaging applications including PET imaging because the scattered events detected will create a background noise and degrade the image contrast.

2.3.2 Physics of Scintillation light

In inorganic scintillator materials such as LYSO, the crystal lattice has discrete energy states for electrons. The lower energy state is called the valence band and the upper energy state is called the conduction band as shown in figure 2.12. In the valence band the electrons are bound in the ground state of the crystal lattice. When a γ-ray interacts with the crystal, it transfers its energy to a valence band electron, thereby exciting it to the conduction band, resulting in a hole in the valence band. These electrons have sufficient energy to become free and could move throughout the crystal. The gap between the valence and conduction band is called the forbidden energy gap or band where electrons can not be found in the pure state of the crystal.

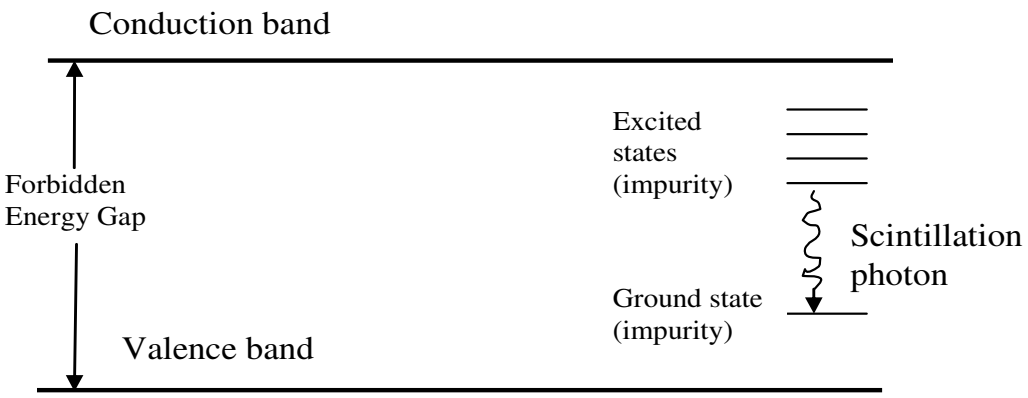

Figure 2.12 Energy bands in an inorganic crystal scintillator doped with an impurity

The excited electron will return to its ground state in the valence band resulting in an emission of an optical photon that is far beyond the energy of visible light i.e. the forbidden energy gap width is such that the emitted photon will have too high an energy to be in the visible range to be detected by photomultiplier tubes (peak quantum efficiency at 420 nm). Therefore an impurity called an activator is added to the crystal, such as cerium (Ce) impurity in LYSO:Ce crystal, that will create a ground state (activator ground state) and an excited state (activator excited state) within the forbidden gap in between the valence and conduction band as shown in the figure 2.12. The created energy states now have a smaller energy gap that will give rise to optical photons with wavelength in the visible range after de-excitation of an electron to the valance band and hence can be detected by conventional PMTs, which are sensitive to visible light.

The energy resolution of a scintillator, that is its ability to resolve two peaks that are close to each other in terms of energy, is directly related to the amount of light emitted from it. The greater the light output from the scintillation detectors the better will be the energy resolution. This will help in rejection of scattered events in the energy spectrum. As well, a high light output will yield an accurate spatial resolution as well as better

timing resolution for reducing the random events and improving the count rate performance of a PET system. However there are certain limits of energy resolution in scintillation detectors. A problem with finding "bright" scintillators that are also "fast" is that a fast emission is generally coupled to low light output of scintillation detectors. Therefore, one typically has to compromise between these two equally important parameters.

2.3.3 Scintillators for PET

The commonly used scintillation crystals in PET scanners and their physical properties are given in Table 2.2. None of the scintillators meet all the criteria mentioned above in section 2.3 for an ideal PET detector and, therefore, one has to compromise. For example, bismuth germanate (BGO) has a very high stopping power (10.4 mm attenuation length) but has low light output of 9000 photons/MeV as well as a long decay time of 300 ns. In contrast, sodium iodide (NaI) has a high light output of 41000 photons/MeV but has a poor stopping power and decay time.

Scintillator	Chemical Formula	Density (g/cm^3)	Attenuation length at 511 keV (mm)	Light yield (photons/MeV)	Decay time (ns)
NaI (Tl)	NaI:Tl	3.67	29.1	41,000	230
CsI (Tl)	CsI:Tl	4.51	22.9	66,000	900
BGO	Bi_4Ge_3O	7.1	10.4	9,000	300
LSO(Ce)	Lu_2SiO_5	7.4	11.4	30,000	40
LYSO (Ce)	$Lu_{1.8}Y_{0.2}SiO_5$: Ce	7.1	12.0	32,700	41
GSO	Gd_2SiO_5	6.7	14.1	8,000	60

Table 2.2 Commonly used scintillator materials in PET imaging with their physical properties important to PET imaging. Data taken from (18)

At present, the most commonly used scintillators for PET are LSO and LYSO, due to a favourable combination of their physical properties shown in Table 2.2. The high stopping power (attenuation length of 12 mm) reduces the length of the crystal required to stop and detect 511 keV photons compared to other scintillators. The fast decay time of 41 ns for high timing resolution allows the data to be acquired at high count rate with minimal detector dead time improving the count rate performance. In addition, the light yield of around 30,000 photons for a 1 MeV gamma ray gives high energy and spatial resolutions. All these properties make LSO or LYSO the scintillator of choice for PET imaging. However, these two scintillator materials are intrinsically radioactive due to 2.4 % of ^{176}Lu that might be a background noise issue in PET studies using low activity. On the other hand this intrinsic radioactivity could be used to calibrate the DOI detectors in a complete PET system that uses LSO or LYSO without the need of an external source (71) (also discussed in Chapter 5). LYSO scintillator crystals have nearly the same physical properties as LSO except for density, but is readily available commercially compared to LSO due to patent protection of LSO.

2.3.3.1 Reflectors

Scintillation light is emitted isotropically from the crystal and only a fraction of this light is directed to the ends of the crystal coupled to PMTs. Therefore reflectors are used to maximize the collection of light from the crystal by wrapping them around the crystal lateral surfaces, resulting in increased light collected by the PMT and improved energy resolution. There are two types of reflector materials: specular, such as Enhanced Specular Reflector (ESR) with a polished metal surface and diffuse, such as Teflon. In a specular reflector, the angle of reflection will be equal to the angle of incidence of light

resulting in a mirror-like reflection whereas in a diffuse reflector the angle of reflection follows a Lambertian distribution that results in an isotropic distribution of reflected light. The light collection from a crystal can also be changed by altering the surface of the crystal. For example, a polished surface or a rough or ground surface will change its energy resolution and DOI resolution, as described in the next section.

2.3.3.2 Surface treatment of scintillators

The idea of altering a crystal surface by surface treatment is as follows: a specular reflection takes place on a polished surface resulting in an increased light collection; while a diffuse reflection occurs on a rough or ground surface where photons are re-emitted in all directions resulting in a loss of light. In conventional scintillation crystal arrays, polished surfaces are typically used to give increased collection of light due to specular reflection. This increased light collection by the photodetector results in improved energy resolution of the PET system. On the other hand, scintillation crystal arrays in DOI detectors typically use rough or ground surfaces that yield a loss in light collection due to diffuse reflection. This loss in light results in an improved DOI resolution as described in section 2.3.5.2. However, one has always to optimize a balance between light collection for maximizing the energy resolution and light losses for DOI resolution in the dual-ended readout DOI detector systems. The optimized scintillation light after crystal surface treatment and wrapping in a suitable reflector is then collected by a photodetector such as photomultiplier tube (PMT), discussed in section 2.3.4, which converts the light into an electrical signal that can be processed and digitized.

2.3.3.3 Optical glue or grease

To detect the emitted light, the scintillator crystal is coupled to a photodetector with an optical glue or grease which has a matching refractive index allowing efficient coupling of the emitted light to the photodetector by minimizing the transmission loss of light. The purpose of optical glue or grease (refractive index ~1.5) here is to remove the air gap, with a refractive index of 1.0, between the crystal end and the photodetector and provide a matching refractive index between photodetector window such as borosilicate glass window of a PMT (refractive index of 1.5) and the scintillator.

2.3.4 Photodetectors for PET

Photodetectors used for PET imaging include: conventional PMT; position sensitive PMT; Avalanche photodiode (APD); silicon photomultiplier tubes (SiPM) also called Geiger-Avalanche Photodiode (G-APD). In this work we only dealt with conventional PMT and PSPMTs, therefore, these two photodetectors will be summarized in the following two sections.

2.3.4.1 Conventional PMT

A photomultiplier tube consists of three parts enclosed in a vacuum tube; a photocathode made up of a bi-alkali material such as cesium antimony (CsSb), an electron multiplication section and a charge collection anode. The photocathode is attached to a transparent glass window and converts the incident light into electrons called photoelectrons. These electrons, after passing through a focusing grid, are picked up by an electrode called a dynode at a potential difference of around 200-400 V. Generally there are around 10 dynodes or stages in a PMT that multiply the electrons.

Each dynode is at a higher potential than the preceding one. The kinetic energy of the electron is equivalent to the accelerating voltage of the dynode. The high speed electron picked up by the dynode excites secondary electrons of that dynode material resulting in the emission of several secondary electrons. These secondary electrons are accelerated towards the next dynode, typically maintained at an accelerating voltage of about 50-150 V higher than the first one. The electron multiplication and acceleration is repeated until the final dynode is reached. The multiplication factor δ of each dynode is given by

δ = (number of secondary electrons emitted)/(primary incident electrons)

If N is the number of stages in a PMT and α is the fraction of all electrons collected by all the dynodes then its overall gain G would be (72)

$$G = \alpha \delta^N \tag{2.16}$$

A typical value of δ for a conventional dynode material is 5 and α could be taken as unity for a well designed PMT then for a 10-stage PMT the gain would be 5^{10} or about 10^7. The gain of a PMT is proportional to applied voltage V and if δ is linearly dependent on dynode voltage then the overall gain would be governed by equation (2.16) with δ replaced by V (i.e. $G = \alpha V^N$). The quantum efficiency or the conversion efficiency of a PMT for incident optical photons is typically 20-30%, meaning that 20-30 photoelectrons are emitted per 100 photons incident on the photocathode. The quantum efficiency varies with the wavelength of emitted photons from the crystal. The peak emission wavelength of LSO or LYSO is 420 nm (73), so PMT peak efficiency must be matched to this wavelength.

2.3.4.2 Position Sensitive Photomultiplier Tubes (PSPMTs)

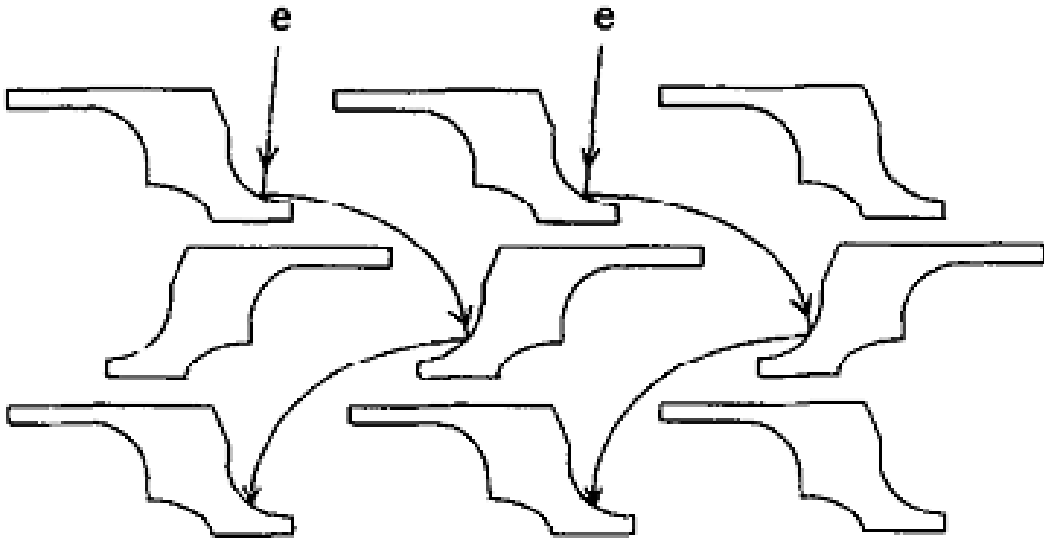

Figure 2.13 Multiple dynode channels of a PSPMT accelerating the photoelectrons in a direction parallel to their incidence path on the face of the PSPMT. The figure is reprinted from reference (74) with permission from Elsevier, Copyright © 1997 Elsevier.

Block detectors containing arrays of pixilated crystals are used in current PET scanner systems. To read each crystal in the array with a separate PMT is expensive and not practical. To avoid these problems, a single position sensitive photomultiplier tube (PSPMT) can be used to read the entire array of crystals in the PET detector. The PSPMT is more compact and has higher spatial resolution. In addition to providing energy of an event, a PSPMT is used to locate each individual crystal in the detector array where an event occurred using the position on the PMT face where the scintillation light strikes. Figure 2.13 shows multiple dynodes channels as accelerating stages for electrons in a PSPMT (74). These dynode channels keep the photoelectrons moving in a direction parallel to their incident path on the face of the PSPMT to preserve the position of interaction of an event.

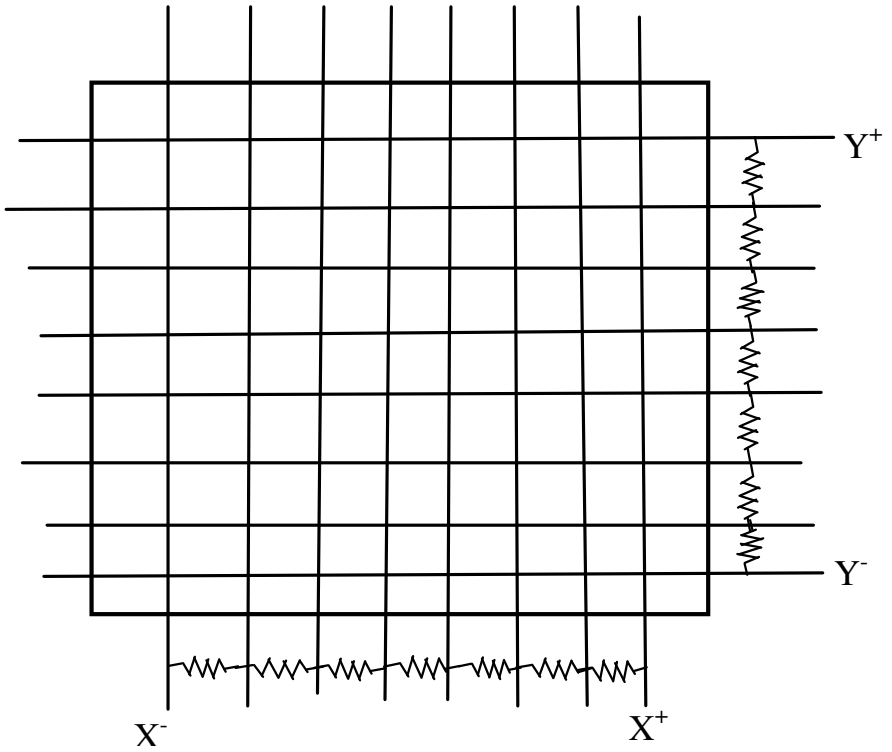

Figure 2.14 A series of wires with a resistor network used in a PSPMT to determine the X and Y coordinates of the position of interaction of an event based on the voltage at each readout point X^+, X^-, Y^+ and Y^-.

To determine the X and Y coordinates of the position of interaction based on the voltage at each readout point X^+, X^-, Y^+ and Y^-, a series of wires with a resistor network is used in a PSPMT as shown in figure 2.14. This design is called resistive division network (75). It would be worth-mentioning here that the diagram shown is specific for a PSPMT that is multi-wire, not multi-anode. Since the voltage decreases as the electronic signal travels through more resistors on its way to the readout point, the voltage in the horizontal (X) and vertical (Y) direction determines the locations of events taking place further to the right or above of the resistors network, respectively. The sum of the voltages at these four readout points gives the energy of the event, i.e.

$$E = X^+ + X^- + Y^+ + Y^- \tag{2.17}$$

A modified Anger logic (76) is used to determine the position of interaction (X, Y) as

$$X = \frac{X^+ - X^-}{X^+ + X^-} \tag{2.18}$$

$$Y = \frac{Y^+ - Y^-}{Y^+ + Y^-} \tag{2.19}$$

After flood irradiation of the whole array in a PET detector, flood histograms are created using these position coordinates of gamma events for individual crystal identification in the array. A typical flood histogram image is shown in figure 2.15.

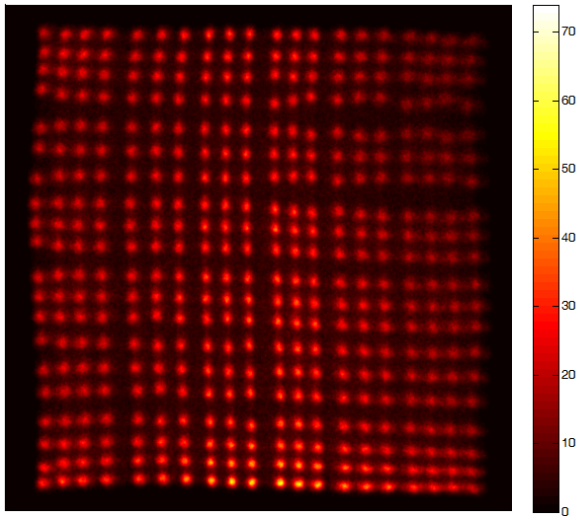

Figure 2.15 Flood histogram image of a 20 × 20 array of Siemens Inveon detector block (Courtesy of Dr. Andrew L. Goertzen, Department of Radiology, University of Manitoba).

2.3.5 Depth of interaction (DOI) detectors in PET

As described earlier in section 2.1.2.1.1, the DOI effect or parallax error degrades the spatial resolution mainly in the radial direction as one move away from the center of the scanner. The ability to obtain DOI information is particularly important for PET systems with small ring diameters as the resolution degrading effects of DOI as we move away from the center of the field of view increase as the ring diameter decreases (27).

The small size of the imaged object and the limited quantity of radiotracer injected into small animals makes it a challenge to obtain clinical quality PET images from preclinical PET systems. Therefore many detector designs, described in the following sub-sections, propose to add DOI capability to the PET imaging system.

2.3.5.1 Different designs of DOI detectors

Ito et al (77) give a nice review of PET detectors with DOI capability. All the popular designs that exist so far including dual-ended readout detector design, Phoswich design and dual layer crystals of offset positions will be described in the following sections.

2.3.5.1.1 Multi-layer design for discrete DOI measurement

Multi-layer design DOI detectors use multiple layers of scintillation crystal arrays. There are several designs under this category that can distinguish individual layers where the photon interaction takes place in the multi-layer detector. These include: phoswich using pulse-shape discrimination (PSD); relative offset dual-layer; and light-sharing design. These designs are discussed in the following sections.

2.3.5.1.1.1 Phoswich design

The phoswich (phosphor sandwich) DOI detector design employs two crystal layers of different scintillation materials both having different decay time constants and read out with the same photodetector coupled at one end (78)(79). Examples of phoswich pairs include NaI(Tl)/BGO and LSO/LuAP (80) (81). The prototype of the high resolution research tomograph (HRRT) (CTI, Knoxville, TN), a dedicated human brain scanner, used a GSO/LSO phoswich block detector design to add DOI capability in its design (82). As an alternative to different scintillation materials with different decay time

constants, two crystal layers of same material with different doping concentrations, changing their decay time constants, have also been used in phoswich designs. For example a later version of HRRT employed a LSO/LSO dual layer with different decay times for its DOI design (83). DOI resolution is extracted using pulse shape discrimination (PSD) methods based on the different decay time constants of two scintillation materials (84,85). Excellent layer identification has been shown by the PSD methods (86). Commercial examples of Phoswich designs include General Electric (GE) eXplore VISTA small animal PET scanner consisting of two crystal layers of LYSO and GSO with different decay time constants of 40 ns and 60 ns, respectively (45).

Disadvantages of phoswich designs include that discrete DOI information is provided by the length of the crystal in a multi-layer crystal design and thus the number of layers limits this information. The length of the crystal layer typically ranges from 5-10 mm (87) and determines the DOI resolution. Complicated pulse shape discrimination circuits or pulse waveform digitization for each channel are required to extract the timing difference between pulses of two types of crystals and remains a major challenge of this detector design. The DOI resolution in this design should be equal to the length of each layer in ideal conditions, however, the small decay time difference between two crystals; multiple interactions involving both layers and light loss at the interface of two materials due to their different refractive indices are some of the factors that degrade the DOI capability of this design. In addition, time performance is affected by the difference in decay times in the phoswich design (87).

2.3.5.1.1.2 Relative offset positions dual-layer crystals

Two layers of the same scintillation materials are used in this design in such a way that the top layer is offset by one half of the crystal pitch with respect to the bottom layer in both x- and y- directions (88)(89) (90) resulting in different light output profiles from the top and bottom layers. Up to four layers of crystals have been read out by applying this approach where a relative offset of all four layers to one half of a crystal pitch was used (91,92). The positions of these layers can be extracted based on the corresponding light output profile where the DOI information can be estimated from the flood histogram image that gives a 2-dimensional position map of crystals calculated from the centroid of light dispersion on a PSPMT. The flood positions of crystals in all layers are separated in the flood histogram due to a shift in the centroid of light dispersion with the offset of crystal layers.

2.3.5.1.1.3 Multi–layer with different crystal shapes

The same goal of relative offset dual-layer design can be achieved with an alternate design with two crystal layers of same scintillation material but different shapes. Peng and Levin (93) proposed a DOI detector module design with two crystal layers in which the top layer consists of four triangular crystals and the bottom layer four rectangular crystals. In this design the base of each triangular layer was twice the pitch of a rectangular layer so that the interface of each layer exactly fit in size with the other. The light output pattern depends on the shape of the crystal the γ-ray photon interacted with. For example, the interaction of photons with the top triangular crystal will result in a special light-focusing pattern. This will enable its differentiation from the photon interaction in the bottom layer rectangular crystal providing a discrete DOI. The complex

fabrication and relatively high cost of manufacturing triangular shape crystals remains a major challenge in this design.

Light-sharing methods (94)(95) can also be used to extract DOI information by utilizing different reflector arrangements in four layers. The light-sharing method was also applied using two and three layers of crystals cut as triangular prisms (96).

2.3.5.1.2 Dual-ended readout detector design for continuous DOI measurement

In this approach, two photodetectors are coupled to a single crystal array at both ends. The DOI is determined from the ratio between the light collected by the two photodetectors. The working principle of a dual-ended readout DOI detector is demonstrated in figure 2.16.

If we irradiate a 10 cm crystal at a location of 1 cm from PMT1, PMT1 gives a larger signal as compared to PMT2 as it is closer to the point of interaction. Now if we irradiate the crystal at a location of 5 cm (central location of the crystal) from PMT1, the two signals will superimpose on each other meaning that the two signals are equal to each other as the position of interaction is equidistant from PMT1 and PMT2. Finally if we irradiate the crystal at a location of 9 cm from PMT1 as shown in the bottom spectrum, the situation is totally reversed as compared to the spectrum on the top (1 cm location). Now the PMT2 signal is larger as compared to PMT1 as the interaction point is closer to PMT2. This means that the ratio of the two PMT signals depends on the irradiation location along the length of the crystal. Therefore this ratio could be used to encode the position of interaction in the axial direction. This approach, however, requires a careful calibration of the detector to establish an accurate relationship between the ratio signal and axial position of interaction as described in Chapter 5.

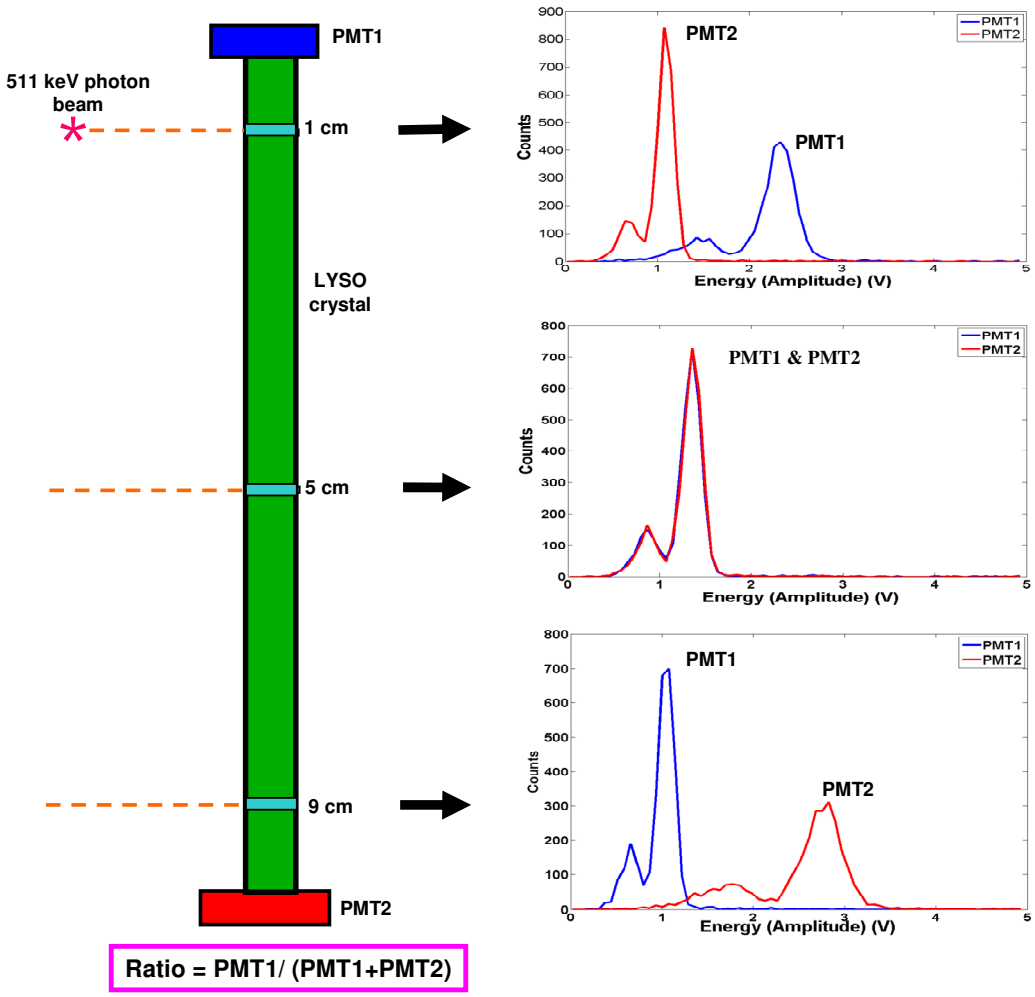

Figure 2.16 Principle of a dual-ended readout DOI detector is demonstrated. The distinction between the PMT1 spectrum (blue) and that of PMT2 (red) at different irradiation locations of LYSO can be easily seen. The spectra are obtained from our own measurements using the setup described later in section 3.2 (Fig. 3.2) of Chapter 3.

The approach of dual-ended readout DOI detector design was first proposed by Shimizu et al (97) where they used two PSPMTs (Hamamatsu R2487) coupled to a 4 × 8 array of 3 × 5 × 50 mm^3 BGO crystals at both ends demonstrating a DOI resolution of 9.5 mm with steps of 10 mm over the 50 mm length. The long crystals were designed to be oriented in the axial direction in a full-ring system and hence DOI resolution in this case is actually the axial spatial resolution for encoding positions of interacting annihilation

photons in the axial light-sharing direction. Moses et al. (98) used a dual-ended readout approach in a single crystal layer detector module consisting of a 2D array of 3 × 3 × 30 mm^3 BGO crystals coupled to an 8 × 8 array of pixilated silicon photodetectors (SiPD) at one end and a single channel PMT at the other end. The SiPD was used to determine which crystal the annihilation photon hit while the PMT was used to give the energy and timing resolutions. The Si detector is needed because it minimally attenuates the 511 keV photons at the entrance side of radially-oriented crystals in the PET ring detector. The DOI is determined from the ratio of the amplitudes of two signals as described earlier. Dual-ended readout of scintillation crystals coupled to APD arrays or PS-APDs at both ends has been extensively explored for adding DOI capability to conventional PET imaging system designs with shorter crystals oriented in the radial direction (98)(99)(100)(101)(102). A DOI resolution of about 1 mm has been demonstrated in the light sharing direction (103)(104) for arrays of 1 × 1 × 20 mm^3 LSO crystals. SiPM arrays have been used at both ends to extract DOI information by applying this design (105).The dual-ended readout design has also been applied to add DOI resolution to PET imaging systems for even smaller crystals of 0.5 mm or 0.75 mm pitch (106). Salvador et al. (107) investigated the design of a small animal PET imaging system using shorter axially oriented 1.5 × 1.5 × 25 mm^3 LYSO crystals with a depth of interaction (DOI) capability, demonstrating an independence of spatial resolution from the detection efficiency. In this work, a spatial resolution of about 1 mm was demonstrated.

This approach has an advantage over multi-layer designs in that continuous DOI information is provided by it with a better DOI resolution; however, it requires twice the number of photodetectors resulting in an increased cost. As the DOI resolution depends

directly on the difference of the signals (or ratio signals) between two photodetectors coupled at the ends therefore a challenge with this design is that the gain of the two photodetectors might change over the course of time. To overcome this problem, a calibration needs to be performed regularly as described later in Chapter 5.

The DOI capability of a dual-ended readout detector can also be used to find the axial position of interaction of annihilation photons in axially oriented dual-ended readout PET designs described in section 2.3.5.3

2.3.5.1.3 Direct measurement of discrete DOI positions

Discrete DOI information can be extracted from the signal generated directly at individual depths using several layers of crystal where individual crystals are coupled to photosensors (108)(109).

An approach in this category of DOI detectors, originally proposed by Levin (110), has been developed at Stanford University where a block detector is constructed by stacking 8 layers of 8 × 8 arrays of 0.91 × 0.91 × 1 mm^3 LYSO crystals. Each crystal layer is mounted on a layer of PS-APDs giving a positioning resolution of about 1 mm that is equal to the small crystal size. The location of each crystal is identified using flood histograms. The larger surface area (0.91 × 1 mm^2) of each small crystal faces the PS-APD, giving a high light output and resulting in excellent energy and timing resolutions. Due to the high light collection and minimized light path length (small crystal size) responsible for high timing performance, this design will be suitable for time-of-flight (TOF) DOI detectors. The requirement of very thin circuit boards and PS-APDs for a good packing fraction and the manufacturing cost of large number of crystals, photosensors and channels will remain a problem for this design.

In another approach, a group at CERN used a 6 × 8 array of 3 × 3 × 100 mm^3 LYSO crystals and 6 × 26 array of 3 × 0.9 × 40 mm^3 wavelength-shifting (WLS) strips isolated optically and inserted perpendicularly on each crystal layer (111). The crystals and WLS strips are coupled at one end to multi pixel photon counters (MPPCs) also called G-APD giving a DOI resolution of > 1.7 mm in the axial direction (87). The high cost due to large number of MPPC photosensors and output signal channels is again a challenge for direct DOI detector designs.

2.3.5.2 Surface treatment and reflectors in DOI detectors

A great deal of research has been done for the optimization of collection of scintillation light using different materials as external reflectors or coatings. Braem et al. and Vilardi et al. (112) (113) investigated different reflector materials and different coating thickness around 10 cm YAP and LYSO crystals and showed that the effective attenuation length of light in the crystal could be tuned to a desired value and could be reduced by a factor of 2 with a Teflon wrapping. They also demonstrated a DOI resolution of 9.3 mm for Teflon wrapped 10 cm polished crystals to be used in their dual-ended readout of axial HPD-PET. A 65 μm thick ESR reflector (Vikuiti-enhanced specular reflector film, 3M) having a reflectivity of 99 % was used around a 1 × 1 × 20 mm^3 LSO crystal and around 1mm FWHM DOI was achieved by a group at UCLA for their dual-ended readout DOI detector modules (103)(114). Trummer et al. (114) carried out an investigation of Teflon, Tyvek and Mylar foil aluminized with 16 nm Al+31 nm MgF_2 reflector materials for de-polished 2 × 2 × 20 mm^3 LuAP and LYSO crystals and demonstrated a DOI resolution of 2 mm which could be further improved by increasing

the number of de-polished surfaces at the cost of light loss which in turns degrades energy resolution.

As discussed in section 2.3.3.1, the idea of improving the DOI resolution by surface treatment of crystal surfaces is that a specular reflection takes place at a polished surface. In contrast, a diffused reflection occurs on the rough surface where photons are re-emitted in all directions resulting in improved DOI resolution. Huber et al. (115) investigated the effect of surface finish on the light collection from polished or acid-etched (acid-polished) LSO crystals, that is achieved by polishing via acid bath, and found a weak dependence of polished surface finish on light collection if it is etched beyond a certain time. Surface treatment of dual APD array readout of LSO crystals was optimized by Shao et al. (101) for spatial and energy resolution using polished, saw-cut and chemical etching surface finish with hot anhydrous phosphoric acid. They found that acid-etching of LSO crystals for 2-3 min gives best performance in terms of DOI resolution (2mm). Shimizu *et al* (97) used coarsely ground bands on a 5 cm BGO crystals oriented in the axial direction and coupled to two PMTs at its ends and demonstrated an axial resolution of 9.5 mm in light sharing direction. This work was patented in 1989 (116) but more extensive results were not published.

2.3.6 Axially oriented dual-ended readout PET designs

In this design of PET detector construction, the crystals are oriented along the axial direction. This approach places the photodetectors at the axial ends of the rings of detectors for signal readout. In detectors of this kind, generally the axial position of interaction is determined by calculating the relative signal registered in the detectors at opposite ends of the crystal. The resolution degrading effects of parallax error in radially

oriented detectors (discussed in section 2.1.2.1.1) can be minimized if the length of the crystal is decreased and the diameter of the ring is reduced but at the cost of the sensitivity of the system. Therefore orienting the crystals in the axial direction in axially-oriented dual-ended readout designs removes the parallax error and increases the sensitivity of the system by using large crystals thereby making the spatial resolution and sensitivity inherently independent from each other.

The axial PET geometry was first proposed by Shimizu *et al* in 1988 using 5 cm long BGO crystal bundles oriented in the axial direction and read out at both ends using photodetectors (97). This detector geometry has also been previously explored by a research group at CERN for human brain imaging using $3.2 \times 3.2 \times 100\text{-}150$ mm^3 LYSO scintillation crystals readout initially by hybrid photon detectors (113)(117) and later by wave length shifting fibers and Geiger-mode avalanche photodiodes (112) (118) but has not been extensively investigated for applications of small animal imaging using smaller crystal sizes. The bore size of a brain scanner is relatively larger than an animal scanner due to the size difference in human head and a mouse or rat.

2.4 Monte Carlo Simulation of scintillation detectors

Monte Carlo simulations are very useful tools used for designing and refining of detector modules to be used in PET imaging systems. Optical photon tracking in scintillation crystals is one of the important parts of these simulations. One of the widely utilized Monte Carlo simulation programs is Geant4 (119). This program allows accurate modelling of radiation sources and detecting instruments, while modelling the optical photon transport in Geant4 is based on DETECT2000 (described in section 2.4.1). GATE (Geant4 Application for Tomographic Emission) (120), which is based on physics models

from Geant4, is widely used in the field of nuclear medicine for modelling radiation sources and their detection in imaging systems. The optical photon transport models of Geant4, however, were not incorporated in GATE until version 4. These DETECT2000 models in Geant4 have now been incorporated in GATE version 6 and currently are in the validation stage (121) (122). Besides the basis of optical photon transport in Geant4, the DETECT2000 package can be independently used for optical photon tracking.

2.4.1 DETECT2000 package

The DETECT2000 Monte Carlo simulation program (123) is used for modeling optical photon transport within scintillator crystals. This code has been widely used in many studies, for example, (124), (125), (126), (127), (128), (129), (130),(131). These simulations are used to predict the performance of single crystals or crystal arrays in a complete detector module and optimize the light output for energy and spatial resolution using different surface treatments and reflectors around the crystals and hence refine detector module design before the actual modules are constructed. This is a process best suited for simulation due to the high cost of the scintillator crystals used in PET detector work.

DETECT2000 generates scintillation photons isotropically within a specified volume or portion of the crystal using random numbers and tracks each photon to its ultimate fate whether it is absorbed, escaped, transmitted or detected. The data recorded for each tracked photon includes decay and delay times, total detection time or elapsed time and last coordinates of photon. The emission spectrum of scintillation photons from a particular crystal, its scintillation light yield and the wavelength dependent quantum efficiency of photodetectors can be modeled in the DETECT2000 simulation. Bulk

absorption and scattering in the crystal under study are modeled using a mean distance travelled by the photon in that crystal for each process.

A general syntax is used for the simulation of a complete detector geometry consisting of either a single crystal or crystal arrays in a module using planes, cylinders, cones or spheres. To simulate reflection of scintillation light from polished, ground, painted or metalized surfaces of crystals, different models describing the optical behavior of the surfaces are used. The optical surfaces in contact with other components or the different components of the crystal itself are treated using Snell's law of refraction of light given by:

$$\frac{\sin\theta_1}{\sin\theta_2} = \frac{n_2}{n_1} \tag{2.20}$$

Where θ_1 and θ_2 are the angles of incidence and refraction in the first and second components, respectively and n_1 and n_2 are the corresponding refractive indices of the components. The detailed use of DETECT2000 in our research work is described in Chapter 6.

Chapter 3 Experimental Setup and Data Acquisition

3.1 Introduction

To carry out the research project described in section 1.2, an experimental setup was established that will be described in this chapter. The methods used for experimental and simulation studies for developing a dual-ended readout detector based on axially oriented 100 mm long LYSO crystals coupled to two PSPMTs at both ends and to be used in a highly compact and portable preclinical PET system are also elaborated.

3.2 Experimental setup and methods

3.2.1 Overview of experimental setup

The experimental setup consists of dual-ended readout of 100 mm long LYSO crystals using position sensitive photomultiplier tubes (PSPMTs) along with an electronically collimated 511 keV beam irradiation arrangement. Dual-ended detector design, data acquisition software and PSPMT pulse processing NIM electronics and electronic collimation of the beam are described here in detail. Methods describing the application of different reflectors around the LYSO crystals and surface treatment of the crystals in this work followed by processing and analysis of data from dual-ended readout detectors are illustrated.

3.2.2 Dual-ended readout detector description and data acquisition

3.2.2.1 Description of design

The schematic diagram of our design concept is shown in figure 3.1 in which 100 mm long LYSO crystals coupled to two PSPMTs at the ends are oriented along the axial direction. This approach places the PSPMTs at the axial ends of the rings of detectors in

our proposed PET, reducing the overall radial extent of the detector ring and associated electronics and, hence, can fit into a bio-safety cabinet. The light-sharing between two PMTs in the dual-ended readout detector is used to encode axial-position of interaction of 511 keV γ-events in the crystals.

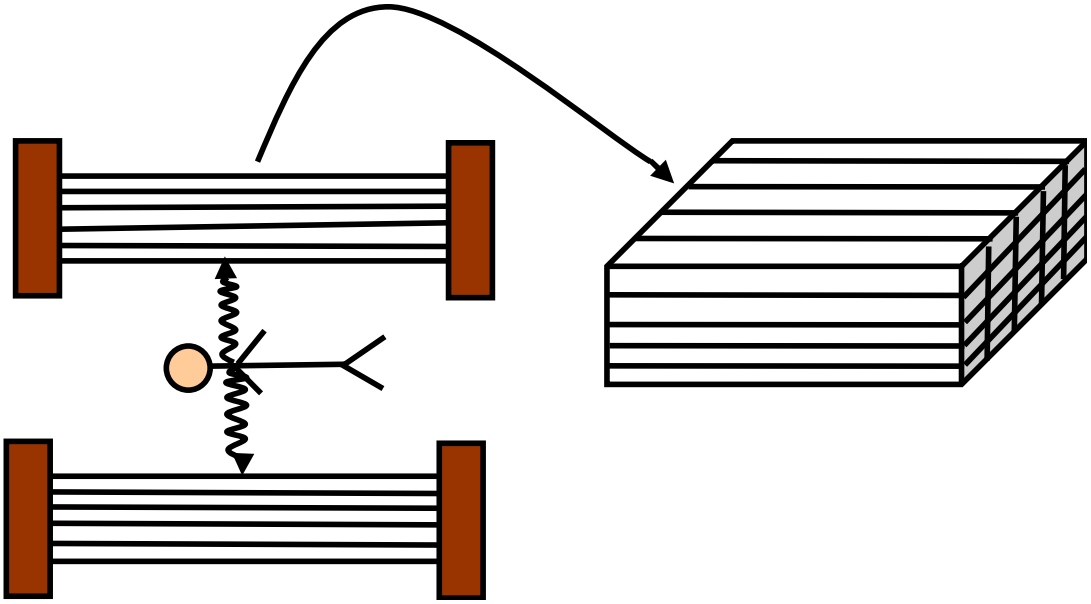

Figure 3.1 Schematic diagram showing axially oriented 100 mm long LYSO scintillator crystals coupled to PSPMTs at two ends in detector modules to be used in our proposed compact preclinical PET imaging system. The axial position of interaction of 511 keV γ-events is determined by the ratio of the two PMT signals.

3.2.2.2 Establishment of experimental setup for dual-ended readout detector

One hundred millimeter long lutetium yttrium oxyorthosilicate (LYSO) scintillator crystals, polished on all sides, were obtained from a commercial supplier (Proteus Inc., Chagrin Falls, OH). The four long sides of a crystal under study were covered with a reflector material as described in section 3.3 and the ends of the crystal were coupled to a pair of Hamamatsu R8900U-00-C12 (Hamamatsu Photonics K.K., Japan) position sensitive photomultiplier tubes (PSPMTs) using Visilox V-788 optical grease to make it a

dual-ended readout detector. An experimental setup was established for the project as shown in figure 3.2.

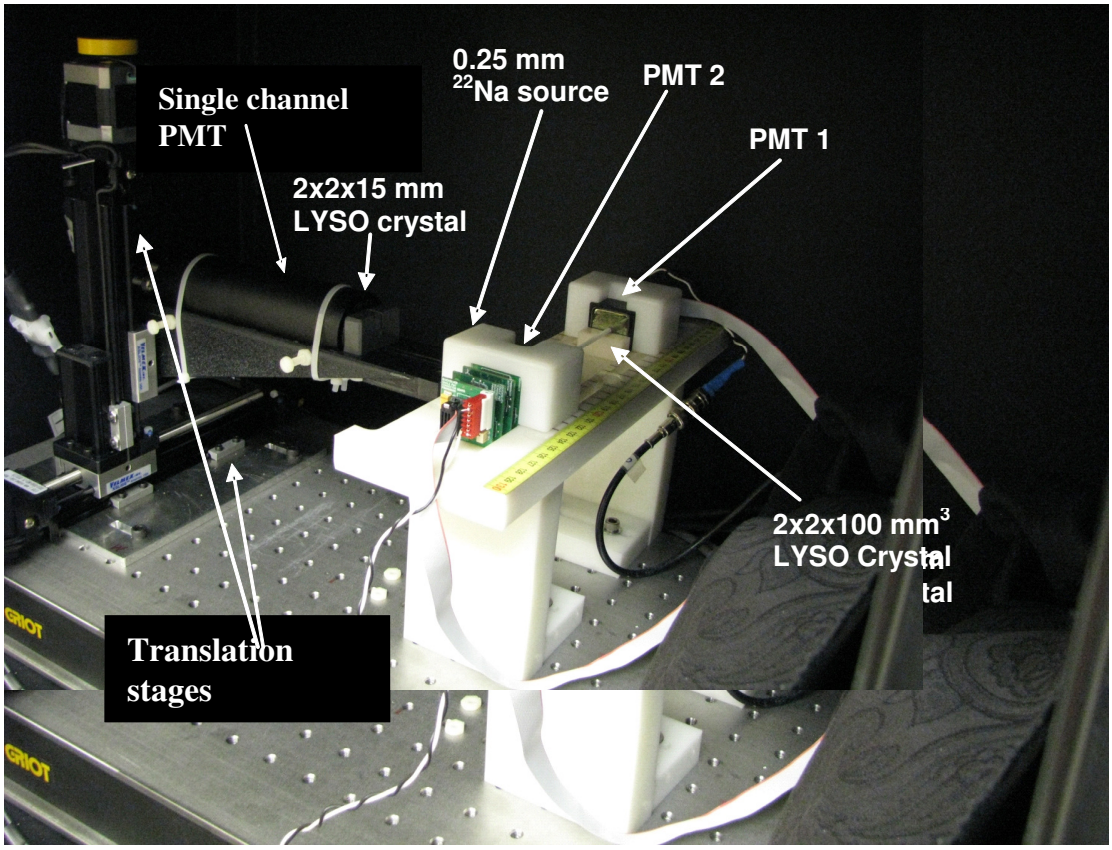

Figure 3.2 Experimental setup established for dual-ended readout of axially-oriented 100 mm long LYSO crystals coupled to PSPMTs at both ends. A 2 × 2 × 15 mm^3 LYSO crystal coupled to a single channel PMT and in alignment with the ^{22}Na source all mounted on a translation table attached to a 2-axis translation stage for electronically collimating 511keV photon beam in a light tight box

A 0.25 mm ^{22}Na source (model MMS09, Eckert & Ziegler Isotope Products, Valencia, CA) embedded in a 1 cm^3 acrylic cube is mounted on a table at a distance of 5 cm from the test crystal, emitting positrons (β^+) that subsequently annihilate with surrounding electrons to emit back-to-back 511 keV photons. A 2 × 2 × 15 mm^3 LYSO crystal coupled to a single channel PMT (Hamamatsu H3178-51) and in alignment with the ^{22}Na source is also mounted on the same table and is used in electronic coincidence (see section 3.2.2.4) with the test crystal . This table was attached to a 2-axis translational

stage that allows the movement of ^{22}Na source, along with the single channel PMT, for irradiating the test crystal. The 2-axis translation stage (XZ-configuration) with 4 inches total travel in the Z-axis (model # XN10-0040-M01-71) and 6 inches total travel in X-axis (model # XN10-0060-M01-71) was purchased from *VELMEX, INC*. (Bloomfield, NY). The X-stage is attached to a single shaft stepper motor (model # PK245-01AA) while the Z-stage is attached to a double-shaft stepper motor (model # PK245-01BA). A stepper motor works on the principle of a DC electric motor but divides a full rotation into a number of equal steps. The position of the motor can then be controlled through a software created in LabWindows to move and hold at one of these steps that subsequently moves the translation stage attached to it.

The PSPMTs were mounted on a Teflon table with holders screwed on it for holding the PSPMT in a fixed position to be coupled to the crystal at both ends as shown in Fig 3.2. Both the tables used in the experimental setup were constructed by Medical Devices at CancerCare Manitoba. The test crystal and the coincidence crystal are at an equal distance of 50 mm from the source. The entire experimental arrangement was placed in a light tight box by mounting the translation stage and the Teflon table on an optical bread board in order to keep every part on the same level and to avoid any movement. The detector response in the light sharing direction is assessed by irradiating the crystal using an electronically collimated 511 keV beam as described in section 3.2.2.4. This experimental arrangement is similar to that reported previously by other groups (99) (100) (101).

3.2.2.3 Pulse processing electronics and data acquisition for PSPMTs

The 12 anode outputs, 6 wires in x-direction and 6 in y-direction, from each PSPMT were multiplexed to four signals, X^+, X^-, Y^+ and Y^- as described in section 2.3.4.2 using Siemens Inveon pre-amplifier stacks (61) (Siemens Preclinical Solutions, Knoxville, TN) and are shown in figure 3.3.

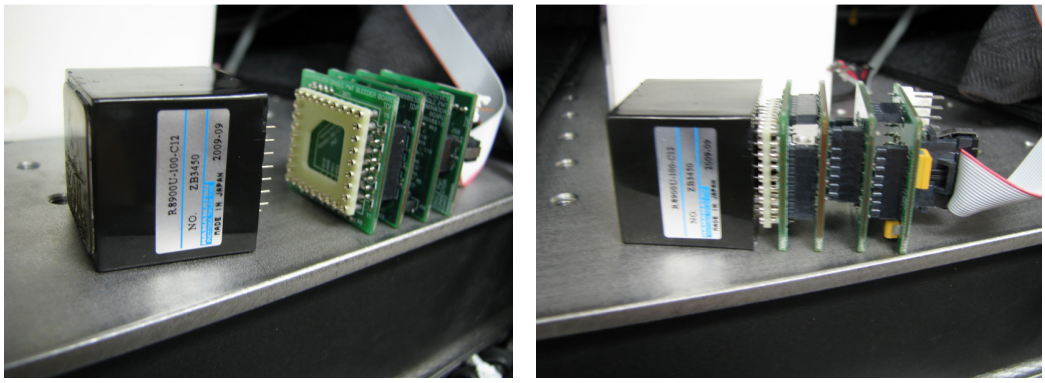

Figure 3.3 Siemens Inveon pre-amplifier stacks connected to a PSPMT

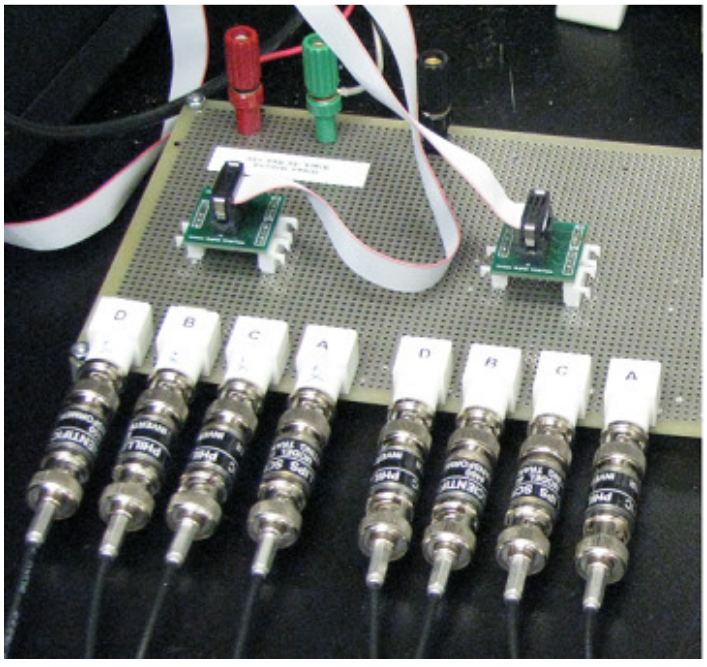

Figure 3.4 Readout board that recieves signal from each detector through ribbon cables and splits it out in to four signals for each detector. Signal inverters connected to the readout board convert positive signals to the negative ones that can be subsequently used by NIM electronics

The bias voltage of -800 V was supplied by a high voltage power supply (ORTEC 556H) and is provided to each PSPMT through its corresponding preamplifier stack. A readout board recieves 4 multiplexed signals from each detector through a 20 pin ribbon cable and splits them out to BNC connectors as shown in figure 3.4. A +5 V & -5 V readout voltage is also provided through the ribbon cable where +5 V are used for power multiplexing electronics. The positive signals from the PSPMTs were converted into negative signals using signal inverters (Phillips 460, Phillips Scientific, Mahweh, NJ, USA), also shown in figure 3.4 that can be used by the nuclear instrumentation module (NIM) equipment as shown in Fig. 3.5. These signals were subsequently processed using standard NIM electronics. A photograph of the bench top data acquisition NIM electronics is shown in figure 3.5 and a schematic drawing of the electronic beam collimation and the PMT signal processing in the bench top data acquisition NIM electronics is shown in figure 3.6.

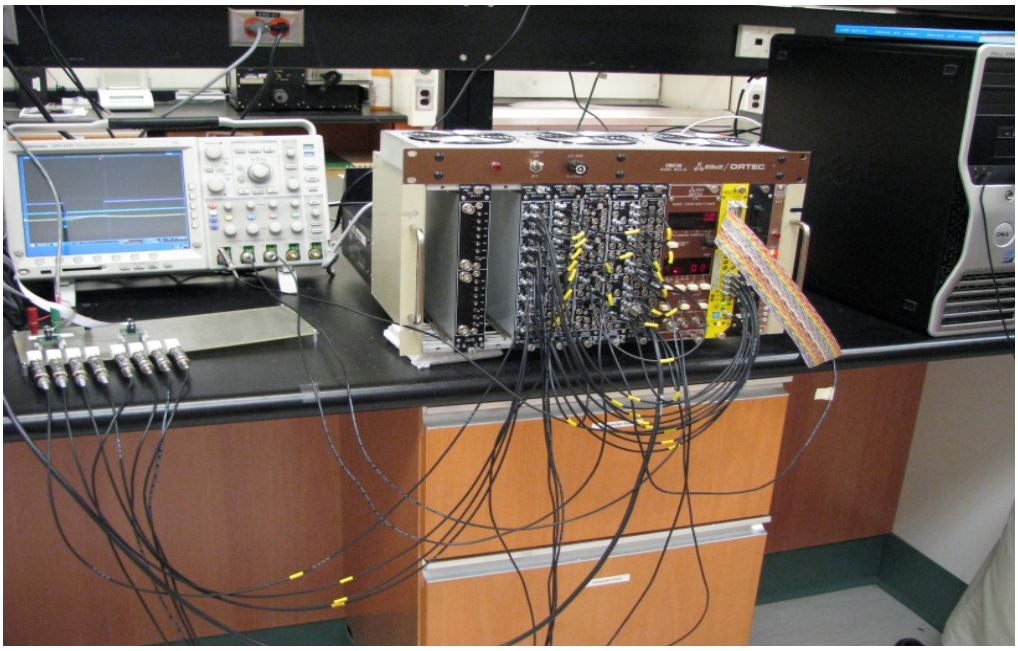

Figure 3.5 Photograph of the bench top data acquisition NIM electronics system during signal processing in this project.

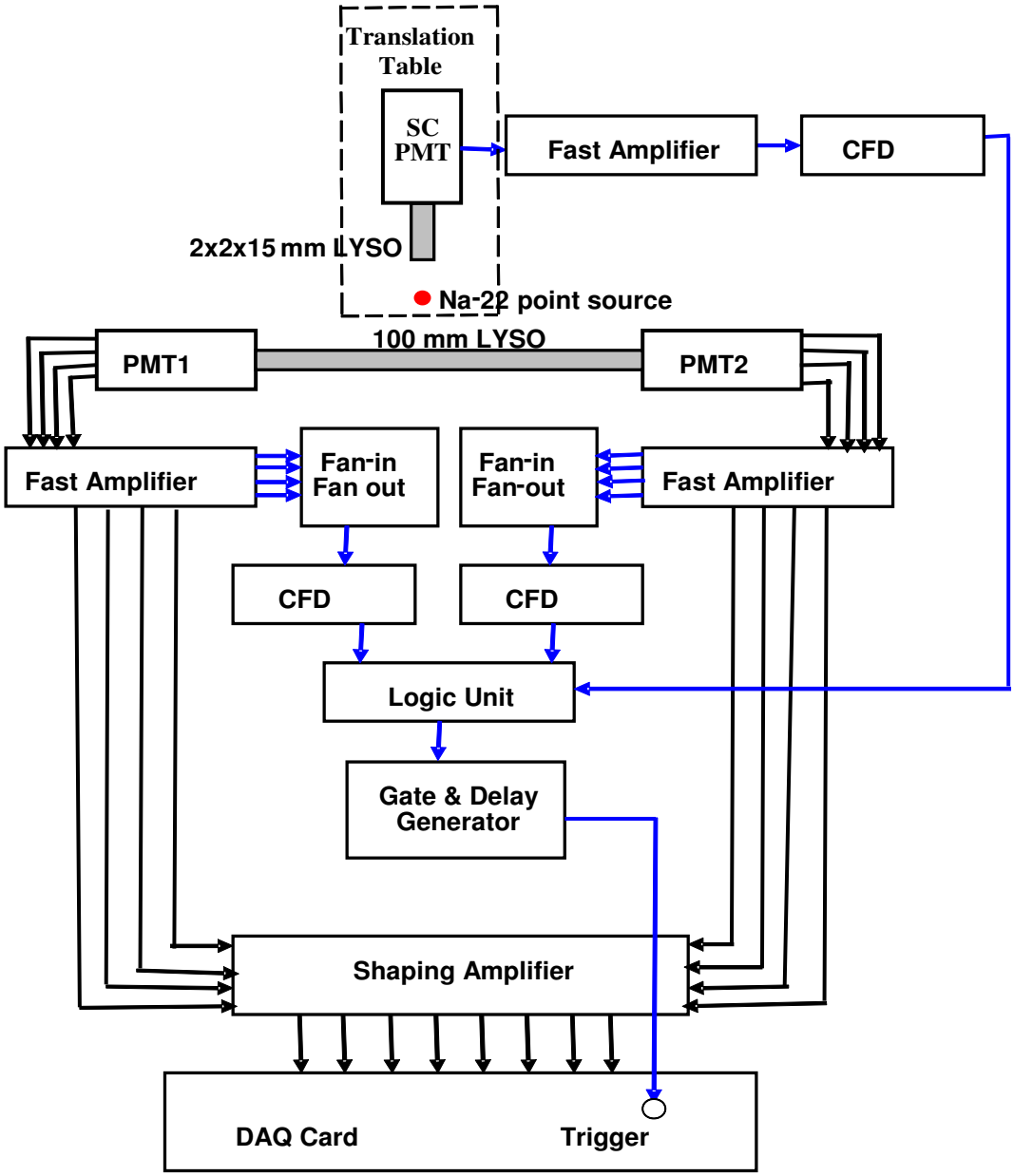

Figure 3.6 Schematic drawing showing the electronic collimation of the 511 keV beam and PMT signal processing in bench top data acquisition NIM electronics. The single channel PMT (SC PMT) and ^{22}Na source are placed on a translation table shown in the dashed rectangle that is attached to a 2-axis translation stage.

The four negative PSPMTs signals from the inverters were fed into four channels of a fast amplifier (Phillips Scientific 778). The minimum gain for this amplifier is 2X. Besides performing minimal shaping and increasing the amplitude by 2 in this study, the

preamplifier splits each signal into two identical parts without altering its shape. One signal path is used for generating timing signals shown in blue in figure 3.6 that goes into a linear Fan-in/Fan-out (Phillips Scientific 740) while the other path shown in black is fed into a shaping amplifier (Mesytec MSCF–16, 16 channel spectroscopy amplifier).

The fan-in/fan-out sums the four signals from each PSPMT and each sum signal is fed into a constant fraction discriminator (CFD) (Phillips Scientific 715) with a width of 20 ns each. The single channel PMT signal from the smaller crystal is also fed into the fast amplifier and then fed into a CFD. All three CFD output signals are fed into a majority logic unit (Phillips Scientific 754), which is used to create a trigger signal. A valid event is defined as an event detected when three CFD signals overlap producing a NIM logic pulse. This is called electronic coincidence. The size of the coincidence window was 40 ns which is the sum of the CFD pulses width. The PSPMT signal, shown in black in figure 3.6, is further amplified and shaped by passing it through a shaping amplifier. The reason for shaping is to reduce the noise and slow the signal so that the Analogue-to-digital converter (ADC) can capture it. As the shaping time of the shaping amplifier used was 250 ns therefore the fast trigger signal from the logic unit has to be delayed by feeding it to a gate and delay generator with a delay of 160 ns. The positive transistor-transistor logic (TTL) output at the end of the gate pulse is passed to the data acquisition (DAQ) card where it triggers to sample the shaped signal from the shaping amplifier and hence is sampled. The eight shaping amplifier output signals are transferred to the DAQ card by a custom cable. The shaped signals are digitized using a National Instruments PCI-6133 PC based data acquisition card (National Instruments Corporation, Austin, TX) running under a National Instruments LabWindows/CVI based interface.

3.2.2.4 Software for data acquisition

I wrote a software in LabWindows/CVI to control the motion of the 2-axis translational stage in the horizontal and vertical directions with stepper motors in the experimental setup as described in section 3.2.2.2. As the ^{22}Na source and the coincidence crystal coupled to the single channel PMT are mounted on the translation stage, it allows the movement of ^{22}Na source, along with the single channel PMT, for irradiating the test crystal in steps. The code for the stage movement control uses the LabWindows functions OpenCom( ) in the main( ) function of the code for opening the COM port and communicating with it using ComWrt( ) function. For a desired distance to be travelled by the stage in horizontal (X) and vertical (Z) directions before irradiation, the code requires number of movement steps given by the translational specifications of the stage as follows:

The stage moves 1.0 mm in one turn or revolution of its bolt and it advances 0.0025 mm (2.5 μm) per step, therefore, the total movement in one revolution (1 mm) would be 400 steps (1/0.0025). For a 1 cm (10 mm) movement, one then has to write 4000 steps. The speed of the motor in steps/sec can also be controlled in the code. The total number of steps to be moved by the stage in horizontal (left or right) and vertical (up or down) and its speed are written within the ComWrt( ) function. The stage can also be set to move to its minimum (origin) or maximum position in the program. The code is attached in Appendix A. This code was then integrated in the existing software being used for acquiring the data without any translation of the irradiation beam (132).

3.2.2.5 Electronic collimation of 511 keV photon beam

Figure 3.7 shows a schematic diagram of the experimental arrangement, in which a single 2 × 2 ×15 mm^3 LYSO crystal coupled to a single channel PMT in alignment with a ^{22}Na point source is used in coincidence with the test LYSO crystal to create the electronically collimated 511 keV photon beam. As described in section 3.2.2.3 and also shown in figure 3.6, all the three CFD output signals (the two PMT signals for the test crystal and the single channel PMT signal from the smaller crystal) are fed into a majority logic unit set at a coincidence level 3 for the detection of a valid event from the three signals in electronic coincidence after creating a trigger signal.

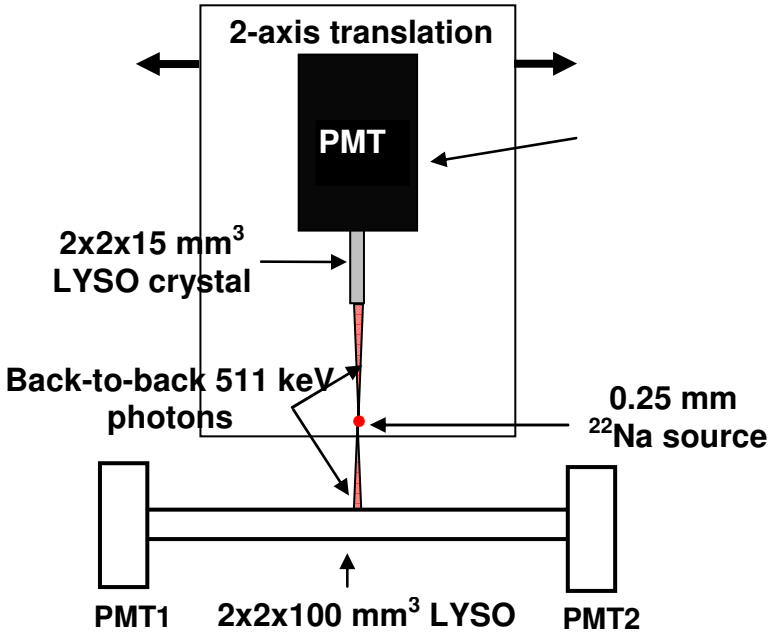

Figure 3.7 Schematic diagram of experimental setup showing electronic collimation of 511 keV beam with translation stages in a light tight box

The ^{22}Na source, small LYSO crystal and single channel PMT are mounted on the 2-axis translation stage in order to allow reproducible and precise positioning of the 511 keV beam. A custom code written in LabWindows as described in 3.2.2.4 was used to

control the movement of the translation stage. The collimated beam so obtained was aimed perpendicular to the long axis of the crystal. The response of the 10 cm long crystals versus irradiation position was determined by irradiating the crystal at nine discrete locations separated by 1 cm each. The beam width on the crystal based on the 2 mm coincidence crystal width and 0.25 mm source diameter was estimated to be 2.5 mm using the following equation (114) and was not corrected for the positron range.

$$R_{beam} = s + \frac{b}{a}(s + w) \tag{3.1}$$

Where R_{beam} is beam width, s is the source size (0.25 mm), w is the crystal width (2 mm), a is the distance of the source from the coincidence crystal surface (50 mm) and b is the distance of the source from the test crystal (50 mm).

3.2.2.6 Locating the ends of the crystal with respect to the translation stage movement

In order to find a relationship between the axial position of interaction of an event and the ratio of the two PMT signals, a discrete irradiation of the crystals in steps of 1 cm is required. Therefore the end points or zero and maximum positions of the crystal with respect to the translation stage over its range of motion must be determined. This enables us to find the position of the translation stage, after moving a certain distance, which corresponds to the zero position of the crystal. To achieve this, the translation stage was moved in steps of 1 mm using the LabWindows code and recording data at each location for a 1 min irradiation. Before this measurement, a coupling and alignment check was made to ensure that the crystal is well coupled and aligned parallel to the stage as described in section 3.2.2.7. Figure 3.8 shows a plot of the counts versus the position of the translation stage. No counts were observed until the movement position crossed the

first end (zero position) of the crystal. Therefore the zero position of the crystal in this case was found to be 37.50 mm with respect to the translation stage movement from its origin. There is a sharp increase in the counts until a plateau is reached. The counts remain uniform over the entire range of the crystal and started to decrease sharply and reach zero when the translation stage reaches the other end (maximum position of 10 cm) of the crystal. The maximum position of the crystal in this case was found to be 137.50 mm with respect to the translation stage movement from its origin. The error bars in the plot are the square root of the counts at each irradiation position of the beam. Similarly, the vertical position of the translation stage at the middle position (i.e. 5 cm) of the crystal was found by moving it in the vertical direction in steps of 1 mm and the counts were recorded at each irradiation position.

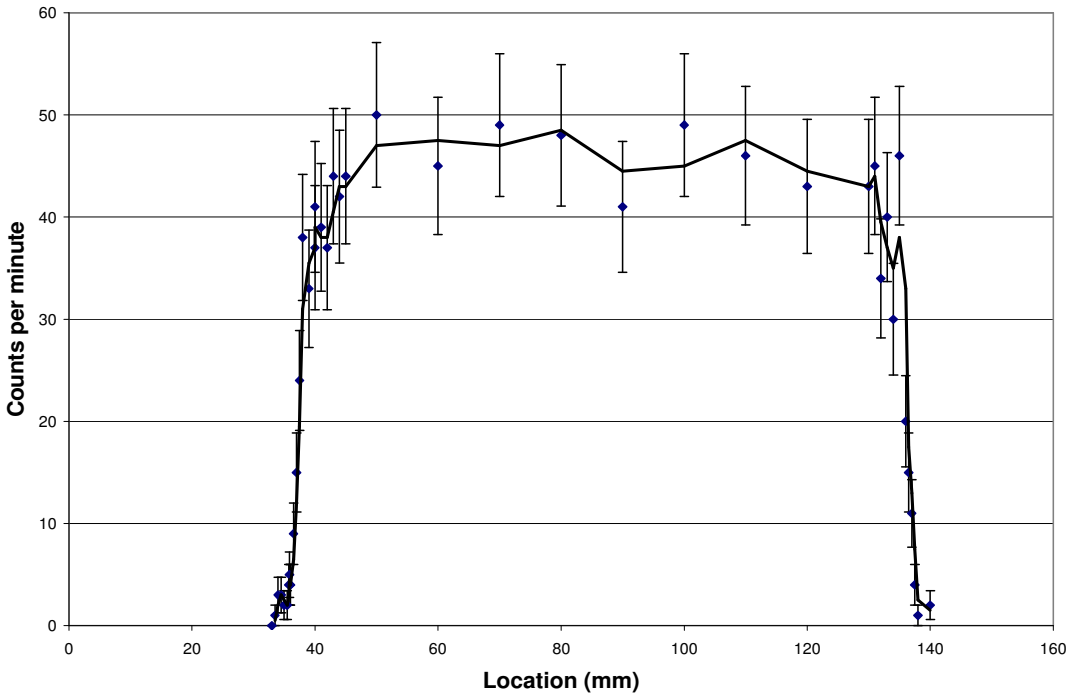

Figure 3.8 Plot of counts versus the distance covered by the translation stage used to locate the end positions of the 100 mm crystal. Note the left end position of the crystal at 37.5 mm and the right end position (100 mm) at 137.5 mm relative to the stage movement position.

In this case the maximum counts were found when the translation stage moved to 24.22 mm in the vertical direction that corresponds to the mid-width of the crystal. Therefore in each subsequent measurement of this crystal the horizontal position of the translation stage would be set at 37.5 mm while its vertical position would be set at 24.22 mm using the LabWindows program. These positions must be measured each time a different geometry of the crystal is used. It is worth-noting that the 100 mm crystal length observed in Fig. 3.8 also confirms the accuracy of the translation stage motion.

3.2.2.7 Alignment of crystal with translation stage and coupling test

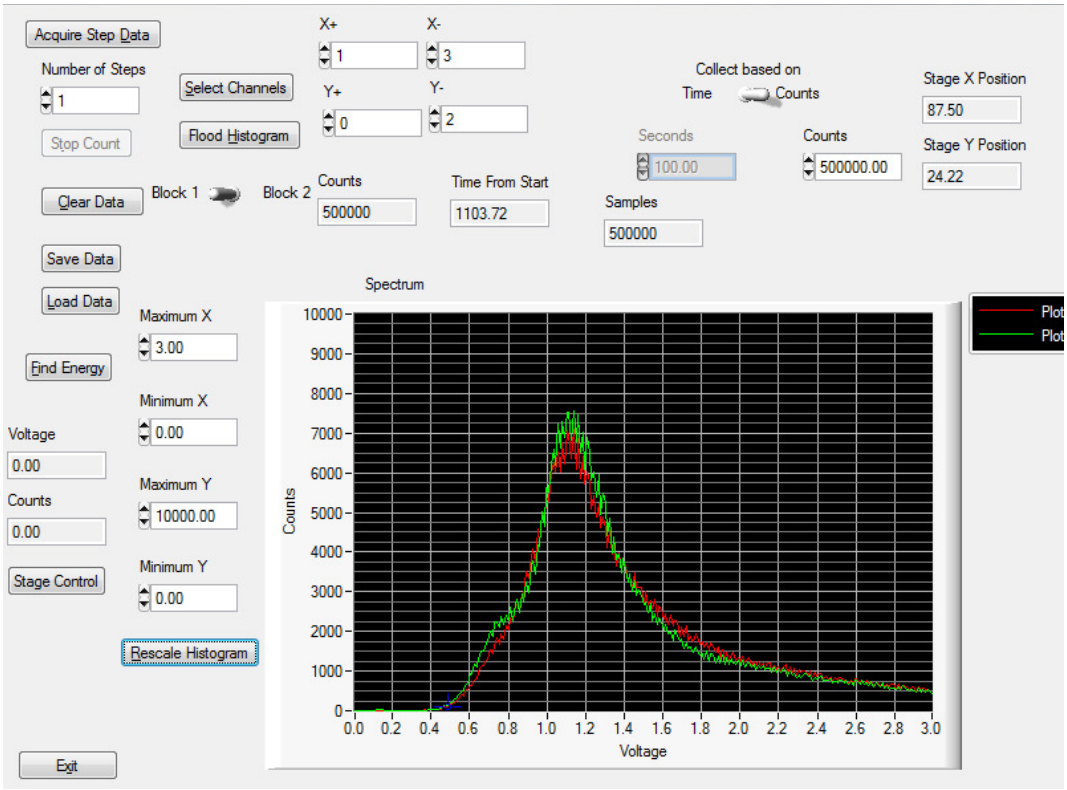

Figure 3.9 Plot of two individual PMT spectra shown in green for PMT1 and red for PMT2 when the crystal is irradiated at its central location (5 cm) in singles mode. Note the overlapping of the two spectra that reflects the good coupling and alignment of the crystal to the two PSPMTs. Also note the stage X position corresponding to the 5 cm irradiation position (central position of the crystal) and Y position of the stage (mid-width of the crystal) found in section 3.2.2.6

To check the alignment of the crystal and its coupling to the PSPMTs, a procedure was established as follows. After coupling the crystal to the PSPMTs, the crystal was irradiated at its central position (5 cm) in singles mode, i.e. using the experimental arrangement shown in figure 3.2 without electronic collimation, for around 100 sec. After looking at the individual PMT spectra on the LabWindows screen as shown in figure 3.9, if the two spectra (green for PMT1 and red for PMT2) overlap then the alignment and coupling are good. Otherwise, the alignment and coupling are repeated and the measurement repeated until the two spectra overlap.

3.2.2.8 Acquisition of data set

The following steps illustrate the use of the LabWindows program for the acquisition of a data set. Refer to figure 3.9 for each step:

- Select channels to be used in measurement by clicking 'select channels' box.
- Type number of steps in the measurement with 'Number of steps' box. Type for example 9 for the nine steps measurement.
- Select 'Counts' icon and type the total number of counts in 'Counts' box to be acquired in each step, for example 15000 in our measurements.
- Set Stage X position to 37.50 and Stage Y position to 24.22, as described in section 3.2.2.6.
- Finally click the 'Acquire Step Data' icon to start the measurement. This step will result in the popup of the directory and files selection on the computer where the acquired data will be stored after each measurement step.

3.2.3 Reflectors for LYSO crystals

For the light collection from LYSO crystals, three different reflector materials, namely Teflon, 3M Vikuiti enhanced specular reflector (ESR) (3M Optical System Division, St. Paul, MN) and Krylon black spray-on paint were applied around the crystals used in this work. This section describes how these reflectors were applied around the crystal. Particularly, the UV irradiation technique for curing optical glue for coupling ESR reflector with the crystals is described in detail.

3.2.3.1 Teflon

A 0.75″ wide piece of the polytetrafluoroethylene (PTFE) Teflon tape equal in length to the crystal was cut and applied by wrapping the crystal with four layers of the Teflon tape. Two such pieces of Teflon tape were required to provide its four layers. This tape is commonly used around scintillation crystals for light collection as well as for sealing pipe thread.

3.2.3.2 Paint

The KRYLON Black paint was sprayed on each lateral surface of the crystal under study with several coatings in a laboratory fume hood. Each coating was allowed to dry before applying the next coating. The coating was kept uniform through the entire length of each crystal.

3.2.3.3 ESR

Initially, the ESR was applied by scoring an 8×100 mm^2 piece so that it would fold around the crystal and then securing it in place by wrapping the exterior with Teflon tape. However, it was observed during the investigation of ESR reflectors around the LYSO crystal that the ESR reflector is not easy to fold, wrap and secure in place around the

crystal. Moreover, there is an air gap between the reflector and crystal surface that could affect the light collection from the crystal. Therefore a UV light curing technique was required to be established and optimized to glue ESR to the crystal using optical adhesive glue and curing it with UV curing spot light equipment.

Dymax OP-20 Optical adhesive Epoxy Glue (DYMAX, Torrington, CT) was purchased from a commercial supplier (Fiber Optic Center Inc., Bedford, MA). A UV curing spot light equipment (Dymax Blue Wave^{TM} 75, Model 40078) was purchased from another commercial supplier (Dymax TecServices, Brampton, ON). The OP-20 adhesive glue was dispensed with a syringe needle on each long crystal surface. The ESR reflector was cut into four pieces of size 2 × 100 mm^2. Each piece was applied to each long surface of the crystal one after the other with the OP-20 adhesive glue dispensed on the crystal. UV irradiation from a Dymax Blue Wave 75 UV Spot Light Source was used to cure the glue-coupled ESR reflector as shown in figure 3.10.

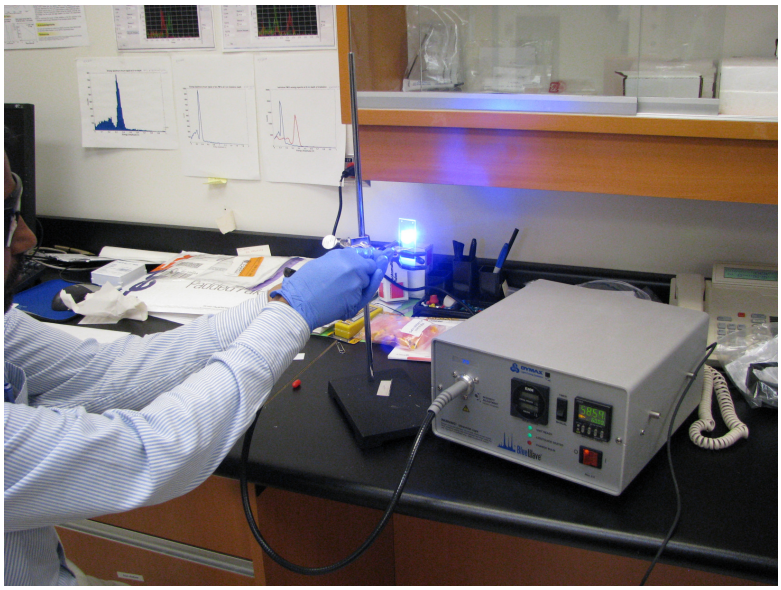

Figure 3.10 UV irradiation from a Dymax Blue Wave 75 UV Spot Light Source for curing OP-20 adhesive glue for coupling ESR reflector to the crystal

An acceptable glue curing was obtained by using the following settings after several trials. The intensity adjustment knob was moved through 180^{o} and the shutter timer was set at 99 s. The UV intensity of the equipment deteriorates with extensive use of its bulb. The bulb intensity typically decreases by about 1 % over a normal use of 8 hours; therefore, the adjustment should be changed above the previous settings periodically in the case of intensive bulb usage in order to achieve an acceptable curing using the procedure described above. Surgical gloves and UV glasses were used during the UV irradiation as a safety measure. The detailed operation procedure of the equipment can be seen in the operation manual (Operational Manual BLUEWAVE 75, UV Curing Spot Light Source, DYMAX, Torrington, CT).

3.2.4 Surface treatment of LYSO crystals

3.2.4.1 Banding methods

Figure 3.11 Creation of etching band patterns on a 3 × 2 × 100 mm LYSO crystal with crystal saw blade

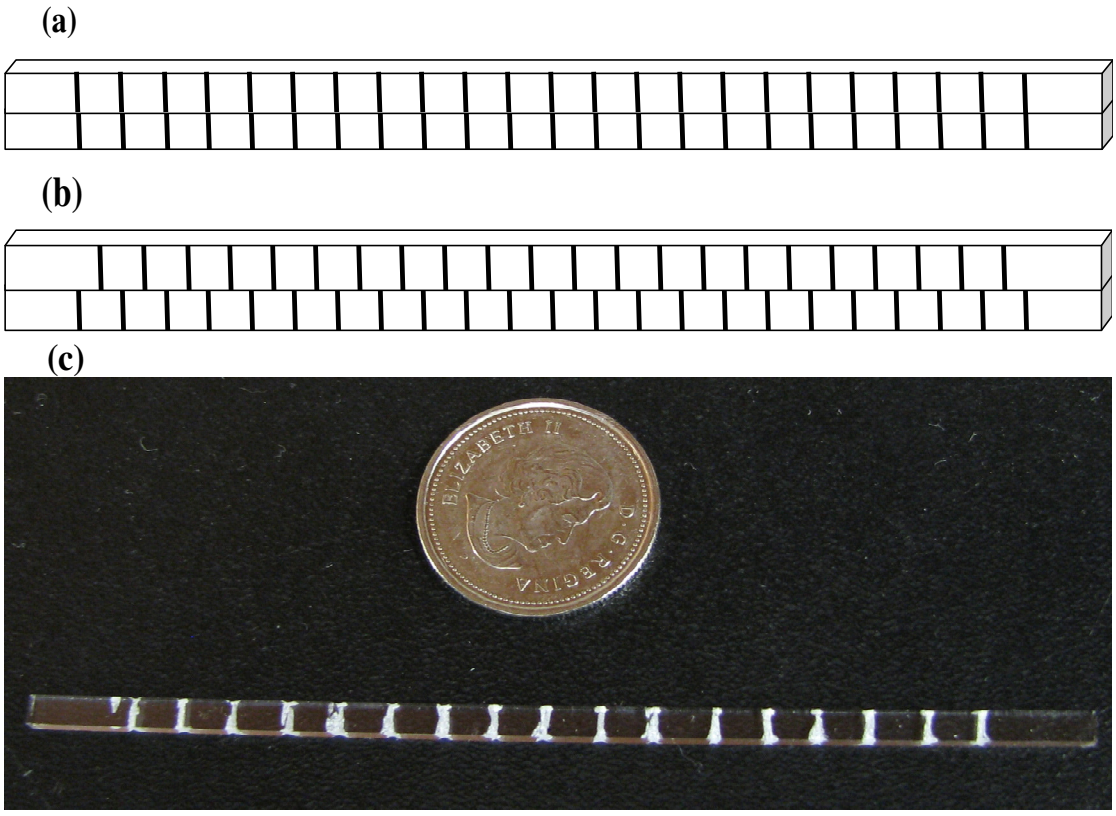

Figure 3.12 (a) Schematic example of coinciding etching band patterns created on the same axial locations of top and bottom surfaces of a 100 mm long LYSO crystal. (b) Schematic example of interleaving etching band patterns created on top and bottom surfaces of a 100 mm long LYSO crystal. (c) Photograph of a 3 × 2 × 100 mm^3 crystal with coinciding etching band patterns on four long surfaces with a Canadian quarter shown for reference.

Etched band patterns were created on 1 to 4 long surfaces of initially polished 3 × 2 × 100 mm^3 LYSO crystals. Each pattern was created by roughing the surface of the crystal using a 0.3 mm wide crystal saw blade (South Bay Technology, San Clemente, California), shown in figure 3.11, to etch bands every 5 mm over the central 80 mm of the crystal as shown in figure 3.12. The average width of the etching bands was measured to be 0.8 mm. The size difference between the etched band and the saw blade was caused by the fact that the etching was done manually. In this study the following etching patterns were investigated:

- Etched bands on 1 side.
- Etched bands on 2 opposite sides with the bands in the same axial location (Figure 3.12(a)).
- Etched bands on all 4 sides with the bands in the same axial location.
- Etched bands on 2 opposite sides with the band locations interleaved (Figure 3.12(b)).

In addition, for one $3 \times 2 \times 100$ mm^3 crystal a single long side was roughed completely using 80-grit sand paper to investigate how this compared to the banding pattern results. In order to investigate the effect of changing the crystal size, 1 and 2 sided banding patterns on $2 \times 2 \times 100$ mm^3 LYSO crystals, obtained from the same supplier and initially polished on all sides, were investigated after wrapping them in Teflon. A smooth $2 \times 2 \times 100$ mm^3 LYSO crystal glued to an ESR reflector was also investigated.

3.2.5 Processing and analysis of data from dual-ended readout design

The sum of two PMT signals (PMT1+PMT2) in the dual-ended readout design was calculated on an event-by-event basis at each irradiation position. This sum was histogrammed to obtain the energy spectrum at each irradiation position. A Gaussian fitting was applied to the photopeak in each energy spectrum to find the peak position and the FWHM of the photopeak (see Appendix B for Matlab script). The relative light collection efficiency at each irradiation position was evaluated by measuring the location of the 511 keV photopeak in the summed energy spectrum. The energy resolution was calculated as the full-width at half maximum (FWHM) of the 511 keV photopeak for each summed spectrum using the following relation:

$$\%\ Energy\ resolution = \frac{FWHM}{Peak\ \ position} \times 100 \tag{3.2}$$

For each event, the ratio of the two PMT signals was calculated to determine the axial location of the event.

$$Ratio = \frac{PMT2}{PMT1 + PMT2} \tag{3.3}$$

The ratio signal for all the events at each location was histogramed and each ratio distribution peak was then fitted with a Gaussian function to determine the peak centroid and the FWHM of each profile. A typical distribution of the ratio signals at nine different locations of the crystal is shown in figure 3.13.

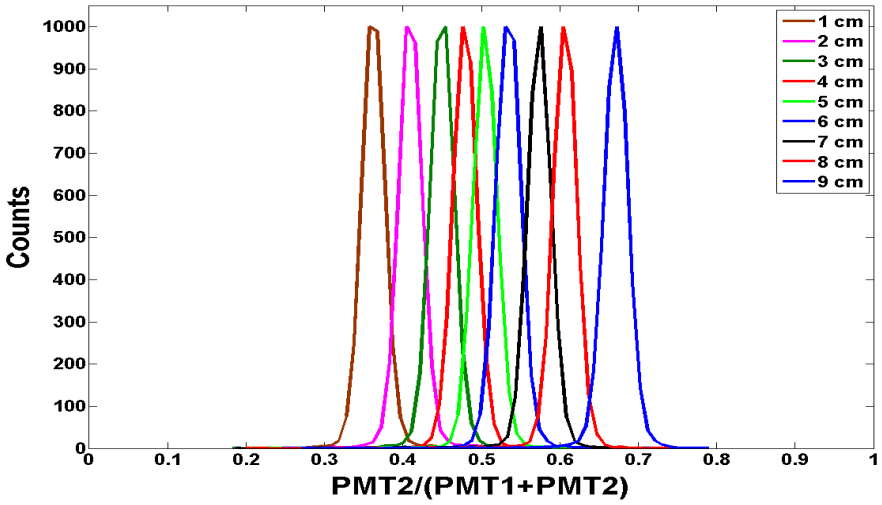

Figure 3.13 A typical distribution of ratio signals at nine different locations of a 100 mm long LYSO crystal wrapped in Teflon reflector

The peak centroid, which gives the mean ratio signal for each location is plotted versus irradiation position and the ratio response is fitted with a third order polynomial (see Appendix B for Matlab script). These ratio-position plots are also known as calibration curves used for axial encoding of events. The spatial resolution of the detector

in the light sharing direction is estimated as the FWHM of the ratio profile at each position divided by the slope of the plot of ratio signal vs. position at each irradiation position.

For the determination of spatial resolution along the light sharing direction, only photopeak events were selected using the energy spectrum at each irradiation position. The energy window for the photopeak events was selected manually in each energy spectrum and was about 20% of peak position on both sides of each photopeak. The light collection, energy resolution and spatial resolution were determined for each crystal under a particular study in the project. The data analysis for all the 9 irradiation positions of the crystals was automated using scripts written in Matlab (The MathWorks, Inc., Natick MA). These Matlab scripts are given in Appendix B.

As the collimated beam width was estimated to be 2.5 mm based on the 2 mm crystal width and 0.25 mm source size as described in section 3.2.2.5, the axial spatial resolution determined in this study could be de-convolved with the beam width to obtain the true spatial resolution using the following relation:

$$R_{meas}^2 = R_{true}^2 + R_{beam}^2 \tag{3.4}$$

where R_{meas} is the measured spatial resolution, R_{true} is true spatial resolution and R_{beam} is the width of the electronically collimated 511 keV photon beam.

3.3 DETECT2000 Monte Carlo simulation

3.3.1 Overview of DETECT2000 simulation

Monte Carlo simulations of the scintillation light transport in our detector crystals were performed using the simulation code DETECT2000 (123). Our focus in this work

was to determine the DETECT2000 simulation parameters required to give good agreement with our measured data in order to benchmark the simulation for this detector geometry and allow the future use of Monte Carlo simulation in refining our detector designs.

3.3.2 Modeling of DOI detector in DETECT2000

For the smooth surface i.e. without any etching bands, the POLISH model of DETECT2000 was used with a reflectivity of 0.95 to simulate Teflon as an external air-coupled diffuse reflector around a $3 \times 2 \times 100$ mm^3 LYSO crystal with a refractive index of 1.82 and decay time of 40 ns. The ends of the crystal were modeled as POLISH without any reflector. For the etching band patterns created on the crystal as described experimentally in section 3.2.4.1, the UNIFIED model with a diffusive lobe constant (DL) of 1, representing the probability of internal Lambertian reflection, and a reflectivity of 0.95 was used to simulate Teflon as an external diffuse reflector. The UNIFIED model allows simulating non-uniform roughness of a surface, such as etching ground bands in this study, through a Gaussian distribution of angle between the mean surface normal and a micro facet normal. For the smooth components of the etched crystal, the same POLISH model used for the case of a smooth crystal with a reflectivity of 0.95 was applied. The details of these DETECT2000 optical models can be found in the reference manual (Moisan *et al* 2000). The different detector parameters and DETECT2000 models used in the simulation study are summarized in Tables 3.1 and 3.2, respectively.

The two PSPMTs at the ends of the crystal were modeled by using the "DETECT" finish on the surface of a 0.8 mm thick borosilicate glass window at each end having a refractive index of 1.5. In DETECT2000, the "DETECT" finish models the photocathode

surface of a PMT. The active area of the photocathode was 23.5×23.5 mm^2 and the same area was modeled for the glass window before the PMT cathode surface. The ends of the crystals were coupled to the PSPMTs using 0.3 mm thick optical grease having a refractive index of 1.463. The long axis of the crystal was aligned with the center of the PMT at each end. The wavelength dependent quantum efficiency of the two PSPMTs, provided by the manufacturer, and the emission spectrum of LYSO (Zhang *et al* 2007) were modeled as given in figure 3.14.

Table 3.1 The physical parameters and their values used in DETECT2000 simulation.

Parameter	Value
LYSO refractive index	1.82
Light yield for 511 keV photon	10000
LYSO decay time	40 ns
Reflectivity of Teflon	0.95
Reflectivity of ESR	0.985
Optical grease refractive index	1.463
Optical grease thickness	0.3 mm
Borosilicate PMT window refractive index	1.5
Borosilicate PMT window thickness	0.8 mm
Borosilicate window area	23.5×23.5 mm^2
PSPMT area	23.5×23.5 mm^2

Table 3.2 The DETECT2000 models used in simulation for different crystal surfaces and etching band conditions

Crystal surface/band condition	DETECT2000 Model used
Smooth surface	POLISH
Smooth surface with ESR	METAL, reflectivity of 0.985 for glued-ESR
Rough band components	UNIFIED, DL 1, reflectivity 0.95 for Teflon
Smooth components	POLISH, reflectivity of 0.92 for air-coupled Teflon
PMT Cathode Surface	DETECT

The complete detector geometry was modeled by creating a total of 39 components for the etching band patterns and the smooth parts of the test crystal in the DETECT2000 input file (for DETECT2000 scripts see Appendix C). 10000 optical photons were simulated at the same depth of the crystal (i.e. central long axis of the crystal) for each

511 keV photon interaction at each location, corresponding to the approximate number of optical photons that we expect to be created for each 511 keV photon interaction in LYSO. In order to achieve a good peak centroid of the ratio of two PMT signals, 10,000 511 keV γ-photons were simulated at each interaction position, 1 through 9 cm in steps of 1 cm, in the crystal.

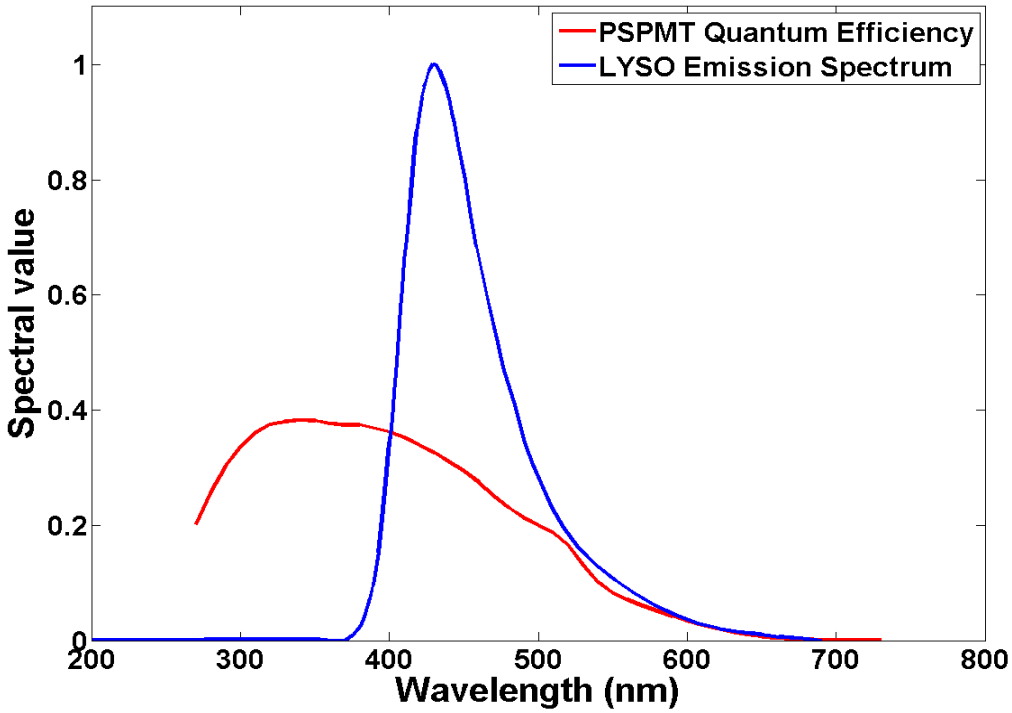

Figure 3.14 Emission spectrum of LYSO (Zhang *et al* 2007) and quantum efficiency of PSPMT used in simulation studies

A shell script was written in Linux (see Appendix D) for simulating the 10000 511 keV photons one-by-one at each interaction position and storing/appending each simulation output data (number of detected optical photons by each PMT at the two ends of the crystal). This shell script also serves to insert a new seed in the input file for random number generator in each γ photon-simulation (i.e. 10000 optical photons). In

addition to smooth surfaces, the following etching patterns as described experimentally in section 3.2.4.1 were simulated for a $3 \times 2 \times 100$ mm^3 crystal:

- Etched bands on 1 side.
- Etched bands on 2 opposite sides with the bands in the same axial location.
- Etched bands on all 4 sides with the bands in the same axial location.

The simulations were repeated for a $2 \times 2 \times 100$ mm^3 LYSO crystal with smooth surfaces and etching band patterns on 1 and 2 opposite sides and wrapped in Teflon reflector. For this crystal, smooth surfaces wrapped in a glued-ESR reflector were also simulated. A glue-coupled ESR reflector on smooth crystal surfaces was modeled as "METAL" with a reflectivity of 0.985 that gives a specular reflector in DETECT2000. The simulation for each crystal with banding patterns or smooth surfaces took approximately 24 hours for all 9 interaction positions on a 64 bit computer with a 3.00 GHz Quad processor (Intel(R) Core (TM)2 Quad CPU Q9650 @ 3.00 GHz) using 4 cores.

3.3.3 Methods for validating results

Various values of reflection coefficient (ranging from 0.5 to 1.0) for a diffuse reflector with the POLISH and PAINT surface models were tested in simulation. A PAINT model with a reflection coefficient simulates a painted or diffuse reflector around a smooth crystal. Light absorption attenuation length λ_a was set to 150 mm and the scattering attenuation length was ignored. Much higher light loss was observed in the case of PAINT compared to POLISH for a 10 cm long crystal. For example, almost no light was detected by the distant PMT at either end even for an irradiation location of 4 or 6 cm of the crystal as shown in figure 3.15; therefore, the POLISH model with a fixed

reflection coefficient of 0.95 was used in the subsequent simulations. Constant optical photon wavelength values, ranging from 300 to 600 nm, were tested before using the LYSO emission spectrum.

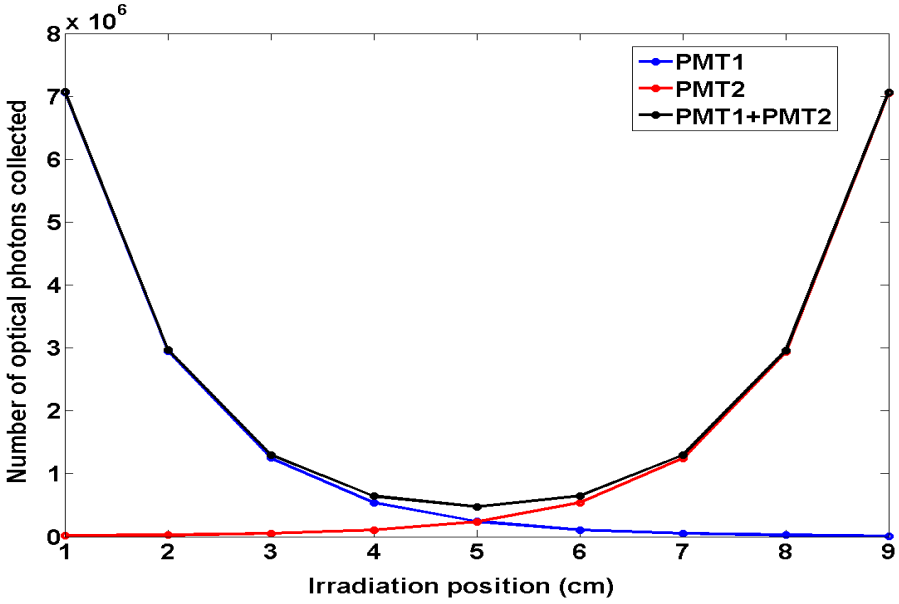

Figure 3.15 Light collected by individual PMTs coupled to a 100 mm long LYSO crystal with smooth surfaces simulated as PAINT with a reflectivity of 1.0. Note almost no light is collected by a distant PMT at 4 or 6 cm location

After fixing the POLISH model with a reflection coefficient of 0.95 and using the LYSO emission spectrum, different light attenuation lengths were tested through simulation 'trial and error' and compared with the experimental results of the smooth crystal. It was found that the light attenuation is the major factor that influences the comparison results. Therefore, different combinations of light absorption attenuation length, λ_a, and scattering attenuation length, λ_s, ranging from 75 – 1000 mm were tested through simulation. The value that best matched our experimental results was determined to be 150 mm for λ_a. This value was then used for all subsequent simulations. The scattering attenuation length, λ_s, was taken to be an infinite value and hence the

attenuation due to scattering was ignored in these simulations. This gives a total bulk attenuation λ_{eff} that is entirely due to the absorption attenuation of light in the clear LYSO crystal according to the following relation:

$$\frac{1}{\lambda_{eff}} = \frac{1}{\lambda_a} + \frac{1}{\lambda_s} \tag{3.5}$$

3.3.4 Effect of band size on spatial resolution, light output and energy resolution

In order to study the effect of etching band size on energy and spatial resolution of the crystal detector, band sizes of 0.6, 0.8, 1, 2 and 3 mm with a fixed band spacing of 1 cm were simulated for the etching band pattern created on one, two and four long surfaces of $3 \times 2 \times 100$ mm^3 LYSO crystals. The simulations in this case were carried out using the procedure described in section 3.3.2.

3.3.5 Simulation output data analysis

As in the case of measurements described in section 3.2.5, the sum of two PMT signals in each simulation, that is the total number of optical photons collected by the two PMTs (PMT1+PMT2), and the ratio, PMT2/(PMT1+PMT2), were calculated on an event-by-event basis. Energy spectra were obtained from the sum signal at each irradiation position, allowing calculation of the photopeak position and the FWHM energy resolution of the photopeak through Gaussian fitting of the peak in each energy spectrum. In contrast to the measurement case, only photopeak events were seen in each energy spectrum due to the identical number of optical photons for each event as no γ-interaction was involved. The ratio of the two PMT signals at each irradiation position was histogramed and the peak centroid and FWHM for each distribution were calculated using Gaussian fitting to each distribution peak. The peak centroid or the mean ratio

signal was plotted vs. irradiation position for each case and fitted with a piecewise or spline interpolation fitting. Spatial resolution in the light sharing direction was obtained by dividing the FWHM of each distribution peak by the slope of the tangent to the fitting curve at each irradiation position. The data analysis was automated by writing scripts in Matlab.

3.4 Summary and introduction of next 3 chapters

In this chapter, we illustrated the establishment of our experimental setup used in the research project and elaborated different methods used for experimental and simulation studies in the project work. The results of our observation studies on dual-ended readout of 100 mm long crystals, such as light collection, spatial and energy resolution and the effect of different reflector materials on light optimization work are discussed in Chapter 4. The calibration of our dual-ended readout of axially-oriented crystals (to be used in a compact PET system) for axial encoding of events using different methods are described in Chapter 5. The detailed experimental and simulation results of surface treatment of 100 mm long crystals using systematic etching band patterns for improving spatial resolution along the light sharing direction of our dual-ended readout design are given in Chapter 6.

Chapter 4 Observations on Dual-Ended Readout of 100 mm Long LYSO Crystals

This chapter is a reformatted paper published in a peer-reviewed journal. The complete citation information of the paper is as follows.

Fazal ur-Rehman, BryanMcIntosh and Andrew L. Goertzen 2011 Observations on dual-ended readout of 100 mm long LYSO crystals Nuclear Instruments and Methods in Physics Research A, 652, 275-9.

4.1 Abstract

We are investigating using dual-ended readout of axially oriented long thin scintillator crystals in detectors for a compact geometry, small ring diameter animal PET system. The axial position of interaction is determined from the light sharing between the two photodetectors at opposite ends of the crystal. We examine the light output, energy resolution and axial spatial resolution of 1.5-5.0 × 2 × 100 mm^3 polished LYSO crystals by irradiating with an electronically collimated beam of 511 keV photons oriented perpendicular to the long axis and readout at either end by position sensitive photomultiplier tubes (PSPMTs). Three reflector materials, namely Teflon, 3M enhanced specular reflector (ESR) and black paint are examined for the 2 × 2 × 100 mm^3 crystal size. The light output increases and energy resolution improves with the crystal cross-section. Generally, the spatial resolution worsens with increasing crystal cross section. For the 2 × 2 × 100 mm^3 crystal size, the mean energy resolution of the photopeak over the nine irradiation positions was 14.4 ± 0.4%, 16.0 ± 1.2% and 28.3 ± 2.1% with mean spatial resolution of 7.0 ± 1.0, 9.4 ± 3.3 and 26.0 ± 5.0 mm using ESR, Teflon and black paint, respectively. ESR reflector gave the best light output, energy and axial spatial resolutions. These characterization results of PSPMT-based dual-ended long LYSO

crystals will be useful in the design of detector modules for a highly compact geometry preclinical PET system using this detector technology.

4.2 Introduction

Dual-ended readout of scintillator crystals has been extensively explored as a way to add depth of interaction (DOI) information to PET imaging systems [1-3]. Detectors of this design require using thin silicon type detectors [4] on at least one end as the 511 keV photons must pass through the detector before entering the scintillator crystal. The ability to obtain DOI information is particularly important for PET systems with small ring diameters as the resolution degrading effects of DOI increase as the ring diameter decreases [5]. We are investigating approaches for developing a small ring diameter compact animal PET system with the goal of developing a low-cost, high sensitivity camera. We propose to make use of arrays of long thin scintillator crystals oriented in the axial direction and read out at either end by low cost position sensitive photomultiplier tubes (PSPMTs) rather than more expensive silicon based detectors. The axial position of interaction is determined from the light sharing between the two PMTs at opposite ends of the crystal. This detector geometry has been explored before for human brain imaging using long 3.2×3.2×100-150 mm^3 LYSO scintillation crystals readout at either end initially by hybrid photon detectors [6] and later by wavelength shifting fibers along with Geiger avalanche photodiodes [7] but has not been extensively investigated for applications of small animal imaging using smaller crystal sizes. In this work, we present data showing the light output, energy resolution and axial spatial resolution of long, thin LYSO crystals wrapped either in Teflon, 3M enhanced specular reflector (ESR), or sprayed-on black paint and readout at either end by PSPMTs.

4.3 Materials and Methods

4.3.1 Experimental Setup

100 mm long lutetium yttrium oxyorthosilicate (LYSO) scintillator crystals with cross sections of 1.5 × 2, 2 × 2, 3 × 2, 4 × 2, and 5 × 2 mm^2 and polished on all sides were obtained from a commercial supplier (Proteus Inc., Chagrin Falls, OH). The four long sides of the crystals were covered with reflector material and the ends of the crystals were coupled to a pair of Hamamatsu R8900U-00-C12 (Hamamatsu Photonics K. K., Japan) PSPMTs using Visilox V-788 optical grease. The PSPMT outputs were multiplexed to four signals, X+, X-, Y+ and Y- using Siemens Inveon pre-amplifier stacks (Siemens Preclinical Solutions, Knoxville, TN) and then subsequently processed using standard NIM electronics. Shaped signals for each detector were digitized using a National Instruments PCI-6133 PC based data acquisition card (National Instruments Corporation, Austin, TX) running under a National Instruments LabWindows/CVI based interface. The detector response in the light sharing direction is assessed by irradiating the crystal using an electronically collimated 511 keV beam as shown in figure 4.1(a). This experimental arrangement is similar to that reported previously by other groups [8-10]. Figure 4.1(b) shows a schematic diagram of this arrangement, in which a single 2 × 2 × 15 mm^3 LYSO crystal coupled to a single channel PMT (Hamamatsu H3178-51) in alignment with a ^{22}Na point source (model MMS09, Eckert & Ziegler Isotope Products, Valencia, CA) is used in coincidence with the test LYSO crystal to create the electronically collimated 511 keV photon beam. The ^{22}Na source, small LYSO crystal, and single channel PMT are mounted on a 2-axis translation stage in order to allow reproducible positioning of the 511 keV beam.

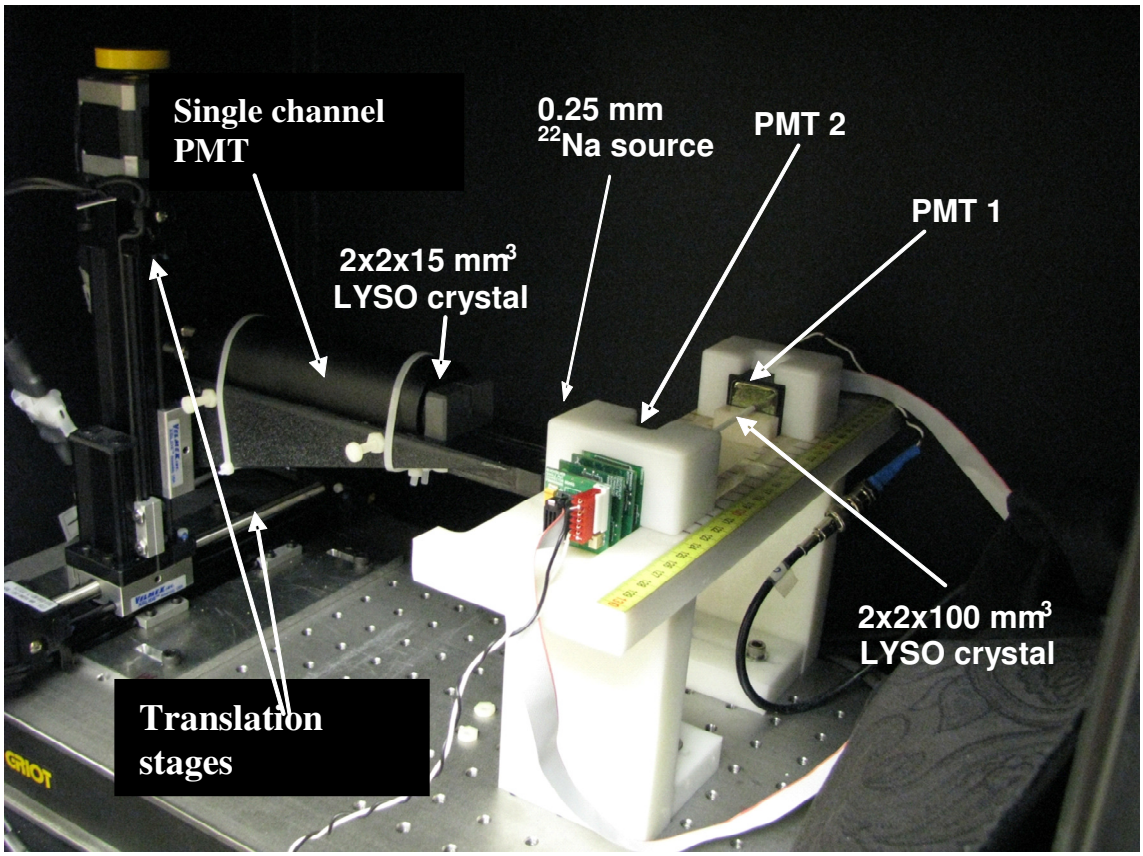

(a)

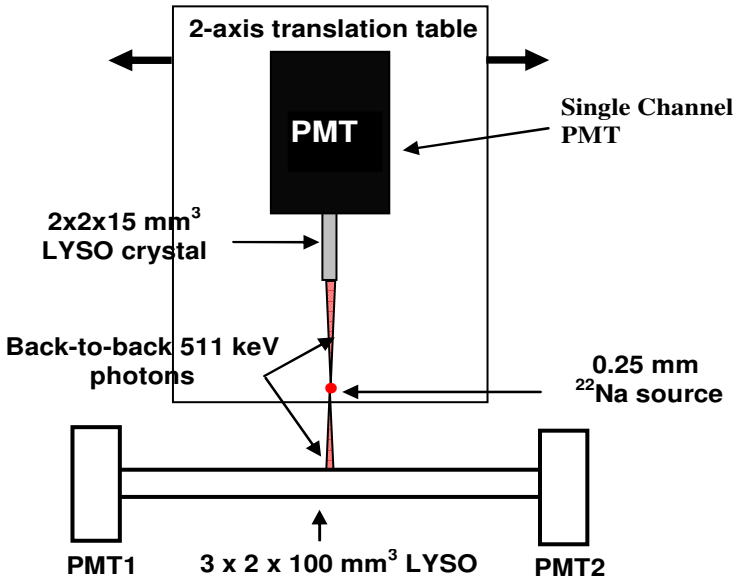

(b)

Figure 4.1 Experimental arrangement for electronically collimating 511 keV photon beam with translation stages in a light tight box. (b) Schematic diagram showing electronic collimation of 511 keV beam.

4.3.2 Light Collection, Energy Resolution and Axial Spatial Resolution

The response of the 10 cm long crystals versus irradiation position was determined by irradiating the crystal at nine discrete locations separated by 1 cm each. At each irradiation position, 10,000 events were collected and for each event, the total signal from the two PSPMTs were digitized and referred to as signals PMT1 and PMT2. A summed energy spectrum was obtained for each beam position by summing the two PMT signals (PMT1+PMT2). The relative light collection efficiency was evaluated by measuring the location of the 511 keV photopeak in the summed signals, with the energy resolution being calculated as the full-width at half maximum (FWHM) of the 511 keV photopeak using this summed spectrum. For each event, the ratio PMT1/(PMT1+PMT2) was calculated to determine the axial location of an event. The mean ratio for each location is plotted versus irradiation position and the ratio response is fitted with a third degree polynomial. The spatial resolution of the detector in the light sharing direction is estimated as the FWHM of the ratio profile at each position divided by the slope of the third degree polynomial fitted curve at each irradiation position. Measurements for light collection, energy resolution, and axial spatial resolution were performed for all crystal sizes with the crystals wrapped in Teflon tape.

4.3.3 Reflector studies

Relative light collection efficiency, energy resolution, and axial spatial resolution were measured for $2 \times 2 \times 100$ mm^3 LYSO crystals using three different reflector materials, namely Teflon, 3M Vikuiti enhanced specular reflector (ESR) and Krylon black spray-on paint. The Teflon was applied by wrapping the crystal with Teflon tape similar to the procedure for section 4.3.2. The ESR was applied by scoring an 8×100

mm^2 piece so that it would fold around the crystal and then securing it in place by wrapping the exterior with Teflon tape. Black paint was sprayed on the crystal with several coatings. Each crystal was coupled to the PMTs at the ends using optical grease as described above and measurements performed as described in section 4.3.2.

4.4 Results & Discussion

4.4.1 Light Collection, Energy Resolution and Axial Spatial Resolution versus Crystal Size

Figure 4.2 shows the relative light output from the five 100 mm long LYSO crystals with different cross-sections of 1.5 × 2 through 5 × 2 mm^2 plotted as a function of irradiation position.

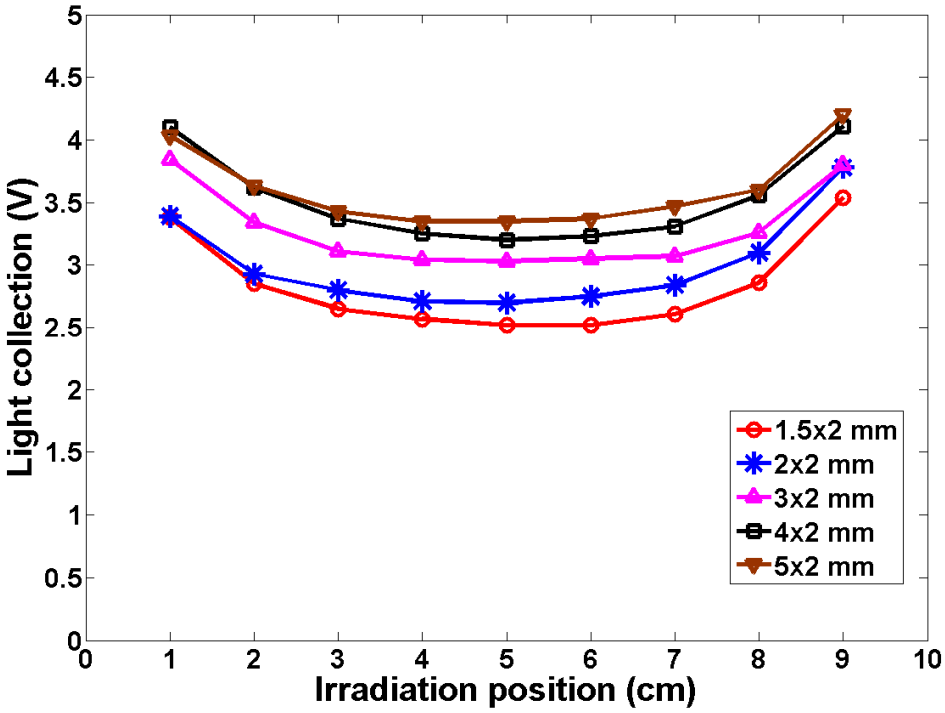

Figure 4.2 Light output as a function of irradiation position for 1.5-5×2×100 mm^3 LYSO crystals wrapped in Teflon.

The light output increases with the crystal cross-section. The energy resolution for each crystal size was found from the FWHM of the photopeak of each sum energy spectrum by fitting a Gaussian curve to the peak. As expected, the energy resolution improves as the cross-section increases due to the increase in light collection as shown in Table 4.1 for all the crystals wrapped in Teflon reflector. The energy resolution ranged from 13.7 - 16 % for all the crystals examined.

Table 4.1 Mean energy resolution, spatial resolution (range) and standard deviation for all the crystals wrapped in Teflon

Crystal cross-section (mm^2)	Energy resolution (%)	Spatial resolution (mm)
1.5×2	14.5 (13.4-15.6) ± 0.8	8.6(4.4-12.7) ± 3.0
2×2	16.0 (14.3-18.0) ± 1.2	9.4(5.0-14.0) ± 3.3
3×2	14.9 (14.0-16.1) ± 0.7	10.1(5.9-14.6) ± 3.2
4×2	14.5 (14.0-16.1) ± 0.7	9.7(5.5-13.9) ± 3.3
5×2	13.7 (12.9-14.8) ± 0.6	10.5(5.2-16.5) ± 4.2

At each irradiation position the ratio of the two PMT signals was histogrammed to determine the shape and width of the ratio. Typical ratio profiles for the nine irradiation positions of a 2×2×100 mm^3 Teflon-wrapped crystal are shown in figure 4.3 (a). Gaussian fitting was used for each profile to find the peak centroid, which gives the mean ratio for that irradiation position, and the FWHM of the profile. The mean ratio signal (i.e. centroid value) was plotted as a function of irradiation position for all the crystals examined. An example plot of this type of plot can be seen in figure 4.3 (b) for the measured profiles of the Teflon wrapped $2 \times 2 \times 100$ mm^3 crystal shown in figure 4.3(a). For the Teflon wrapped crystals, a 3^{rd} degree polynomial is required to fit to the data due to the non-linear relationship between ratio signal and irradiation position. The ratio signal for a Teflon-wrapped crystal is not linearly dependent with irradiation position as has been observed by others for the case of a smaller crystal (i.e. 20 mm long) [1] where

a linear relationship is assumed. Calculating the spatial resolution in the light sharing direction for the 100 mm long Teflon wrapped crystals was thus done by dividing the FWHM of each ratio profile with the slope of the tangent to the third degree polynomial fitted curve at each beam position instead of using a straight line fit to the data. Figure 4.4 shows the spatial resolution in the light sharing direction for the Teflon wrapped crystals as a function of irradiation position. The best spatial resolution measured was 8.6 ± 3.0 mm for the 1.5 × 2 mm^2 crystal and the worst was 10.5 ± 4.2 mm for the 5 × 2 mm^2 crystal as shown in Table 4.1. These values of spatial resolutions are comparable to the spatial resolution of 9.3 ± 0.3 mm for a 3.2 × 3.2 × 100 mm^3 LYSO Teflon-wrapped crystal given in literature [11]. As expected, the spatial resolution is symmetric about the central (5 cm) irradiation position and is in general a parabolic function of position. Generally, the spatial resolution improves with decreasing crystal cross-section due to the more light losses along the length of the crystal.

4.4.2 Reflector studies

The ESR covered crystal gave approximately 22% higher relative light output compared to the Teflon wrapped crystal as shown in figure 4.5 for a 2 × 2 × 100 mm^3 crystal. The left panel of figure 4.3 (a, c, e) shows the profiles of the ratio of PMT signals for each beam location for a 2 × 2 × 100 mm^3 LYSO crystal when (a) Teflon, (c) ESR and (e) black paint were used as reflector materials. In the case of Teflon, as shown in figure 4.3(a), the peaks at the end irradiation positions are well resolved whereas the peaks at the middle are poorly resolved, reflecting the reduced spatial resolution in this region. The results from the ESR wrapped crystal showed a more uniform spatial response, allowing us to resolve the peaks in the central region of the crystal as shown in

figure 4.3(c). For the crystal covered in black paint, all the peaks are very poorly resolved, as shown in the profiles in figure 4.3(e), resulting in a generally poor spatial resolution.

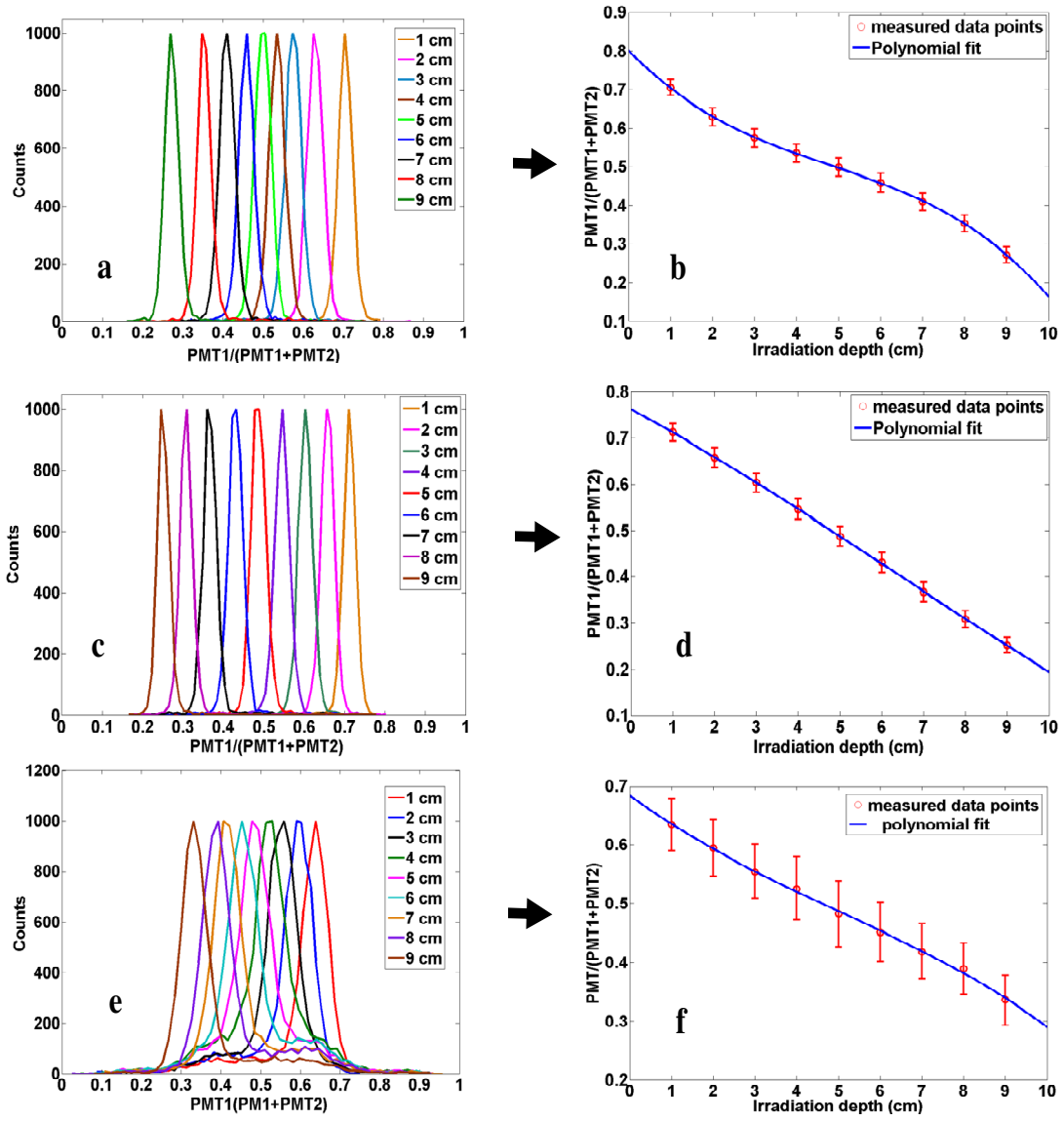

Figure 4.3 Left panel: Profiles of the ratio of PMT signals for the nine irradiation positions for Teflon reflector (a), ESR reflector (c) and black paint (e). Right panel: Corresponding mean ratio of PMT signals as a function of irradiation position for a 2×2×100 mm^3 LYSO crystal with error bars representing FWHM of profiles of the plots in the left panel. The nine irradiation positions were each separated by 1 cm.

For this case the errors in the ratio versus position plot shown in figure 4.3(f) are large due to the large FWHM of the profiles. The peak ratio signal and FWHM of the profiles were calculated by fitting Gaussian curves to each profile as described above for the Teflon wrapped crystals of various sizes. The right panel of figure 4.3 (b, d, f) shows the plot of mean ratio signal versus irradiation position and the third degree polynomial fitting to the data for the three reflectors. Figure 4.6 compares the spatial resolution in the light sharing direction as a function of irradiation position for a 2 × 2 × 100 mm^3 LYSO crystal when ESR, Teflon and black paint were used as reflector materials. The black paint shows the worst resolution of 26.0 ± 5.0 mm due to more light absorption in it whereas the ESR shows the best resolution of 7.0 ± 1.0 mm in this study which can also be seen in the ratio profiles of figure 4.3. Table 4.2 presents the mean spatial and energy resolution for a 2 × 2 × 100 mm^3 crystal over the nine irradiation positions when ESR, Teflon and black paint were used as reflectors. The best energy resolution of 14.4 ± 0.4% and the best axial spatial resolution of 7.0 ± 1.0 mm are achieved using the ESR reflector.

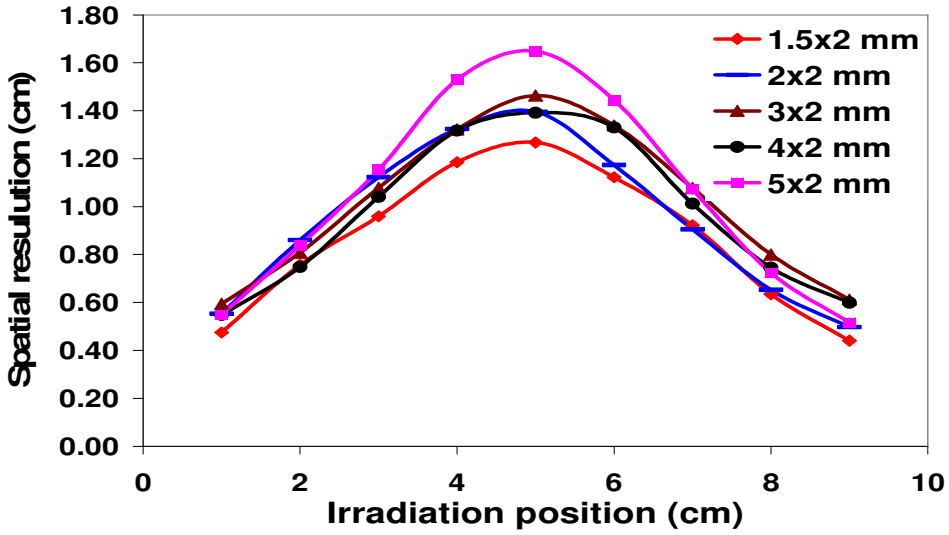

Figure 4.4 Spatial resolution as a function of irradiation position of 1.5-5×2×100 mm^3 LYSO crystals wrapped in Teflon.

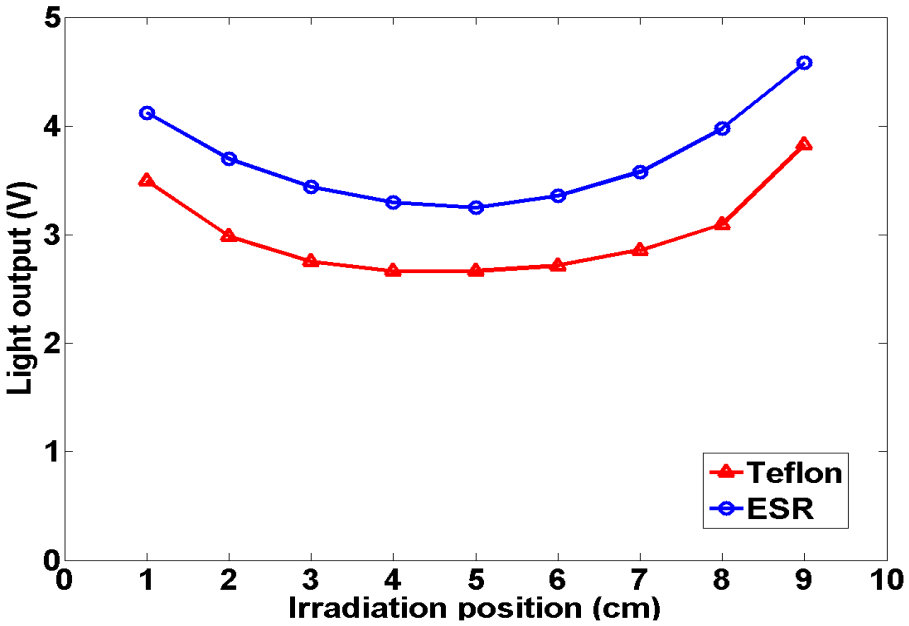

Figure 4.5 Comparison of light output from a 2×2×100 mm^3 LYSO crystal for ESR and Teflon. Note the improved light collection for the ESR wrapped crystal.

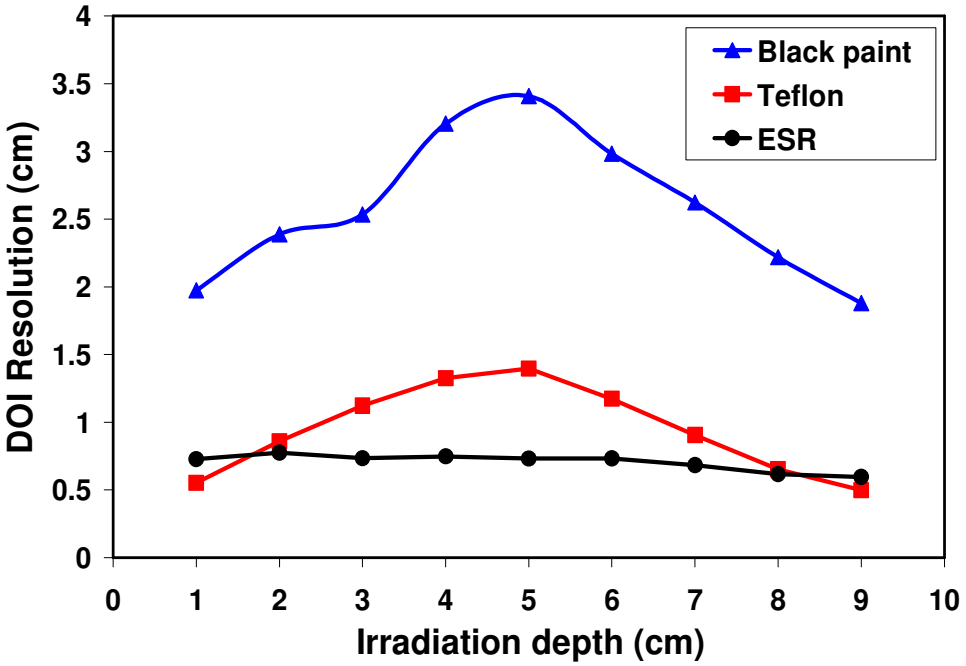

Figure 4.6 Comparison of spatial resolution of a 2×2×100 mm^3 LYSO crystal for ESR, Teflon and black paint. Note the nearly uniform resolution of the ESR wrapped crystal.

Table 4.2 Spatial resolution and energy resolution of a 2×2×100 mm^3 LYSO crystal for different reflectors

Reflector	Energy resolution (%)	Spatial resolution (mm)
3M ESR	14.4 ± 0.4	7.0 ± 1.0
Teflon	16.0 ± 1.2	9.4 ± 3.3
Black Paint	28.3 ± 2.1	26.0 ±5.0

4.5 Conclusion

We examined the light output, energy resolution, and axial spatial resolution of 1.5-5 × 2 × 100 mm^3 LYSO scintillator crystals readout at either end by PSPMTs. The light collection efficiency and energy resolution were observed to improve with increasing crystal cross-section. Generally, the spatial resolution worsens with increasing crystal cross section due to less loss of light along the axis of the crystals. For a 2 × 2 × 100 mm^3 crystal, the mean energy resolution and standard deviation of the photopeak over the nine irradiation positions was 14.4 ± 0.4%, 16.0 ± 1.2% and 28.3 ±2.1% while the mean spatial resolution and standard deviation over the nine irradiation positions was 7.0 ± 1.0 mm, 9.4 ± 3.3 mm, and 26.0 ± 5.0 mm using ESR, Teflon and black paint, respectively, as reflector materials. The best light collection, energy resolution and axial spatial resolution were obtained using the ESR reflector in this study. These characterization results of PSPMT-based dual-ended readout of long LYSO crystals will be useful in the design of detector modules for a compact geometry, small ring diameter preclinical PET scanner system using this detector technology.

References

[1] Yang et al., Depth of interaction calibration for PET detectors with dual-ended readout by PSAPDs, Phys. Med. and Biol. 54 (2009) 433.

[2] Burr et al., Evaluation of a prototype small animal PET detector with depth-of-interaction encoding, IEEE Trans. Nucl. Sci. 51(2004)1791.

[3] Moses et al., Design studies for a PET detector module using a PIN photodiode to measure depth of interaction, IEEE Trans. Nucl. Sci. 41(1994)1441.
[4] Shao et al., R. Yao, T. Ma, Design studies of a high resolution PET detector using APD arrays, IEEE Trans. Nucl. Sci., 47(2000) 1051.
[5] S. R. Cherry, J. A. Sorenson, M. E. Phelps, Physics in Nuclear Medicine, third ed., Saunders, Philadelphia, 2003.
[6] A. Braem et al., Feasibility of a novel design of high resolution parallax-free Compton enhanced PET scanner dedicated to brain research, Phys. Med. and Biol. 49 (2004) 2547.
[7] Braem et al., AX PET: A novel PET detector concept with full 3D reconstruction, Nucl. Instr. And Meth. A 610(2009)192.
[8] Yang et al., Depth of interaction resolution measurements for a high resolution PET detector using position sensitive avalanche photodiodes, Phys. Med. Biol. 51 (2006) 2131.
[9] Dokhale et al., Performance measurements of a depth-encoding PET detector module based on position-sensitive APD readout, Phys. Med. Biol., 49 (2004) 4293.
[10] Shao et al., Dual APD Array Readout of LSO Crystals: Optimization of Crystal Surface Treatment, IEEE Trans. Nucl. Sci., 49(2002) 649.
[11] Braem et al., Scintillator studies for the HPD-PET concept, Nucl. Instr. And Meth. A 571 (2007) 419.

Chapter 5 Calibration of dual-ended readout of axially oriented 100 mm long LYSO crystals for use in a compact PET system

This chapter is a reformatted paper published in a peer-reviewed journal. The complete citation information of the paper is as follows.

Fazal ur-Rehman and Andrew L. Goertzen 2012 Calibration of Dual-Ended Readout of Axially Oriented 100-mm long LYSO Crystals for Use in a Compact PET System IEEE Transactions on Nuclear Science 59, 561-7.

5.1 Abstract

We are investigating the use of 100 mm long axially oriented scintillator crystals read out at either end by position sensitive photomultiplier tubes (PSPMTs) for application to a small animal PET system. A system design of this type requires a robust and efficient calibration of the detector response in the light sharing direction in order to accurately decode the location of photon interaction. In this work we evaluate methods for determining the axial positioning calibration of dual-ended readout of 2 × 2 × 100 mm^3 LYSO crystals wrapped in either Teflon or 3M Enhanced Specular Reflector (ESR). We compare a collimated irradiation method with a uniform irradiation method recently proposed by Shao. In the collimated irradiation method, an electronically collimated beam of 511 keV photons aimed perpendicular to the long axis of the crystal is used to irradiate the crystal at nine locations in steps of 1 cm. The ratio of the two PMT signals at each irradiation position is used to give the axial-positioning calibration relating ratio signal to position. In the method by Shao, the crystal was irradiated using either a uniform ^{68}Ge line source, a ^{22}Na point source, or the intrinsic background activity in the LYSO. To check the validity of both calibration methods for unbalanced detectors, three

voltage variations ranging from 750-800 V were used for the two PMTs. For cases with balanced detector gains, the calibration curves obtained using uniform irradiation and Shao's method agreed very well with the reference curve obtained from the collimated irradiation measurements. For the case with detectors that had unbalanced gain, agreement between uniform irradiation and collimated irradiation methods was only achieved if the trigger threshold energies of the two PMTs were adjusted to give similar singles events rates in both PMTs. These findings suggest that Shao's calibration method using uniform irradiation will provide a simple, accurate and rapid method for calibration of 100 mm long dual-ended readout detectors.

5.2 Introduction

We are investigating approaches for developing a small ring diameter compact preclinical positron emission tomography (PET) imaging system with the goal of developing a low-cost, high sensitivity camera. We propose to make use of arrays of long thin scintillator crystals oriented in the axial direction and read out at either end by low cost position sensitive photomultiplier tubes (PSPMTs). A schematic of the system concept is shown in figure 5.1 together with a photo of a mockup of the proposed system. The axial position of interaction of detected 511 keV photons in the crystals will be determined from the light sharing between the two PSPMTs in the dual-ended readout detector. This detector geometry has been previously explored by others for human brain imaging using long $3.2 \times 3.2 \times 100\text{-}150$ mm^3 LYSO scintillation crystals readout at either end initially by hybrid photon detectors [1,2] and later by wave length shifting fibers along with Geiger avalanche photodiodes [3] but has not been extensively investigated for applications of small animal imaging using smaller crystal sizes. Salvador et al. [4]

investigated the design of a small animal PET imaging system using shorter axially oriented 1.5 × 1.5 × 25 mm^3 LYSO crystals with a depth of interaction (DOI) capability, demonstrating an independence of spatial resolution from the detection efficiency. In this work, a spatial resolution of about 1 mm was demonstrated.

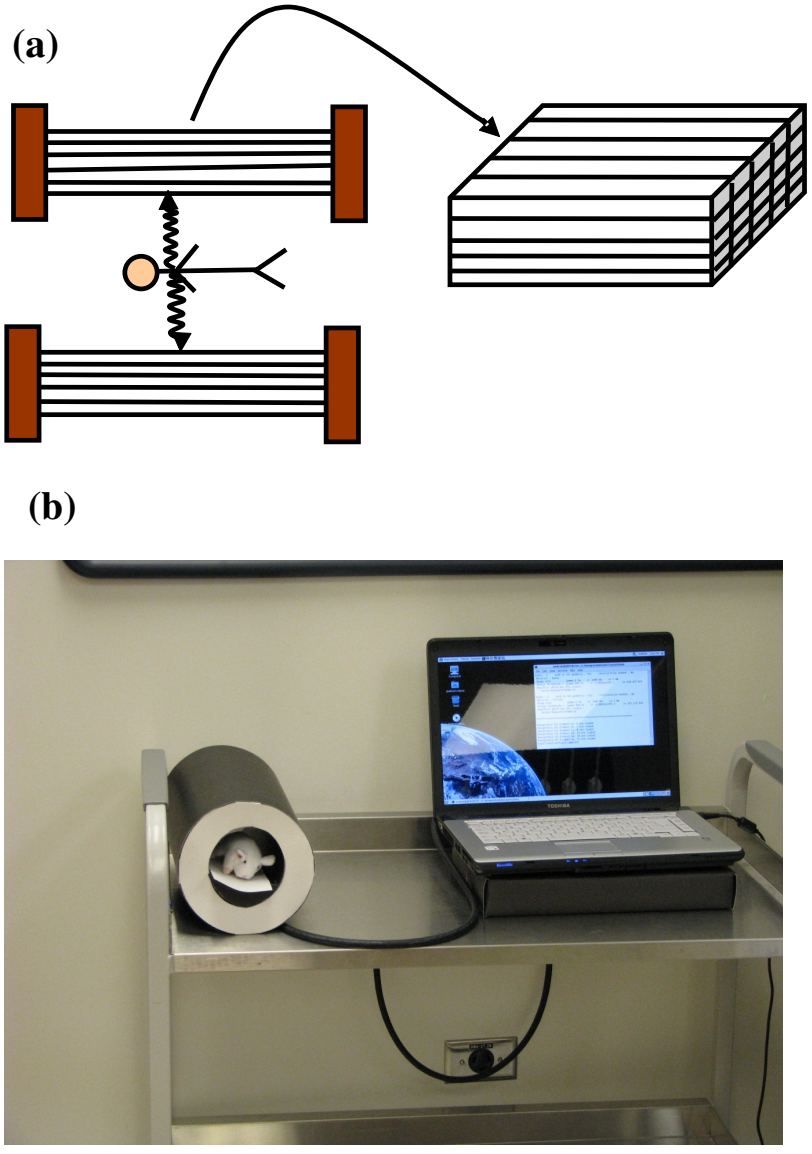

Figure 5.1 (a) Schematic of axially oriented crystal bundles (b) Photograph of a mockup of our design concept for a highly compact and portable PET imaging system.

Dual-ended readout of scintillation crystals has also been extensively explored for adding DOI capability to conventional PET imaging system designs with shorter crystals oriented in the radial direction [5-10]. We have previously reported some of our observations on dual-ended readout of 100 mm long LYSO crystals to be used in our proposed compact PET imaging system including light output, energy resolution, spatial resolution and the effect of reflectors on these parameters [11].

Accurate and robust calibration of dual-ended readout detectors is an essential condition for implementing the use of this detector design into a complete PET imaging system. A factor that can complicate the calibration of dual-ended readout detectors is the use of unmatched or unbalanced detectors. This scenario can arise in the initial construction of a dual-ended readout detector through the use of unmatched detectors due to unavailability or prohibitive cost of a matched pair or due to a detector design that purposefully uses unmatched detector types, such as a silicon detector on one end and a PMT on the other (e.g. [9]). Alternatively, the case of unmatched detectors can arise over time due to variations in the change in gains of individual detectors as a system ages.

In this work we examine two approaches for performing the axial-positioning calibration of $2 \times 2 \times 100$ mm^3 LYSO crystals wrapped in either Teflon or 3M ESR reflectors and read out at both ends by PSPMTs. In the first approach, a collimated 511 keV photon beam irradiates the crystal in discrete steps while in the second approach a rapid calibration is performed using a uniform flood irradiation and the method proposed by Shao [12]. The robustness of the uniform irradiation method is examined for a variety of source configurations including point source, line source and intrinsic radioactivity of

LYSO. In addition, we examine the utility of this method in the presence of purposefully unbalanced detectors.

5.3 Methods

5.3.1 Axial Positioning Calibration: Collimated irradiation method

The experimental setup used in the collimated irradiation method of calibration has been described previously [11] but for the sake of completeness will be described here briefly. $2 \times 2 \times 100$ mm^3 lutetium yttrium oxyorthosilicate (LYSO) crystals, mechanically polished on all sides, were obtained from a commercial supplier (Proteus Inc., Chagrin Falls, OH). All surfaces of the crystals were visually free of any defects or chipping from cutting. Crystals were wrapped in either Teflon tape or covered with 3M Vikuiti^{TM} ESR reflector (3M Optical System Division, St. Paul, MN). The Teflon was applied by wrapping the crystal with 4 layers of Teflon tape. The ESR was applied by scoring an 8×100 mm^2 piece so that it would fold around the crystal and then securing it in place by wrapping the exterior with Teflon tape.

The crystal was coupled at the small ends to a pair of Hamamatsu R8900U-00-C12 (Hamamatsu Photonics K.K., Japan) position sensitive photomultiplier tubes (PSPMTs) using Visilox V-788 optical grease. The PSPMT outputs were processed using preamplifier stacks from Siemens Inveon detectors (Siemens Preclinical Solution, Knoxville, TN) and the outputs of the preamplifier stack for each PSPMT were summed using a Phillips Scientific 740 linear fan-in (Phillips Scientific, Mahweh, NJ). This summation ignores the position sensitive capability of the PSPMTs, effectively treating them as if they were single channel PMTs.

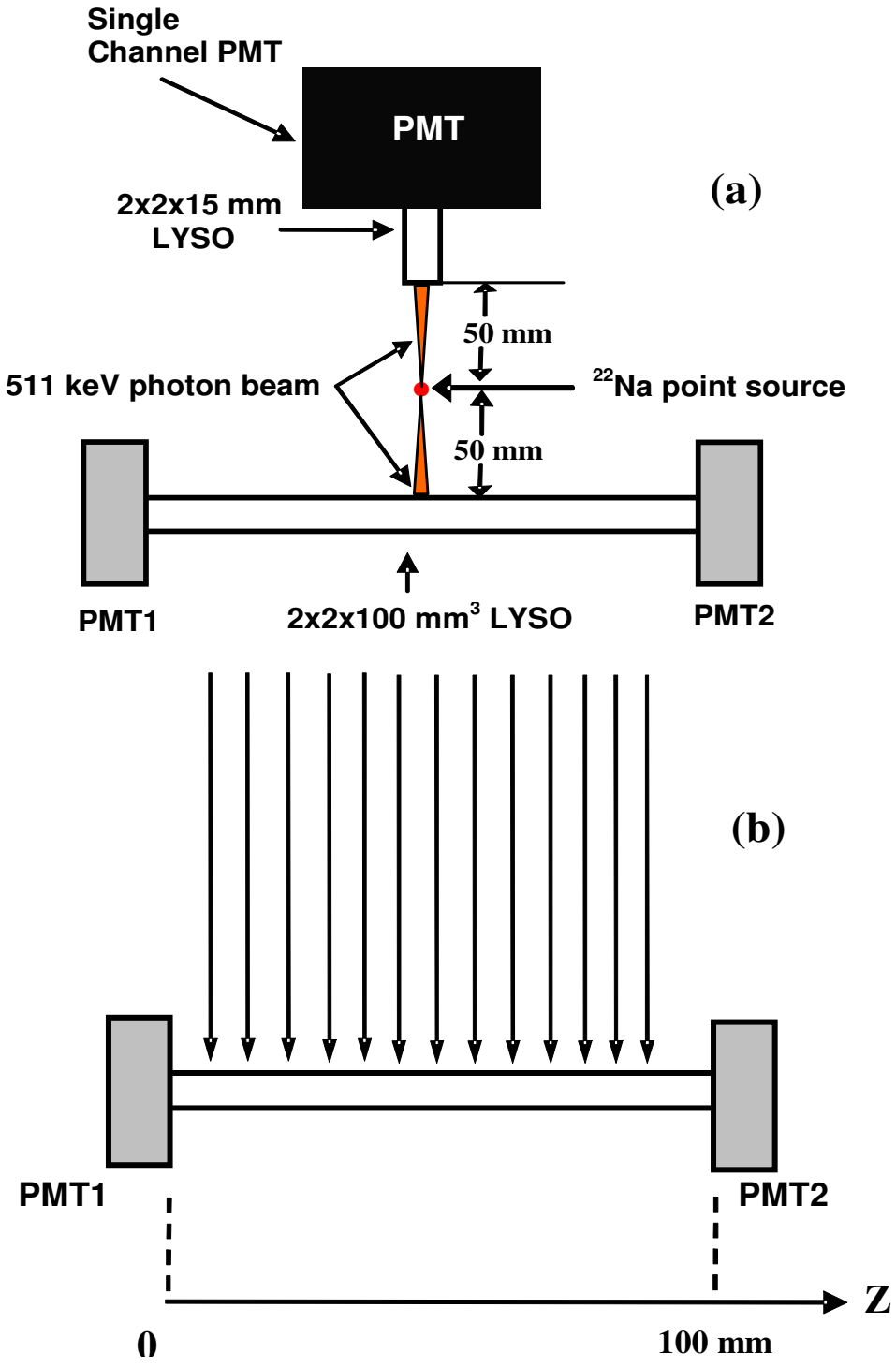

Figure 5.2 Schematic diagram (not to scale) showing (a) the experimental arrangement for electronically collimating the 511 keV photon beam and (b) the experimental arrangement for uniform irradiation required for axial-positioning calibration using the uniform irradiation method.

For the initial collimated irradiation measurements both PSPMTs were operated at 800 V. Each PSPMT was connected to its own constant fraction discriminator (CFD) (Phillips Scientific 715) and a logic unit (Phillips Scientific 754) was used to accept only events that generated a valid single event in both detectors. A CFD was used for this work instead of a leading edge discriminator due to the availability of this equipment in our lab. The shaped signals for each detector were digitized using a National Instruments PCI-6133 PC based data acquisition card (National Instruments Corporation, Austin, TX) running under a National Instruments LabWindows/CVI based interface.

A single $2 \times 2 \times 15$ mm^3 LYSO crystal coupled to a single channel PMT (Hamamatsu H3178-51) was used in coincidence with the 100 mm long test LYSO crystal for electronically collimating the 511 keV photon beam as shown schematically in figure 5.2(a). This approach is similar to the one used by other groups for DOI calibration [5-7]. The ^{22}Na source and single channel PMT were positioned on a two axis translation stage with the collimated 511 keV beam aimed perpendicular to the long axis of the crystal. The crystal was irradiated at nine different locations by moving the ^{22}Na source and single channel PMT in steps of 1 cm, with around 15,000 events collected at each step. For these measurements the CFD threshold levels were set just above the noise level in order to capture as much of the energy spectrum as possible. The acquisition of the data for the nine measurements required approximately 18 hours.

The ratio of the two PMT signals, PMT1/(PMT1+PMT2), was calculated on an event-by-event basis. This ratio was histogrammed for each position and the centroid of the distribution peak was calculated in order to determine the axial positioning calibration curve relating the ratio signal to irradiation position. The calibration curve obtained using

the collimated irradiation method was taken as the 'gold standard' for comparison with subsequent calibration methods since the location of irradiation was precisely known for this case.,

5.3.2 Axial Positioning Calibration: Uniform irradiation method (Shao Method)

The dual-ended readout detector was set up as described above for the collimated method but without the coincidence of the single channel PMT. The schematic of the experimental arrangement for uniform irradiation of the 100 mm long LYSO crystal in this case is shown in figure 5.2(b). The 100 mm long crystal was irradiated uniformly first with a 0.25 mCi ^{68}Ge line source with length of 19.2 cm, oriented parallel to the long axis of the crystal and placed at a distance of 25 cm from the long axis of the test crystal. The crystal was then irradiated with a 17.85 μCi ^{22}Na point source positioned 10 cm from the long axis of the crystal. These uniform irradiation datasets were used to determine the axial-positioning calibration using the method by Shao [12]. The distance of 10 cm was chosen for ^{22}Na source because this distance was equivalent to the length of the crystal and would allow the examination of the robustness of the calibration method for a case with modest non-uniformity of irradiation. In this method the position of interaction of γ-events is calculated from the probability density functions (PDF) (i.e. normalized histogram counts) of the ratio of the two PMT signals referred to as PMT1 and PMT2. Around 100,000 events were collected in this case. The ratio PMT1/(PMT1+PMT2) calculated for each γ-event was plotted vs. the calculated position of interaction assuming a uniform distribution to obtain the calibration curve and compared with that obtained from the collimated irradiation method described in section A. The analysis was performed using scripts written in Matlab (The MathWorks, Inc., Natick, MA) to

automate the data analysis. Acquisition of data for the flood irradiation method required around 10 minutes.

5.3.3 Calibration of Unbalanced Detectors with External Source

To check the validity of both calibration methods for unbalanced detectors, the voltage applied to the two PSPMTs was varied to 750 V - 800 V, 800 V - 800 V, and 800V - 750 V (PMT1 - PMT2). These cases are subsequently referred to as 750PMT1-800PMT2, 800PMT1-800PMT2 and 800PMT1-750PMT2. For each voltage setting data were acquired and analyzed using both the collimated irradiation method of section A and the flood irradiation method of section B. The same experimental procedures described in sections A and B were used to determine the axial positioning calibration curves for each voltage variation setting. Data were acquired for both Teflon-wrapped and ESR-glued 2 × 2 × 100 mm^3 LYSO crystals. For these measurements, the ESR reflector was applied by cutting four pieces of 2 x 100 mm^2 sizes and gluing them to the long surfaces of the crystal using Dymax OP-20 optical adhesive glue (DYMAX, Torrington, CT) and curing it with a Dymax Blue Wave 75 UV Spot Light Source.

When the PMT voltage is altered the gain changes, resulting in an expansion or compression of the energy spectrum and a subsequent change in the event rate for that PMT because there are either more events that surpass the threshold of the CFD for an increase in voltage or fewer events that trigger the CFD for a decrease in voltage. This leads to an imbalance in the singles event rate recorded by each of these two detectors in the dual-ended readout configuration and can lead to a non-uniform probability density function for the events, thus invalidating the assumption of uniformity of events in the method. To study the effect of differing singles event rates in the two detectors we

adjusted the CFD settings for the two PMTs to either balance or unbalance the number of single events triggered by the CFDs for the two detectors. Differences in the axial positioning calibration due to differences in the singles rate were examined for both the 800PMT1-800PMT2 case and the cases with different applied voltages. In addition, for the 800PMT1-800PMT2 case, the dependence of the calibration curve on the CFD threshold was examined by adjusting the two CFDs in unison to achieve matched singles rates over a range of count rates, equivalent to adjusting the lower level discriminator in full PET system. For each data set, the energy resolution was determined from the energy spectrum that is the sum of the two PMT signals and the spatial resolution calculated as described in sections 5.2.1 and 5.2.3.

5.3.4 Calibration of Unbalanced Detectors with LYSO Intrinsic Activity

The LYSO has a background intrinsic activity of 276Bq/cm^3 from ^{176}Lu. The intrinsic activity of the 2 × 2 × 100 mm^3 LYSO crystal (110.4 Bq) was therefore used to verify if the Shao calibration method is still valid without using an external source for balanced and unbalanced detectors and to find the possibility of calibrating our proposed complete PET scanner with intrinsic activity instead of using an external source. The ESR-glued crystal described in section C was used for three voltage variations, 750PMT1-800PMT2, 800PMT1-800PMT2, and 800PMT1-750PMT2. Around 5000000 events were collected for each voltage variation applied. The same experimental procedure for the determination of axial positioning calibration curve in each case was used as described in section 5.2.3 for the uniform irradiation method.

5.4 Results

5.4.1 Calibration of Balanced Detectors and Comparison

The photopeak position for the individual PMT energy spectra at both ends of a Teflon wrapped 2 × 2 × 100 mm^3 LYSO crystal and their sum energy spectrum (PMT1+PMT2) obtained from the collimated irradiation method are plotted as a function of irradiation position in figure 5.3.

As expected, the photopeak amplitude of each individual PMT decreases as the irradiation point moves away from the PMT. At the centre of the crystal (i.e. the 5 cm position), the photopeak amplitude decreases by approximately 50% relative to the value measured at the 1 cm position. In comparison, Yang et al. [5] measured a decrease of 20% for 20 mm long crystals in their DOI detector work.

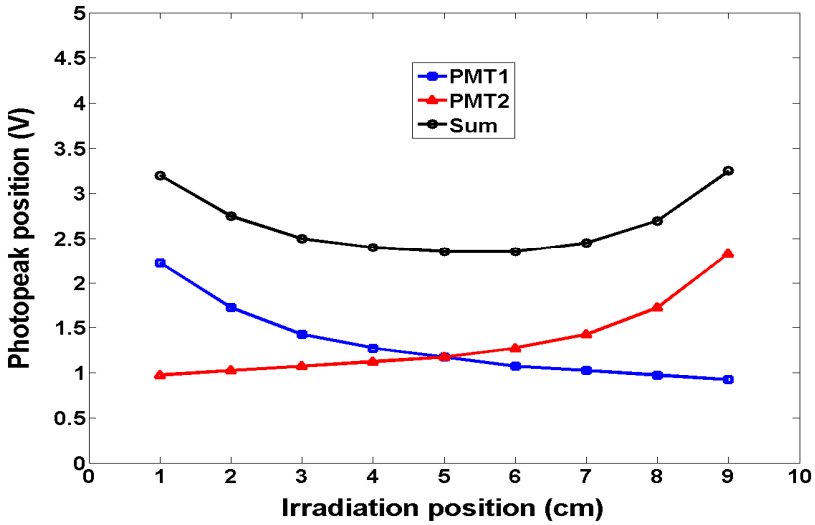

Figure 5.3 Photopeak position for the individual PMT energy spectra at both ends of a Teflon wrapped 2×2×100 mm^3 LYSO crystal and for the summed energy spectrum (PMT1+PMT2) as a function of irradiation position.

A key difference in our results compared to those of Yang et al. is that in Yang's work the photopeak amplitude determined as the sum of the two detectors was constant for events throughout the crystal while in our case for the 100 mm long crystal the amplitude of the sum signal is not constant over the length of the crystal, rather following a parabolic function vs. position. This difference is most likely due to the much longer crystal length used in this present work as compared to the work of Yang. The symmetry of the sum photopeak position suggests that the PMTs remained stable over the approximately 18 hour measurement period. Figure 5.4 shows the energy spectra obtained from the sum of the two PMT signals at three positions. In each case, the 511 keV photopeak is clearly seen and the fraction of counts in the Compton region of the spectrum is approximately the same. The average energy resolution for the nine irradiation positions was 15.4 ± 1.3%.

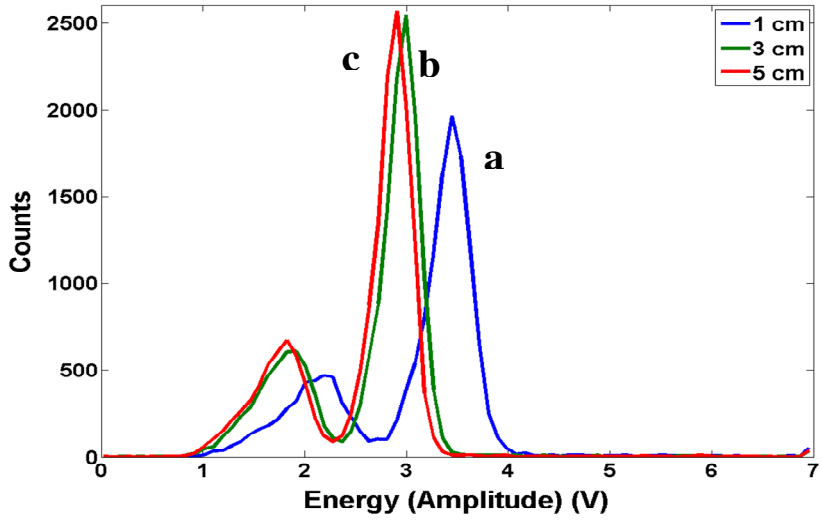

Figure 5.4 Typical energy spectrum obtained from the sum of two PMT signals at irradiation position of (a) 1 cm (b) 3 cm and (c) 5 cm from PMT1 for a Teflon –wrapped crystal.

Figure 5.5 plots the ratio of the two PMT signals, PMT1/(PMT1+PMT2), at the nine irradiation positions of the crystal for the Teflon-wrapped and ESR covered crystals used in this study. For each irradiation position, the centre position value and the FWHM of the distribution were calculated by fitting a Gaussian curve to each distribution.

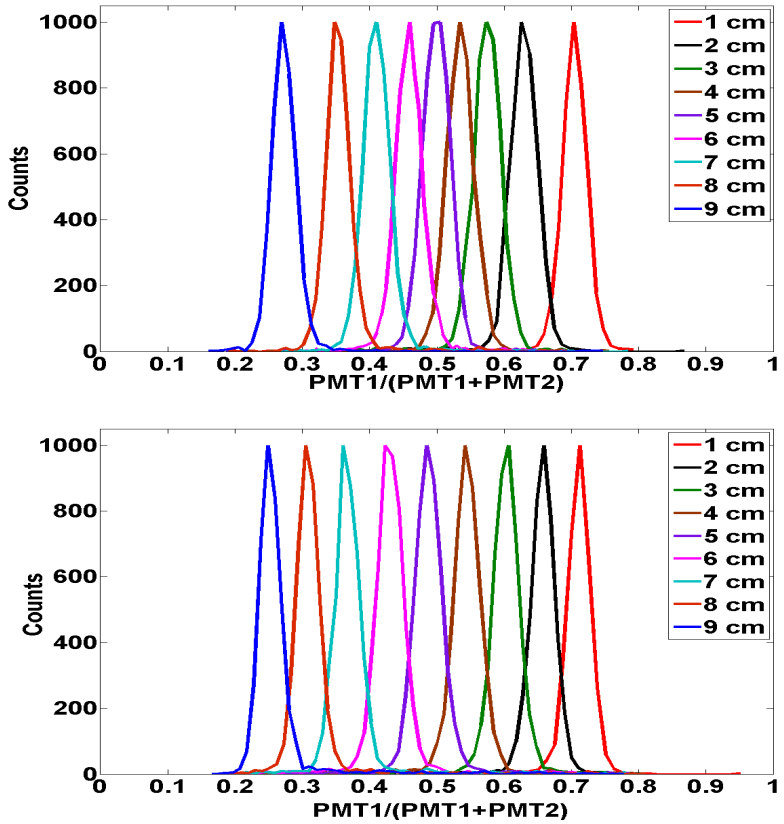

Figure 5.5 Distribution of the ratio of PMT signals at nine collimated beam irradiation positions for (a) Teflon wrapped crystal and (b) ESR covered crystal.

It can be clearly seen that the distribution of the peaks due to the nine irradiation positions is more uniform for the ESR covered crystal than for the Teflon wrapped crystal as the peaks are more uniformly spaced. The spatial resolution in the light sharing direction for these two cases was calculated as the FWHM of the profile divided by the slope of the tangent to a plot of the centre position vs. irradiation position, similar to the

method of Yang [5]. For the Teflon wrapped crystal the spatial resolution ranged from 5.0 mm at the 1 and 9 cm position to 14.0 mm at the 5 cm position (average 9.4 ± 3.3 mm) while for the ESR covered crystal the average spatial resolution was 7.0 ± 1.0 mm.

The centre position for each of the nine irradiation positions vs. irradiation position are plotted in figure 5.6 (b) for the Teflon wrapped crystal and figure 5.6 (d) for the ESR covered crystal, with the error bars corresponding to the FWHM values of the profiles in figure 5.5. As expected from the distribution of the ratio profiles, the calibration curve for the Teflon wrapped crystal has the shape of a 3rd order polynomial, where the ends have a greater slope than in the middle, while the calibration curve for the ESR covered crystal has a nearly linear shape. The 3rd order polynomial shape is different from results reported for shorter 20 mm long crystals (e.g. [13]) in which the calibration curve typically has a linear shape. Figures 5.6 (a) and (c) show the distributions of the ratio of the two PMT signals for uniform irradiation of Teflon-wrapped and ESR covered 2 × 2 × 100 mm^3 LYSO crystals, respectively, with a ^{22}Na point source. The non-uniform axial spatial resolution of the Teflon wrapped crystal leads to a ratio distribution plot that has a highly centre-peaked shape while the nearly uniform spatial resolution of the ESR covered crystal leads to a very uniformly shaped ratio distribution plot. Figures 5.6 (b) and (d) show the plots of the calibration curves obtained for the Teflon wrapped and ESR covered crystals, respectively, using the Shao method for calibration. In both cases there is excellent agreement with the gold-standard measurement of the collimated irradiation method. Similar results (not shown) were obtained for both crystals when irradiated uniformly with the ^{68}Ge line source.

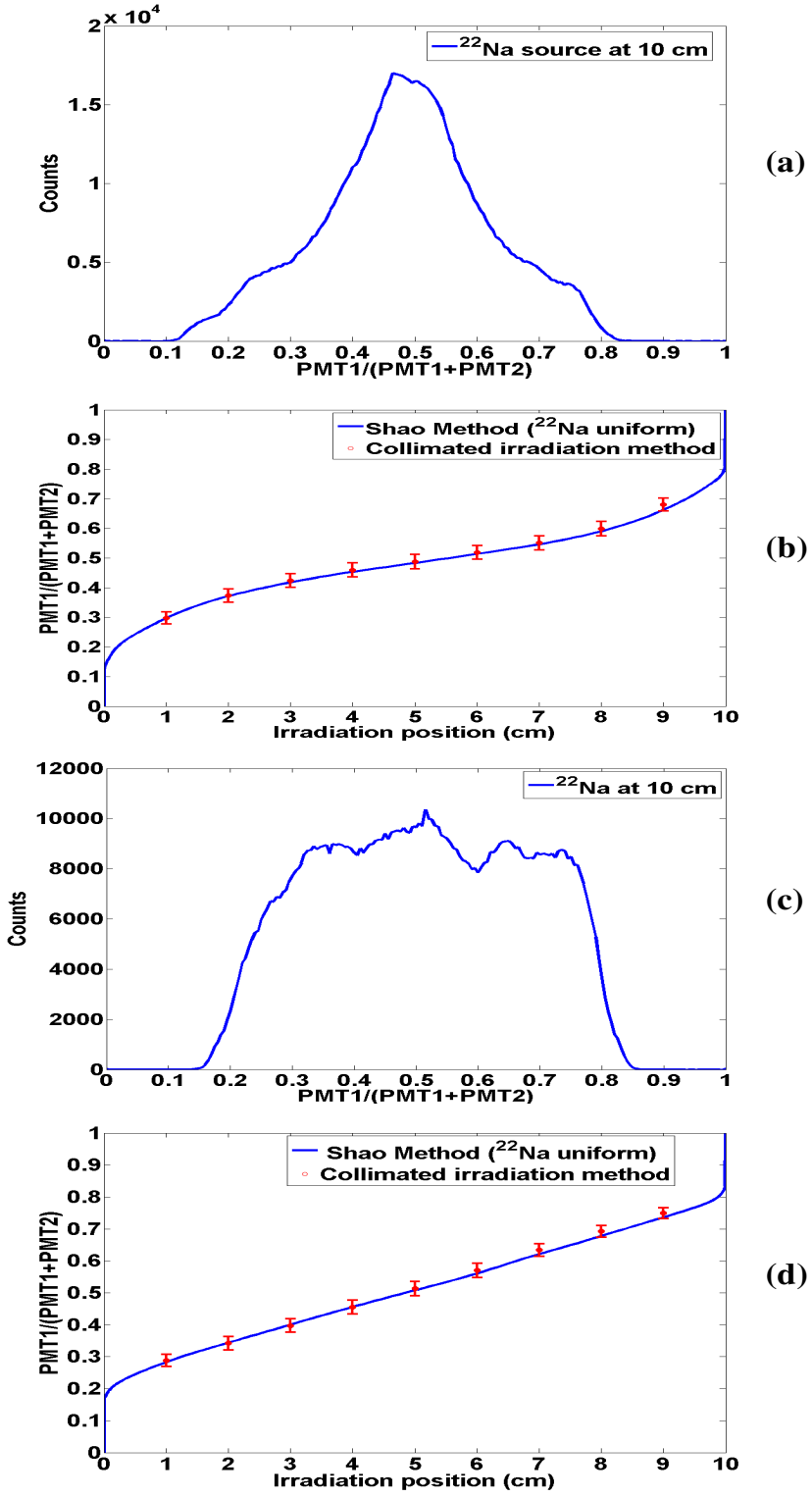

Figure 5.6 Distributions of the ratio of two PMT signals for uniformly irradiated (a) Teflon-wrapped and (c) ESR covered crystal and the resulting calibration curve for (b) Teflon-wrapped and (d) ESR covered crystal, compared with the 'gold standard' points measured using the collimated irradiation method. The irradiation source was the ^{22}Na source.

5.4.2 Calibration of Unbalanced Detectors with External Source

Table 5.1 Energy resolution of 511 keV photons averaged over nine irradiation positions of Teflon-wrapped crystal at different voltage variations

Voltage variation (V)	Energy Resolution (%)
750PMT1-800PMT2	15.50 ± 2.82
800PMT1-800PMT2	15.43 ± 1.27
800PMT1-750PMT2	15.42 ± 1.52

Table 5.1 gives the average energy resolution at 511 keV and standard deviation from the nine collimated beam irradiation positions for each voltage variation for the Teflon wrapped crystal. The energy resolution remains stable at about 15.5% over the range of voltages tested showing that the energy resolution does not significantly depend on the gain variation over the range tested. When the high voltage of a PMT was changed from 800V to 750 V there was a resulting change in the gain of approximately 50%. In order to maintain a similar singles event rate in the reduced voltage detector it was necessary to lower the CFD setting from 1.5 V to 1 V. The energy resolutions at 511 keV for the uniform irradiation methods are shown in Table 5.2. Due to the variation in photopeak position with irradiation location (as shown in figure 5.3) the energy resolution for uniform irradiation, at 18%, is worse than for collimated irradiation.

Table 5.2 Energy resolution of 511 keV photons for uniform irradiation of Teflon-wrapped crystal with ^{22}Na point source at different voltage variations

Voltage variation (V)	Energy Resolution (%)
750PMT1-800PMT2	17.45
800PMT1-800PMT2	18.58
800PMT1-750PMT2	17.94

Figure 5.7 shows the calibration curves and results of the collimated irradiation measurements for the three voltage variations tested for the ESR-glued crystal without adjustment of the CFDs to alter the singles event rates in the two detectors.

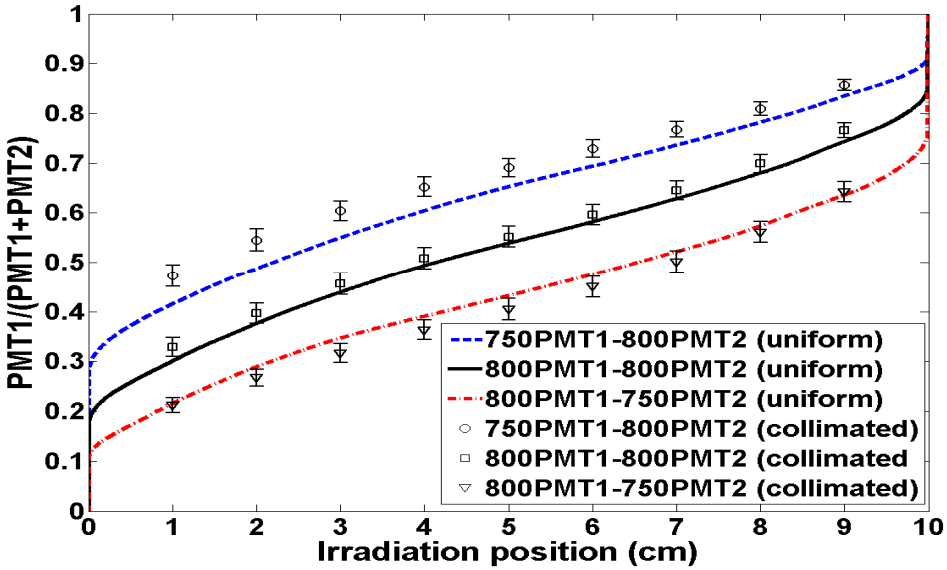

Figure 5.7 Axial positioning calibration curves for three voltage variations using both calibration methods for the ESR covered crystal without compensation for different singles rates in the detectors.

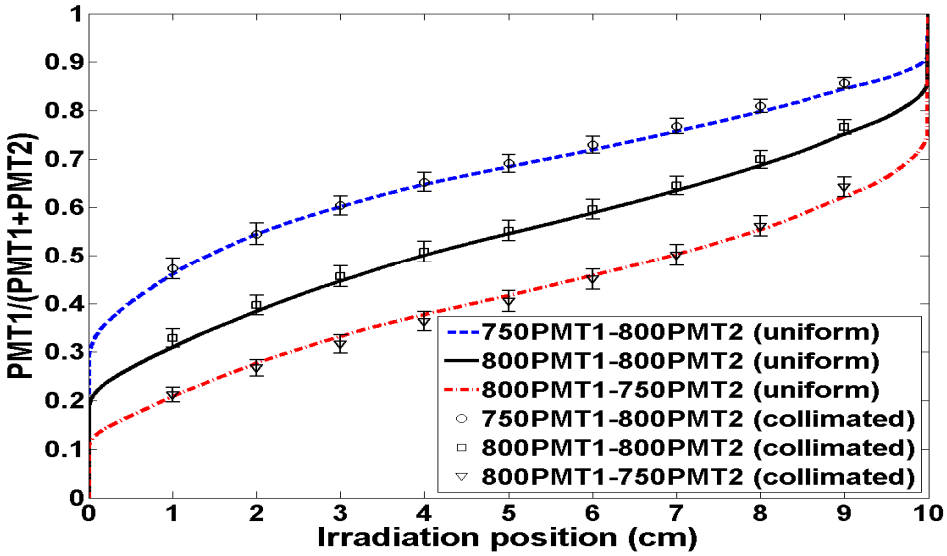

Figure 5.8 Axial positioning calibrations for three voltage variations using both calibration methods for the ESR covered crystal with adjustment of CFD thresholds to balance the number of single events in each detector.

The data show that the calibration curves obtained from the uniform irradiation method do not correlate with the gold standard measurement of the collimated irradiation measurement method, indicating that the uniform irradiation method is sensitive to gain variation in the detectors, likely because the gain variation leads to a non-uniform spatial distribution of events that are above the threshold for both detectors. The discrepancy in the two methods in terms of position estimation is ranging from about 15% to 76%. Similar results (not shown) were obtained for a Teflon wrapped crystal.

Figure 5.8 shows the calibration curves and results of the collimated irradiation measurements for the three voltage variations tested for the same ESR-glued crystal used for the results of figure 5.7 but after adjustment to the CFD settings to balance the singles event rates in the two detectors. In this case the calibration curves obtained from the uniform irradiation method are in excellent agreement with the results obtained from the collimated irradiation method. The agreement between these two methods suggests that balancing the singles rate in the two detectors by adjusting the CFD thresholds restores the spatial uniformity of the events that are above the threshold for triggering both detectors. Again, similar results (not shown) were obtained for the Teflon wrapped crystal.

The dependence of the calibration curve on the CFD threshold setting was examined by adjusting the two CFDs for the two detectors to vary the singles events rate from 500 counts per second (cps) to 2,500 cps while maintaining equal event rates in the two detectors. Figure 5.9 shows the calibration curves obtained from these measurements plotted together with the measurements obtained from the collimated irradiation method. The data show that there is excellent agreement between the calibration curves for all

singles event rates except for very low count rates (500 cps). At this event rate, the CFD setting was at an average of approximately 425 keV, but due to the spatial dependence of the photopeak voltage this setting meant that for some regions of the crystal significant fractions of the photopeak events were being excluded.

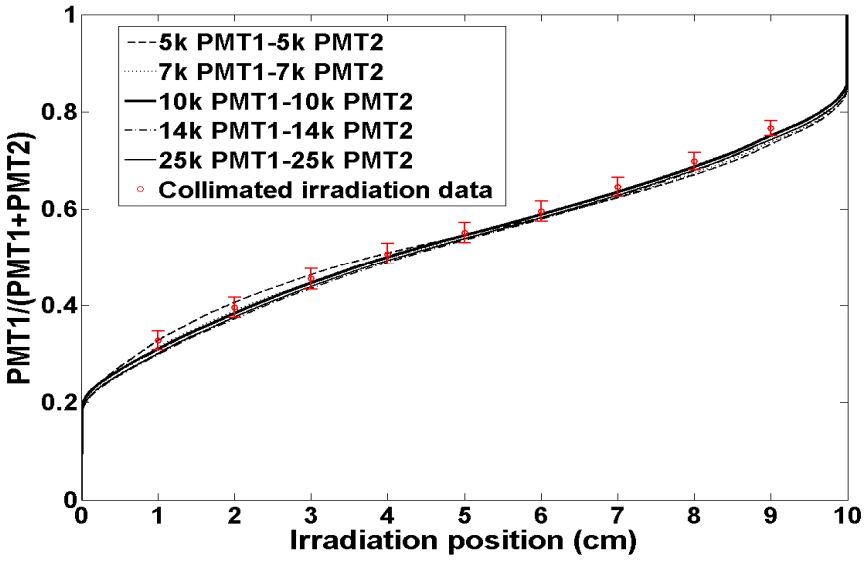

Figure 5.9 Calibration curves obtained for five different singles event rates in the two detectors, created by varying the CFD thresholds, compared with the results obtained from the collimated irradiation measurement. In the legend 5K, 10k etc refer to the number of counts per 10 seconds.

From the figure it is obvious that the agreement is improved for lower values of the CFD (e.g. the 2,500 cps CFD setting corresponded to approximately 120 keV). This suggests that the calibration method is mostly insensitive to the energy threshold applied during the acquisition of data, provided that the number of singles events in each detector is balanced.

5.4.3 Calibration of Unbalanced Detectors with LYSO Intrinsic Activity

Figure 5.10 shows the calibration curves obtained for the three voltage variations tested using the intrinsic radioactivity of the LYSO crystal as a source together with the

results obtained from the ^{22}Na point source irradiation for the ESR-glued crystal. The singles event rates for the two detectors were balanced for all acquisitions by adjusting the CFD thresholds for the two detectors. There is excellent agreement between the two methods, suggesting that the intrinsic radioactivity of the LYSO crystal is suitable for calibration of the detectors.

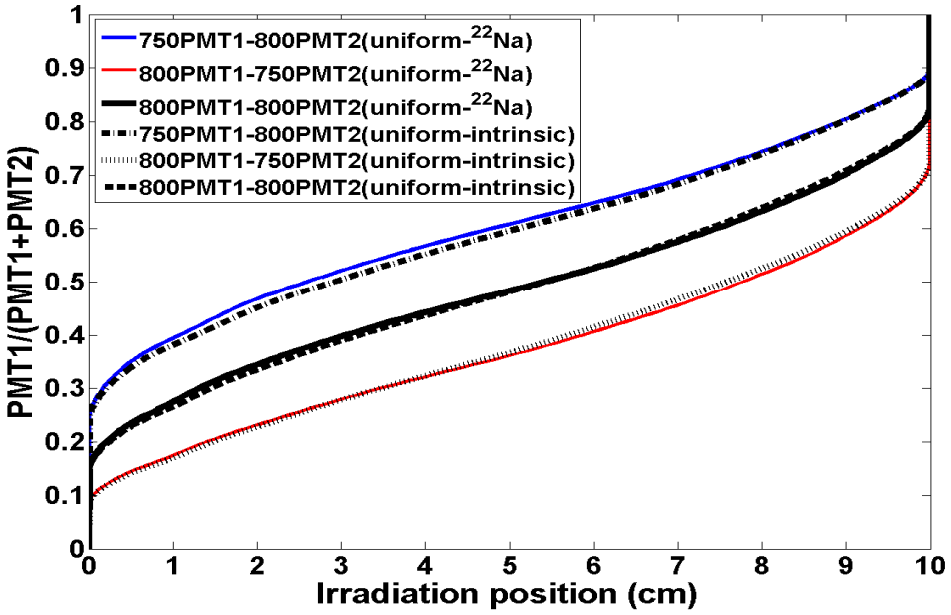

Figure 5.10 Calibration curves obtained using the intrinsic radiation present in LYSO and an external ^{22}Na source.

5.5 Discussion and Conclusion

In this work we examine the axial positioning calibration of dual-ended readout detectors that use 2 × 2 × 100 mm^3 LYSO crystals coupled to PSPMTs for the case of both balanced and unbalanced detectors using the calibration method proposed by Shao [12] and comparing it to the gold standard of 511 keV collimated beam irradiation of discrete points of the crystal. The calibration results from the uniform irradiation method were found to be highly dependent on the relative singles event rates measured in the two

detectors of the dual-ended readout design. Balancing the singles event rates in both detectors by adjusting the signal trigger threshold resulted in calibration curves that showed excellent agreement with the measurements obtained with the collimated source. These results suggest that for our crystal geometry and configuration, $2 \times 2 \times 100$ mm^3 LYSO polished on all sides and covered in either Teflon or ESR reflector, balancing the singles event rates for the two detectors is sufficient to ensure the assumption of uniform spatial density of events which the method of Shao requires.

Similar calibration results were obtained for source geometries of a ^{22}Na point source at 10 cm from the crystal, a 19.2 cm long ^{68}Ge line source located 25 cm from the crystal, and using the intrinsic radioactivity of the LYSO crystal. Although Shao's method is based on the assumption of a uniform exposure of the crystal to the radiation, these results suggest that the calibration method is relatively insensitive to the source geometry. This implies that when using Shao's calibration method in a complete PET system that uses dual-ended readout detectors the calibration will be insensitive to minor variations in the placement of calibration sources.

Our results show that the calibration method of Shao works well for both the cases of uniform and non-uniform spatial resolution, as was encountered for the ESR-covered and Teflon-wrapped crystals. In previous work, such as that of Yang et al. [13] for 20 mm long crystals with a different surface finish, there is generally an inherent assumption of a linear dependence of the ratio signal of the two detectors in a DOI design vs. position of irradiation. In this work, we demonstrate that this assumption is not required and that the calibration methods tested are robust and accurate for the case for non-linear calibration

curves. This result will be of general interest to other groups investigating dual-ended readout detector designs, including those with shorter crystal lengths.

In conclusion, the two methods were found to be equivalent for a range of crystal reflector materials, irradiation source geometries, and for cases of linear and non-linear dependence of the calibration curve with irradiation position. The calibration method based on uniform irradiation was found to be highly sensitive to imbalances in the singles event rate in the two detectors of the dual-ended readout design that occurred when the detectors were unbalanced by varying the applied high voltage. Compensating for the different event levels by adjusting the threshold level of the detector CFDs proved to be a robust and simple way to restore the accuracy of the calibration method based on uniform irradiation of the crystal. Implementation of this method will significantly simplify the calibration of our dual-ended readout detector modules, especially for the cases of a large number of crystals in a 2D crystal array in a detector of our proposed complete scanner, allowing rapid collection of calibration data in a few minutes with a line source or overnight using the intrinsic LYSO radioactivity.

REFERENCES

[1] I. Vilardi, A. Braem, E. Chesi, F. Ciocia, N. Colonna, F. Corsi, F. Cusanno, R. D. Leo, A. Dragone, F. Garibaldi, C. Joram, L. Lagamba, S. Marrone, E. Nappi, J. Seguinot, G. Tagliente, A. Valentini, P. Weilhammer and H. Zaidi, "Optimization of the effective light attenuation length of YAP:Ce and LYSO:Ce crystals for a novel geometrical PET concept," *Nucl. Instr. Meth*., vol. 564, pp. 506-514, 2006.

[2] J. Seguinot *et al*, "Novel geometrical concept of high performance brain PET scanner-principle, design and performance estimates" *CERN PH-EP/2004-050 II Nuovo Cimento,* vol. 29C, pp. 429-63, 2006.

[3] A. Braem, C. Joram, J. Seguinot, G. Dissertori, L. Djambazov, W. Lustermann, F. Nessi-Tedaldi, F. Pauss, D. Schinzel, P. Solevi, C. Lacasta, J. F. Oliver, M. Rafecas, R. De Leo, E. Nappi, I. Vilardi, E. Chesi, E. Cochran, K. Honscheid, H. Kagan, A. Rudge, S. Smith, P. Weilhammer, I. Johnson, D. Renker, N. Clinthorne, S. Huh, E.

Bolle, S. Stapnes and F. Meddi, “AX PET: A novel PET detector concept with full 3D reconstruction,” *Nucl. Instr. And Meth. A*, vol. 610, pp. 192-195, 2009.

[4] S. Salvador, D. Huss, and D. Brasse, “Design of a high performances small animal PET system with axial oriented crystals and DOI capability” *IEEE Trans. Nucl. Sci,,* vol. 56, pp. 17-23, 2009.

[5] Y. Yang, P. A. Dokhale, R. W. Silverman, K. S. Shah, M. A. McClish, R. Farrell, G. Entine and S. R. Cherry, "Depth of interaction resolution measurements for a high resolution PET detector using position sensitive avalanche photodiodes,” *Phys. Med. Biol.*, vol. 51, , pp. 2131-2142, 2006.

[6] P. A. Dokhale, R. W. Silverman, K. S. Shah, R. Grazioso, R. Farrell, J. Glodo, M. A. McClish, G. Entine, V. H. Tran, and S. R. Cherry, "Performance measurements of a depth-encoding PET detector module based on position-sensitive avalanche photodiode read-out,” *Phys. Med. Biol.*, vol. 49, pp. 4293-4304, 2004.

[7] Y. Shao, K. Meadors, R. W. Silverman, R. Farrell, L. Cirignano, R. Grazioso, K. S. Shah, and S. R. Cherry, “Dual APD array readout of LSO crystals: Optimization of crystal surface treatment,” *IEEE Trans. Nucl. Sci.*, Vol. 49, No. 3 pp. 649-654, June 2002.

[8] K. C. Burr and A. Ivan, “Evaluation of a prototype small-animal PET detector with depth-of-interaction encoding” *IEEE Trans. Nucl. Sci.* vol. 51, pp. 1791-98, 2004.

[9] W. W. Moses and S. E. Derenzo, “Design studies for a PET detector module using a PIN photodiode to measure depth of interaction” *IEEE Trans. Nucl. Sci.*, vol. 41, pp. 1441-45, 1994.

[10] C. Bircher and Y. Shao, “Use of internal scintillator radioactivity to calibrate DOI function of a PET detector with a dual-ended-scintillator readout” Med. Phys. Vol. 39 (2), pp. 777-787, 2012.

[11] F. ur-Rehman, B. McIntosh and A. L. Goertzen, “Observations on dual-ended readout of 100 mm long LYSO crystals,” *Nucl. Instr. Meth. A (NIMA)*, Vol. 652, pp. 275-279, 2011. doi: 10.1016/j.nima.2010.08.015

[12] Y. Shao, R. Yao and T. Ma, "A novel method to calibrate DOI function of a PET detector with a dual-ended-scintillator readout,” *Med. Phys.* Vol. 35 (12), pp. 5829-5840, December 2008.

[13] Y. Yang, J. Qi, Y. Wu, S. S. James, R. Farrell, P. A. Dokhale, K. S. Shah and S. R. Cherry, “Depth of interaction calibration for PET detectors with dual-ended readout by PSAPDs*,”* *Phys. Med. Biol*., vol. 54, , 433-445, 2009.

Chapter 6 Use of systematic surface roughing to enhance the spatial resolution of dual-ended readout of axially-oriented 100 mm long LYSO crystals: Measurement and simulation

This chapter is a reformatted paper prepared for publication and will be submitted to a peer-reviewed journal. The partial citation information of the paper is as follows.

Fazal ur-Rehman, Yuan-Chuan Tai and Andrew L. Goertzen 2012 Use of systematic surface roughing to enhance the spatial resolution of dual-ended readout of axially-oriented 100 mm long LYSO Crystals: Measurement and simulation

6.1 Abstract

In this work we explore the effects of using regular patterns of surface roughing to modulate the light transport in a dual-ended readout detector for PET imaging that uses 100 mm long LYSO crystals oriented in the axial direction. The long surfaces of 3 × 2 × 100 mm^3 and 2 × 2 × 100 mm^3 LYSO crystals, initially polished on all sides, were systematically roughed in a band pattern with 0.8 mm bands of roughed surface spaced at 5 mm increments over the central 8 cm of the crystal length. Cases of 1 to 4 surfaces of the crystal roughed with this pattern were explored. Each crystal was then wrapped in Teflon and read out at either end using position sensitive photomultiplier tubes (PSPMTs). An electronically collimated 511 keV photon beam was oriented perpendicular to the long direction of the crystal and data acquired at discrete locations along the crystal length. The ratio of two PMT signals was used to find the axial position of interaction and spatial resolution in the light sharing direction while their sum was used to determine the light output and energy resolution. The spatial resolution improved from an average of 9.1 mm with no surface treatment to 5.6, 4.7 or 4.2 mm for banding patterns on 1, 2 or 4 surfaces, respectively. The roughed surfaces resulted in degraded energy resolution, with a decrease from 11.1% FWHM for the untreated crystal to 12.0%,

13.5%, and 13.6% for the patterns on 1, 2, and 4 surfaces, respectively. When the spatial resolution is corrected for the beam width, we estimate the resolution for the case of 4 banded surfaces to be 3.4 mm FWHM. The same spatial resolution was obtained when interleaving bands were created on only two opposite surfaces with a better energy resolution of 12.2%. The measured results were used to calibrate Monte Carlo simulations using DETECT2000, which showed good agreement with the experimental results.

6.2 Introduction

We propose to make use of arrays of long thin scintillator crystals oriented in the axial direction and read out at either end by low cost position sensitive photomultiplier tubes (PSPMTs) to construct a compact animal PET system. The schematic diagram of our design concept is shown in figure 6.1 along with a mockup of our system design concept. This axial PET geometry was first proposed by Shimizu *et al* (1988) using 5 cm long BGO crystal bundles oriented in the axial direction and read out at both ends using photodetectors but a complete PET system based on this design was never constructed.

This detector geometry has also been previously explored by others for human brain imaging using 3.2 × 3.2 × 100-150 mm^3 LYSO scintillation crystals readout initially by hybrid photon detectors (Seguinot *et al* 2006, Vilardi *et al* 2006) and later by wave length shifting fibers and Geiger-mode avalanche photodiodes (Braem *et al* 2006) but has not been extensively investigated for applications of small animal imaging using smaller crystal sizes. Samuel *et al.* (Samuel *et al* 2009) investigated the design of a small animal PET imaging system using shorter axially oriented 1.5 × 1.5 × 20 mm^3 LYSO crystals with a depth of interaction (DOI) capability, demonstrating an independence of spatial

resolution from the detection efficiency. In this work, a spatial resolution of about 1 mm was demonstrated.

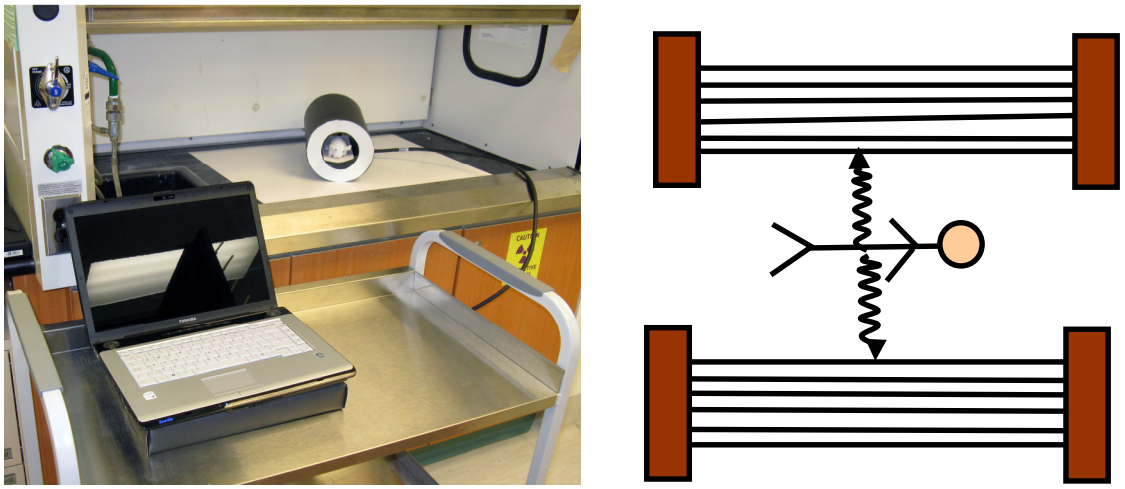

Figure 6.1 Left: A photograph of a mockup of system design concept. The system is shown within a laboratory fume hood with comparable dimensions to a biosafety cabinet. The cylindrical detector geometry has a rat sized stuffed animal in it for scale. The laptop computer for data acquisition sits on top of a compact electronics cabinet. Right: Schematic diagram showing axially oriented crystals coupled to PSPMTs at two ends in detector modules to be used in our proposed compact preclinical PET imaging system.

Dual-ended readout of scintillation crystals has been extensively explored for adding DOI capability to the PET imaging system designs with shorter crystals oriented in the radial direction (Yang *et al* 2006, Dokhale *et al* 2004, Shao *et al* 2002, Burr *et al* 2004, Moses *et al* 1994, Bircher *et al* 2012, Saha *et al* 2004, Anfré *et al* 2007). We have previously reported some of our observations on dual-ended readout of 100 mm long LYSO crystals to be used in our proposed compact PET imaging system such as light output, energy resolution, spatial resolution and the effect of different reflector materials on these parameters (ur-Rehman *et al* 2011). A spatial resolution of about 7 mm in the light sharing direction was reported for an enhanced specular reflector (ESR) covered 2 × 2 × 100 mm^3 LYSO crystal in that study. In a following study we examined the axial positioning calibration of dual-ended readout of axially oriented 100 mm long LYSO

crystals for use in a compact PET system (ur-Rehman and Goertzen 2012) where we evaluated two methods of calibration for balanced and unbalanced detectors using LYSO intrinsic activity and external point and line sources.

In our proposed compact PET the axial position of interaction of detected 511 keV photons in the crystals will be encoded from the light sharing between the two PSPMTs in the dual-ended readout detector. A key to good resolution in the axial encoding direction is to optimize the balance between light collection for maximizing the energy resolution and light losses for axial encoding of spatial resolution. Therefore particular attention is paid to the light collection optimization in this research. In our previous study we achieved a spatial resolution of 7 mm using different reflector materials (ur-Rehman *et al* 2011), however, the design criteria of our proposed scanner demands a spatial resolution of better than 3 mm. Therefore, in this work we explore the effects of modulating the light transport in the crystal by grinding different banding patterns along the long surfaces of the LYSO crystals with the goal of improving the spatial resolution of crystals in the light sharing direction. The concept of banding patterns was originally proposed by Shimizu *et al* (1988) where they used 5 cm long BGO crystals oriented in the axial direction, demonstrating an axial resolution of 9.5 mm with coarsely ground bands. This work was patented in 1989 (Yamashita *et al* 1989) but more extensive results were not published. To our knowledge, this approach has not been examined for LYSO crystals or with newer generation PSPMTs. The measured results from our work are used to benchmark Monte Carlo simulations performed with the program DETECT2000 (Moisan *et al* 2000) for optical photon transport within the crystals in this study. This code has been used previously in many studies, for example, (Cayouette *et al* 2002,

Tsang *et al* 1995, Steinbach *et al* 2010, Peng *et al* 2011) but has not been used for dual-ended readout detectors with 100 mm long crystals. We are then able to use the benchmarked DETECT2000 software for predicting the performance of banding patterns that were not investigated experimentally.

6.3 Materials and Methods

6.3.1 Experimental Measurements

6.3.1.1 Scintillator crystal band etching

Etched band patterns were created on 1 to 4 long surfaces of initially polished 3 × 2 × 100 mm^3 LYSO crystals obtained from a commercial supplier (Proteus Inc., Chagrin Falls, OH). Each pattern was created by roughing the surface of the crystal using a 0.3 mm wide crystal saw blade (South Bay Technology, San Clemente, California) to etch bands every 5 mm over the central 80 mm of the crystal as shown in figure 6.2. The average width of the etching bands was measured to be 0.8 mm. The size difference between the etched band and the saw blade was caused by the fact that the etching was done manually. In this study the following etching patterns were investigated:

- Etched bands on 1 side.
- Etched bands on 2 opposite sides with the bands in the same axial location (Figure 6.2(a)).
- Etched bands on all 4 sides with the bands in the same axial location.
- Etched bands on 2 opposite sides with the band locations interleaved (Figure 6. 2(b)).

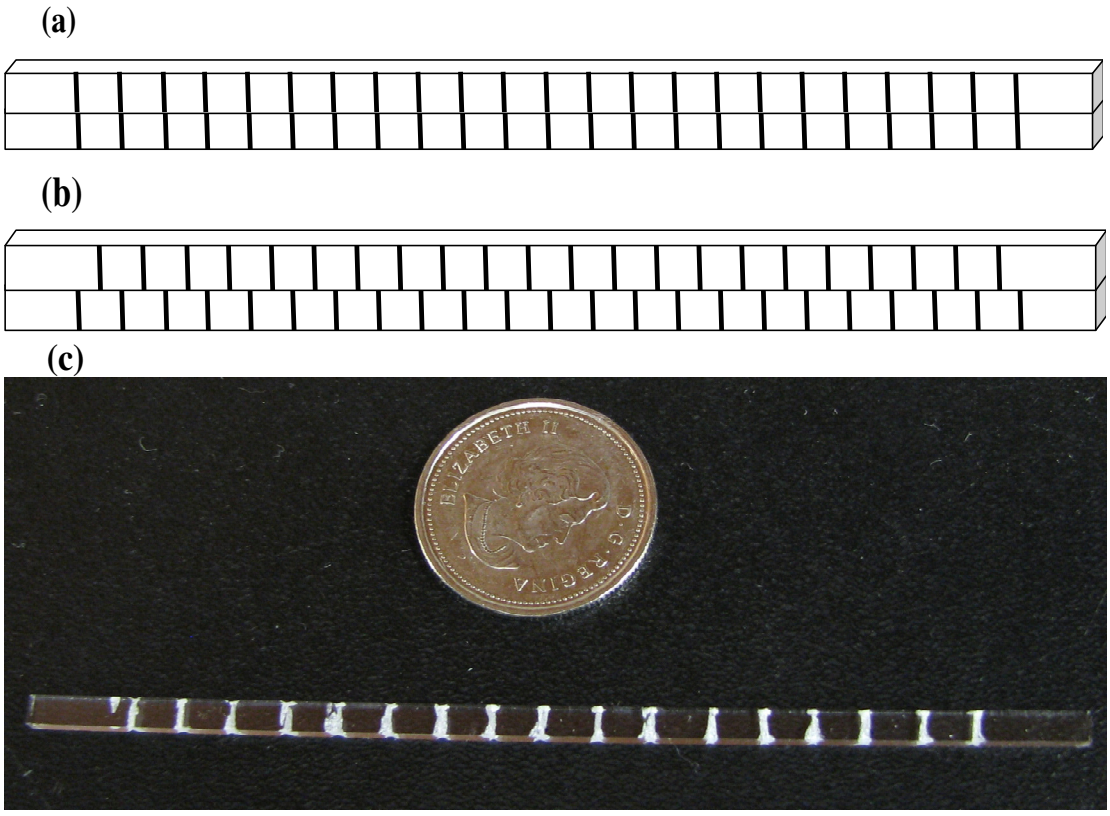

Figure 6.2 (a) Schematic example of coinciding etching band patterns created on the same axial locations of top and bottom surfaces of a 100 mm long LYSO crystal. (b) Schematic example of interleaving etching band patterns created on top and bottom surfaces of a 100 mm long LYSO crystal. (c) Photograph of a 3 × 2 × 100 mm^3 crystal with coinciding etching band patterns on four long surfaces with a Canadian quarter shown for reference.

In addition, for one 3 × 2 × 100 mm^3 crystal a single long side was roughed completely using sand paper to investigate how this compared to the banding pattern results. In order to investigate the effect of changing the crystal size, 1 and 2 sided banding patterns were also investigated for 2 × 2 × 100 mm^3 LYSO crystals obtained from the same supplier and initially polished on all sides and wrapped in Teflon. For this crystal, smooth surfaces glued to a 3M Vikuiti^{TM} Enhanced Specular reflector (ESR) (3M Optical System Division, St. Paul, MN) were also investigated. The ESR reflector was cut into four pieces of 2 × 100 mm^2 size and then each piece was glued to each long

surface of the crystal one after the other using Dymax OP-20 optical adhesive glue (DYMAX, Torrington, CT). The glued-ESR was cured by irradiating it with UV light from a Dymax Blue Wave 75 UV Spot Light Source.

6.3.1.2 Data acquisition

Scintillator crystals were wrapped in 4 layers of Teflon tape and the ends coupled to a pair of Hamamatsu R8900U-100-C12 (Hamamatsu Photonics K. K., Japan) PSPMTs using optical grease (Visilox V-788). The PSPMT outputs were multiplexed to four signals, X+, X-, Y+ and Y- using Siemens Inveon pre-amplifier stacks (Siemens Preclinical Solutions, Knoxville, TN) and then subsequently processed using standard NIM electronics as shown schematically in figure 6.3. Shaped signals for each detector were digitized using a National Instruments PCI-6133 PC based data acquisition card (National Instruments Corporation, Austin, TX) running under a National Instruments LabWindows/CVI based interface. The detector response in the light sharing direction for each crystal is assessed by irradiating the crystal using an electronically collimated 511 keV beam, also shown schematically in figure 6.3. In this arrangement a single $2 \times 2 \times 15$ mm^3 LYSO crystal, coupled to a single channel PMT (Hamamatsu H3178-51), is aligned with a 50 μCi ^{22}Na point source (model MMS09, Eckert & Ziegler Isotope Products, Valencia, CA) with a diameter of 0.25 mm. This detector is used in coincidence with the test LYSO crystal to create the electronically collimated 511 keV photon beam. The ^{22}Na source, small LYSO crystal and single channel PMT are mounted on a translation table attached to a 2-axis translation stage in order to allow reproducible and precise positioning of the 511 keV beam. The test crystal and the coincidence crystal are at an equal distance of 50 mm from the source.

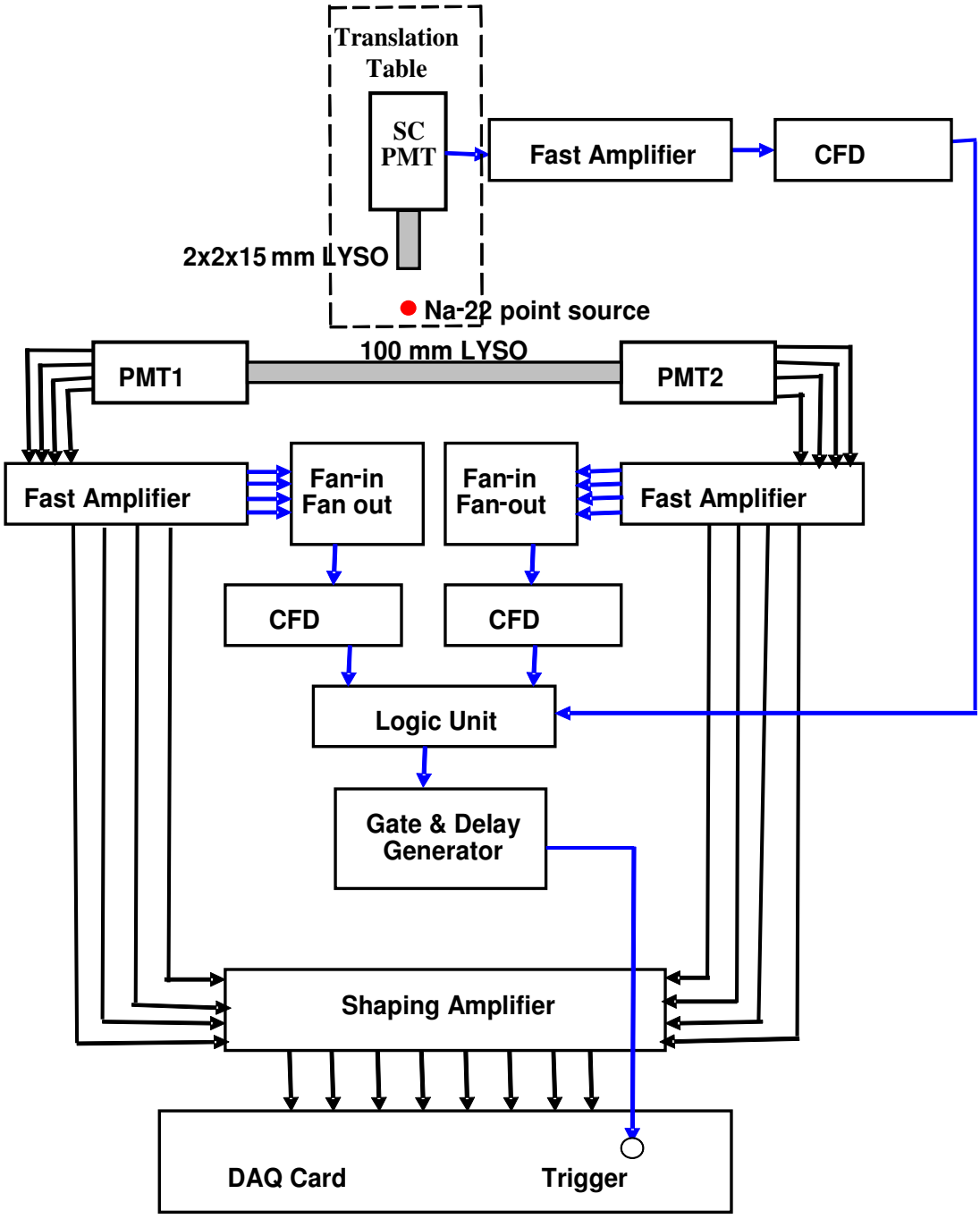

Figure 6.3 Schematic drawing showing the electronic collimation of 511 keV beam and PMT signal processing in bench top data acquisition NIM Electronics. The single channel PMT (SC PMT) and ^{22}Na source are placed on a translation table shown in dotted rectangle that is attached to a 2-axis translation stage.

The response of the 10 cm long crystals for various etching band patterns versus irradiation position was determined by irradiating the crystal at nine discrete locations

separated by 1 cm each. The beam was estimated to be 2.5 mm wide on the surface of the crystal based on the 2 mm size of the crystal used for the collimating detector and the 0.25 mm source size. The beam width was not corrected for ^{22}Na positron range.

At each irradiation position, events were collected for 1500 seconds, or about 10000 counts per position. For each event, the total signal from each of the two PSPMTs was digitized and is referred to as signals PMT1 and PMT2. The total number of detected coincidence events at each irradiation position was recorded for each banding patterns.

6.3.1.3 Data Analysis

A summed energy spectrum was obtained for each beam position by summing the two PMT signals (PMT1+PMT2). The relative light collection efficiency at each irradiation position was evaluated by measuring the location of the 511 keV photopeak in the summed energy spectra. The energy resolution was calculated as the full-width at half maximum (FWHM) of the 511 keV photopeak for each summed spectrum by fitting a Gaussian function to the photopeak. For each event, the ratio PMT1/(PMT1+PMT2) was calculated to determine the axial location of the event. The ratio signal for all the events at each location was histogramed and each ratio distribution peak was fitted with a Gaussian function to determine the peak centroid and the FWHM of each profile. The peak centroid that gives the mean ratio for each location is plotted versus irradiation position and the ratio response is fitted with a third degree polynomial. The spatial resolution of the detector in the light sharing direction is estimated as the FWHM of the ratio profile at each position divided by the slope of the plot of ratio signal vs. position at each irradiation position. The light output, energy resolution and spatial resolution were determined for each banding patterns and surface treatment and the results were

compared with those of the polished crystal with no etching bands. The data analysis was automated using scripts written in Matlab (The MathWorks, Inc., Natick MA). As the collimated beam width was estimated to be 2.5 mm based on the 2 mm crystal width and 0.25 mm source size, the axial spatial resolution determined in this study was deconvolved with the beam width to obtain the true spatial resolution using the following relation:

$$R_{meas}^2 = R_{true}^2 + R_{beam}^2 \quad (1)$$

where R_{meas} is the measured spatial resolution, R_{true} is true spatial resolution and R_{beam} is the width of the electronically collimated 511 keV photon beam.

6.3.2 DETECT2000 Monte Carlo Simulation

6.3.2.1 Modeling of smooth crystals and etching band patterns

Monte Carlo simulations of the scintillation light transport in our detector crystals were performed using the simulation code DETECT2000 (Moisan *et al* 2000). Our focus in this work was to determine the DETECT2000 simulation parameters required to give good agreement with our measured data in order to benchmark the simulation for this detector geometry and allow the future use of Monte Carlo simulation in refining our detector designs. For the smooth surface i.e. without any etching bands, the POLISH model of DETECT2000 was used with a reflectivity of 0.95 to simulate Teflon as an external air-coupled diffuse reflector around a 3 × 2 × 100 mm^3 LYSO crystal with a refractive index of 1.82 and decay time of 40 ns. The ends of the crystal were modeled as POLISH without any reflector. For the etching band patterns created on the crystal as described in section 2.1.1, the UNIFIED model with a diffusive lobe constant (DL) of 1,

representing the probability of internal Lambertian reflection, and a reflectivity of 0.95 was used to simulate Teflon as an external diffuse reflector. The UNIFIED model allows simulating non-uniform roughness of a surface, such as etching ground bands in this study, through a Gaussian distribution of angle between the mean surface normal and a micro facet normal. For the smooth components of the etched crystal, the same POLISH model used for the case of smooth crystal with a reflectivity of 0.95 was applied. The details of these DETECT2000 optical models can be found in the reference manual (Moisan *et al* 2000). The different detector parameters and DETECT2000 models used in the simulation study are summarized in Tables 6.1 and 6.2, respectively.

Table 6.1 The physical parameters and their values used in DETECT2000 simulation.

Parameter	Value
LYSO refractive index	1.82
Light yield for 511 keV photon	10000
LYSO decay time	40 ns
Reflectivity of Teflon	0.95
Reflectivity of ESR	0.985
Optical grease refractive index	1.463
Optical grease thickness	0.3 mm
Borosilicate PMT window refractive index	1.5
Borosilicate PMT window thickness	0.8 mm
Borosilicate window area	23.5×23.5 mm^2
PSPMT area	23.5×23.5 mm^2

Table 6.2 The DETECT2000 models used in simulation for different crystal surfaces and etching band conditions

Crystal surface/band condition	DETECT2000 Model used
Smooth surface	POLISH
Smooth surface with ESR	METAL, reflectivity of 0.985 for glued-ESR
Rough band components	UNIFIED, DL 1, reflectivity 0.92 for Teflon
Smooth components	POLISH, reflectivity 0.92 for air-coupled Teflon
PMT Cathode Surface	DETECT

Different combinations of light absorption attenuation length, λ_a, and scattering attenuation length, λ_s, ranging from 75 – 1000 mm were tested through simulation. The

value that best matched our experimental results was determined to be 150 mm for λ_a. This value was then used for all simulations. The scattering attenuation length, λ_s, was taken to be an infinite value and hence the attenuation due to scattering was ignored in these simulations. This gives a total bulk attenuation λ_{eff} that is entirely due to the absorption attenuation of light in the clear LYSO crystal according to the following relation:

$$\frac{1}{\lambda_{eff}} = \frac{1}{\lambda_a} + \frac{1}{\lambda_s} \tag{2}$$

The two PSPMTs at the ends of the crystal were modeled by using the "DETECT" finish on the surface of a 0.8 mm thick borosilicate glass window at each end having a refractive index of 1.5. In DETECT2000, the "DETECT" finish models the photocathode surface of a PMT. The active area of the photocathode was 23.5×23.5 mm^2 and the same area was modeled for the glass window before the PMT cathode surface. The ends of the crystals were coupled to the PSPMTs using 0.3 mm thick optical grease having a refractive index of 1.463. The long axis of the crystal was aligned with the center of the PMT at each end. The wavelength dependent quantum efficiency of the two PSPMTs, provided by the manufacturer, and the emission spectrum of LYSO (Zhang *et al* 2007) were modeled as given in figure 6.4. The complete detector geometry was modeled by creating a total of 39 components for the etching band patterns and the smooth parts of the test crystal in the DETECT2000 input file. 10000 optical photons were simulated at the same depth of the crystal (i.e. central long axis of the crystal) for each 511 keV photon interaction at each location, corresponding to the approximate number of optical photons that we expect to be created for each 511 keV photon interaction in LYSO. In

order to achieve a good peak centroid of the ratio of two PMT signals, 10,000 511 keV photons were simulated at each interaction position, 1 through 9 cm in steps of 1 cm, in the crystal.

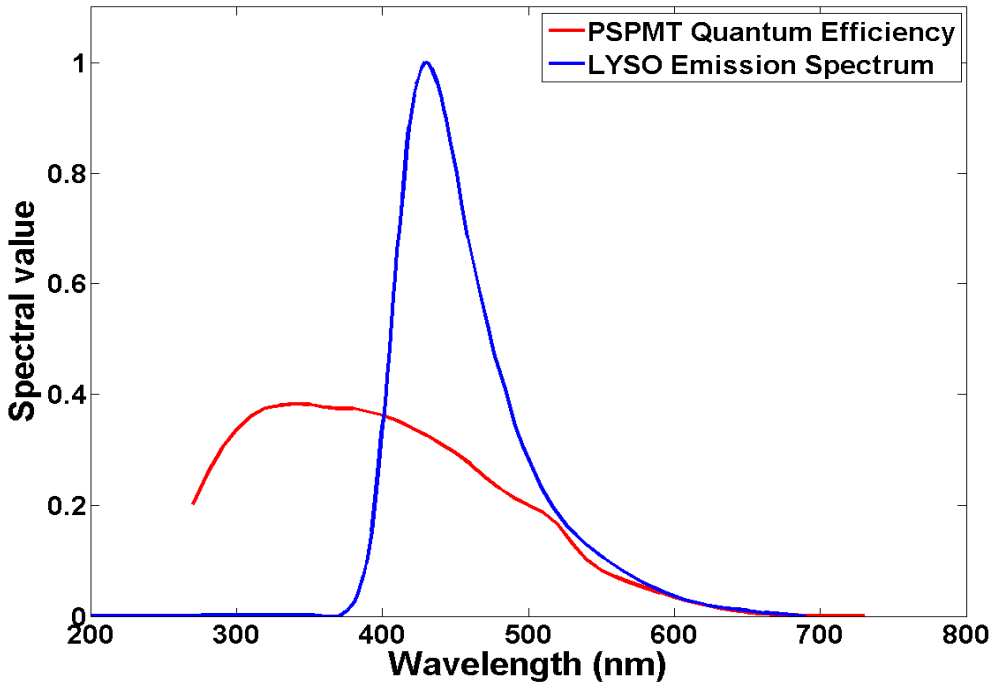

Figure 6.4 Emission spectrum of LYSO (Zhang *et al* 2007) and quantum efficiency of PSPMT used in simulation studies

A shell script was written in Linux for simulating the 10000 511 keV photons one-by-one at each interaction position and storing/appending each simulation output data (number of detected optical photons by each PMT at the two ends of the crystal). This shell script also serves to insert a new seed in the input file for random number generator in each γ photon-simulation (i.e. 10000 optical photons). In addition to smooth surfaces, the following etching patterns were simulated for a $3 \times 2 \times 100$ mm^3 crystal:

- Etched bands on 1 side.
- Etched bands on 2 opposite sides with the bands in the same axial location.

- Etched bands on all 4 sides with the bands in the same axial location.

The simulations were repeated for a 2 × 2 × 100 mm^3 LYSO crystal with smooth surface and etching band patterns on 1 and 2 opposite sides and wrapped in Teflon reflector. For this crystal, smooth surfaces wrapped in a glued-ESR reflector were also simulated. A glue-coupled ESR reflector on smooth crystal surfaces was modeled as "METAL" with a reflectivity of 0.985 that gives a specular reflector in DETECT2000. The simulation for each crystal with banding pattern or smooth surfaces took approximately 24 hours for all 9 interaction positions on a 64 bit computer with a 3.00 GHz Quad processor (Intel(R) Core (TM)2 Quad CPU Q9650 @ 3.00 GHz).

6.3.2.2 Effect of etching band size on spatial resolution, light output and energy resolution

In order to study the effect of etching band size on energy and spatial resolution of the crystal detector, band sizes of 0.6, 0.8, 1, 2 and 3 mm were simulated for the etching band pattern created on one, two and four long surfaces of 3 × 3 × 100 mm^3 LYSO crystal. The simulations in this case were carried out using the same procedure described in section 6.3.2.1.

6.3.2.3 Simulation output data analysis

As in the case of measurements described in section 6.3.1.3, the sum of two PMT signals (here the total number of optical photons collected by the two PMTs), PMT1+PMT2, and the ratio, PMT2/(PMT1+PMT2), were calculated on an event-by-event basis. Energy spectra were obtained from the sum signal at each irradiation position, allowing calculation of the photopeak position and energy resolution similar to the method for the measured data. The ratio of the two PMT signals at each irradiation

position was histogramed and the peak centroid and FWHM for each distribution was calculated using Gaussian fitting to each distribution peak. The peak centroid or the mean ratio signal was plotted vs. irradiation position for each case and fitted with a piecewise interpolation fitting. Spatial resolution in the light sharing direction was obtained by dividing the FWHM of each distribution peak by the slope of the tangent to the fitting curve at each irradiation position. For each simulation, the results were compared with the equivalent measured data set. The data analysis was automated by writing scripts in Matlab.

6.4 Results

6.4.1 Measured Data

6.4.1.1 Spatial dependence of coincidence events for different etching bands

The number of coincidence events at each irradiation position for each etching band and the completely roughed surface of the $3 \times 2 \times 100$ mm^3 crystal are plotted in figure 6.5. It should be kept in mind that during all these measurement cases the CFD levels of both PMTs were set just above the noise floor and these settings remained constant for each of these acquisitions. For the crystal with no etching bands, the number of coincident events remained constant over the entire length of the crystal. For 2 etched surfaces the number of coincidence events recorded is non-uniform over the length of the crystal, having a parabolic shape with a maximum in the middle of the crystal. With etching applied to an increasing number of surfaces this effect becomes more pronounced and there is a corresponding drop in the total number of coincidence events recorded. This effect was the largest for the crystal with one completely rough surface, which had

nearly zero coincidence counts at the irradiation locations closest to the ends of the crystal.

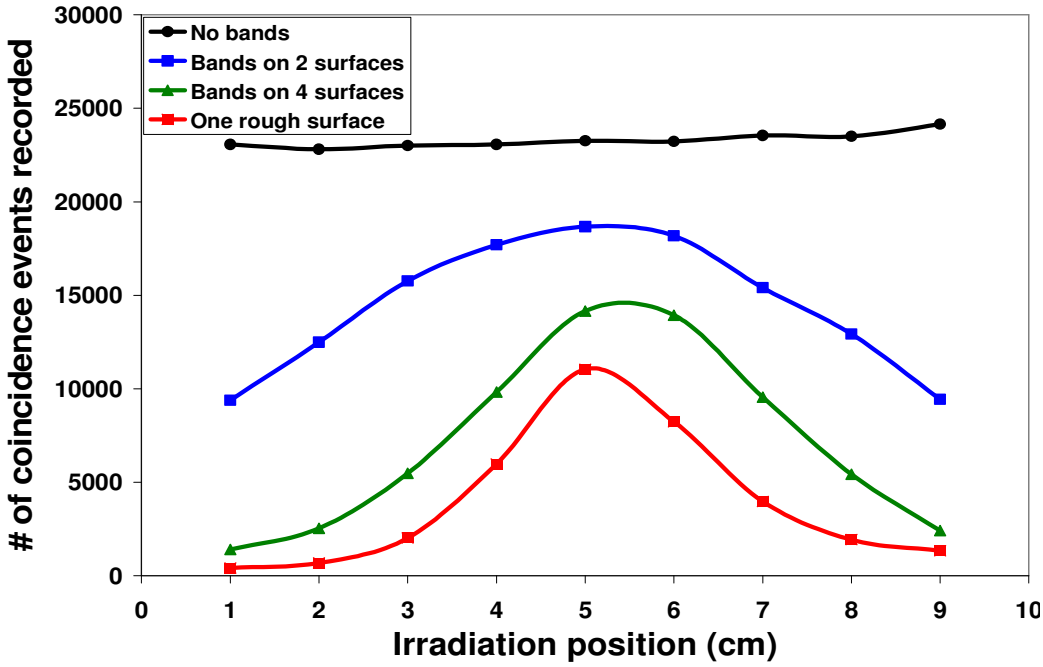

Figure 6.5 The number of coincidence events at each irradiation position recorded for different etching bands and surface treatment for a 3x2x100 mm^3 crystal.

This is because events close to the end of the crystal are unlikely to result in sufficient light collection in the distant PMT to produce a signal above the threshold of the CFD. This effect can be better understood by examining the position dependent energy spectra shown in figure 6.6. As the number of etched surfaces increases, there is a sharp drop in the amplitude of the photopeak in the distant PMT, resulting in a drop in the number of events that generate a valid signal above threshold in both PMTs. In contrast, at the center of the crystal (5 cm location) the light is shared equally between the two PMTs and thus is more likely to results in a coincidence event. It can be seen in figure 6.6 that the Compton continuum is highly attenuated for the 1 and 9 cm irradiation positions for the case of two etched surfaces and is not visible at all for the 1 and 9 cm irradiation

positions for the case of four etched surfaces. This demonstrates that the loss of coincidence events preferentially affects the lower energy Compton scatter events while largely preserving the number of photopeak events for the case of up to two etched surfaces. Similar results (not shown) were obtained for $2 \times 2 \times 100$ mm^3 crystals.

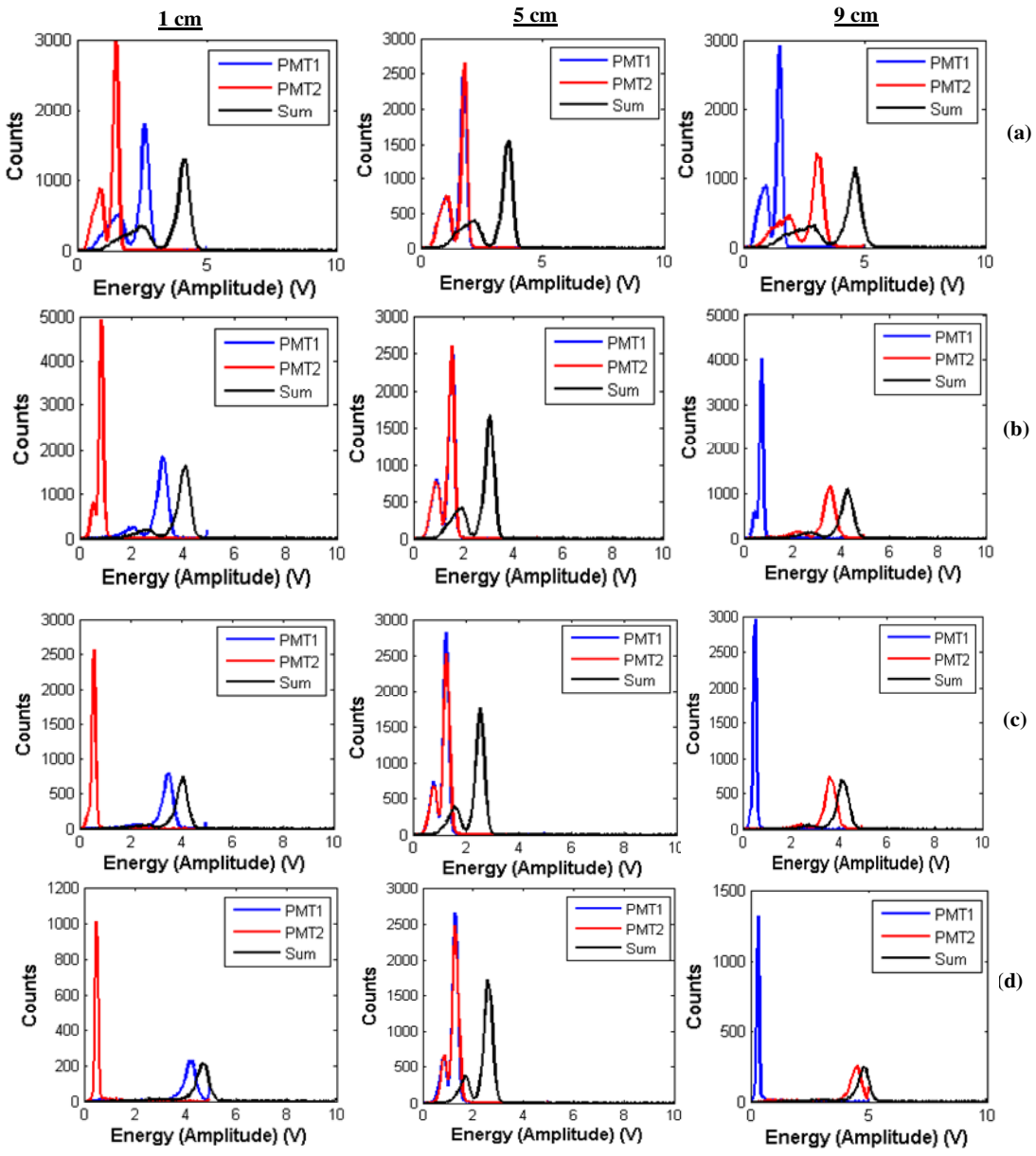

Figure 6.6 Individual PMT1, PMT2 and sum PMT1+PMT2 spectra at 1, 5 and 9 cm position for different surface treatment (a) no etching bands (b) bands on one surface (c) bands on two surfaces and (d) bands on four surfaces, corresponding to the coincidence events behavior shown in figure 6.5.

6.4.1.2 Effect of different etching bands on spatial resolution, light output and energy resolution

The ratio of two PMT signals PMT2/(PMT1+PMT2) at nine different irradiation positions of the crystal was histogramed to see the distribution of ratio signal at each irradiation position. The distribution of the ratio of two PMT signals at nine irradiation positions for different ground band patterns and surface treatment and their corresponding mean ratio signals plotted vs. irradiation position are shown in figure 6.7. The error bars show the FWHM of each ratio profile and the solid line in blue is a third degree polynomial fitting to the data shown in solid circles in each plot of right panel of the figure. For the case of the crystal with smooth sides (Figure 6.7(a)), the ratio profiles show significant overlap, resulting in poor spatial resolution. As shown in figure 6.8, the spatial resolution for this case ranges from 5.2 mm at the ends of the crystal to 12.8 mm at the centre, with an average of 9.1 mm over the 9 positions. The spatial resolution in this case is symmetric about the central position and is a parabolic function of position. The corresponding ratio-position plot shows an increasing slope at the end positions of the crystal. In comparison, for even one etched surface, the ratio profiles of figure 6.7(b) show significantly less overlap, resulting in an improved spatial resolution by a factor of more than 2, with values that range from 3.7 mm at the ends to 6.4 mm in the middle of the crystal (Figure 6.8), with an average of 5.6 mm. The corresponding ratio vs. position plot is linear. The cases of 2 and 4 etched surfaces, shown in figures 6.7(c) and 6.7(d), were very similar to each other, with a mean spatial resolution of 4.7 and 4.2 mm, respectively, with decreasing slopes of ratio-position plots at the end of the crystal.

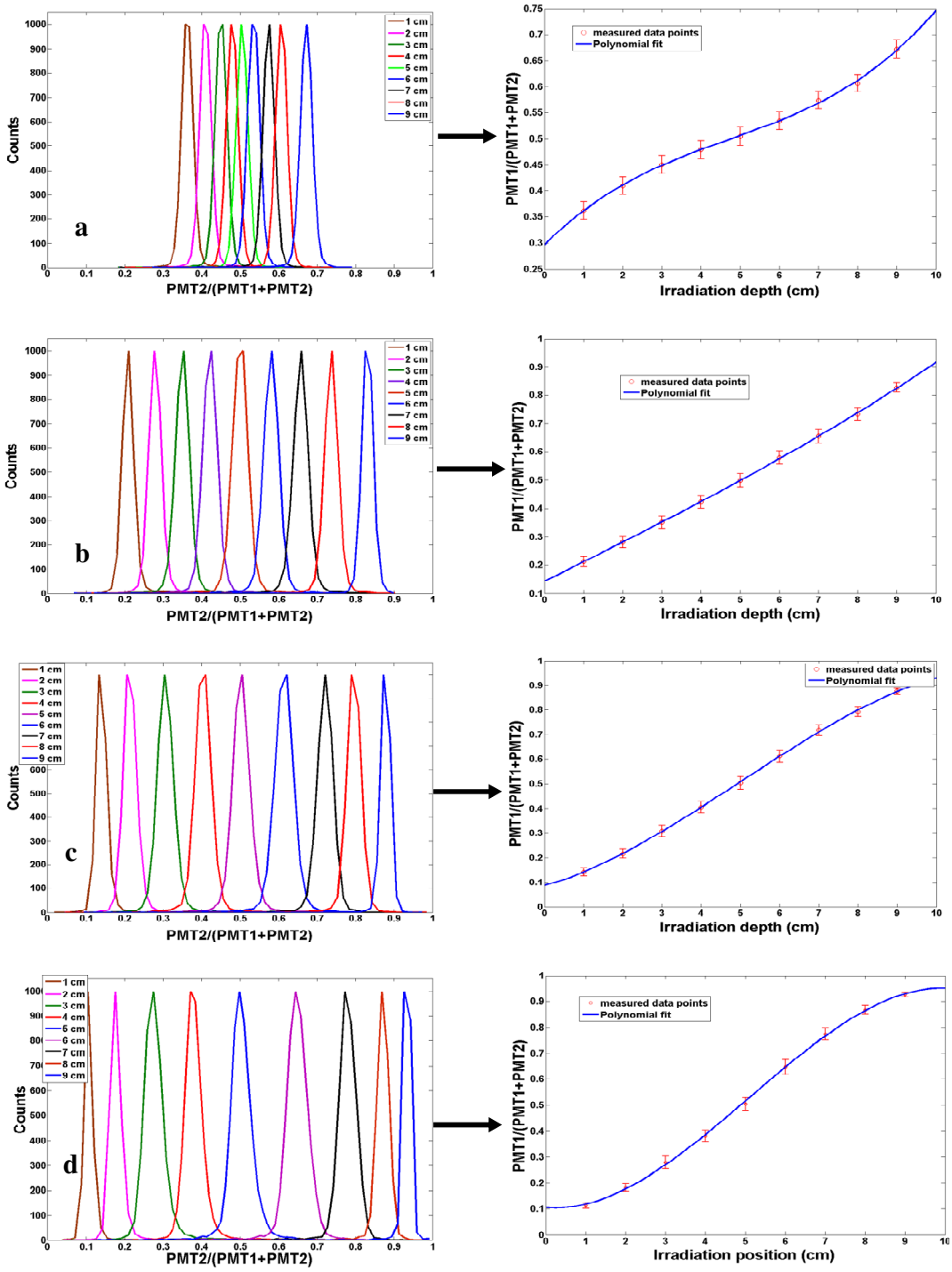

Figure 6.7 Left panel: The distribution of the ratio of two PMT signals at each irradiation position for different surface treatments: (a) no etching bands (b) etching bands on one long surface (c) etching bands on two long surfaces (d) etching bands on four long surfaces. Right panel: mean ratio signals plotted vs. irradiation position corresponding to the cases in (a), (b), (c) and (d), respectively.

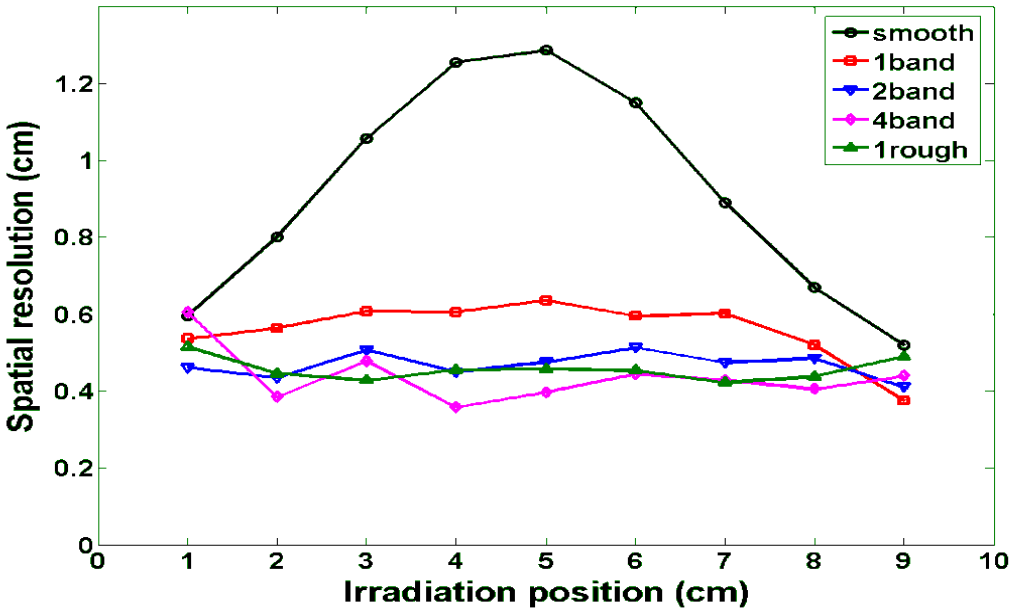

Figure 6.8 Spatial resolution in the light sharing direction of Teflon wrapped 3 × 2 × 100 mm^3 long LYSO crystal as a function of position for different ground bands and surface treatment

More importantly, the spatial resolution is nearly constant across the length of the crystal as shown in figure 6.8. The ratio position plot for the case of one rough surface (not shown) was very similar to the case of 4 banded surfaces.

Figure 6.9 shows the 511 keV photopeak position of the crystal with different etching band patterns and surface treatment plotted as a function of irradiation position. As expected, with etching applied to an increasing number of surfaces there was a corresponding drop in light collection, as shown in figure 6.9. The case of one rough surface showed considerably worse light collection than even the case of 4 banded surfaces. This drop in light collection efficiency resulted in a degradation in the energy resolution from 11.1 % for the smooth crystal to 13.6% for the crystal with bands on 4 sides. The results for each case, including energy resolution and measured and true spatial resolution, are summarized in Table 6.3.

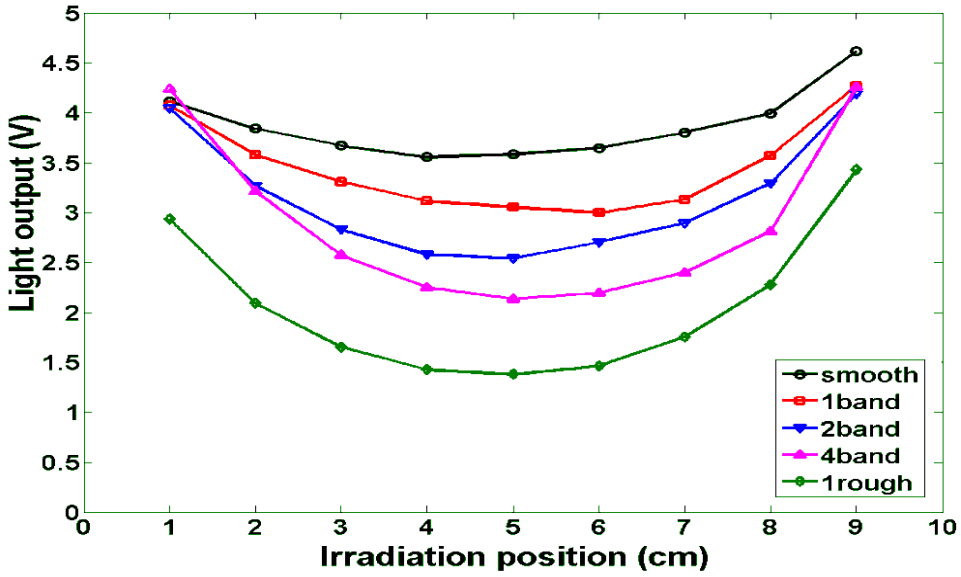

Figure 6.9 Light output as a function of irradiation position for different etching band patterns and surface treatment of 3 × 2 × 100 mm^3 crystals wrapped in Teflon.

While the case of one rough surface of the crystal gave peak separation results comparable to those obtained for the case of etching band patterns in two long surfaces, with an average spatial resolution of 4.6 mm, the light output was greatly decreased as shown in figure 6.9, resulting in an energy resolution of 15%.

Table 6.3 Energy resolution, measured spatial resolution and true spatial resolution for different surface treatment averaged over nine irradiation positions of the 3 × 2 × 100 mm^3 crystal

Surface treatment	Energy resolution (%)	Measured spatial resolution R_{meas} (mm)	True spatial resolution R_{true} (mm)
No etching bands	11.1	9.1	8.7
Bands on one surface	12.0	5.6	5.0
One surface rough	15.1	4.6	3.8
Bands on two surfaces	13.5	4.7	3.9
Bands on four surfaces	13.6	4.2	3.4
Interleaving bands on two opposite surfaces	12.2	4.2	3.4

When the spatial resolution is corrected for the 2.5 mm width of the 511 keV beam, a best average resolution of 3.4 mm is obtained for the crystal etched on four sides and represents an approximately 3-fold improvement as compared with the resolution of the

smooth crystal. The same resolution of 3.4 mm was obtained when interleaving bands were created on only two opposite surfaces of the crystal with a better energy resolution of 12.2% and more uniform distribution of coincidence events in the crystal. A 2 × 2 × 100 mm^3 LYSO crystal with coinciding etching bands on two opposite surfaces also gave similar results of 3.4 mm for spatial resolution.

6.4.2 DETECT2000 Simulation Results

6.4.2.1 Effect of different etching bands on spatial resolution, light output and energy resolution

Figure 6.10 illustrates a comparison of (i) measurement and (ii) DETECT2000 simulation results obtained for the distribution of the ratio of two PMT signals at each irradiation position for the different ground band patterns. In both the measurement and simulation results, the dynamic ranges of the ratio and the individual peak separation are comparable. The spatial resolution results calculated from the DETECT2000 results are plotted in figure 6.11. There is an excellent agreement between the simulation results seen in figure 6.11 and the measurement results shown in figure 6.8 for all the cases of etching band patterns. For the smooth crystal, the simulation results gave a uniform spatial resolution over the entire length of the crystal while the measured data showed a parabolic dependence of spatial resolution on position.

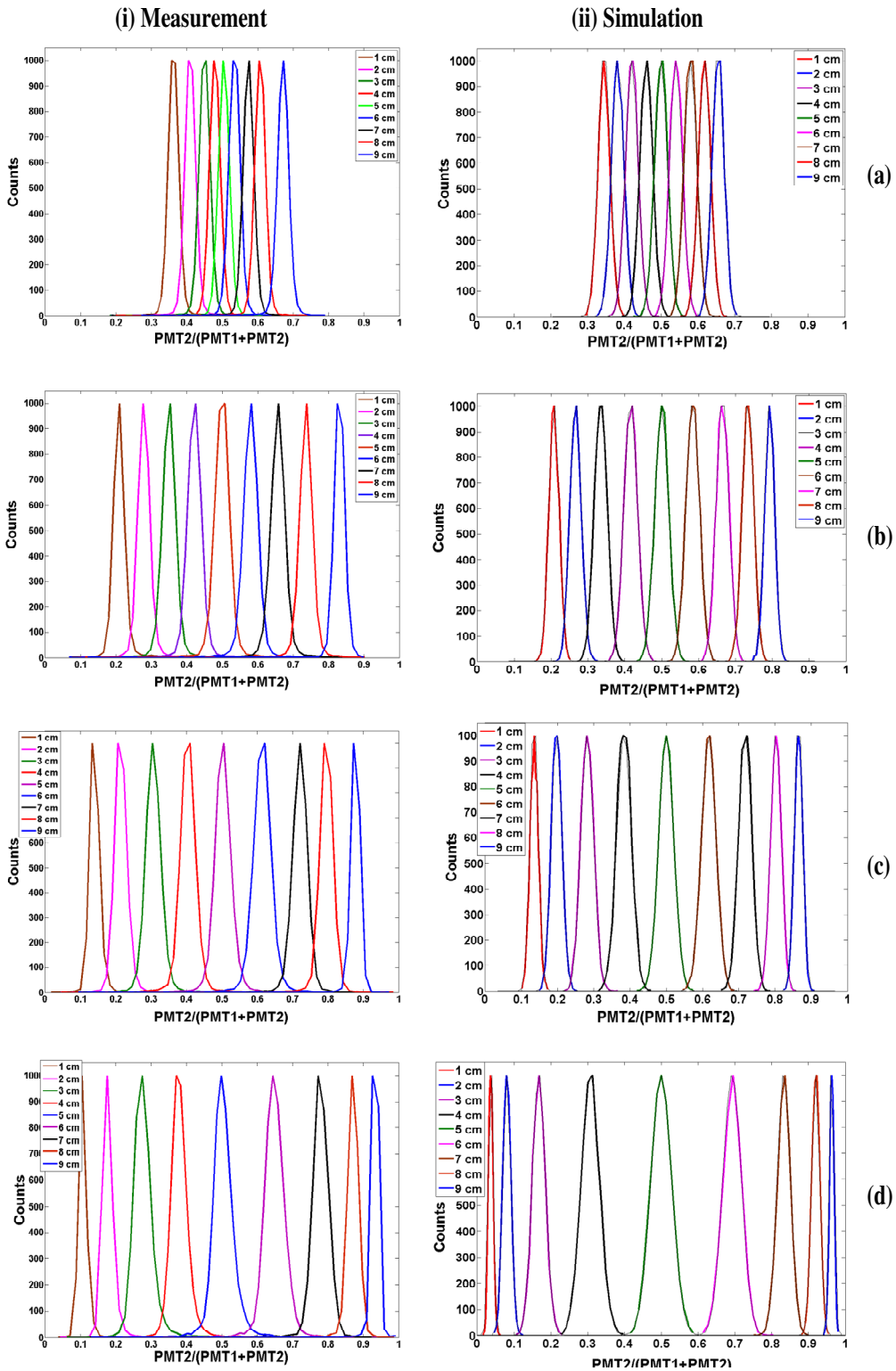

Figure 6.10 Comparison of (i) measurement (left panel) and (ii) DETECT2000 simulation (right panel) results for the distribution of the ratio of two PMT signals at each irradiation position for different surface treatment (a) smooth crystal. (b) one band (c) two bands and (d) four bands.

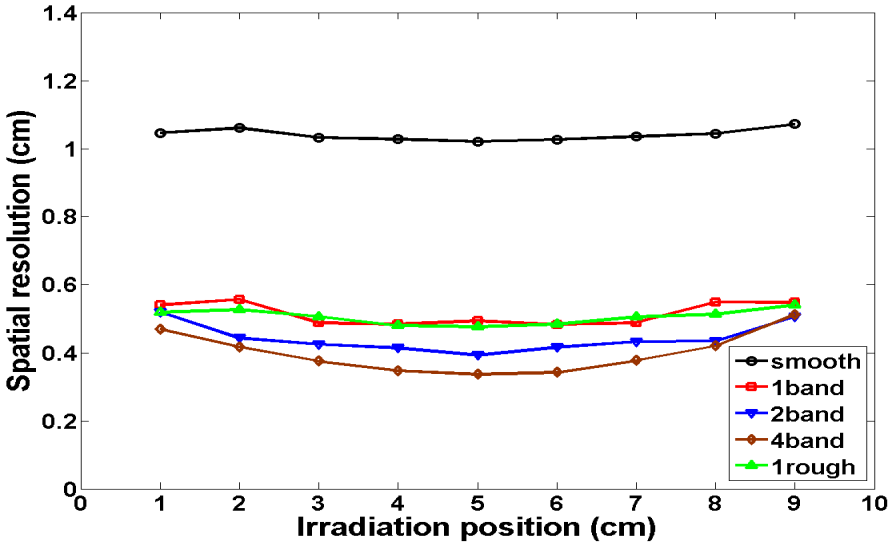

Figure 6.11 Spatial resolution in the light sharing direction of a Teflon wrapped 3 × 2 × 100 mm^3 long LYSO crystal as a function of position for different ground bands and surface treatment obtained from DETECT2000 simulation.

Despite these differences, the average spatial resolutions for the simulated and measured data are comparable in this case, as shown in Table 6.4.

Table 6.4 Energy resolution, measured spatial resolution and actual spatial resolution for different surface treatment averaged over nine irradiation positions of the 3 × 2 × 100 mm^3 crystal – a comparison of measurement and simulation results

Surface treatment	Energy resolution (%)		Spatial resolution (mm)	
	Measurement	Simulation	Measurement	Simulation
No etching bands	11.1	7.8	9.1	10.4
Bands on one surface	12.0	8.2	5.6	5.5
Bands on two surfaces	13.5	8.7	4.7	4.7
Bands on four surfaces	13.6	10.3	4.2	4.1

Despite widely varying the parameters of the DETECT2000 simulation we were not able to recreate the parabolic shape of the measured spatial resolution data for the smooth

Teflon wrapped $3 \times 2 \times 100$ mm^3 crystal. Similar behavior (not shown) was observed for the case of a $2 \times 2 \times 100$ mm^3 smooth LYSO crystal wrapped in a glued-coupled ESR reflector, where the average simulated spatial resolution of 7.13 mm agreed very well with the measured average value of 7.16 mm.

The photopeak position for different etching band patterns and surface treatments obtained from DETECT2000 simulation are plotted as a function of irradiation position in figure 6.12. As described in section 6.4.1.2, with etching applied to an increasing number of surfaces there was a corresponding drop in light collection. The results of energy resolution and spatial resolution averaged over the nine irradiation positions for different etching band patterns and surface treatment of $3 \times 2 \times 100$ mm^3 crystals obtained from measurement and simulation are summarized together in Table 6.4. Simulation results showed that the spatial resolution improved from an average of 10.4 mm with no surface treatment to 5.5, 4.7 or 4.1 mm for banding patterns on 1, 2 or 4 surfaces, respectively. The results showed an excellent agreement in the spatial resolution for the measured and simulated results for all etching band patterns. The energy resolution obtained from the simulation results is consistently better than the measured energy resolution; however this appears to have minimal impact in the spatial resolution results. We would expect the better energy resolution from the simulation than the measurement because we did not vary the number of optical photons created for each event at each interaction position on the long axis of the crystal i.e. the full energy events corresponding to 511 keV are considered in simulation. The simulation results (not shown here) for a $2 \times 2 \times 100$ mm^3 crystal with smooth surfaces and etching band patterns also showed an excellent agreement with the corresponding measurement results.

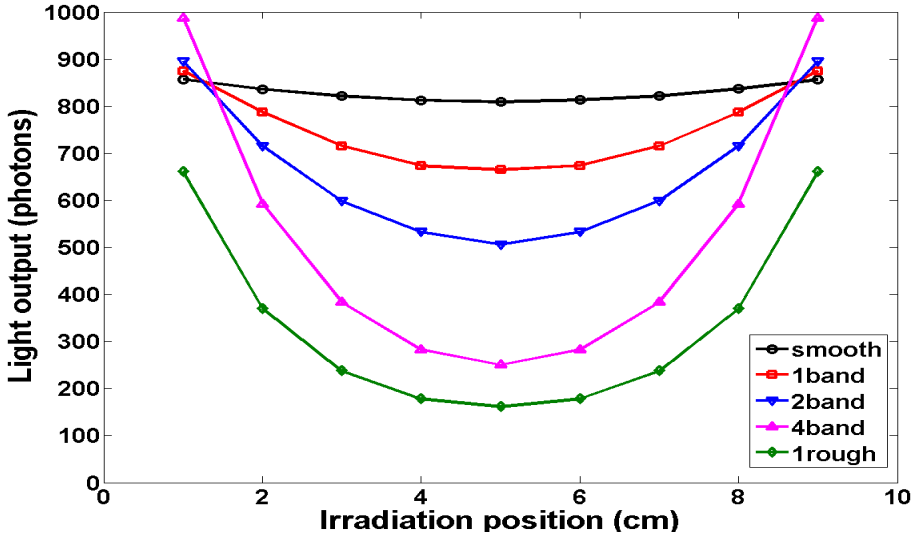

Figure 6.12 Light output as a function of irradiation position for different etching band patterns and surface treatment of 3 × 2 × 100 mm^3 crystals wrapped in Teflon obtained from DETECT2000 simulation.

6.4.2.2 Effect of etc hing band size on spatial resolution, light output and energy resolution

Figure 6.13(a) shows the ratio distribution peaks at nine irradiation positions of a 3 × 2 × 100 mm^3 crystal with etching bands on its two opposite surfaces when the etching band size was 0.6 mm, 1 mm, 2 mm and 3 mm. Clearly the peak separation is increasing with increase of band size resulting in improvement in the corresponding spatial resolution for 0.6, 1and 2 mm band size, as shown in figure. 6.13(b), due to the light loss with the increase in the band width as shown in figure 6.13(c).

Table 6.5 also shows the effect of band size on the energy and spatial resolution of a 3 × 2 × 100 mm^3 LYSO crystal detector when the etching bands with band size ranging from 0.6 – 3 mm were created on its one, two and four long surfaces in simulation studies. In all the cases of etching bands, the spatial resolution improves as the band size is increased above 0.6 mm but begins to degrade for the larger band sizes.

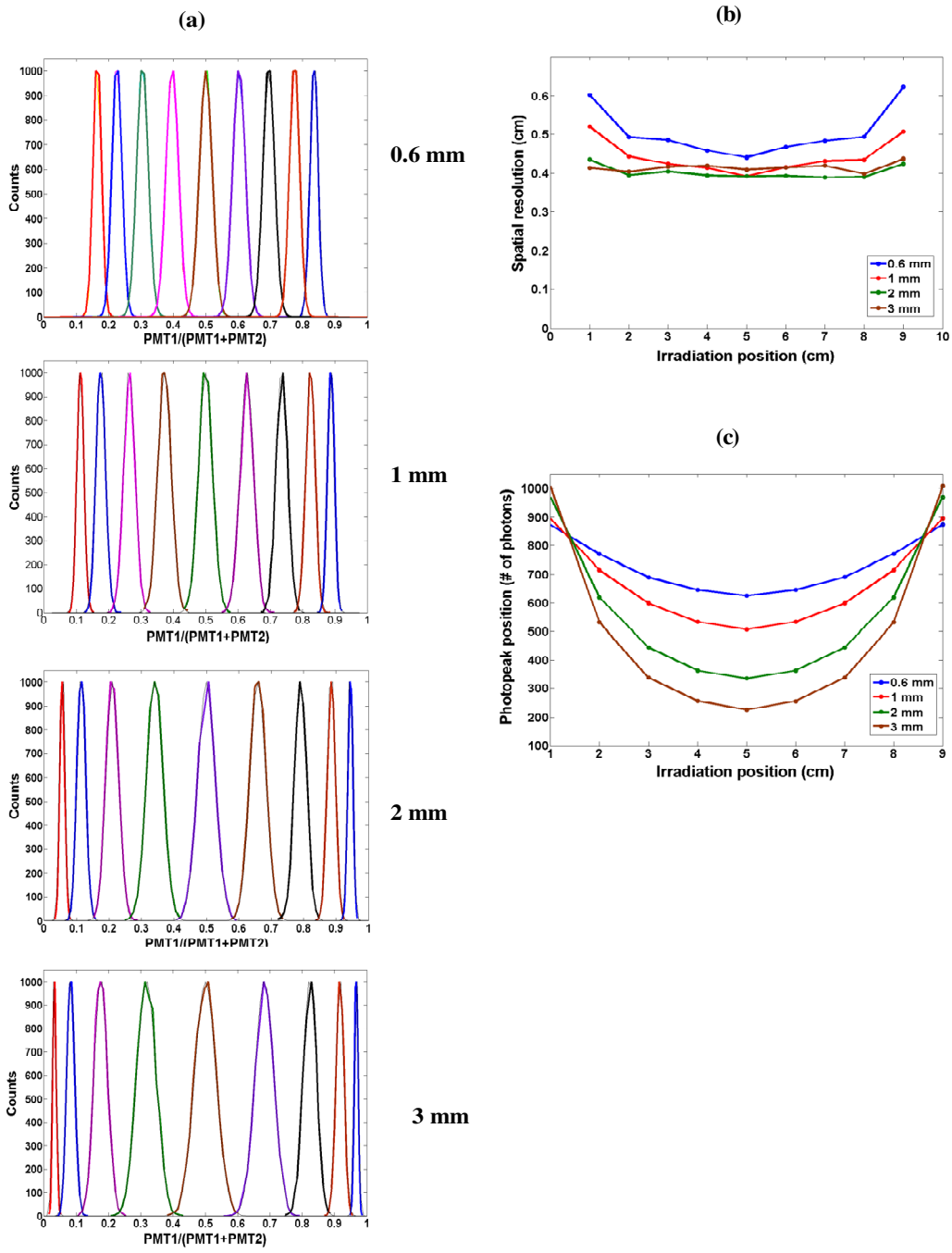

Figure 6.13 (a) Ratio distribution peaks at nine irradiation positions of a $3 \times 2 \times 100$ mm^3 crystal with etching bands on two opposite surfaces for the etching band size of 0.6 mm, 1 mm, 2 mm and 3 mm (b) corresponding spatial resolution vs. position for 0.6, 1, 2 and 3 mm band size and (c) Light output vs. irradiation position for 0.6, 1, 2 and 3 mm band size.

For all band sizes the energy resolution degrades slightly with the increase in band width as expected due to the increased light loss with the increase of band width. For

example, in the case of two banded surfaces, the spatial resolution improves from 5.0 mm for 0.6 mm band size to 4.0 mm for a band size of 2 mm, with corresponding energy degradation from 8.4 % to 10.1 %. With a further increase in the band size to 3 mm for this case, the spatial resolution starts deteriorating as shown in the table and figure 6.13(b). For the four-side banded crystal, the spatial resolution starts deteriorating even for the 2 mm band size. These data suggest that the optimum band size is in the 1-2 mm range.

Table 6.5 Effect of band size on the energy and spatial resolution of a 3 × 2 × 100 mm^3 LYSO crystal when the etching bands were created on its one, two and four long surfaces using DETECT2000 simulation program.

Band size (mm)	Energy resolution (%)			Spatial resolution (mm)		
	1 band	2 bands	4 bands	One band	Two bands	Four bands
0.6	7.9	8.4	9.6	6.2	5.0	4.1
0.8	8.2	8.7	10.3	5.6	4.7	4.1
1	8.3	8.9	10.9	5.2	4.4	3.9
2	9.0	10.1	14.9	4.6	4.0	4.5
3	9.8	11.5	20.3	4.4	4.1	5.8

6.5 Discussion and conclusions

In this work we explored the effects of modulating the light transport in initially polished 3 × 2 × 100 mm^3 and 2 × 2 × 100 mm^3 LYSO crystals, readout at either end by PSPMTs, by creating etched band patterns on one to four of their long surfaces. The spatial resolution improved from an average of 9.1 mm with no surface treatment to 5.6, 4.7 or 4.2 mm for banding patterns on 1, 2 or 4 surfaces, respectively. As expected, the

total light collected decreased with increasing number of roughed surfaces, resulting in a decrease in the energy resolution from 11.1% FWHM for the untreated crystal to 12.0%, 13.5%, and 13.6% for the patterns on 1, 2, and 4 surfaces, respectively. When the spatial resolution is corrected for the beam width, we estimate the resolution for the case of 4 banded surfaces to be 3.4 mm FWHM. The same spatial resolution of 3.4 mm was obtained when interleaving bands were created on only two opposite surfaces with a better energy resolution of 12.2% suggesting that the interleaving bands are more effective in modulating the light transport, resulting in an improved resolution. An advantage of the interleaved banding pattern is that there is better uniformity of event rates across the length of the crystal as compared to the banding pattern on all four long surfaces, which gave relatively few events above trigger threshold at the ends of the crystal. For this reason, it is unlikely that a banding pattern on all four sides would be used in practice. A $2 \times 2 \times 100$ mm^3 LYSO crystal with coinciding etching bands on two opposite surfaces also gave similar results for spatial and energy resolutions, showing that the improvements in spatial resolution can be realized for a range of crystal sizes.

We expect that using the banding pattern for our detector modules will not compromise the sensitivity of the detector, since the loss of events due to decrease light collection primarily affects lower energy events in the Compton continuum. In addition, etching the banding pattern on two sides of a $2 \times 2 \times 100$ mm^3 LYSO crystal resulted in a loss in mass of 0.02 g for the 2.85 g crystal, suggesting that there will not be significant loss in sensitivity due to loss of volume of scintillator material.

As the beam location is always centered at the etched bands on the crystal in our measurement and simulation, we did a simulation at one location by centering the beam

at 1.25 cm from the edge to see if there is any change in the intensity of light. We obtain the ratio distribution peak at this location having the similar shape and width as we obtain before at 1 cm centered at the etched band.

There is excellent agreement between the measurement and DETECT2000 Monte Carlo simulation results obtained for different etching band patterns. By validating this simulation against our measured results we will be able to use this simulation to predict the performance of a complete detector module design and optimize both the spacing and size of the etched pattern on the crystals. This is a process best suited for simulation due to the high cost of the scintillator crystals used in this work.

The promising improvement in spatial resolution observed both in measurement and Monte Carlo simulation of this study fulfils the design criteria of our proposed compact preclinical PET system based on axially-oriented dual-ended readout detectors. In future, we will investigate approaches of irregular spacing of the bands along the length of the crystal, with the aim of constructing a complete detector module for use in our proposed compact preclinical PET system.

References

Anfré, P, Dujardin, C, Jean-Marie Fourmigué, J-M, Hautefeuille, B, Lebbou, K, Pédrini, C, Perrodin, D, and Tillement, O 2007 Evaluation of Fiber-Shaped LYSO for Double Readout Gamma Photon Detection *IEEE Trans. Nucl. Sci.* **54** 391-7

Bircher C and Shao Y 2012 Use of internal scintillator radioactivity to calibrate DOI function of a PET detector with a dual-ended-scintillator readout *Med. Phys.* 39 (2) 777-787

Braem A *et al.* 2009 AX PET: A novel PET detector concept with full 3D reconstruction *Nucl. Instr. Meth.* A **610** 192-5

Burr K C and Ivan A 2004 Evaluation of a prototype small-animal PET detector with depth-of-interaction encoding *IEEE Trans. Nucl. Sci.* **51** 1791-98

Cayouette, F, Moisan, C, and Thomson, C, J 2002 Monte-Carlo modeling of scintillator crystal performance for stratified PET detectors with DETECT2000 *IEEE Trans. Nucl. Sci. Conf. Rec.* 1997-2001

Dokhale P A, Silverman R W, Shah K S, Grazioso R, Farrell R, Glodo J, McClish M A, Entine G, Tran V H, and Cherry S R 2004 Performance measurements of a depth-encoding PET detector module based on position-sensitive avalanche photodiode read-out *Phys. Med. Biol.* **49** 2004 4293-4304

Moisan, C, Cayouette, F, and McDonald, G 2000 DETECT2000, The Object Oriented C++ Language Version of DETECT, A Program for Modeling Optical Properties of Scientillators, Quebec City, QU, Canada: Lavel University, Version 5.0.

Moses W W and Derenzo S E 1994 Design studies for a PET detector module using a PIN photodiode to measure depth of interaction *IEEE Trans. Nucl. Sci.* **41** 1441-45

Peng, H, Olcott, P, D, Spanoudaki, V., and Levin, C., S., 2011 Investigation of a clinical PET detector module design that employs larger-area avalanche photodetectors *Phys. Med. Biol*. **56** 3603-27

Saha, L, Saitoh, K and Kobayashi, S 2004 Study of DOI resolution and imaging resolution of a PET device *Nucl. Instr. Meth.* A **527** 27-34

Samuel S, Daniel H, and David B 2002 Design of a high performances small animal PET system with axial oriented crystals and DOI capability *IEEE Trans. Nucl. Sci.* **49** 17-23

Seguinot J *et al.* 2006 Novel geometrical concept of high performance brain PET scanner-principle, design and performance estimates *CERN PH-EP/2004-050 II Nuovo Cimento* **29C** 429-63

Shao Y, Yao R and Ma T 2008 A novel method to calibrate DOI function of a PET detector with a dual-ended-scintillator readout *Med. Phys.* **35** 5829-40

Shao Y, Meadors K, Silverman R W, Farrell R, Cirignano L, Grazioso R, Shah K S, and Cherry S R 2002 Dual APD array readout of LSO crystals: Optimization of crystal surface treatment *IEEE Trans. Nucl. Sci.* **49** 649-54

Shimizu K, Ohmura T, Watanabe M, Uchida H and Yamashita T 1988 Development of 3-D Detector System for Positron CT *IEEE Trans. Nucl. Sci.* **35** 717-720

Steinbach, C., O., Szlavecz, A., Benyo, B., Bukki, T., and Lorincz, E. 2010 Validation of Dtect2000-Based PetDetSim by Simulated and Measured Light Output of Scintillator Crystal Pins for PET Detectors *IEEE Trans. Nucl. Sci.* **47** 2460-2467

Tsung, G., Moisan, C., and Rogers, J., G. A Simulation to Model Positron Encoding Multicrystal PET Detectors *IEEE Trans. Nucl. Sci.* **42** NO. 6 2236-2243

Ur-Rehman F, McIntosh B and Goertzen A L 2011 Observations on dual-ended readout of 100 mm long LYSO crystals *Nucl. Instr. Meth.* A **652** 275-279 doi: 10.1016/j.nima.2010.08.015

Ur-Rehman F, Tai Y-C and Goertzen A L 2012 Calibration of Dual-Ended Readout of Axially Oriented 100 mm Long LYSO Crystals for Use in a Compact PET System *IEEE Trans. Nucl. Sci.* **59** NO. 3 561-567.

Vilardi I *et al.* 2006 Optimization of the effective light attenuation length of YAP:Ce and LYSO:Ce crystals for a novel geometrical PET concept *Nucl. Instr. Meth* A **564** 506-14

Yang Y, Dokhale P A, Silverman R W, Shah K S, McClish M A, Farrell R, Entine G and Cherry S R 2006 Depth of interaction resolution measurements for a high resolution PET detector using position sensitive avalanche photodiodes *Phys. Med. Biol.* **51** 2131-42

Yang Y, Qi J, Wu Y, James S S, Farrell R, Dokhale P A, Shah K S and Cherry S R 2009 Depth of interaction calibration for PET detectors with dual-ended readout by PSAPDs *Phys. Med. Biol*. **54** 433-45

Yamashita T, Uchida H, Shimizu K and Omura T 1989 Scintillation detector for three-dimensionally measuring the gamma-ray absorption position and positron CT apparatus utilizing the scintillation detector *US Patent number*: 4823016

Zhang, L., Mao, R., and Zhu, R. 2007 Emission spectra of LSO and LYSO crystals excited by UV light, X-ray and γ-ray Proc. IEEE Nuclear Science Symposium, Conf. Rec. 4574-4580

Chapter 7 Discussion and conclusion

7.1 Discussion

On our road to the development of a highly compact and portable preclinical PET imaging system, we have optimized the light collection of our dual-ended readout axially-oriented detectors, based on 100 mm long LYSO crystals readout at both ends by PMTs, for spatial and energy resolution through use of (i) different reflector materials and (ii) surface treatment of the crystals. In the reflector studies, a spatial resolution of 7 mm was achieved for an ESR covered crystal. This spatial resolution was further improved to 3.4 mm (corrected for the beam width) with a corresponding energy resolution of 13.6% when systematic etching band patterns were created on four long surfaces of $3 \times 2 \times 100$ mm^3 LYSO crystals wrapped in Teflon tape through experimental studies on surface treatment and ground banding patterns. The same spatial resolution was obtained when interleaving bands were created on only two opposite surfaces with a better energy resolution of 12.2% suggesting that the interleaving bands are more effective in modulating light transport, resulting in an improved resolution in this case.

These experimental results were used to benchmark Monte Carlo simulations for our particular detector geometry performed with the program DETECT2000 for optical photon transport within the crystals. We were then able to use the benchmarked DETECT2000 software for predicting the performance of banding patterns that were not investigated experimentally. By benchmarking this simulation against our measured results we are now able to use this simulation to predict the performance of a complete detector module design and optimize both the spacing and size of the etched patterns on

the crystals, as this is a process best suited for simulation due to the high cost of the crystals used in this extensive work.

The promising improvement in spatial resolution in the light-sharing direction observed both in the experiments and Monte Carlo simulations fulfils the design criteria of our proposed compact preclinical PET system based on axially-oriented dual-ended readout detectors. The approach of orienting the crystals in the axial direction in this design reduces the overall radial extent of the detector ring and associated electronics and, hence, can fit into a bio-safety cabinet for preclinical studies or alternatively on a lab bench top for research activities. This orientation of the crystals also removes the parallax error or resolution degradation, found in PET with radially oriented crystals, and increases the sensitivity of the system by using large crystals thereby making the spatial resolution and sensitivity inherently independent from each other.

Our experimental results showed that the coinciding etching band patterns created on only two opposite surfaces of a $2 \times 2 \times 100$ mm^3 Teflon-wrapped LYSO crystal, compared to the bands created on four long surfaces of a $3 \times 2 \times 100$ mm^3 crystal, resulted in a corrected spatial resolution of 3.4 mm. Therefore further investigation on the size and spacing of bands for further improving the spatial resolution will be carried out on $2 \times 2 \times 100$ mm^3 LYSO crystals by creating bands on only two opposite surfaces, with the goal of using this dimension of crystal in the construction of a complete detector module for use in our proposed compact preclinical PET imaging system.

In our light collection optimization work through use of different reflector materials, a spatial resolution of about 7 mm was achieved for an ESR covered $2 \times 2 \times 100$ mm^3 smooth-crystal. Therefore with an ESR-coupled $2 \times 2 \times 100$ mm^3 banded-crystal in a

future experimental study, we expect a further improvement in the spatial resolution achieved in the case of a Teflon-wrapped banded-crystal after optimization of both the band spacing and size through simulation and subsequently validated in experiment. Although we have used the "Metal" model of DETECT2000 to simulate a specular reflector such as ESR optically coupled to smooth surfaces of a $2 \times 2 \times 100$ mm^3 LYSO crystal, DETECT2000 can not model a specular reflector (ESR) optically coupled to rough or ground crystal surfaces. Therefore the optimized crystal banding patterns for spacing and size to achieve the best possible resolution of a Teflon-wrapped crystal through simulation could then be coupled to an ESR reflector for an experiment to see if the resolution could further be improved as we are expecting.

In the calibration part of our project, we have calibrated our dual-ended readout of axially-oriented 100 mm long LYSO crystals for use in the compact PET system using collimated irradiation and uniform flood-irradiation methods. The robustness of the uniform irradiation method was examined for a variety of source configurations including point source, line source and intrinsic radioactivity of LYSO in addition to examining its utility and limitations in the presence of unbalanced detectors. The calibration for each configuration was carried out to establish an accurate relationship between the ratio of two PMT signals and the axial position of interaction that could then be used for encoding the axial position of interactions of individual detected annihilation events based on the ratio of their two PMT signals during PET imaging. An excellent agreement was found between the two methods for the balanced detectors. For the case of unbalanced detectors, the agreement between the two methods is only achieved if the trigger threshold energies of the two PMTs were adjusted to give similar single-event

rates in both PMTs during uniform flood irradiation. Implementation of this method will significantly simplify the calibration of our dual-ended readout detector modules, especially for the cases of a large number of crystals in a 2D crystal array in a detector of our proposed complete scanner with a line source or overnight using the intrinsic LYSO radioactivity.

7.2 Future directions

This section describes where the project work will be going in future. In this regard, a few directions and guidelines based on the work done in this project are proposed. These include the optimization of inter-band spacing as well as the corresponding band size for further improvement in axial spatial resolution, timing properties of dual-ended readout axial detector for possible TOF-PET applications with DOI information, and construction of two detector modules based on the results of single crystals, as described in the following sections.

7.2.1 Optimizing inter-band spacing and related band size

After benchmarking the DETECT2000 Monte Carlo simulations for our particular detector geometry against our experimental results we are now able to predict the performance of banding patterns on the crystals that were not investigated experimentally. Therefore, in the future, this work could be extended to optimize both the spacing and size of banding patterns created in the same axial locations (coinciding bands) and with the locations interleaved (interleaving bands) on only two opposite surfaces of $2 \times 2 \times 100$ mm^3 LYSO crystals, with the goal of further improving spatial resolution in the axial direction. An axial spatial resolution of better than 3 mm is

expected in this work. After refining the detector design with the benchmarked DETECT2000 simulation, one would subsequently be able to predict the performance of a complete detector module before the actual module is constructed.

7.2.1.1 Coinciding etching band patterns

To optimize the inter-band spacing for the bands created in the same axial locations on the top and bottom surfaces of 2 × 2 × 100 mm^3 LYSO crystals, the following three configurations, also shown in figure 7.1, are proposed:

- Etching bands from 1 cm through 9 cm with 1 cm band spacing (Figure 7.1(b))
- Etching bands from 2 cm through 8 cm with 2 cm band spacing (Figure 7.1(c))
- Etching bands from 2 cm through 8 cm with 3 cm spacing (Figure 7.1(d))

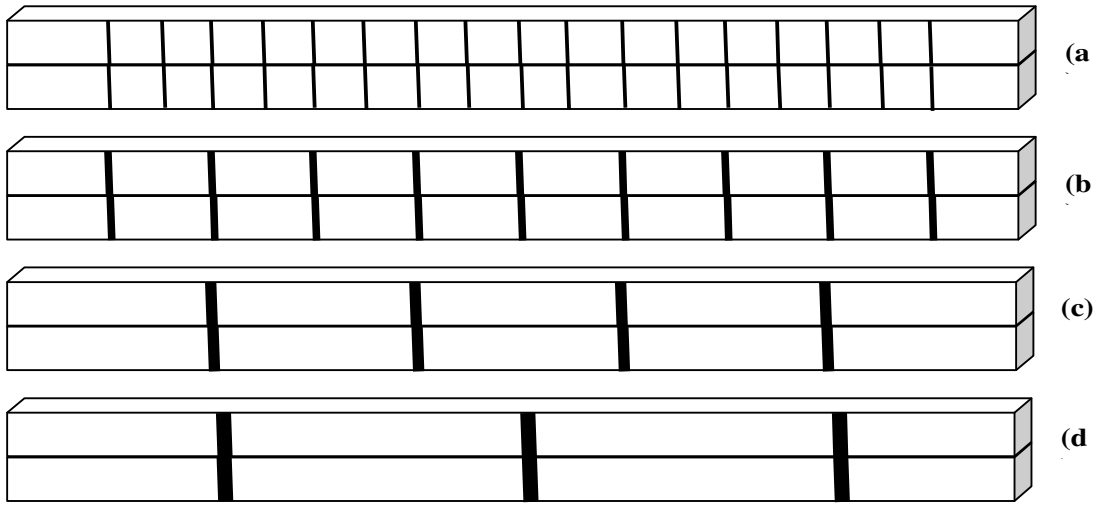

Figure 7.1 Schematic of coinciding etching band patterns on top and bottom surfaces of a 2 × 2 × 100 mm^3 crystal with varying band spacing and band width (a) etching bands from 1 cm through 9 cm with 0.5 cm band spacing (b) etching bands from 1 cm through 9 cm with 1 cm band spacing (c) etching bands from 2 cm through 8 cm with 2 cm band spacing and (d) etching bands from 2 cm through 8 cm with 3 cm band spacing

The bands should be symmetric about the central position (5 cm) of the crystal in all the above mentioned configurations of etching bands. The band sizes of 0.6, 0.8, 1, 2 and

3 mm could be simulated for each of the above cases to see their effects on energy and spatial resolutions and hence determine the optimized band size and spacing for the best possible spatial resolution in this study. The simulations would be carried out using the procedure described in section 3.3.2.

7.2.1.2 Interleaving bands

To optimize the inter-band spacing for the etching band patterns with the band locations interleaved created on the top and bottom surfaces of 2 × 2 × 100 mm^3 LYSO crystals, the following three configurations, also shown in Figure 7.2, are proposed:

- Etching bands from 1 cm through 9 cm with 1 cm band spacing (Figure 7.2(b))
- Etching bands from 2 cm through 8 cm with 2 cm band spacing (Figure7.2(c))
- Etching bands from 2 cm through 8 cm with 3 cm spacing (Figure 7.2(d))

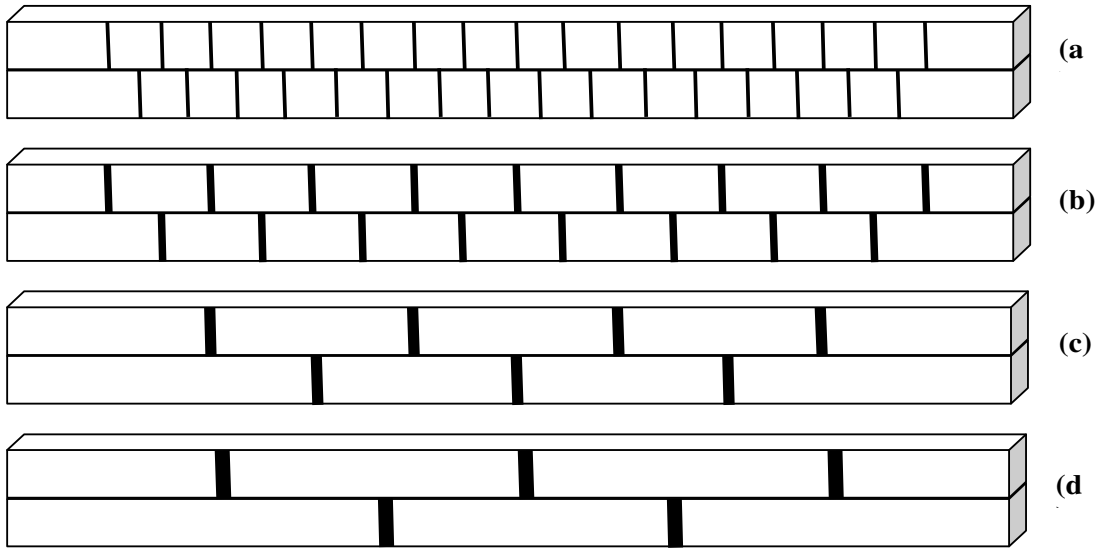

Figure 7.2 Schematic interleaved etching band patterns on top and bottom surfaces of a 2 × 2 × 100 mm^3 crystal with varying band spacing and band width (a) etching bands from 1 cm through 9 cm with 0.5 cm band spacing (b) etching bands from 1 cm through 9 cm with 1 cm band spacing (c) etching bands from 2 cm through 8 cm with 2 cm band spacing and (d) etching bands from 2 cm through 8 cm with 3 cm band spacing

The bands would be symmetric about the central position (5 cm) of the crystal in each configuration. Again, the band sizes of 0.6, 0.8, 1, 2 and 3 mm could be simulated for each of the above cases to see their effects on energy and spatial resolutions and hence optimize the band size and spacing for the best possible spatial resolution. The simulations would be carried out using the procedure described in section 3.3.2.

7.2.2 Timing resolution of long axial crystals

The timing resolution (or timing accuracy) ΔT of a TOF-PET scanner is measured as the FWHM of the response function of time difference in arrival of two annihilation photons detected in coincidence by two opposite detector crystals in the detector ring. This timing resolution is then used to determine position information of the annihilation event in TOF-PET. It depends on electronic timing circuits and scintillation crystals properties such as size and decay time constant. In scintillation crystals, annihilation photons travel at the speed of light (c) in a straight path while the optical photons travel with a reduced speed of c/n, where n is the refractive index of crystals. The optical photons travel in a straight path but are reflected many times in small cross-sectional area in scintillation crystals, resulting in a further reduction in the speed. This means that the propagation speed required for the overall timing resolution ΔT of a TOF-PET scanner becomes slower after the annihilation photons are converted into the optical photons at a particular depth-of-interaction (DOI) inside the crystals. DOI information can be used to examine this intrinsic timing error (contributing to the overall timing resolution) due to the difference in propagation speed of annihilation photons and optical photons inside the scintillation crystals. Therefore, there is an increasing interest to correct this timing walk as a function of interaction position (irradiation position) in the crystal through DOI

measurement in TOF-PET. This improves the timing accuracy (133), resulting in improved gain in sensitivity (or signal-to-noise ratio) of TOF-PET because of the fact that the relative gain in sensitivity is inversely proportional to the overall timing resolution of the scanner (134). Although the current TOF-PET systems have a timing resolution of around 300 ps which is not enough for the DOI to have a considerable effect (135), however, as the timing resolution significantly progresses to ~100 ps DOI information for timing walk correction becomes a prominent factor (77).

We have been working on balancing the axial resolution and energy resolution in the optimization of light collection work through use of different reflector materials and surface treatment or banding patterns. Now for the possible TOF-PET applications of dual-ended readout axial detectors based on fast and bright LYSO crystals, the problem of balancing axial resolution and timing resolution would be very interesting and could well be examined using methods similar to those described by Spanoudaki and Levin (135) where they investigated the temporal resolution limits of scintillation detection from pixilated elements through experiment and simulation. The benchmarked DETECT2000 model of our scintillation crystals with the roughed bands on them could be used for studying the timing properties of these detectors. This simulation could be used for examining the optical photon arrival time properties at the ends of the crystal. What timing pickoff approach will give the best timing signal could be modeled in simulation and then examined in experiment.

7.2.3 Design and construction of two axially encoded detector modules

Based on the results obtained from measurements and simulations with single crystals, two detector modules can be constructed, each consisting of an array of the 100

mm long LYSO crystals read out at both ends by PSPMTs. Preliminary designs can examine 10 × 5 arrays of crystals (about 20 × 10 mm^2 total) wrapped in the optimal reflector material and subjected to the optimal surface treatment and banding pattern determined. These arrays will be coupled to the PSPMTs at both ends. These detector modules will be evaluated by measuring their energy resolution and spatial resolution similar to the methods used for evaluating the properties of the single crystal detectors. To study the inter-crystal scatter (cross-talk) and its effect on resolution, an angular collimated beam of ^{22}Na could be used to irradiate the detector module. These results will be compared with those of normal incidence beam irradiation investigated before. The individual crystals in the detector module will be identified with flood histograms using crystal lookup table in these studies.

The two modules will be operated in coincidence mode for measuring their intrinsic spatial resolution and timing performance. For intrinsic spatial resolution, a ^{22}Na source will be placed midway between the modules and will be moved in steps perpendicularly to a line joining the two modules and coincidence events will be recorded. The FWHM of the response of coincidence events with source position (point spread function) will give the intrinsic spatial resolution of the detector modules. For the timing resolution measurement, the source will remain stationary between the modules operated in coincidence. The timing resolution will be measured as the FWHM of the response of coincidence events function of the two modules operated in coincidence. GATE simulations can be used at this stage to validate these results and predict the performance of a complete compact PET scanner based on the results achieved so far.

7.3 Conclusion

A promising improvement in spatial resolution in the light-sharing direction of axially-oriented dual-ended readout detectors based on 100 mm long LYSO crystals has been achieved through use of different reflector materials and surface treatment or banding patterns in this project. This fulfils the design criteria of our proposed compact preclinical PET system. Orienting the crystals in the axial direction in this design will enable the system to fit into a biosafety cabinet for preclinical studies or on a lab bench-top for research activities. This also removes the parallax error or resolution degradation and increases the sensitivity of the system by using large crystals. The benchmarked DETECT2000 simulation for our unique detector geometry against our experimental results can now be used to predict the performance of a complete detector module design and optimize both the spacing and size of the etched patterns on the crystals as well as for other PET applications. The implementation of flood irradiation method in our proposed PET will provide a simple axial-positioning calibration with a single measurement. The method will significantly simplify the calibration of these dual-ended readout detectors in a complete scanner with a line source or overnight using the intrinsic LYSO radioactivity. A few future directions and guidelines based on the wok we have done so far in this project are proposed such as possible TOF-PET applications of these dual-ended readout axially-oriented detectors based on fast and bright LYSO crystals.

Appendices

Appendix A

LabWindows code for 2-axis translation stage movement in the experimental setup

```
// Title:          Translation stage motion control:
// Purpose:        2-axis translation stage movement in experimental setup
// Created on:  8/31/2009 at 9:47:11 AM by Fazal ur-Rehman.

// Include files
#include <rs232.h>
#include <utility.h>
#include <cviddc.h>
#include <analysis.h>
#include <ansi_c.h>
#include <cvirte.h>
#include <userint.h>
#include "toolbox.h"
#include "math.h"
#include <NIDAQmx.h>
#include <formatio.h>
#include "sample1.h"
static DDCFileHandle FileHandle;
static DDCFileHandle FileHandle;
static int panelHandel;

// Static global variables

static int panelHandle;

// Global functions
void menu(void);
void check_spelling(void);
void correct_errors(void);
void display_errors(void);

/// The main function

int main (int argc, char *argv[])
{
   int error = 0;
         double countingtime;
```

```
   /* initialize and load resources */
   OpenCom(2,"COM2");                          % opens the com port
   nullChk (InitCVIRTE (0, argv, 0));
   errChk (panelHandle = LoadPanel (0, "sample1.uir", PANEL));

   /* display the panel and run the user interface */
         //errchk (GetPanelMenuBar (panelHandle));
   errChk (DisplayPanel (panelHandle));
   errChk (RunUserInterface ());

Error:
   /* clean up */
   DiscardPanel (panelHandle);
   return 0;
}


///  Exit when the user dismisses the panel.

int CVICALLBACK panelCB (int panel, int event, void *callbackData,
       int eventData1, int eventData2)
{
   if (event == EVENT_CLOSE)
      QuitUserInterface (0);
   return 0;
}

int CVICALLBACK QuitCallback (int panel, int control, int event,
                  void *callbackData, int eventData1, int eventData2)
{
         switch (event)
         {
         case EVENT_COMMIT:
                        QuitUserInterface(0);

                        break;
         case EVENT_RIGHT_CLICK:
                  MessagePopup ("QUIT Button", "This button will exit the program");

                        break;
         }
         return 0;
}
```

// 2-axis translation stage movement in experimental setup

```
//ComWrt(2,"F,C,S1M600,I1M500,R",20);   // down
 //ComWrt(2,"F,C,S1M600,I1M-500,R",21);   // up
 //ComWrt(2,"F,C,S2M600,I2M500,R",20);   // right
 //ComWrt(2,"F,C,S2M600,I2M-500,R",21);   // left
 //ComWrt(2,"F,C,S1M4500,I1M-0,S2M4500,I2M-0,I1M36700,I2M25950,R",52);

  int CVICALLBACK MoveLeft (int panel, int control, int event,
                  void *callbackData, int eventData1, int eventData2)
{

          char abc[]="F,C,S2M3000,I2M-3000,R";
                  switch (event)
                  {
                          case EVENT_COMMIT:
          ComWrt(2,"F,C,S2M3000,I2M-500,R",21);

          // left    The COM port should be opened   using  OpenCom(2, "COM2");  in the
          main() programe before the execution of the above statement

          break;
                          case EVENT_RIGHT_CLICK:

MessagePopup ("Move leftButton", "This button will move motor 2 in the left by 500
steps");

                                  break;
                          default:

                                  break;
                  }

            return (0);

}

int CVICALLBACK MoveRight (int panel, int control, int event,
                  void *callbackData, int eventData1, int eventData2)
{

          switch (event)
          {
                  case EVENT_COMMIT:
```

```
        ComWrt(2,"F,C,S2M3000,I2M500,R",20);   // right
                        break;
                case EVENT_RIGHT_CLICK:

MessagePopup ("Move right Button", "This button will move motor 2 in the right by 500
steps");
                        break;
                        default:
                        break;
        }
return (0);
}

int CVICALLBACK MoveUp (int panel, int control, int event,
                void *callbackData, int eventData1, int eventData2)
{
        switch (event)
        {
                case EVENT_COMMIT:
                        ComWrt(2,"F,C,S1M3000,I1M-500,R",21);  // up
                        break;

                case EVENT_RIGHT_CLICK:
MessagePopup ("Move up Button", "This button will move motor 1 in the upward
direction by 500 steps");
                        break;
                        default:
                        break;
        }
        return 0;
}

int CVICALLBACK MoveDown (int panel, int control, int event,
                void *callbackData, int eventData1, int eventData2)
{
        switch (event)
        {
                case EVENT_COMMIT:
                        ComWrt(2,"F,C,S1M3000,I1M500,R",20); //down
                        break;

                case EVENT_RIGHT_CLICK:
MessagePopup ("Move down Button", "This button will move motor 1 in the downward
direction by 500 steps");
                        break;
                        default:
```

```
                        break;
        }
        return 0;
}

  void CVICALLBACK MotorMovement (int menuBar, int menuItem, void
*callbackData, int panel)
  {
        int i;

        switch(menuItem)
        {
                case MENUBAR_MOVE_MOTOR1_MOVEUP:
                     ComWrt(2,"F,C,S1M3000,I1M-500,R",21); // up
                        break;

                case MENUBAR_MOVE_MOTOR1_MOVEDOWN:        // down
                    ComWrt(2,"F,C,S1M3000,I1M500,R",20);
                        break;

                case MENUBAR_MOVE_MOTOR1_SETTOZEROUP:// Set to zero (up)
                        ComWrt(2,"F,C,S1M3000,I1M-0,R",19);
                        break;

                case MENUBAR_MOVE_MOTOR1_SETTOMAXDOWN: // set to max
                                                                (down)
                        ComWrt(2,"F,C,S1M3000,I1M0,R",18);
                        break;

                 case MENUBAR_MOVE_MOTOR2_MOVERIGHT:
                          ComWrt(2,"F,C,S2M3000,I2M500,R",20);  // right
                          break;

                case MENUBAR_MOVE_MOTOR2_MOVELEFT:
                        ComWrt(2,"F,C,S2M3000,I2M-500,R",21);  // left
                        break;

                case MENUBAR_MOVE_MOTOR2_SETTOZEROLEFT: // Set to zero
                                                                (left)
                         ComWrt(2,"F,C,S2M3000,I2M-0,R",19);
                        break;

                case MENUBAR_MOVE_MOTOR2_SETTOMAXRIGHT: // Set to max
                                                                (right)
                         ComWrt(2,"F,C,S2M3000,I2M0,R",18);
                         break;
```

```
                case MENUBAR_MOVE_MOTOR2_STARTIRRADIATION:  // Start
                                                    // beam irradiation from 1 cm through 9 cm
                        ComWrt(2,"F,C,S2M3000,I2M-0,R",19);
                        Delay(10);

                       for (i=0; i<9; i++) {

                        ComWrt(2,"F,C,S2M3000,I2M1000,R",22);

                        SetCtrlVal (panelHandle, PANEL_POSITION, i+1);
                        SetCtrlVal (panelHandle, PANEL_STEPS, 1000*(i+1));
                        Delay(5);
                                }
                         break;
                        default:
                         break;
        }
  }

int CVICALLBACK Mot2Settozero (int panel, int control, int event,
                void *callbackData, int eventData1, int eventData2)
{
        switch (event)
        {
                case EVENT_COMMIT:
                ComWrt(2,"F,C,S2M3000,I2M-0,R",19);  // Set Motor2
                                                        (horizontal) to zero
                        break;

                case EVENT_RIGHT_CLICK:
MessagePopup ("Set to zero Button", "This button will move motor 2 to home position in
the left");
                        break;
                        default:
                        break;
        }
        return 0;
}

int CVICALLBACK Motor1SetToZero (int panel, int control, int event,
                void *callbackData, int eventData1, int eventData2)
{
        switch (event)
        {
                case EVENT_COMMIT:
```

```
                    ComWrt(2,"F,C,S1M3000,I1M-0,R",19);
                        break;
                case EVENT_RIGHT_CLICK:

MessagePopup ("Set to zero Button", "This button will move motor 1 up to home
position");
                        break;
                        default:
                        break;
        }
        return 0;
}

int CVICALLBACK SetToMaxRight (int panel, int control, int event,
                void *callbackData, int eventData1, int eventData2)
{
        switch (event)
        {
                case EVENT_COMMIT:
                        ComWrt(2,"F,C,S2M3000,I2M0,R",18);
                        break;

                case EVENT_RIGHT_CLICK:
MessagePopup ("Set to max Button", "This button will move motor 2 to max position on
the right");
                        break;
                       default:
                       break;
        }
        return 0;
}

int CVICALLBACK SetToMaxDown (int panel, int control, int event,
                void *callbackData, int eventData1, int eventData2)
{
        switch (event)
        {
                case EVENT_COMMIT:
                        ComWrt(2,"F,C,S1M3000,I1M0,R",18);
                        break;
                case EVENT_RIGHT_CLICK:
MessagePopup ("Set to max Button", "This button will move motor 1 to max position
downward");
                        break;
                        default:
                        break;
```

```
	}
	return 0;
}

int CVICALLBACK StartIrradiation (int panel, int control, int event,
		void *callbackData, int eventData1, int eventData2)
{

  char
ninesteps[9][22]={"F,C,S2M3000,I2M1000,R","F,C,S2M3000,I2M2000,R","F,C,S2M30
00,I2M3000,R","F,C,S2M3000,I2M4000,R","F,C,S2M3000,I2M5000,R","F,C,S2M3000
,I2M6000,R","F,C,S2M3000,I2M7000,R","F,C,S2M3000,I2M8000,R","F,C,S2M3000,I2
M9000,R"};
  int i;
  double countingtime;
  double time;
  double counter=0;
	switch (event)
	{
		case EVENT_COMMIT:
			ComWrt(2,"F,C,S2M3000,I2M-0,R",19);
			Delay(10);
	for (i=0; i<9; i++) {
				ComWrt(2,"F,C,S2M4000,I2M2000,R",22);
		GetCtrlVal(panelHandle, PANEL_TOTALTIME, &countingtime);
					ResetTimer (panelHandle, PANEL_TIMER);
					 time=Timer();
					if(time<=countingtime){
			SetCtrlVal(panelHandle, PANEL_COUNTER,i+1);
			SetCtrlVal(panelHandle, PANEL_TIMECONTROL,time);}

			SetCtrlVal (panelHandle, PANEL_POSITION, i+1);
			SetCtrlVal (panelHandle, PANEL_STEPS, 2000*(i+1));
			   Delay(5);
				}
			break;

		case EVENT_RIGHT_CLICK:
MessagePopup ("Start Irradiation Button", "This button will start the irradiation of
collimated beam from 1cm through 9 cm");
			break;
		default:
			break;
	}
	return 0;
}
```

Appendix B Matlab scripts for data analysis

Matlab script for Individual PMT energy spectra

```
clear all
close all
data1=importdata('step1');
data2=importdata('step2');
data3=importdata('step3');
data4=importdata('step4');
data5=importdata('step5');
data6=importdata('step6');
data7=importdata('step7');
data8=importdata('step8');
data9=importdata('step9');
data={data1,data2,data3,data4,data5,data6,data7,data8,data9};

%Deleting the negative values in the data file%

for j=1:9
    k=0;
    stoppoint=size(data{j}(:,1));
  for i=1:stoppoint(1)
    if(data{j}(i,1)>0&&data{j}(i,2)>0)  % Selection of positive values
only
       k=k+1;
       PMT{j}(k,1)=data{j}(i,1);
       PMT{j}(k,2)=data{j}(i,2);
    end
  end
end

x=[0.025:0.05:4.975];

for i=1:9


figure

  A=hist(PMT{i}(:,1),x);
  B=hist(PMT{i}(:,2),x);

plot(x, A,'LineWidth',2)
hold on
plot(x, B, 'red','LineWidth',2)
xlabel('Energy (Amplitude) (V)', 'fontsize',12,'fontweight','b')
ylabel('Counts','fontsize',12,'fontweight','b')
title(['Energy spectra of individual PMT signals at ', int2str(i),'cm
irradiation depth'],'fontsize',12,'fontweight','b')
legend('PMT1', 'PMT2')
end
```

% Matlab script for Sum PMT1+PMT2 energy spectra

```
close all
clear all

%%%%%%%%%%%%%%%%%%%%%%%%%%%%%%%%%%%%%%%%%%%%%%%%%%%%%%%%%%%%%%%%%%%%%%%%%%%%
% Importing data files from Fazal's Folder to MATLAB structure   %
%%%%%%%%%%%%%%%%%%%%%%%%%%%%%%%%%%%%%%%%%%%%%%%%%%%%%%%%%%%%%%%%%%%%%%%%%%%%
data1=importdata('step1');
data2=importdata('step2');
data3=importdata('step3');
data4=importdata('step4');
data5=importdata('step5');
data6=importdata('step6');
data7=importdata('step7');
data8=importdata('step8');
data9=importdata('step9');
data={data1,data2,data3,data4,data5,data6,data7,data8,data9};

for j=1:9
    k=0;
    stoppoint=size(data{j}(:,1));
  for i=1:stoppoint(1)
    if(data{j}(i,1)>0&&data{j}(i,2)>0) %Selection of positive values
       k=k+1;
       PMT{j}(k,1)=data{j}(i,1);
       PMT{j}(k,2)=data{j}(i,2);
    end
  end
end



%%%%%%%%%%%%%%%%%%%%%%%%%%%%%%%%%%%%%%%%%%%%%%%%%%%%%%%%%%%%%%%%%%%%%%%%%%%%
% Summing both PMTs signals and plotting energy spectra %
%%%%%%%%%%%%%%%%%%%%%%%%%%%%%%%%%%%%%%%%%%%%%%%%%%%%%%%%%%%%%%%%%%%%%%%%%%%%

for i=1:9

sum{i}(:,1)=data{i}(:,1)+ data{i}(:,2);

[C, cplotaxis]=hist(sum{i},55);

figure
plot(cplotaxis, C,'LineWidth',2);
xlabel('Energy (Amplitude) (V)', 'fontsize',12,'fontweight','b')
ylabel('Counts','fontsize',12,'fontweight','b')
title(['Energy spectrum of summed signal of two PMTs at ',
int2str(i),'cm irradiation depth'],'fontsize',12,'fontweight','b')
end
```

% Matlab script for Light output and energy resolution calculation from photo peak using Gaussian fitting

```
close all
clear all

%%%%%%%%%%%%%%%%%%%%%%%%%%%%%%%%%%%%%%%%%%%%%%%%%%%%%%%%%%%%%%%%%%%%%%%%
% Importing data files from Fazal Folder to MATLAB structure   %
%%%%%%%%%%%%%%%%%%%%%%%%%%%%%%%%%%%%%%%%%%%%%%%%%%%%%%%%%%%%%%%%%%%%%%%%
data1=importdata('step1');
data2=importdata('step2');
data3=importdata('step3');
data4=importdata('step4');
data5=importdata('step5');
data6=importdata('step6');
data7=importdata('step7');
data8=importdata('step8');
data9=importdata('step9');
data={data1,data2,data3,data4,data5,data6,data7,data8,data9};


for i=1:9

 %%%%%%%%%%%%%%%%%%%%%%%%%%%%%%%%%%%%%%%%%%%%%%%%%%%%%%%%%%%%%%%%%%%%%%%%
% Summing four digitized signals of each PMT if not summed in the NIM %
%%%%%%%%%%%%%%%%%%%%%%%%%%%%%%%%%%%%%%%%%%%%%%%%%%%%%%%%%%%%%%%%%%%%%%%%

%data{i}(:,9)=data{i}(:,1)+data{i}(:,2)+data{i}(:,3)+data{i}(:,4);
%data{i}(:,10)=data{i}(:,5)+data{i}(:,6)+data{i}(:,7)+data{i}(:,8);

%%%%%%%%%%%%%%%%%%%%%%%%%%%%%
% Summing both PMTs signals %
%%%%%%%%%%%%%%%%%%%%%%%%%%%%%

    data{i}(:,3)=data{i}(:,1)+ data{i}(:,2);
end

%%%%%%%%%%%%%%%%%%%%%%%%%%%%%%%%%%%%%%%%%%%%%%%%%%%%%%%%%%%%%%%%%%%%%%%%
% To calcultae Energy resolution and plottingenergy %
% spectra all together for 9 irradiation depths     %
%%%%%%%%%%%%%%%%%%%%%%%%%%%%%%%%%%%%%%%%%%%%%%%%%%%%%%%%%%%%%%%%%%%%%%%%

 % selection of photopeak - an example for 9 energy spectra
lowerthreshold=[2.974,2.226,2.347,2.106,2.089,2.124,2.161,2.282,2.762];
upperthreshold=[4.711,3.951,3.563,3.475,3.492,3.309,3.449,3.579,4.431];

for j=1:9
    k=0;
    stoppoint=size(data{j}(:,3));
  for i=1:stoppoint(1)
    if(data{j}(i,3)>lowerthreshold(j)&&data{j}(i,3)<upperthreshold(j))
% Selection of photopeak events only where lower is left and upper is
right of each photopeak
       k=k+1;
```

```
        sumresolution{j}(k,1)=data{j}(i,3);
        PMT1photopeak{j}(k,1)=data{j}(i,1);
        PMT2photopeak{j}(k,1)=data{j}(i,2);
    end
  end
end


 figure
for i=1:9


    X=0:0.001:10;

    % Gaussian fitting to photopeak
    [mu,sigma]=normfit(sumresolution{i});
    y = normpdf(X,mu,sigma);
    Max=max(y);
    y = (1150/Max).*y; %for scalling

    FWHM(i)= 2.35*sigma;
    Peak(i)=mu;
    Energyresolu(i)=(FWHM(i)/Peak(i))*100;
    Energyresolution(i,2)=Energyresolu(i);
    Energyresolution(i,3)=Peak(i);
    plot(X,y, 'red')
    xlabel('Energy (Amplitude) (V)', 'fontsize',12,'fontweight','b')
    ylabel('Counts','fontsize',12,'fontweight','b')
    title('Gaussian fitting of Photopeak of summed signal of two PMTs
at 9 irradiation depths','fontsize',12,'fontweight','b')
    hold on
    [A, aplotaxis]=hist(sumresolution{i}(:,1));
    Max=max(A);
    A = (1150/Max).*A;
    plot(aplotaxis,A)

end
legend('0 cm','1 cm','2 cm','3 cm','4 cm','5 cm','6 cm','7 cm','8 cm')
hold
DOI=[1,2,3,4,5,6,7,8,9];
Energyresolution(:,1)=[1,2,3,4,5,6,7,8,9];
figure;
plot(Energyresolution(:,1), Energyresolution(:,2),'bo')
axis([0 10 0 18])
xlabel('Irradiation depth (cm)', 'fontsize',12,'fontweight','b')
ylabel('Energy Resolution (%)','fontsize',12,'fontweight','b')
title('Energy resolution as a function of irradiation depth (crystal3-
1, LYSO+Teflon)','fontsize',12,'fontweight','b')
figure;
plot(Energyresolution(:,1), Energyresolution(:,3), 'ro')
axis([0 10 0 4])
xlabel('Irradiation depth (cm)', 'fontsize',12,'fontweight','b')
ylabel('Light output (V)','fontsize',12,'fontweight','b')
title('Light output as a function of irradiation depth (crystal3-1,
LYSO+Teflon)','fontsize',12,'fontweight','b')
```

% Matlab script for Polynomial fitting and spatial resolution – an example

```
close all
clear all

%%%%%%%%%%%%%%%%%%%%%%%%%%%%%%%%%%%%%%%%%%%%%%%%%%%%%%%%%%%%%%%%%%%%%%%%%%%
% Importing data files from Fazal Folder to MATLAB structure   %
%%%%%%%%%%%%%%%%%%%%%%%%%%%%%%%%%%%%%%%%%%%%%%%%%%%%%%%%%%%%%%%%%%%%%%%%%%%
data1=importdata('step1');
data2=importdata('step2');
data3=importdata('step3');
data4=importdata('step4');
data5=importdata('step5');
data6=importdata('step6');
data7=importdata('step7');
data8=importdata('step8');
data9=importdata('step9');
data={data1,data2,data3,data4,data5,data6,data7,data8,data9};

for i=1:9

%%%%%%%%%%%%%%%%%%%%%%%%%%%%%%%%%%%%%%%%%%%%%%%%%%%%%%%%%%%%%%%%%%%%%%%%%%%
% Summing both PMTs signals and plotting energy spectra all together %
%%%%%%%%%%%%%%%%%%%%%%%%%%%%%%%%%%%%%%%%%%%%%%%%%%%%%%%%%%%%%%%%%%%%%%%%%%%

 data{i}(:,3)=data{i}(:,1)+ data{i}(:,2);

end



%%%%%%%%%%%%%%%%%%%%%%%%%%%%%%%%%%%%%%%%%%%%%%%%%%%%%%%%%%%%%%%%%%%%%%%%%%%
% To calcultae Energy resolution and plottingenergy %
% spectra all together for 9 irradiation depths     %
%%%%%%%%%%%%%%%%%%%%%%%%%%%%%%%%%%%%%%%%%%%%%%%%%%%%%%%%%%%%%%%%%%%%%%%%%%%

lowerthreshold=[2.974,2.226,2.347,2.106,2.089,2.124,2.161,2.282,2.762];
upperthreshold=[4.711,3.951,3.563,3.475,3.492,3.309,3.449,3.579,4.431];

for j=1:9
    k=0;
    stoppoint=size(data{j}(:,3));
  for i=1:stoppoint(1)
    if(data{j}(i,3)>lowerthreshold(j)&&data{j}(i,3)<upperthreshold(j))
% Selection of photopeak events only
       k=k+1;
       sumresolution{j}(k,1)=data{j}(i,3);
       PMT1photopeak{j}(k,1)=data{j}(i,1);
       PMT2photopeak{j}(k,1)=data{j}(i,2);
    end
  end
end

Colors=['y','m','c','r','g','b','k','r','b'];
figure;
```

```
 for i=1:9

photopeakratio{i}=PMT2photopeak{i}(:,1)./(PMT1photopeak{i}(:,1)+PMT2pho
topeak{i}(:,1));
%Average(i,2)=mean(ratio{i});
[D, dplotaxis]=hist(photopeakratio{i},55);
Max = max(D);
D=(1000/Max).*D;
%axes('FontSize', 14,'fontweight','b');
plot(dplotaxis, D, Colors(i),'LineWidth',2);
axis([0 1 0 1050])

xlabel('PMT1/(PMT1+PMT2)', 'fontsize',12,'fontweight','b')
ylabel('Counts','fontsize',12,'fontweight','b')
title('Signal ratio profiles at different irradiation depths (photopeak
events) - LYSO polished+Teflon (crystal3-
1)','fontsize',12,'fontweight','b')
hold on
end

%set(0,'DefaultAxesColorOrder','y','m','c','r','g''b','k','r','y')
legend('1 cm','2 cm','3 cm','4 cm','5 cm','6 cm','7 cm','8 cm','9 cm')



%%%%%%%%%%%%%%%%%%%%%%%%%%%%%%%%%%%%%%%%%%%%%%%%%%%%%%%%%%%%%%%%%%%%%%%%
%%%%%%%%%%%%%%%%%%%
% To calcultae Signal Ratios and mean ratio and plotting mean ratio
Gaussian fitting vs %
% irradiation depth all together for 9 irradiation depths
%
%%%%%%%%%%%%%%%%%%%%%%%%%%%%%%%%%%%%%%%%%%%%%%%%**%%%%%%%%%%%%%%%%%%%%%%%%
%%%



%%%%%%%%%%%%%%%%%%%%%%%%%%%%%%%%%%%%%%%%%%%%%%%%%%%%%%%%%%%%%%%%%%%%%%%%
% Refining further the distribution peaks for Gaussian fitting%
%%%%%%%%%%%%%%%%%%%%%%%%%%%%%%%%%%%%%%%%%%%%%%%%%%%%%%%%%%%%%%%%%%%%%%%%


lowercut=[0.2457,0.3102,0.3506,0.3902,0.424,0.4524,0.4833,0.5277,0.6208
];
uppercut=[0.3577,0.4259,0.4965,0.5139,0.5565,0.5814,0.6108,0.6709,0.748
];

for j=1:9
    k=0;
    stoppoint=size(photopeakratio{j}(:,1));
  for i=1:stoppoint(1)

if(photopeakratio{j}(i,1)>lowercut(j)&&photopeakratio{j}(i,1)<uppercut(
j))  % ratioprofile cut events only
```

```
       k=k+1;
       photopeakratio{j}(k,1)=photopeakratio{j}(i,1);
    end
  end
end


%%%%%%%%%%%%%%%%%%%%%%%%%%%%%%%%%%%%%%%%%%%%%%%%%%%%
% Gaussian fitting of smooth ratio signals   %
%%%%%%%%%%%%%%%%%%%%%%%%%%%%%%%%%%%%%%%%%%%%%%%%%%%%**

Colors=['y','m','c','r','g','b','k','r','b'];

for i=1:9
    X=0:0.01:1;
    [mu,sigma]=normfit(photopeakratio{i});
    y = normpdf(X,mu,sigma);
    Max=max(y);
    y=(1000/Max).*y;
    FWHM(i)=2.35*sigma;
    Mean(i)=mu;
    Average(i,2)=Mean(i)  %mean(ratiophotopeak{i});
    %axes('FontSize', 14,'fontweight','b');
    plot(X,y,'black')
    xlabel('PMT1/(PMT1+PMT2)', 'fontsize',12,'fontweight','b')
    ylabel('Counts','fontsize',12,'fontweight','b')
    title('Gaussian Fitting of signal ratio profiles at different
irradiation depths (photopeak events)-LYSO polished+Teflon (Crystal3-
1)','fontsize',12,'fontweight','b')

    Average(i,3)=FWHM(i);
    Average(i,4)=FWHM(i)/2;
    hold on
end
    legend('1 cm','2 cm','3 cm','4 cm','5 cm','6 cm','7 cm','8 cm','9
cm')
    FWHM
    Mean

  hold
%%%%%%%%%%%%%%%%%%%%%%%%%%%%%%%%%%%%%%%%%%%%%%%%%%%%%%%%%%%%%%%%%%%%%%%%%%%%%%%
% Polynomial fitting of the mean signal ratio vs irradiation depth  %
%%%%%%%%%%%%%%%%%%%%%%%%%%%%%%%%%%%%%%%%%%%%%%%%%%%%%%%%%%%%%%%%%%%%%%%%%%%%%%%

Average(1:9,1)=[1,2,3,4,5,6,7,8,9];
x=Average(1:9,1);
y= Average(1:9,2);
%average=mean(data(1:9,2))
E=Average(1:9,4);
vertical9=y(9)
figure
errorbar(x,y,E, 'ro')
%plot(x,y,'ro')
hold on
%xfit = linspace(x(1),x(end),1000);
```

```
xfit = linspace(0,10,1000);
p = polyfit(x,y,3) % Compute conditioned fit
yfit = polyval(p,xfit);

%xfit = linspace(x(1),x(end),1000);
xfit = linspace(0,10,1000);
plot(xfit,yfit,'b-', 'linewidth', 2) % Plot conditioned fit vs. x data
ylabel('PMT1/(PMT1+PMT2)', 'fontsize',12,'fontweight','b')
xlabel('Irradiation depth (cm)', 'fontsize',12,'fontweight','b')
title('Signal ratio as a function of irradiation depth - Polynomial
fitting-LYSO polished+Teflon (Crystal3-
1)','fontsize',12,'fontweight','b')
legend('measured data points', 'Polynomial fit')

%%%%%%%%%%%%%%%%%%%%%%%%%%%%%%%%%%%%%%%%%%%%%%%%%%%%%%%%%%%%%%%%%%%%%%%%%%%%
%%
% To find the slope of the tangent to the polynimial curve i.e dy/dx at
%
% irradiation point
%
%%%%%%%%%%%%%%%%%%%%%%%%%%%%%%%%%%%%%%%%%%%%%%%%%%%%%%%%%%%%%%%%%%%%%%%%%%%%
%%
k=polyder(p)
for x=1:9
    y=k(1)*x^2+k(2)*x+k(3) % dy/dx = k1x^2+k2x+k3
    Average(x,5)=y;
    DOIR(x)=Average(x,4)./Average(x,5);
    Average(x,6)=DOIR(x)
end
hold
%%%%%%%%%%%%%%%%%%%%%%%%%%%%%%%%%%%%%%%%%%%%%%%%%%%%%%%%%%%%%%%%%%%%%%%%%%%%
% Plotting DOI Resolution vs Irradiation depth %
%%%%%%%%%%%%%%%%%%%%%%%%%%%%%%%%%%%%%%%%%%%%%%%%%%%%%%%%%%%%%%%%%%%%%%%%%%%%**%%
figure
plot(Average(1:9,1),Average(1:9,6),'ro');
ylabel('DOI Resolution (cm)', 'fontsize',12,'fontweight','b')
xlabel('Irradiation depth (cm)', 'fontsize',12,'fontweight','b')
title('DOI Resolution as a function of irradiation depth - from
polyfit-LYSO polished+Teflon (Crystal3-
1)','fontsize',12,'fontweight','b')
```

% Matlab script for piece-wise or spline fitting and spatial resolution – an example

```
close all
clear all

%%%%%%%%%%%%%%%%%%%%%%%%%%%%%%%%%%%%%%%%%%%%%%%%%%%%%%%%%%%%%%%%%%%%%%%%%%%%
%                                                                             %
%    Importing data files from Fazal Folder to MATLAB structure               %
%                                                                             %
%%%%%%%%%%%%%%%%%%%%%%%%%%%%%%%%%%%%%%%%%%%%%%%%%%%%%%%%%%%%%%%%%%%%%%%%%%%%

%for i=1:9          %writing the segment of the code given below in a
loop for multiple files
%data{i}=importdata(['step',num2str(i)]);
%end

data1=importdata('step1.dat');
data2=importdata('step2.dat');
data3=importdata('step3.dat');
data4=importdata('step4.dat');
data5=importdata('step5.dat');
data6=importdata('step6.dat');
data7=importdata('step7.dat');
data8=importdata('step8.dat');
data9=importdata('step9.dat');
data={data1,data2,data3,data4,data5,data6,data7,data8,data9};

for i=1:9

%%%%%%%%%%%%%%%%%%%%%%%%%%%%%%%%%%%%%%%%%%%%%%%%%%%%%%%%%%%%%%%%%%%%%%%%%%%%
% Summing both PMTs signals and plotting energy spectra all together %
%%%%%%%%%%%%%%%%%%%%%%%%%%%%%%%%%%%%%%%%%%%%%%%%%%%%%%%%%%%%%%%%%%%%%%%%%%%%

 sum{i}(:,1)=data{i}(:,1)+ data{i}(:,2);

end


%%%%%%%%%%%%%%%%%%%%%%%%%%%%%%%%%%%%%%%%%%%%%%%%%%%%%%%%%%%%%%%%%%%%%%%%%%%%
% Calculating ratio signal and plotting distribution of ratio signals%
%%%%%%%%%%%%%%%%%%%%%%%%%%%%%%%%%%%%%%%%%%%%%%%%%%%%%%%%%%%%%%%%%%%%%%%%%%%%

Colors=['y','m','c','r','g','b','k','r','b'];
figure;

for i=1:9

photopeakratio{i}=data{i}(:,2)./((data{i}(:,1))+data{i}(:,2));
%Average(i,2)=mean(ratio{i});
[D, dplotaxis]=hist(photopeakratio{i},20);
Max = max(D);
D=(1000/Max).*D;
%axes('FontSize', 14,'fontweight','b');
```

```
plot(dplotaxis, D, Colors(i),'LineWidth',2);
axis([0 1 0 1050])

xlabel('PMT1/(PMT1+PMT2)', 'fontsize',12,'fontweight','b')
ylabel('Counts','fontsize',12,'fontweight','b')
title('Signal ratio profiles at different irradiation depths (photopeak
events) - LYSO polished+Teflon ','fontsize',12,'fontweight','b')
hold on
end

legend('1 cm','2 cm','3 cm','4 cm','5 cm','6 cm','7 cm','8 cm','9 cm')


%%%%%%%%%%%%%%%%%%%%%%%%%%%%%%%%%%%%%%%%%%%%%%
% Gaussian fitting of smooth ratio signals   %
%%%%%%%%%%%%%%%%%%%%%%%%%%%%%%%%%%%%%%%%%%%%**

Colors=['y','m','c','r','g','b','k','r','b'];

for i=1:9
    X=0:0.01:1;
    [mu,sigma]=normfit(photopeakratio{i});
    y = normpdf(X,mu,sigma);
    Max=max(y);
    y=(1000/Max).*y;
    FWHM(i)=2.35*sigma;
    Mean(i)=mu;
    Average(i,2)=Mean(i); %mean(photopeakratio{i}); %
    %axes('FontSize', 14,'fontweight','b');
    plot(X,y,'black')
    xlabel('PMT1/(PMT1+PMT2)', 'fontsize',12,'fontweight','b')
    ylabel('Counts','fontsize',12,'fontweight','b')
    title('Gaussian Fitting of signal ratio profiles at different
irradiation depths (photopeak events)-LYSO polished+Teflon (Crystal3-
1)','fontsize',12,'fontweight','b')

    Average(i,3)=FWHM(i);
    Average(i,4)=FWHM(i)/2;
    hold on
end
    legend('1 cm','2 cm','3 cm','4 cm','5 cm','6 cm','7 cm','8 cm','9
cm')
    FWHM
    Mean

  hold
%%%%%%%%%%%%%%%%%%%%%%%%%%%%%%%%%%%%%%%%%%%%%%%%%%%%%%%%%%%%%%%%%%%%%
% Polynomial fitting of the mean signal ratio vs irradiation depth  %
%%%%%%%%%%%%%%%%%%%%%%%%%%%%%%%%%%%%%%%%%%%%%%%%%%%%%%%%%%%%%%%%%%%%%

Average(1:9,1)=[1,2,3,4,5,6,7,8,9];
x=Average(1:9,1);
y= Average(1:9,2);
%average=mean(data(1:9,2))
E=Average(1:9,4);
```

```
vertical9=y(9)
figure
errorbar(x,y,E, 'ro')
%plot(x,y,'ro')
hold on
%xfit = linspace(x(1),x(end),1000);

xfit = linspace(0,10,1000);%linspace(0,10,1000);
pp = spline(x,y); %or pp=mkpp(x,y); % piece-wise or spline fitting
yfit = ppval(pp, xfit);


xfit = linspace(0,10,1000);
plot(xfit,yfit,'b-', 'linewidth', 2) % Plot conditioned fit vs. x data
ylabel('PMT1/(PMT1+PMT2)', 'fontsize',12,'fontweight','b')
xlabel('Irradiation depth (cm)', 'fontsize',12,'fontweight','b')
title('Signal ratio as a function of irradiation depth - Polynomial
fitting-LYSO polished+Teflon (Crystal3-
1)','fontsize',12,'fontweight','b')
legend('measured data points', 'Polynomial fit')

%%%%%%%%%%%%%%%%%%%%%%%%%%%%%%%%%%%%%%%%%%%%%%%%%%%%%%%%%%%%%%%%%%%%%%%%%%%%
%%
% To find the slope of the tangent to the polynimial curve i.e dy/dx at
%
% at each irradiation point
%
%%%%%%%%%%%%%%%%%%%%%%%%%%%%%%%%%%%%%%%%%%%%%%%%%%%%%%%%%%%%%%%%%%%%%%%%%%%%
%%
[breaks,coefs,l,k,d] = unmkpp(pp)

hold on

cc1 = [coefs(1,1), coefs(1,2),coefs(1,3),coefs(1,4)];
cc2 = [coefs(2,1), coefs(2,2),coefs(2,3),coefs(2,4)];
cc3 = [coefs(3,1), coefs(3,2),coefs(3,3),coefs(3,4)];
cc4 = [coefs(4,1), coefs(4,2),coefs(4,3),coefs(4,4)];
cc5 = [coefs(5,1), coefs(5,2),coefs(5,3),coefs(5,4)];
cc6 = [coefs(6,1), coefs(6,2),coefs(6,3),coefs(6,4)];
cc7 = [coefs(7,1), coefs(7,2),coefs(7,3),coefs(7,4)];
cc8 = [coefs(8,1), coefs(8,2),coefs(8,3),coefs(8,4)];

pp1 = mkpp([1 2],cc1);
pp2 = mkpp([2 3],cc2);
pp3 = mkpp([3 4],cc3);
pp4 = mkpp([4 5],cc4);
pp5 = mkpp([5 6],cc5);
pp6 = mkpp([6 7],cc6);
pp7 = mkpp([7 8],cc7);
pp8 = mkpp([8 9],cc8);

%Plotting each piecewise plot separately
% xx1 = 1:0.1:2;
% plot(xx1,ppval(pp1,xx1),'r-')
% hold on
```

```
% xx2 = 2:0.1:3;
% plot(xx2,ppval(pp2,xx2),'r-')
% hold on
% xx3 = 3:0.1:4;
% plot(xx3,ppval(pp3,xx3),'r-')
% hold on
% xx4 = 4:0.1:5;
% plot(xx4,ppval(pp4,xx4),'r-')
% hold on
% xx5 = 5:0.1:6;
% plot(xx5,ppval(pp5,xx5),'r-')
% hold on
% xx6 = 6:0.1:7;
% plot(xx6,ppval(pp6,xx6),'r-')
% hold on
% xx7 = 7:0.1:8;
% plot(xx7,ppval(pp7,xx7),'r-')
% hold on
% xx8 = 8:0.1:9;
% plot(xx8,ppval(pp8,xx8),'r-')
% hold on

dpp = mkpp(breaks,repmat(k-1:-1:1,d*l,1).*coefs(:,1:k-1),d);
xx=1:0.01:8;
%plot(xx,ppval(dpp,xx),'k-');

%{for x=1:9
   xx=1:9
    %y=coefs(x,1)*3*x^2+coefs(x,2)*2*x+coefs(x,3) % dy/dx =
k1x^2+k2x+k3, slope of the tangent to the calibration curve at each
irradiation position
    y=ppval(dpp,xx)
    Average(:,5)=y;
    DOIR=Average(:,3)./Average(:,5);
    Average(:,6)=DOIR

%end
hold
%%%%%%%%%%%%%%%%%%%%%%%%%%%%%%%%%%%%%%%%%%%%%%%%%%%%%%%%
% Plotting DOI Resolution vs Irradiation depth %
%%%%%%%%%%%%%%%%%%%%%%%%%%%%%%%%%%%%%%%%%%%%%%%%%%%%%%%%**%%
figure
plot(Average(1:9,1),Average(1:9,6),'ro');
ylabel('DOI Resolution (cm)', 'fontsize',12,'fontweight','b')
xlabel('Irradiation depth (cm)', 'fontsize',12,'fontweight','b')
title('DOI Resolution as a function of irradiation depth - peicewise
interpolation-LYSO polished+1band+Teflon
','fontsize',12,'fontweight','b')
```

% An example of the implementation of Shao calibration method in Matlab

```
close all
clear all

data1=importdata('uniform1Na10cmsamesingles'); %750PMT1-800PMT2
data2=importdata('uniform2Na10cmsamesingles'); %800PMT1-800PMT2
data3=importdata('uniform3Na10cmsamesingles'); %8000PMT1-750PMT2

data={data1,data2,data3};

%%%%%%%%%%%%%%%%%%%%%%%%%%%%%%%%%%%%%%%%%%%%%%%%%%%%%%%%%%%%%%%%%%%%%%%%%%%%
%
% An implimentation of Shao Calibration method in matlab
%
%%%%%%%%%%%%%%%%%%%%%%%%%%%%%%%%%%%%%%%%%%%%%%%%%%%%%%%%%%%%%%%%%%%%%%%%%%%%
%

for i=1:3

ratio{i}=(data{i}(:,2)./(data{i}(:,1)+data{i}(:,2)));
                                                        %R=PMT2/(PMT1+PMT2)
x=[0:0.0005:1];
H = hist(ratio{i},x);
Q=0;
for k=1:2001
Q=Q+H(k)%*0.005; continuous sum of histogram counts where H(k)is the
histogram count of signal ratio k
end
PDF=H/Q; %probability density function is the normalized histogram cont
D=10;               %length of LYSO = 10 cm
QPDF=0;
for k=1:2001
    QPDF=QPDF+PDF(k)%*0.005; continous summation of PDF from 0 to k (or
R). This sum gives the position of interaction in the crystal
    QF(k)=QPDF; %storing each QPDF in an array
    z(k)=D*QPDF;
end

Colors=['y','m','c','r','g','b','k','r','b'];

plot(z,x,Colors(i),'linewidth', 2);
hold on
axis([0 10 0 1])

end
```

Appendix C DETECT2000 scripts

; DETECT2000 script for optical photon transport in a smooth 3x2x100 mm LYSO Crystal wrapped in Teflon

```
; Define materials
DMAT1, 1.82NV, 150ADV,
900000000000000000000000000000000000000000000000000SDV, 1PLF, DT1,
40TAU, 1.0TAUW        ;LYSO crystal
DMAT2, 1.463NV                                          ; Optical
Grease VISILOX V-788
DMAT3, 1.50NV                                            ; Borosilicate
glass RI=1.5

; Define the surface finish
DFIN1, DETECT, 1QEF                                                ;PMT
Cathode surface on both sides of the crystal
DFIN2, POLISH, 0.60RCV                             ; 4 long polished
surfaces of the crystal wrapped in Teflon tape with RC=0.99
DFIN3, POLISH                                                ; 2 end
faces of the crystal and optical grease

; Define the six planes bounding the crystal and two other planes for
end faces of glue orthogonal to Z-axis
DPLN1, -1.5X
DPLN2,  1.5X
DPLN3, -1Y
DPLN4,  1Y
DPLN5, -50Z
DPLN6, 50Z
DPLN7, -50.3Z                       ; Optical grease (0.1 mm) end face
(facing orthogonal to negative Z-axis)
DPLN8, 50.3Z    ; Optical grease end face orthogonal to positive Z-axis
DPLN9, 51.1z      ; 0.8 mm PMT glass window slab face on the right side
DPLN10, -51.1z      ;0.8 mm PMT glass window slab face on the left side
DPLN101, -11.75X                    ; Area of photocathode and glass
window is 23.5x23.5 mm2
DPLN202, 11.75X
DPLN303, -11.75Y
DPLN404, 11.75Y

; Define the three components with 2 materials
COMP1, MAT2          ; optical grease ON THE LEFT END
SURF, FIN3, PLN7, ZL, C4
SURF, FIN3, PLN5, ZS, C2
SURF, FIN3, PLN1, XL
SURF, FIN3, PLN2, XS
SURF, FIN3, PLN3, YL
SURF, FIN3, PLN4, YS

COMP2, MAT1          ;LYSO CRYSTAL
SURF, FIN3, PLN5, ZL, C1
SURF, FIN3, PLN6, ZS, C3
SURF, FIN2, PLN1, XL
SURF, FIN2, PLN2, XS
```

```
SURF, FIN2, PLN3, YL
SURF, FIN2, PLN4, YS

COMP3, MAT2     ; optical grease ON THE RIGHT END
SURF, FIN3, PLN6, ZL, C2
SURF, FIN3, PLN8, ZS, C5
SURF, FIN3, PLN1, XL
SURF, FIN3, PLN2, XS
SURF, FIN3, PLN3, YL
SURF, FIN3, PLN4, YS

COMP4, MAT3          ; 0.8 mm PMT Window glass slab on the left
SURF, FIN1, PLN10, ZL
SURF, FIN3, PLN7, ZS, C1
SURF, FIN3, PLN101, XL
SURF, FIN3, PLN202, XS
SURF, FIN3, PLN303, YL
SURF, FIN3, PLN404, YS

COMP5, MAT3          ; 0.8 mm PMT Window glass slab on the right
SURF, FIN3, PLN8, ZL, C3
SURF, FIN1, PLN9, ZS
SURF, FIN3, PLN101, XL
SURF, FIN3, PLN202, XS
SURF, FIN3, PLN303, YL
SURF, FIN3, PLN404, YS



LIFE1000

;FATES file for each history recording
;FATES1


SEED10000

GEN, MAT1, -0XS, 0XL, -0YS, 0YL, -40ZS, -40ZL   ;Generate optical
photons at the 1 cm of the crystal from PMT1 (0,0,-40)

RUN10000

END
```

; DETECT2000 script for optical photon transport in with etching bands on four long surfaces of 3x2x100 mm LYSO Crystal wrapped in Teflon

```
; Define materials
DMAT1, 1.82NV, 150ADV,
900000000000000000000000000000000000000000000000000SDV, 1PLF, DT1,
40TAU, 1.0TAUW      ; LYSO crystal
DMAT2, 1.463NV                          ; Optical Grease VISILOX V-788
DMAT3, 1.5NV                            ; Borosilicate glass RI=1.5

; Define the surface finish
DFIN1, DETECT, 1QEF  ; PMT Cathode surface on both sides of the crystal
```

```
DFIN2, POLISH, 0.92RCV         ; 4 long polished surfaces of crystal;
wrapped in Teflon with RC=0.92 or so
DFIN3, POLISH           ; 2 end faces of the crystal and optical grease
DFIN4, UNIFIED, 1DLV, 0.92RCV             ; Ground bands covered with
diffusive reflector (Teflon Tap)


; Define the six planes bounding the crystal and two other planes for
end faces of glue orthogonal to Z-axis
DPLN1, -1.5X
DPLN2,  1.5X
DPLN3, -1Y
DPLN4,  1Y
DPLN5, -51.1z     ; 0.8 mm PMT glass window slab face on the left side
DPLN6, -50.3Z      ; Optical grease (0.3 mm) end face (facing
orthogonal to negative Z-axis)
DPLN7, -50Z

DPLN8, -40.5Z           ; a ground etching band of 1.0 mm
DPLN9, -39.5Z
DPLN10, -35.5Z
DPLN11, -34.5Z
DPLN12, -30.5Z
DPLN13, -29.5Z
DPLN14, -25.5Z
DPLN15, -24.5Z
DPLN16, -20.5Z
DPLN17, -19.5Z
DPLN18, -15.5Z
DPLN19, -14.5Z
DPLN20, -10.5Z
DPLN21, -9.5Z
DPLN22, -5.5Z
DPLN23, -4.5Z
DPLN24, -0.5Z
DPLN25, 0.5Z
DPLN26, 4.5Z
DPLN27, 5.5Z
DPLN28, 9.5Z
DPLN29, 10.5Z
DPLN30, 14.5Z
DPLN31, 15.5Z
DPLN32, 19.5Z
DPLN33, 20.5Z
DPLN34, 24.5Z
DPLN35, 25.5Z
DPLN36, 29.5Z
DPLN37, 30.5Z
DPLN38, 34.5Z
DPLN39, 35.5Z
DPLN40, 39.5Z
DPLN41, 40.5Z

DPLN42 50Z
DPLN43, 50.3Z   ; Optical grease end face orthogonal to positive Z-axis
DPLN44, 51.1z    ; 0.8 mm PMT glass window slab face on the right side
```

```
DPLN101, -11.75X
DPLN202,  11.75X
DPLN303, -11.75Y
DPLN404,  11.75Y


; Define 39 components with 3 materials

COMP1, MAT3          ; 0.8 mm PMT Window glass slab on the left
SURF, FIN1, PLN5, ZL
SURF, FIN3, PLN6, ZS, C2
SURF, FIN3, PLN101, XL
SURF, FIN3, PLN202, XS
SURF, FIN3, PLN303, YL
SURF, FIN3, PLN404, YS


COMP2, MAT2          ; optical grease ON THE LEFT END
SURF, FIN3, PLN6, ZL, C1
SURF, FIN3, PLN7, ZS, C3
SURF, FIN3, PLN1, XL
SURF, FIN3, PLN2, XS
SURF, FIN3, PLN3, YL
SURF, FIN3, PLN4, YS

COMP3, MAT1          ;LYSO CRYSTAL
SURF, FIN3, PLN7, ZL, C2
SURF, FIN3, PLN8, ZS, C4
SURF, FIN2, PLN1, XL
SURF, FIN2, PLN2, XS
SURF, FIN2, PLN3, YL
SURF, FIN2, PLN4, YS

COMP4, MAT1
SURF, FIN3, PLN8, ZL, C3
SURF, FIN3, PLN9, ZS, C5
SURF, FIN4, PLN1, XL     ; Ground etching bands of 1.0 mm on 4 surfaces

SURF, FIN4, PLN2, XS
SURF, FIN4, PLN3, YL
SURF, FIN4, PLN4, YS
COMP5, MAT1
SURF, FIN3, PLN9, ZL, C4
SURF, FIN3, PLN10, ZS, C6
SURF, FIN2, PLN1, XL
SURF, FIN2, PLN2, XS
SURF, FIN2, PLN3, YL
SURF, FIN2, PLN4, YS

COMP6, MAT1
SURF, FIN3, PLN10, ZL, C5
SURF, FIN3, PLN11, ZS, C7
SURF, FIN4, PLN1, XL
SURF, FIN4, PLN2, XS
SURF, FIN4, PLN3, YL
SURF, FIN4, PLN4, YS
```

```
COMP7, MAT1
SURF, FIN3, PLN11, ZL, C6
SURF, FIN3, PLN12, ZS, C8
SURF, FIN2, PLN1, XL
SURF, FIN2, PLN2, XS
SURF, FIN2, PLN3, YL
SURF, FIN2, PLN4, YS

COMP8, MAT1
SURF, FIN3, PLN12, ZL, C7
SURF, FIN3, PLN13, ZS, C9
SURF, FIN4, PLN1, XL
SURF, FIN4, PLN2, XS
SURF, FIN4, PLN3, YL
SURF, FIN4, PLN4, YS

COMP9, MAT1
SURF, FIN3, PLN13, ZL, C8
SURF, FIN3, PLN14, ZS, C10
SURF, FIN2, PLN1, XL
SURF, FIN2, PLN2, XS
SURF, FIN2, PLN3, YL
SURF, FIN2, PLN4, YS

COMP10, MAT1
SURF, FIN3, PLN14, ZL, C9
SURF, FIN3, PLN15, ZS, C11
SURF, FIN4, PLN1, XL
SURF, FIN4, PLN2, XS
SURF, FIN4, PLN3, YL
SURF, FIN4, PLN4, YS

COMP11, MAT1
SURF, FIN3, PLN15, ZL, C10
SURF, FIN3, PLN16, ZS, C12
SURF, FIN2, PLN1, XL
SURF, FIN2, PLN2, XS
SURF, FIN2, PLN3, YL
SURF, FIN2, PLN4, YS

COMP12, MAT1
SURF, FIN3, PLN16, ZL, C11
SURF, FIN3, PLN17, ZS, C13
SURF, FIN4, PLN1, XL
SURF, FIN4, PLN2, XS
SURF, FIN4, PLN3, YL
SURF, FIN4, PLN4, YS

COMP13, MAT1
SURF, FIN3, PLN17, ZL, C12
SURF, FIN3, PLN18, ZS, C14
SURF, FIN2, PLN1, XL
SURF, FIN2, PLN2, XS
SURF, FIN2, PLN3, YL
SURF, FIN2, PLN4, YS

COMP14, MAT1
```

```
SURF, FIN3, PLN18, ZL, C13
SURF, FIN3, PLN19, ZS, C15
SURF, FIN4, PLN1, XL
SURF, FIN4, PLN2, XS
SURF, FIN4, PLN3, YL
SURF, FIN4, PLN4, YS

COMP15, MAT1
SURF, FIN3, PLN19, ZL, C14
SURF, FIN3, PLN20, ZS, C16
SURF, FIN2, PLN1, XL
SURF, FIN2, PLN2, XS
SURF, FIN2, PLN3, YL
SURF, FIN2, PLN4, YS

COMP16, MAT1
SURF, FIN3, PLN20, ZL, C15
SURF, FIN3, PLN21, ZS, C17
SURF, FIN4, PLN1, XL
SURF, FIN4, PLN2, XS
SURF, FIN4, PLN3, YL
SURF, FIN4, PLN4, YS

COMP17, MAT1
SURF, FIN3, PLN21, ZL, C16
SURF, FIN3, PLN22, ZS, C18
SURF, FIN2, PLN1, XL
SURF, FIN2, PLN2, XS
SURF, FIN2, PLN3, YL
SURF, FIN2, PLN4, YS

COMP18, MAT1
SURF, FIN3, PLN22, ZL, C17
SURF, FIN3, PLN23, ZS, C19
SURF, FIN4, PLN1, XL
SURF, FIN4, PLN2, XS
SURF, FIN4, PLN3, YL
SURF, FIN4, PLN4, YS

COMP19, MAT1
SURF, FIN3, PLN23, ZL, C18
SURF, FIN3, PLN24, ZS, C20
SURF, FIN2, PLN1, XL
SURF, FIN2, PLN2, XS
SURF, FIN2, PLN3, YL
SURF, FIN2, PLN4, YS

COMP20, MAT1
SURF, FIN3, PLN24, ZL, C19
SURF, FIN3, PLN25, ZS, C21
SURF, FIN4, PLN1, XL
SURF, FIN4, PLN2, XS
SURF, FIN4, PLN3, YL
SURF, FIN4, PLN4, YS

COMP21, MAT1
SURF, FIN3, PLN25, ZL, C20
```

```
SURF, FIN3, PLN26, ZS, C22
SURF, FIN2, PLN1, XL
SURF, FIN2, PLN2, XS
SURF, FIN2, PLN3, YL
SURF, FIN2, PLN4, YS

COMP22, MAT1
SURF, FIN3, PLN26, ZL, C21
SURF, FIN3, PLN27, ZS, C23
SURF, FIN4, PLN1, XL
SURF, FIN4, PLN2, XS
SURF, FIN4, PLN3, YL
SURF, FIN4, PLN4, YS

COMP23, MAT1
SURF, FIN3, PLN27, ZL, C22
SURF, FIN3, PLN28, ZS, C24
SURF, FIN2, PLN1, XL
SURF, FIN2, PLN2, XS
SURF, FIN2, PLN3, YL
SURF, FIN2, PLN4, YS

COMP24, MAT1
SURF, FIN3, PLN28, ZL, C23
SURF, FIN3, PLN29, ZS, C25
SURF, FIN4, PLN1, XL
SURF, FIN4, PLN2, XS
SURF, FIN4, PLN3, YL
SURF, FIN4, PLN4, YS

COMP25, MAT1
SURF, FIN3, PLN29, ZL, C24
SURF, FIN3, PLN30, ZS, C26
SURF, FIN2, PLN1, XL
SURF, FIN2, PLN2, XS
SURF, FIN2, PLN3, YL
SURF, FIN2, PLN4, YS

COMP26, MAT1
SURF, FIN3, PLN30, ZL, C25
SURF, FIN3, PLN31, ZS, C27
SURF, FIN4, PLN1, XL
SURF, FIN4, PLN2, XS
SURF, FIN4, PLN3, YL
SURF, FIN4, PLN4, YS

COMP27, MAT1
SURF, FIN3, PLN31, ZL, C26
SURF, FIN3, PLN32, ZS, C28
SURF, FIN2, PLN1, XL
SURF, FIN2, PLN2, XS
SURF, FIN2, PLN3, YL
SURF, FIN2, PLN4, YS

COMP28, MAT1
SURF, FIN3, PLN32, ZL, C27
SURF, FIN3, PLN33, ZS, C29
```

```
SURF, FIN4, PLN1, XL
SURF, FIN4, PLN2, XS
SURF, FIN4, PLN3, YL
SURF, FIN4, PLN4, YS

COMP29, MAT1
SURF, FIN3, PLN33, ZL, C28
SURF, FIN3, PLN34, ZS, C30
SURF, FIN2, PLN1, XL
SURF, FIN2, PLN2, XS
SURF, FIN2, PLN3, YL
SURF, FIN2, PLN4, YS

COMP30, MAT1
SURF, FIN3, PLN34, ZL, C29
SURF, FIN3, PLN35, ZS, C31
SURF, FIN4, PLN1, XL
SURF, FIN4, PLN2, XS
SURF, FIN4, PLN3, YL
SURF, FIN4, PLN4, YS

COMP31, MAT1
SURF, FIN3, PLN35, ZL, C30
SURF, FIN3, PLN36, ZS, C32
SURF, FIN2, PLN1, XL
SURF, FIN2, PLN2, XS
SURF, FIN2, PLN3, YL
SURF, FIN2, PLN4, YS

COMP32, MAT1
SURF, FIN3, PLN36, ZL, C31
SURF, FIN3, PLN37, ZS, C33
SURF, FIN4, PLN1, XL
SURF, FIN4, PLN2, XS
SURF, FIN4, PLN3, YL
SURF, FIN4, PLN4, YS

COMP33, MAT1
SURF, FIN3, PLN37, ZL, C32
SURF, FIN3, PLN38, ZS, C34
SURF, FIN2, PLN1, XL
SURF, FIN2, PLN2, XS
SURF, FIN2, PLN3, YL
SURF, FIN2, PLN4, YS

COMP34, MAT1
SURF, FIN3, PLN38, ZL, C33
SURF, FIN3, PLN39, ZS, C35
SURF, FIN4, PLN1, XL
SURF, FIN4, PLN2, XS
SURF, FIN4, PLN3, YL
SURF, FIN4, PLN4, YS

COMP35, MAT1
SURF, FIN3, PLN39, ZL, C34
SURF, FIN3, PLN40, ZS, C36
SURF, FIN2, PLN1, XL
```

```
SURF, FIN2, PLN2, XS
SURF, FIN2, PLN3, YL
SURF, FIN2, PLN4, YS

COMP36, MAT1
SURF, FIN3, PLN40, ZL, C35
SURF, FIN3, PLN41, ZS, C37
SURF, FIN4, PLN1, XL
SURF, FIN4, PLN2, XS
SURF, FIN4, PLN3, YL
SURF, FIN4, PLN4, YS

COMP37, MAT1
SURF, FIN3, PLN41, ZL, C36
SURF, FIN3, PLN42, ZS, C38
SURF, FIN2, PLN1, XL
SURF, FIN2, PLN2, XS
SURF, FIN2, PLN3, YL
SURF, FIN2, PLN4, YS


COMP38, MAT2                          ; optical grease ON THE RIGHT END
SURF, FIN3, PLN42, ZL, C37
SURF, FIN3, PLN43, ZS, C39
SURF, FIN3, PLN1, XL
SURF, FIN3, PLN2, XS
SURF, FIN3, PLN3, YL
SURF, FIN3, PLN4, YS


COMP39, MAT3          ; 0.8 mm PMT Window glass slab 23.5x23.5 mm2 on
the right
SURF, FIN3, PLN43, ZL, C38
SURF, FIN1, PLN44, ZS
SURF, FIN3, PLN101, XL
SURF, FIN3, PLN202, XS
SURF, FIN3, PLN303, YL
SURF, FIN3, PLN404, YS



LIFE1000

;FATES file for each history recording
;FATES1
SEED10000


GEN, MAT1, -0XS, 0XL, -0YS, 0YL, -40ZS, -40ZL   ; Generate optical
photons at the 1 cm of the crystal from PMT1 (0, 0,-40)

RUN10000

END
```

; DETECT2000 script for interleaved etching band patterns created in a 2x2x100 mm LYSO Crystal wrapped in Teflon

```
; Define materials
DMAT1, 1.82NV, 150ADV,
900000000000000000000000000000000000000000000000000000SDV, 1PLF, DT1,
40TAU, 1.0TAUW   ; LYSO crystal
DMAT2, 1.463NV                                          ; Optical
Grease VISILOX V-788
DMAT3, 1.5NV                                            ; Borosilicate
glass RI=1.5

; Define the surface finish
DFIN1, DETECT, 1QEF  ; PMT Cathode surface on both sides of the crystal
DFIN2, POLISH, 0.92RCV         ; 4 long polished surfaces of crystal
wrapped in Teflon with RC=0.92 or so
DFIN3, POLISH                                             ;2 end faces
of the crystal and optical grease
DFIN4, UNIFIED, 1DLV, 0.92RCV             ; Ground bands covered with
diffusive reflector (Teflon Tap)


; Define the six planes bounding the crystal and two other planes for
end faces of glue orthogonal to Z-axis
DPLN1, -1X
DPLN2,  1X
DPLN3, -1Y
DPLN4,  1Y
DPLN5, -51.1z     ; 0.8 mm PMT glass window slab face on the left side
DPLN6, -50.3Z      ; Optical grease (0.3 mm) end face (facing
orthogonal to negative Z-axis)
DPLN7, -50Z

DPLN8, -40.5Z           ; a ground etching band of 1.0 mm
DPLN9, -39.5Z
DPLN10, -38.0Z          ; interleaved bands on top and bottom surfaces
DPLN11, -37.0Z
DPLN12, -35.5Z
DPLN13, -34.5Z
DPLN14, -33.0Z
DPLN15, -32.0Z
DPLN16, -30.5Z
DPLN17, -29.5Z
DPLN18, -28.0Z
DPLN19, -27.0Z
DPLN20, -25.5Z
DPLN21, -24.5Z
DPLN22, -23.0Z
DPLN23, -22.0Z
DPLN24, -20.5Z
DPLN25, -19.5Z
DPLN26, -18.0Z
DPLN27, -17.0Z
DPLN28, -15.5Z
DPLN29, -14.5Z
DPLN30, -13.0Z
DPLN31, -12.0Z
```

```
DPLN32, -10.5Z
DPLN33, -9.5Z
DPLN34, -8.0Z
DPLN35, -7.0Z
DPLN36, -5.5Z
DPLN37, -4.5Z
DPLN38, -3.0Z
DPLN39, -2.0Z
DPLN40, -0.5Z
DPLN41, 0.5Z
DPLN42, 2.0Z
DPLN43, 3.0Z
DPLN44, 4.5Z
DPLN45, 5.5Z
DPLN46, 7.0Z
DPLN47, 8.0Z
DPLN48, 9.5Z
DPLN49, 10.5Z
DPLN50, 12.0Z
DPLN51, 13.0Z
DPLN52, 14.5Z
DPLN53, 15.5Z
DPLN54, 17.0Z
DPLN55, 18.0Z
DPLN56, 19.5Z
DPLN57, 20.5Z
DPLN58, 22.0Z
DPLN59, 23.0Z
DPLN60, 24.5Z
DPLN61, 25.5Z
DPLN62, 27.0Z
DPLN63, 28.0Z
DPLN64, 29.5Z
DPLN65, 30.5Z
DPLN66, 32.0Z
DPLN67, 33.0Z
DPLN68, 34.5Z
DPLN69, 35.5Z
DPLN70, 37.0Z
DPLN71, 38.0Z
DPLN72, 39.5Z
DPLN73, 40.5Z

DPLN74 50Z
DPLN75, 50.3Z               ; Optical grease end face orthogonal to
positive Z-axis
DPLN76, 51.1z               ; 0.8 mm PMT glass window slab face on the
right side

DPLN101, -11.75X
DPLN202,  11.75X
DPLN303, -11.75Y
DPLN404,  11.75Y


; Define 71 components with 3 materials
```

```
COMP1, MAT3          ; 0.8 mm PMT Window glass slab on the left
SURF, FIN1, PLN5, ZL          ; define the surface finish
SURF, FIN3, PLN6, ZS, C2
SURF, FIN3, PLN101, XL
SURF, FIN3, PLN202, XS
SURF, FIN3, PLN303, YL
SURF, FIN3, PLN404, YS


COMP2, MAT2          ; optical grease ON THE LEFT END
SURF, FIN3, PLN6, ZL, C1
SURF, FIN3, PLN7, ZS, C3
SURF, FIN3, PLN1, XL
SURF, FIN3, PLN2, XS
SURF, FIN3, PLN3, YL
SURF, FIN3, PLN4, YS

COMP3, MAT1          ;LYSO CRYSTAL
SURF, FIN3, PLN7, ZL, C2
SURF, FIN3, PLN8, ZS, C4
SURF, FIN2, PLN1, XL
SURF, FIN2, PLN2, XS
SURF, FIN2, PLN3, YL
SURF, FIN2, PLN4, YS

COMP4, MAT1
SURF, FIN3, PLN8, ZL, C3
SURF, FIN3, PLN9, ZS, C5
SURF, FIN4, PLN1, XL
SURF, FIN2, PLN2, XS
SURF, FIN2, PLN3, YL
SURF, FIN2, PLN4, YS        ; Ground etching band of 0.8 mm

COMP5, MAT1
SURF, FIN3, PLN9, ZL, C4
SURF, FIN3, PLN10, ZS, C6
SURF, FIN2, PLN1, XL
SURF, FIN2, PLN2, XS
SURF, FIN2, PLN3, YL
SURF, FIN2, PLN4, YS

COMP6, MAT1
SURF, FIN3, PLN10, ZL, C5
SURF, FIN3, PLN11, ZS, C7
SURF, FIN2, PLN1, XL
SURF, FIN4, PLN2, XS
SURF, FIN2, PLN3, YL
SURF, FIN2, PLN4, YS

COMP7, MAT1
SURF, FIN3, PLN11, ZL, C6
SURF, FIN3, PLN12, ZS, C8
SURF, FIN2, PLN1, XL
SURF, FIN2, PLN2, XS
SURF, FIN2, PLN3, YL
SURF, FIN2, PLN4, YS
```

```
COMP8, MAT1
SURF, FIN3, PLN12, ZL, C7
SURF, FIN3, PLN13, ZS, C9
SURF, FIN4, PLN1, XL
SURF, FIN2, PLN2, XS
SURF, FIN2, PLN3, YL
SURF, FIN2, PLN4, YS

COMP9, MAT1
SURF, FIN3, PLN13, ZL, C8
SURF, FIN3, PLN14, ZS, C10
SURF, FIN2, PLN1, XL
SURF, FIN2, PLN2, XS
SURF, FIN2, PLN3, YL
SURF, FIN2, PLN4, YS

COMP10, MAT1
SURF, FIN3, PLN14, ZL, C9
SURF, FIN3, PLN15, ZS, C11
SURF, FIN2, PLN1, XL
SURF, FIN4, PLN2, XS
SURF, FIN2, PLN3, YL
SURF, FIN2, PLN4, YS

COMP11, MAT1
SURF, FIN3, PLN15, ZL, C10
SURF, FIN3, PLN16, ZS, C12
SURF, FIN2, PLN1, XL
SURF, FIN2, PLN2, XS
SURF, FIN2, PLN3, YL
SURF, FIN2, PLN4, YS

COMP12, MAT1
SURF, FIN3, PLN16, ZL, C11
SURF, FIN3, PLN17, ZS, C13
SURF, FIN4, PLN1, XL
SURF, FIN2, PLN2, XS
SURF, FIN2, PLN3, YL
SURF, FIN2, PLN4, YS

COMP13, MAT1
SURF, FIN3, PLN17, ZL, C12
SURF, FIN3, PLN18, ZS, C14
SURF, FIN2, PLN1, XL
SURF, FIN2, PLN2, XS
SURF, FIN2, PLN3, YL
SURF, FIN2, PLN4, YS

COMP14, MAT1
SURF, FIN3, PLN18, ZL, C13
SURF, FIN3, PLN19, ZS, C15
SURF, FIN2, PLN1, XL
SURF, FIN4, PLN2, XS
SURF, FIN2, PLN3, YL
SURF, FIN2, PLN4, YS

COMP15, MAT1
```

```
SURF, FIN3, PLN19, ZL, C14
SURF, FIN3, PLN20, ZS, C16
SURF, FIN2, PLN1, XL
SURF, FIN2, PLN2, XS
SURF, FIN2, PLN3, YL
SURF, FIN2, PLN4, YS

COMP16, MAT1
SURF, FIN3, PLN20, ZL, C15
SURF, FIN3, PLN21, ZS, C17
SURF, FIN4, PLN1, XL
SURF, FIN2, PLN2, XS
SURF, FIN2, PLN3, YL
SURF, FIN2, PLN4, YS

COMP17, MAT1
SURF, FIN3, PLN21, ZL, C16
SURF, FIN3, PLN22, ZS, C18
SURF, FIN2, PLN1, XL
SURF, FIN2, PLN2, XS
SURF, FIN2, PLN3, YL
SURF, FIN2, PLN4, YS

COMP18, MAT1
SURF, FIN3, PLN22, ZL, C17
SURF, FIN3, PLN23, ZS, C19
SURF, FIN2, PLN1, XL
SURF, FIN4, PLN2, XS
SURF, FIN2, PLN3, YL
SURF, FIN2, PLN4, YS

COMP19, MAT1
SURF, FIN3, PLN23, ZL, C18
SURF, FIN3, PLN24, ZS, C20
SURF, FIN2, PLN1, XL
SURF, FIN2, PLN2, XS
SURF, FIN2, PLN3, YL
SURF, FIN2, PLN4, YS

COMP20, MAT1
SURF, FIN3, PLN24, ZL, C19
SURF, FIN3, PLN25, ZS, C21
SURF, FIN4, PLN1, XL
SURF, FIN2, PLN2, XS
SURF, FIN2, PLN3, YL
SURF, FIN2, PLN4, YS

COMP21, MAT1
SURF, FIN3, PLN25, ZL, C20
SURF, FIN3, PLN26, ZS, C22
SURF, FIN2, PLN1, XL
SURF, FIN2, PLN2, XS
SURF, FIN2, PLN3, YL
SURF, FIN2, PLN4, YS

COMP22, MAT1
SURF, FIN3, PLN26, ZL, C21
```

```
SURF, FIN3, PLN27, ZS, C23
SURF, FIN2, PLN1, XL
SURF, FIN4, PLN2, XS
SURF, FIN2, PLN3, YL
SURF, FIN2, PLN4, YS

COMP23, MAT1
SURF, FIN3, PLN27, ZL, C22
SURF, FIN3, PLN28, ZS, C24
SURF, FIN2, PLN1, XL
SURF, FIN2, PLN2, XS
SURF, FIN2, PLN3, YL
SURF, FIN2, PLN4, YS

COMP24, MAT1
SURF, FIN3, PLN28, ZL, C23
SURF, FIN3, PLN29, ZS, C25
SURF, FIN4, PLN1, XL
SURF, FIN2, PLN2, XS
SURF, FIN2, PLN3, YL
SURF, FIN2, PLN4, YS

COMP25, MAT1
SURF, FIN3, PLN29, ZL, C24
SURF, FIN3, PLN30, ZS, C26
SURF, FIN2, PLN1, XL
SURF, FIN2, PLN2, XS
SURF, FIN2, PLN3, YL
SURF, FIN2, PLN4, YS

COMP26, MAT1
SURF, FIN3, PLN30, ZL, C25
SURF, FIN3, PLN31, ZS, C27
SURF, FIN2, PLN1, XL
SURF, FIN4, PLN2, XS
SURF, FIN2, PLN3, YL
SURF, FIN2, PLN4, YS

COMP27, MAT1
SURF, FIN3, PLN31, ZL, C26
SURF, FIN3, PLN32, ZS, C28
SURF, FIN2, PLN1, XL
SURF, FIN2, PLN2, XS
SURF, FIN2, PLN3, YL
SURF, FIN2, PLN4, YS

COMP28, MAT1
SURF, FIN3, PLN32, ZL, C27
SURF, FIN3, PLN33, ZS, C29
SURF, FIN4, PLN1, XL
SURF, FIN2, PLN2, XS
SURF, FIN2, PLN3, YL
SURF, FIN2, PLN4, YS

COMP29, MAT1
SURF, FIN3, PLN33, ZL, C28
SURF, FIN3, PLN34, ZS, C30
```

```
SURF, FIN2, PLN1, XL
SURF, FIN2, PLN2, XS
SURF, FIN2, PLN3, YL
SURF, FIN2, PLN4, YS

COMP30, MAT1
SURF, FIN3, PLN34, ZL, C29
SURF, FIN3, PLN35, ZS, C31
SURF, FIN2, PLN1, XL
SURF, FIN4, PLN2, XS
SURF, FIN2, PLN3, YL
SURF, FIN2, PLN4, YS

COMP31, MAT1
SURF, FIN3, PLN35, ZL, C30
SURF, FIN3, PLN36, ZS, C32
SURF, FIN2, PLN1, XL
SURF, FIN2, PLN2, XS
SURF, FIN2, PLN3, YL
SURF, FIN2, PLN4, YS

COMP32, MAT1
SURF, FIN3, PLN36, ZL, C31
SURF, FIN3, PLN37, ZS, C33
SURF, FIN4, PLN1, XL
SURF, FIN2, PLN2, XS
SURF, FIN2, PLN3, YL
SURF, FIN2, PLN4, YS

COMP33, MAT1
SURF, FIN3, PLN37, ZL, C32
SURF, FIN3, PLN38, ZS, C34
SURF, FIN2, PLN1, XL
SURF, FIN2, PLN2, XS
SURF, FIN2, PLN3, YL
SURF, FIN2, PLN4, YS

COMP34, MAT1
SURF, FIN3, PLN38, ZL, C33
SURF, FIN3, PLN39, ZS, C35
SURF, FIN2, PLN1, XL
SURF, FIN4, PLN2, XS
SURF, FIN2, PLN3, YL
SURF, FIN2, PLN4, YS

COMP35, MAT1
SURF, FIN3, PLN39, ZL, C34
SURF, FIN3, PLN40, ZS, C36
SURF, FIN2, PLN1, XL
SURF, FIN2, PLN2, XS
SURF, FIN2, PLN3, YL
SURF, FIN2, PLN4, YS

COMP36, MAT1
SURF, FIN3, PLN40, ZL, C35
SURF, FIN3, PLN41, ZS, C37
SURF, FIN4, PLN1, XL
```

```
SURF, FIN2, PLN2, XS
SURF, FIN2, PLN3, YL
SURF, FIN2, PLN4, YS

COMP37, MAT1
SURF, FIN3, PLN41, ZL, C36
SURF, FIN3, PLN42, ZS, C38
SURF, FIN2, PLN1, XL
SURF, FIN2, PLN2, XS
SURF, FIN2, PLN3, YL
SURF, FIN2, PLN4, YS

COMP38, MAT1
SURF, FIN3, PLN42, ZL, C37
SURF, FIN3, PLN43, ZS, C39
SURF, FIN2, PLN1, XL
SURF, FIN4, PLN2, XS
SURF, FIN2, PLN3, YL
SURF, FIN2, PLN4, YS

COMP39, MAT1
SURF, FIN3, PLN43, ZL, C38
SURF, FIN3, PLN44, ZS, C40
SURF, FIN2, PLN1, XL
SURF, FIN2, PLN2, XS
SURF, FIN2, PLN3, YL
SURF, FIN2, PLN4, YS

COMP40, MAT1
SURF, FIN3, PLN44, ZL, C39
SURF, FIN3, PLN45, ZS, C41
SURF, FIN4, PLN1, XL
SURF, FIN2, PLN2, XS
SURF, FIN2, PLN3, YL
SURF, FIN2, PLN4, YS

COMP41, MAT1
SURF, FIN3, PLN45, ZL, C40
SURF, FIN3, PLN46, ZS, C42
SURF, FIN2, PLN1, XL
SURF, FIN2, PLN2, XS
SURF, FIN2, PLN3, YL
SURF, FIN2, PLN4, YS

COMP42, MAT1
SURF, FIN3, PLN46, ZL, C41
SURF, FIN3, PLN47, ZS, C43
SURF, FIN2, PLN1, XL
SURF, FIN4, PLN2, XS
SURF, FIN2, PLN3, YL
SURF, FIN2, PLN4, YS

COMP43, MAT1
SURF, FIN3, PLN47, ZL, C42
SURF, FIN3, PLN48, ZS, C44
SURF, FIN2, PLN1, XL
SURF, FIN2, PLN2, XS
```

```
SURF, FIN2, PLN3, YL
SURF, FIN2, PLN4, YS

COMP44, MAT1
SURF, FIN3, PLN48, ZL, C43
SURF, FIN3, PLN49, ZS, C45
SURF, FIN4, PLN1, XL
SURF, FIN2, PLN2, XS
SURF, FIN2, PLN3, YL
SURF, FIN2, PLN4, YS

COMP45, MAT1
SURF, FIN3, PLN49, ZL, C44
SURF, FIN3, PLN50, ZS, C46
SURF, FIN2, PLN1, XL
SURF, FIN2, PLN2, XS
SURF, FIN2, PLN3, YL
SURF, FIN2, PLN4, YS

COMP46, MAT1
SURF, FIN3, PLN50, ZL, C45
SURF, FIN3, PLN51, ZS, C47
SURF, FIN2, PLN1, XL
SURF, FIN4, PLN2, XS
SURF, FIN2, PLN3, YL
SURF, FIN2, PLN4, YS

COMP47, MAT1
SURF, FIN3, PLN51, ZL, C46
SURF, FIN3, PLN52, ZS, C48
SURF, FIN2, PLN1, XL
SURF, FIN2, PLN2, XS
SURF, FIN2, PLN3, YL
SURF, FIN2, PLN4, YS

COMP48, MAT1
SURF, FIN3, PLN52, ZL, C47
SURF, FIN3, PLN53, ZS, C49
SURF, FIN4, PLN1, XL
SURF, FIN2, PLN2, XS
SURF, FIN2, PLN3, YL
SURF, FIN2, PLN4, YS

COMP49, MAT1
SURF, FIN3, PLN53, ZL, C48
SURF, FIN3, PLN54, ZS, C50
SURF, FIN2, PLN1, XL
SURF, FIN2, PLN2, XS
SURF, FIN2, PLN3, YL
SURF, FIN2, PLN4, YS

COMP50, MAT1
SURF, FIN3, PLN54, ZL, C49
SURF, FIN3, PLN55, ZS, C51
SURF, FIN2, PLN1, XL
SURF, FIN4, PLN2, XS
SURF, FIN2, PLN3, YL
```

```
SURF, FIN2, PLN4, YS

COMP51, MAT1
SURF, FIN3, PLN55, ZL, C50
SURF, FIN3, PLN56, ZS, C52
SURF, FIN2, PLN1, XL
SURF, FIN2, PLN2, XS
SURF, FIN2, PLN3, YL
SURF, FIN2, PLN4, YS

COMP52, MAT1
SURF, FIN3, PLN56, ZL, C51
SURF, FIN3, PLN57, ZS, C53
SURF, FIN4, PLN1, XL
SURF, FIN2, PLN2, XS
SURF, FIN2, PLN3, YL
SURF, FIN2, PLN4, YS

COMP53, MAT1
SURF, FIN3, PLN57, ZL, C52
SURF, FIN3, PLN58, ZS, C54
SURF, FIN2, PLN1, XL
SURF, FIN2, PLN2, XS
SURF, FIN2, PLN3, YL
SURF, FIN2, PLN4, YS

COMP54, MAT1
SURF, FIN3, PLN58, ZL, C53
SURF, FIN3, PLN59, ZS, C55
SURF, FIN2, PLN1, XL
SURF, FIN4, PLN2, XS
SURF, FIN2, PLN3, YL
SURF, FIN2, PLN4, YS

COMP55, MAT1
SURF, FIN3, PLN59, ZL, C54
SURF, FIN3, PLN60, ZS, C56
SURF, FIN2, PLN1, XL
SURF, FIN2, PLN2, XS
SURF, FIN2, PLN3, YL
SURF, FIN2, PLN4, YS

COMP56, MAT1
SURF, FIN3, PLN60, ZL, C55
SURF, FIN3, PLN61, ZS, C57
SURF, FIN4, PLN1, XL
SURF, FIN2, PLN2, XS
SURF, FIN2, PLN3, YL
SURF, FIN2, PLN4, YS

COMP57, MAT1
SURF, FIN3, PLN61, ZL, C56
SURF, FIN3, PLN62, ZS, C58
SURF, FIN2, PLN1, XL
SURF, FIN2, PLN2, XS
SURF, FIN2, PLN3, YL
SURF, FIN2, PLN4, YS
```

```
COMP58, MAT1
SURF, FIN3, PLN62, ZL, C57
SURF, FIN3, PLN63, ZS, C59
SURF, FIN2, PLN1, XL
SURF, FIN4, PLN2, XS
SURF, FIN2, PLN3, YL
SURF, FIN2, PLN4, YS

COMP59, MAT1
SURF, FIN3, PLN63, ZL, C58
SURF, FIN3, PLN64, ZS, C60
SURF, FIN2, PLN1, XL
SURF, FIN2, PLN2, XS
SURF, FIN2, PLN3, YL
SURF, FIN2, PLN4, YS

COMP60, MAT1
SURF, FIN3, PLN64, ZL, C59
SURF, FIN3, PLN65, ZS, C61
SURF, FIN4, PLN1, XL
SURF, FIN2, PLN2, XS
SURF, FIN2, PLN3, YL
SURF, FIN2, PLN4, YS

COMP61, MAT1
SURF, FIN3, PLN65, ZL, C60
SURF, FIN3, PLN66, ZS, C62
SURF, FIN2, PLN1, XL
SURF, FIN2, PLN2, XS
SURF, FIN2, PLN3, YL
SURF, FIN2, PLN4, YS

COMP62, MAT1
SURF, FIN3, PLN66, ZL, C61
SURF, FIN3, PLN67, ZS, C63
SURF, FIN2, PLN1, XL
SURF, FIN4, PLN2, XS
SURF, FIN2, PLN3, YL
SURF, FIN2, PLN4, YS

COMP63, MAT1
SURF, FIN3, PLN67, ZL, C62
SURF, FIN3, PLN68, ZS, C64
SURF, FIN2, PLN1, XL
SURF, FIN2, PLN2, XS
SURF, FIN2, PLN3, YL
SURF, FIN2, PLN4, YS

COMP64, MAT1
SURF, FIN3, PLN68, ZL, C63
SURF, FIN3, PLN69, ZS, C65
SURF, FIN4, PLN1, XL
SURF, FIN2, PLN2, XS
SURF, FIN2, PLN3, YL
SURF, FIN2, PLN4, YS
```

```
COMP65, MAT1
SURF, FIN3, PLN69, ZL, C64
SURF, FIN3, PLN70, ZS, C66
SURF, FIN2, PLN1, XL
SURF, FIN2, PLN2, XS
SURF, FIN2, PLN3, YL
SURF, FIN2, PLN4, YS

COMP66, MAT1
SURF, FIN3, PLN70, ZL, C65
SURF, FIN3, PLN71, ZS, C67
SURF, FIN2, PLN1, XL
SURF, FIN4, PLN2, XS
SURF, FIN2, PLN3, YL
SURF, FIN2, PLN4, YS

COMP67, MAT1
SURF, FIN3, PLN71, ZL, C66
SURF, FIN3, PLN72, ZS, C68
SURF, FIN2, PLN1, XL
SURF, FIN2, PLN2, XS
SURF, FIN2, PLN3, YL
SURF, FIN2, PLN4, YS

COMP68, MAT1
SURF, FIN3, PLN72, ZL, C67
SURF, FIN3, PLN73, ZS, C69
SURF, FIN4, PLN1, XL
SURF, FIN2, PLN2, XS
SURF, FIN2, PLN3, YL
SURF, FIN2, PLN4, YS

COMP69, MAT1
SURF, FIN3, PLN73, ZL, C68
SURF, FIN3, PLN74, ZS, C70
SURF, FIN2, PLN1, XL
SURF, FIN2, PLN2, XS
SURF, FIN2, PLN3, YL
SURF, FIN2, PLN4, YS

COMP70, MAT2                          ; optical grease ON THE RIGHT END
SURF, FIN3, PLN74, ZL, C69
SURF, FIN3, PLN75, ZS, C71
SURF, FIN3, PLN1, XL
SURF, FIN3, PLN2, XS
SURF, FIN3, PLN3, YL
SURF, FIN3, PLN4, YS


COMP71, MAT3          ; 0.8 mm PMT Window glass slab 23.5x23.5 mm2 on
the right
SURF, FIN3, PLN75, ZL, C70
SURF, FIN1, PLN76, ZS
SURF, FIN3, PLN101, XL
SURF, FIN3, PLN202, XS
SURF, FIN3, PLN303, YL
SURF, FIN3, PLN404, YS
```

```
LIFE1000

;FATES file for each history recording
;FATES1


SEED10000


GEN, MAT1, -0XS, 0XL, -0YS, 0YL, -40ZS, -40ZL   ; Generate optical
photons at the 1 cm of the crystal from PMT1 (0,0,-40)

RUN10000

END
```

Appendix D Linux shell script to run DETECT2000 simulation 10000 times, append/store the output data and change the seed in each simulation

 # Linux shell script to run each DETECT simulation 10000 times at each gamma interaction position of the crystal (1-9 cm)

```
count1=1
while [ $count1 -le 9 ]                    # Changing the interaction position 1-9 cm by
do
                                           # selecting a new Detect input file each time

  count2=1
  while [ $count2 -le 10000 ]              # 10000 gamma simulations
  do                                       # 1 gamma simulation is 10000 optical photons

        sed -i 395d fourband$count1.det                    # delete line 395 in the input
                                                           # Detect file one band?
        sed -i "395iSEED$count2" fourband$count1.det       # add new SEED to
                                                           #line 395 of the same input file

        cat fourband$count1.det | Detect2000       # Run Detect2000 simulation
        cat pmt.dat>>step$count1.dat               # Append the output data from
                                                   #pmt.dat to step?.dat file for each simulation
        rm pmt.dat                                 # Delete pmt.dat file after appending the data


    shift
    count2=`expr $count2 + 1`
  done


 shift
 count1=`expr $count1 + 1`
done
```

References

(1) Phelps ME. PET: the merging of biology and imaging into molecular imaging. Journal of Nuclear Medicine 2000;41(4):661-681.

(2) Ido T, Wan CN, Casella V, Fowler J, Wolf A, Reivich M, et al. Labeled 2‐deoxy‐D‐glucose analogs. 18F‐labeled 2‐deoxy‐2‐fluoro‐D‐glucose, 2‐deoxy‐2‐fluoro‐D‐mannose and 14C‐2‐deoxy‐2‐fluoro‐D‐glucose. J Labelled Compd Radiopharmaceut 1978;14(2):175-183.

(3) Tewson TJ, Welch MJ, Raichle ME. 18F]-labeled 3-deoxy-3-fluoro-D-glucose: synthesis and preliminary biodistribution data. J Nucl Med 1978 Dec;19(12):1339-1345.

(4) Phelps M, Huang S, Hoffman E, Selin C, Sokoloff L, Kuhl D. Tomographic measurement of local cerebral glucose metabolic rate in humans with (F‐18) 2‐fluoro‐2‐deoxy‐D‐glucose: validation of method. Ann Neurol 1979;6(5):371-388.

(5) Reske SN, Kotzerke J. FDG-PET for clinical use. European Journal of Nuclear Medicine and Molecular Imaging 2001;28(11):1707-1723.

(6) Chen W, Cloughesy T, Kamdar N, Satyamurthy N, Bergsneider M, Liau L, et al. Imaging proliferation in brain tumors with 18F-FLT PET: comparison with 18F-FDG. Journal of Nuclear Medicine 2005;46(6):945-952.

(7) van Waarde A, Cobben DCP, Suurmeijer AJH, Maas B, Vaalburg W, de Vries EFJ, et al. Selectivity of 18F-FLT and 18F-FDG for differentiating tumor from inflammation in a rodent model. Journal of Nuclear Medicine 2004;45(4):695.

(8) Evans RD. The atomic nucleus. : McGraw-Hill New York; 1955.

(9) Patro A, Sen P. Parapositronium lifetime. Journal of Physics A: General Physics 1971;4:856.

(10) Levin CS, Hoffman EJ. Calculation of positron range and its effect on the fundamental limit of positron emission tomography system spatial resolution. Phys Med Biol 1999;44:781.

(11) Fermi E, Orear J. Nuclear physics: a course given by Enrico Fermi at the University of Chicago. : University of Chicago press; 1974.

(12) Yamamoto YL, Thompson CJ, Diksic M, Meyer E, Feindel WH. Positron emission tomography. Radiation Physics and Chemistry (1977) 1984;24(3-4):385-403.

(13) Cho Z, Chan J, Ericksson L, Singh M, Graham S, MacDonald N, et al. Positron ranges obtained from biomedically important positron-emitting radionuclides. J.Nucl.Med., v.16, no.12, pp.1174-1176 1975;16(12).

(14) Phelps ME, Hoffman EJ, Huang SC, Ter-Pogossian MM. Effect of positron range on spatial resolution. Journal of nuclear medicine: official publication, Society of Nuclear Medicine 1975;16(7):649.

(15) Derenzo SE. Precision measurement of annihilation point spread distributions for medically important positron emitters. 2010.

(16) Palmer MR, Brownell GL. Annihilation density distribution calculations for medically important positron emitters. Medical Imaging, IEEE Transactions on 1992;11(3):373-378.

(17) Sanchez-Crespo A, Andreo P, Larsson SA. Positron flight in human tissues and its influence on PET image spatial resolution. European journal of nuclear medicine and molecular imaging 2004;31(1):44-51.

(18) Colombino P, Fiscella B, Trossi L. Study of positronium in water and ice from 22 to-144 C by annihilation quanta measurements. Il Nuovo Cimento (1955-1965) 1965;38(2):707-723.

(19) Berko S, Hereford FL. Experimental studies of positron interactions in solids and liquids. Reviews of Modern Physics 1956;28(3):299.

(20) Humm JL, Rosenfeld A, Guerra AD. From PET detectors to PET scanners. European journal of nuclear medicine and molecular imaging 2003;30(11):1574-1597.

(21) Daube-Witherspoon ME, Muehllehner G. Treatment of axial data in three-dimensional PET. J Nucl Med 1987;28(11):1717-1724.

(22) Kinahan PE, Rogers J. Analytic 3D image reconstruction using all detected events. Nuclear Science, IEEE Transactions on 1989;36(1):964-968.

(23) Liu X, Defrise M, Michel C, Sibomana M, Comtat C, Kinahan P, et al. Exact rebinning methods for three-dimensional PET. Medical Imaging, IEEE Transactions on 1999;18(8):657-664.

(24) Hudson HM, Larkin RS. Accelerated image reconstruction using ordered subsets of projection data. Medical Imaging, IEEE Transactions on 1994;13(4):601-609.

(25) Defrise M, Kinahan P. Data acquisition and image reconstruction for 3D PET. DEVELOPMENTS IN NUCLEAR MEDICINE 1998;32:11-54.

(26) Liow JS, Strother S. The convergence of object dependent resolution in maximum likelihood based tomographic image reconstruction. Phys Med Biol 1993;38:55.

(27) Cherry SR, Sorenson JA, Phelps ME. Physics in nuclear medicine. : Elsevier/Saunders; 2012.

(28) Lee J. Technical advances in current PET and hybrid imaging systems. Open Nucl Med J 2010;2:192-208.

(29) Phelps ME. PET: molecular imaging and its biological applications. : Springer Verlag; 2004.

(30) Chow PL, Rannou FR, Chatziioannou AF. Attenuation correction for small animal PET tomographs. Phys Med Biol 2005;50:1837.

(31) Chien KR. Genes and physiology: molecular physiology in genetically engineered animals. J Clin Invest 1996;97(4):901.

(32) Chatziioannou AF. Molecular imaging of small animals with dedicated PET tomographs. Eur J Nucl Med 2002;29(1):98-114.

(33) Lecomte R, Cadorette J, Rodrigue S, Lapointe D, Rouleau D, Bentourkia M, et al. Initial results from the Sherbrooke avalanche photodiode positron tomograph. Nuclear Science, IEEE Transactions on 1996;43(3):1952-1957.

(34) Watanabe M, Okada H, Shimizu K, Omura T, Yoshikawa E, Kosugi T, et al. A high resolution animal PET scanner using compact PS-PMT detectors. Nuclear Science, IEEE Transactions on 1997;44(3):1277-1282.

(35) Bruyndonckx P, Liu X, Tavernier S, Zhang S. Performance study of a 3D small animal PET scanner based on BaF< sub> 2</sub> crystals and a photo sensitive wire chamber. Nuclear Instruments and Methods in Physics Research Section A: Accelerators, Spectrometers, Detectors and Associated Equipment 1997;392(1):407-413.

(36) Bloomfield P, Myers R, Hume S, Spinks T, Lammertsma A, Jones T. Three-dimensional performance of a small-diameter positron emission tomograph. Phys Med Biol 1997;42:389.

(37) Jeavons A, Chandler R, Dettmar C. A 3D HIDAC-PET camera with sub-millimetre resolution for imaging small animals. Nuclear Science, IEEE Transactions on 1999;46(3):468-473.

(38) Weber S, Bauer A, Herzog H, Kehren F, Muhlensiepen H, Vogelbruch J, et al. Recent results of the TierPET scanner. Nuclear Science, IEEE Transactions on 2000;47(4):1665-1669.

(39) Cherry S, Shao Y, Silverman R, Meadors K, Siegel S, Chatziioannou A, et al. MicroPET: a high resolution PET scanner for imaging small animals. Nuclear Science, IEEE Transactions on 1997;44(3):1161-1166.

(40) Tai Y, Chatziioannou A, Siegel S, Young J, Newport D, Goble R, et al. Performance evaluation of the microPET P4: a PET system dedicated to animal imaging. Phys Med Biol 2001;46:1845.

(41) Knoess C, Siegel S, Smith A, Newport D, Richerzhagen N, Winkeler A, et al. Performance evaluation of the microPET R4 PET scanner for rodents. European journal of nuclear medicine and molecular imaging 2003;30(5):737-747.

(42) Tai YC, Ruangma A, Rowland D, Siegel S, Newport DF, Chow PL, et al. Performance evaluation of the microPET focus: a third-generation microPET scanner dedicated to animal imaging. Journal of nuclear medicine 2005;46(3):455-463.

(43) Visser EP, Disselhorst JA, Brom M, Laverman P, Gotthardt M, Oyen WJG, et al. Spatial resolution and sensitivity of the Inveon small-animal PET scanner. Journal of Nuclear Medicine 2009;50(1):139-147.

(44) Kim JS, Lee JS, Im KC, Kim SJ, Kim SY, Lee DS, et al. Performance measurement of the microPET Focus 120 scanner. Journal of Nuclear Medicine 2007;48(9):1527.

(45) Wang Y, Seidel J, Tsui BMW, Vaquero JJ, Pomper MG. Performance evaluation of the GE healthcare eXplore VISTA dual-ring small-animal PET scanner. Journal of Nuclear Medicine 2006;47(11):1891-1900.

(46) Cherry SR, Gambhir SS. Use of positron emission tomography in animal research. ILAR journal 2001;42(3):219-232.

(47) Strome EM, Doudet DJ. Animal models of neurodegenerative disease: insights from in vivo imaging studies. Molecular Imaging and Biology 2007;9(4):186-195.

(48) Adonai N, Nguyen KN, Walsh J, Iyer M, Toyokuni T, Phelps ME, et al. Ex vivo cell labeling with 64Cu–pyruvaldehyde-bis (N4-methylthiosemicarbazone) for imaging cell trafficking in mice with positron-emission tomography. Proc Natl Acad Sci U S A 2002;99(5):3030.

(49) Dandekar M, Tseng JR, Gambhir SS. Reproducibility of 18F-FDG microPET studies in mouse tumor xenografts. Journal of Nuclear Medicine 2007;48(4):602-607.

(50) Abbey CK, Borowsky AD, McGoldrick ET, Gregg JP, Maglione JE, Cardiff RD, et al. In vivo positron-emission tomography imaging of progression and transformation in a mouse model of mammary neoplasia. Proc Natl Acad Sci U S A 2004;101(31):11438.

(51) Yang Y, Rendig S, Siegel S, Newport DF, Cherry SR. Cardiac PET imaging in mice with simultaneous cardiac and respiratory gating. Phys Med Biol 2005;50:2979.

(52) Bergmann R, Pietzsch J. Small animal positron emission tomography in food sciences. Amino Acids 2005;29(4):355-376.

(53) Wu JC, Inubushi M, Sundaresan G, Schelbert HR, Gambhir SS. Positron emission tomography imaging of cardiac reporter gene expression in living rats. Circulation 2002;106(2):180-183.

(54) MacLaren DC, Toyokuni T, Cherry SR, Barrio JR, Phelps ME, Herschman HR, et al. PET imaging of transgene expression. Biol Psychiatry 2000;48(5):337-348.

(55) Yaghoubi SS, Couto MA, Chen CC, Polavaram L, Cui G, Sen L, et al. Preclinical safety evaluation of 18F-FHBG: a PET reporter probe for imaging herpes simplex virus type 1 thymidine kinase (HSV1-tk) or mutant HSV1-sr39tk's expression. Journal of Nuclear Medicine 2006;47(4):706-715.

(56) Hargreaves R. The role of molecular imaging in drug discovery and development. Clinical Pharmacology & Therapeutics 2008;83(2):349-353.

(57) Hichwa R. Are animal scanners really necessary for PET? Journal of Nuclear Medicine 1994;35(8):1396-1397.

(58) Phelps ME. Positron emission tomography provides molecular imaging of biological processes. Proceedings of the National Academy of Sciences 2000;97(16):9226.

(59) Tai YC, Chatziioannou AF, Yang Y, Silverman RW, Meadors K, Siegel S, et al. MicroPET II: design, development and initial performance of an improved microPET scanner for small-animal imaging. Phys Med Biol 2003;48:1519.

(60) Cherry S, Shao Y, Silverman R, Meadors K, Siegel S, Chatziioannou A, et al. MicroPET: a high resolution PET scanner for imaging small animals. Nuclear Science, IEEE Transactions on 1997;44(3):1161-1166.

(61) Design and performance of a new pixelated-LSO/PSPMT gamma-ray detector for high resolution PET imaging. Nuclear Science Symposium Conference Record, 2007. NSS'07. IEEE: IEEE; 2007.

(62) Bao Q, Newport D, Chen M, Stout DB, Chatziioannou AF. Performance evaluation of the Inveon dedicated PET preclinical tomograph based on the NEMA NU-4 standards. Journal of Nuclear Medicine 2009;50(3):401.

(63) Missimer J, Madi Z, Honer M, Keller C, Schubiger A, Ametamey SM. Performance evaluation of the 16-module quad-HIDAC small animal PET camera. Phys Med Biol 2004;49:2069.

(64) Ziegler SI, Pichler BJ, Boening G, Rafecas M, Pimpl W, Lorenz E, et al. A prototype high-resolution animal positron tomograph with avalanche photodiode arrays and LSO crystals. European Journal of Nuclear Medicine and Molecular Imaging 2001;28(2):136-143.

(65) Siegel S, Vaquero J, Aloj L, Seidel J, Jagoda E, Gandler W, et al. Initial results from a PET/planar small animal imaging system. Nuclear Science, IEEE Transactions on 1999;46(3):571-575.

(66) Chatziioannou AF, Cherry SR, Shao Y, Silverman RW, Meadors K, Farquhar TH, et al. Performance evaluation of microPET: a high-resolution lutetium oxyorthosilicate PET scanner for animal imaging. Journal of Nuclear Medicine 1999;40(7):1164.

(67) Brambilla M, Secco C, Dominietto M, Matheoud R, Sacchetti G, Inglese E. Performance characteristics obtained for a new 3-dimensional lutetium oxyorthosilicate–based whole-body PET/CT scanner with the National Electrical Manufacturers Association NU 2-2001 Standard. Journal of Nuclear Medicine 2005;46(12):2083-2091.

(68) Attix FH, Attix FH. Introduction to radiological physics and radiation dosimetry. 1986.

(69) Podgoršak EB. Radiation physics for medical physicists. : Springer Verlag; 2006.

(70) PET: physics, instrumentation, and scanners. PET: Springer; 2006.

(71) Bircher C, Shao Y. Use of internal scintillator radioactivity to calibrate DOI function of a PET detector with a dual-ended-scintillator readout. Med Phys 2012;39(2):777.

(72) Knoll GF. Radiation detection and measurement. : John Wiley & Sons Inc; 2000.

(73) Emission spectra of LSO and LYSO crystals excited by UV light, x-ray and γ-ray. Nuclear Science Symposium Conference Record, 2007. NSS'07. IEEE: IEEE; 2007.

(74) Yoshizawa Y, Takeuchi J. The latest vacuum photodetector. Nuclear Instruments and Methods in Physics Research Section A: Accelerators, Spectrometers, Detectors and Associated Equipment 1997 3/1;387(1–2):33-37.

(75) Olcott PD, Talcott JA, Levin CS, Habte F, Foudray AMK. Compact readout electronics for position sensitive photomultiplier tubes. Nuclear Science, IEEE Transactions on 2005;52(1):21-27.

(76) Anger HO. Scintillation camera. Rev Sci Instrum 1958;29(1):27-33.

(77) Ito M, Hong SJ, Lee JS. Positron emission tomography (PET) detectors with depth-of-interaction (DOI) capability. Biomedical Engineering Letters 2011;1(2):70-81.

(78) Mosset JB, Devroede O, Krieguer M, Rey M, Vieira JM, Jung J, et al. Development of an optimized LSO/LuYAP phoswich detector head for the Lausanne ClearPET demonstrator. Nuclear Science, IEEE Transactions on 2006;53(1):25-29.

(79) Seidel J, Vaquero JJ, Green MV. Resolution uniformity and sensitivity of the NIH ATLAS small animal PET scanner: comparison to simulated LSO scanners without depth-of-interaction capability. Nuclear Science, IEEE Transactions on 2003;50(5):1347-1350.

(80) Karp JS, Daube-Witherspoon ME. Depth-of-interaction determination in NaI (Tl) and BGO scintillation crystals using a temperature gradient. Nuclear Instruments and Methods in Physics Research Section A: Accelerators, Spectrometers, Detectors and Associated Equipment 1987;260(2-3):509-517.

(81) Jung JH, Choi Y, Chung YH, Devroede O, Krieguer M, Bruyndonckx P, et al. Optimization of LSO/LuYAP phoswich detector for small animal PET. Nuclear Instruments and Methods in Physics Research Section A: Accelerators, Spectrometers, Detectors and Associated Equipment 2007;571(3):669-675.

(82) Schmand M, Eriksson L, Casey M, Andreaco M, Melcher C, Wienhard K, et al. Performance results of a new DOI detector block for a high resolution PET-LSO research tomograph HRRT. Nuclear Science, IEEE Transactions on 1998;45(6):3000-3006.

(83) Wienhard K, Schmand M, Casey M, Baker K, Bao J, Eriksson L, et al. The ECAT HRRT: performance and first clinical application of the new high resolution research tomograph. Nuclear Science, IEEE Transactions on 2002;49(1):104-110.

(84) Seidel J, Vaquero J, Siegel S, Gandler W, Green M. Depth identification accuracy of a three layer phoswich PET detector module. Nuclear Science, IEEE Transactions on 1999;46(3):485-490.

(85) Chandrikamohan P, Devol TA. Comparison of Pulse Shape Discrimination Methods for Phoswich and CsI: Tl Detectors. IEEE Trans Nucl Sci 2007;54:398-403.

(86) Streun M, Brandenburg G, Larue H, Saleh H, Zimmermann E, Ziemons K, et al. Pulse shape discrimination of LSO and LuYAP scintillators for depth of interaction detection in PET. Nuclear Science, IEEE Transactions on 2003;50(3):344-347.

(87) Lewellen TK. Recent developments in PET detector technology. Phys Med Biol 2008;53:R287.

(88) Thompson CJ, Goertzen AL. Evaluation of a 16: 3 Signal Multiplexor to Acquire Signals From a SPM Array With Dual and Single Layer LYSO Crystal Blocks. Nuclear Science, IEEE Transactions on 2011(99):1-1.

(89) Liu H, Omura T, Watanabe M, Yamashita T. Development of a depth of interaction detector for γ-rays. Nuclear Instruments and Methods in Physics Research Section A: Accelerators, Spectrometers, Detectors and Associated Equipment 2001;459(1):182-190.

(90) Zhang N, Thompson CJ, Togane D, Cayouette F, Nguyen KQ. Anode position and last dynode timing circuits for dual-layer BGO scintillator with PS-PMT based modular PET detectors. Nuclear Science, IEEE Transactions on 2002;49(5):2203-2207.

(91) Ito M, Lee JS, Kwon SI, Lee GS, Hong B, Lee KS, et al. A four-layer DOI detector with a relative offset for use in an animal PET system. Nuclear Science, IEEE Transactions on 2010;57(3):976-981.

(92) Chung YH, Hwang JY, Baek CH, Lee SJ, Ito M, Lee JS, et al. Monte Carlo simulation of a four-layer DOI detector with relative offset in animal PET. Nuclear Instruments and Methods in Physics Research Section A: Accelerators, Spectrometers, Detectors and Associated Equipment 2011;626:43-50.

(93) Peng H, S Levin C. Recent developments in PET instrumentation. Curr Pharm Biotechnol 2010;11(6):555-571.

(94) Murayama H, Ishibashi I, Uchida H, Omura T, Yamashita T. Depth encoding multicrystal detectors for PET. Nuclear Science, IEEE Transactions on 1998;45(3):1152-1157.

(95) Tsuda T, Murayama H, Kitamura K, Yamaya T, Yoshida E, Omura T, et al. A four-layer depth of interaction detector block for small animal PET. Nuclear Science, IEEE Transactions on 2004;51(5):2537-2542.

(96) DOI PET detectors with scintillation crystals cut as triangular prisms. Nuclear Science Symposium Conference Record, 2008. NSS'08. IEEE: IEEE; 2008.

(97) Shimizu K, Ohmura T, Watanabe M, Uchida H, Yamashita T. Development of 3-D detector system for positron CT. Nuclear Science, IEEE Transactions on 1988;35(1):717-720.

(98) Moses W, Derenzo SE. Design studies for a PET detector module using a PIN photodiode to measure depth of interaction. Nuclear Science, IEEE Transactions on 1994;41(4):1441-1445.

(99) Yang Y, Dokhale PA, Silverman RW, Shah KS, McClish MA, Farrell R, et al. Depth of interaction resolution measurements for a high resolution PET detector using position sensitive avalanche photodiodes. Phys Med Biol 2006;51:2131.

(100) Dokhale P, Silverman R, Shah K, Grazioso R, Farrell R, Glodo J, et al. Performance measurements of a depth-encoding PET detector module based on position-sensitive avalanche photodiode read-out. Phys Med Biol 2004;49:4293.

(101) Shao Y, Meadors K, Silverman R, Farrell R, Cirignano L, Grazioso R, et al. Dual APD array readout of LSO crystals: optimization of crystal surface treatment. Nuclear Science, IEEE Transactions on 2002;49(3):649-654.

(102) Burr KC, Ivan A, Castleberry DE, LeBlanc JW, Shah KS, Farrell R. Evaluation of a prototype small-animal PET detector with depth-of-interaction encoding. Nuclear Science, IEEE Transactions on 2004;51(4):1791-1798.

(103) Yang Y, Wu Y, Qi J, St James S, Du H, Dokhale PA, et al. A prototype PET scanner with DOI-encoding detectors. Journal of Nuclear Medicine 2008;49(7):1132.

(104) Yang Y, Qi J, Wu Y, St James S, Farrell R, Dokhale PA, et al. Depth of interaction calibration for PET detectors with dual-ended readout by PSAPDs. Phys Med Biol 2009;54:433.

(105) Shao Y, Li H, Gao K. Initial experimental studies of using solid-state photomultiplier for PET applications. Nuclear Instruments and Methods in Physics Research Section A: Accelerators, Spectrometers, Detectors and Associated Equipment 2007;580(2):944-950.

(106) James SS, Yang Y, Wu Y, Farrell R, Dokhale P, Shah KS, et al. Experimental characterization and system simulations of depth of interaction PET detectors using 0.5 mm and 0.7 mm LSO arrays. Phys Med Biol 2009;54:4605.

(107) Salvador S, Huss D, Brasse D. Design of a high performances small animal PET system with axial oriented crystals and DOI capability. Nuclear Science, IEEE Transactions on 2009;56(1):17-23.

(108) Rafecas M, Boning G, Pichler B, Lorenz E, Schwaiger M, Ziegler S. A Monte Carlo study of high-resolution PET with granulated dual-layer detectors. Nuclear Science, IEEE Transactions on 2001;48(4):1490-1495.

(109) McElroy D, Hoose M, Pimpl W, Spanoudaki V, Schüler T, Ziegler S. A true singles list-mode data acquisition system for a small animal PET scanner with independent crystal readout. Phys Med Biol 2005;50:3323.

(110) Levin CS. Design of a high-resolution and high-sensitivity scintillation crystal array for PET with nearly complete light collection. Nuclear Science, IEEE Transactions on 2002;49(5):2236-2243.

(111) Braem A, Chesi E, Joram C, Séguinot J, Weilhammer P, De Leo R, et al. High precision axial coordinate readout for an axial 3-D PET detector module using a wave length shifter strip matrix. Nuclear Instruments and Methods in Physics Research Section A: Accelerators, Spectrometers, Detectors and Associated Equipment 2007;580(3):1513-1521.

(112) Braem A, Chesi E, Ciocia F, De Leo R, Joram C, Lagamba L, et al. Scintillator studies for the HPD-PET concept. Nuclear Instruments and Methods in Physics Research Section A: Accelerators, Spectrometers, Detectors and Associated Equipment 2007 2/1;571(1–2):419-424.

(113) Vilardi I, Braem A, Chesi E, Ciocia F, Colonna N, Corsi F, et al. Optimization of the effective light attenuation length of YAP: Ce and LYSO: Ce crystals for a novel geometrical PET concept. Nuclear Instruments and Methods in Physics Research Section A: Accelerators, Spectrometers, Detectors and Associated Equipment 2006;564(1):506-514.

(114) Trummer J, Auffray E, Lecoq P. Depth of interaction resolution of LuAP and LYSO crystals. Nuclear Instruments and Methods in Physics Research Section A: Accelerators, Spectrometers, Detectors and Associated Equipment 2009;599(2-3):264-269.

(115) Huber JS, Moses WW, Andreaco MS, Loope M, Melcher CL, Nutt R. Geometry and surface treatment dependence of the light collection from LSO crystals. Nuclear Instruments and Methods in Physics Research Section A: Accelerators, Spectrometers, Detectors and Associated Equipment 1999 11/21;437(2–3):374-380.

(116) Yamashita T, Uchida H, Shimizu K, Omura T. Scintillation detector for three-dimensionally measuring the gamma-ray absorption position and a positron CT apparatus utilizing the scintillation detector 1989.

(117) Séguinot J, Braem A, Chesi E, Joram C, Mathot S, Weilhammer P, et al. Novel geometrical concept of a high-performance brain PET scanner. Principle, design and performance estimates. NUOVO CIMENTO-SOCIETA ITALIANA DI FISICA SEZIONE C 2006;29(4):429.

(118) Beltrame P, Bolle E, Braem A, Casella C, Chesi E, Clinthorne N, et al. The AX-PET demonstrator--Design, construction and characterization. Nuclear Instruments and Methods in Physics Research Section A: Accelerators, Spectrometers, Detectors and Associated Equipment 2011.

(119) Agostinelli S, Allison J, Amako K, Apostolakis J, Araujo H, Arce P, et al. GEANT4—a simulation toolkit. Nuclear Instruments and Methods in Physics Research Section A: Accelerators, Spectrometers, Detectors and Associated Equipment 2003;506(3):250-303.

(120) Jan S, Santin G, Strul D, Staelens S, Assie K, Autret D, et al. GATE: a simulation toolkit for PET and SPECT. Phys Med Biol 2004;49:4543.

(121) Van Der Laan D, Schaart DR, Maas MC, Beekman FJ, Bruyndonckx P, Van Eijk CWE. Optical simulation of monolithic scintillator detectors using GATE/GEANT4. Phys Med Biol 2010;55:1659.

(122) Janecek M, Moses WW. Simulating scintillator light collection using measured optical reflectance. Nuclear Science, IEEE Transactions on 2010;57(3):964-970.

(123) Moisan C, Cayouet F, McDonald G. DETECT2000: the object oriented C language version of DETECT: a program for modeling optical properties of scintillators. Department of Electrical and Computer Engineering at Laval University.Quebec City, Quebec, Canada 2000.

(124) Cayouette F, Moisan C, Zhang N, Thompson CJ. Monte Carlo modeling of scintillator crystal performance for stratified PET detectors with DETECT2000. Nuclear Science, IEEE Transactions on 2002;49(3):624-628.

(125) Lerche CW, Ros A, Herrero V, Esteve R, Monzo JM, Sebastia A, et al. Dependency of energy-, position-and depth of interaction resolution on scintillation crystal coating and geometry. Nuclear Science, IEEE Transactions on 2008;55(3):1344-1351.

(126) Tsang G, Moisan C, Rogers J. A simulation to model position encoding multicrystal PET detectors. Nuclear Science, IEEE Transactions on 1995;42(6):2236-2243.

(127) Steinbach CO, Szlavecz A, Benyo B, Bukki T, Lorincz E. Validation of Detect2000-Based PetDetSim by Simulated and Measured Light Output of Scintillator Crystal Pins for PET Detectors. Nuclear Science, IEEE Transactions on 2010;57(5):2460-2467.

(128) Moisan C, Vozza D, Loope M. Simulating the performances of an LSO based position encoding detector for PET. Nuclear Science, IEEE Transactions on 1997;44(6):2450-2458.

(129) Peng H, Olcott PD, Spanoudaki V, Levin CS. Investigation of a clinical PET detector module design that employs large-area avalanche photodetectors. Phys Med Biol 2011;56:3603.

(130) Knoll GF, Knoll TF, Henderson TM. Light collection in scintillation detector composites for neutron detection. Nuclear Science, IEEE Transactions on 1988;35(1):872-875.

(131) Spanoudaki VC, Levin C. Investigating the temporal resolution limits of scintillation detection from pixellated elements: comparison between experiment and simulation. Phys Med Biol 2011;56:735.

(132) McIntosh B Validation of a simulation model of intrinsic ^{176}Lu activity in LSO-based preclinical PET systems. M.Sc. Thesis 2010, University of Manitoba, Winnipeg, Canada.

(133) Timing resolution improved by DOI information in an LYSO TOF-PET detector. Nuclear Science Symposium Conference Record, 2007. NSS'07. IEEE: IEEE; 2007.

(134) Budinger TF. Time-of-flight positron emission tomography: status relative to conventional PET. Journal of nuclear medicine 1983;24(1):73-78.

(135) Spanoudaki VC, Levin C. Investigating the temporal resolution limits of scintillation detection from pixellated elements: comparison between experiment and simulation. Phys Med Biol 2011;56:735.